

Sheffield Hallam University

Thin film calixresorcinarene membranes for chemical sensing.

WILKOP, Thomas.

Available from the Sheffield Hallam University Research Archive (SHURA) at:

<http://shura.shu.ac.uk/20538/>

A Sheffield Hallam University thesis

This thesis is protected by copyright which belongs to the author.

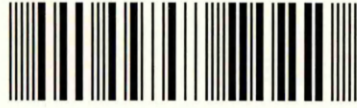
The content must not be changed in any way or sold commercially in any format or medium without the formal permission of the author.

When referring to this work, full bibliographic details including the author, title, awarding institution and date of the thesis must be given.

Please visit <http://shura.shu.ac.uk/20538/> and <http://shura.shu.ac.uk/information.html> for further details about copyright and re-use permissions.

LEARNING CENTRE
CITY CAMPUS, POND STREET,
SHEFFIELD, S1 1WB.

101 659 915 3



Fines are charged at 50p per hour

28 APR 2005

4.15

24 AUG 2005 Jp

ProQuest Number: 10701185

All rights reserved

INFORMATION TO ALL USERS

The quality of this reproduction is dependent upon the quality of the copy submitted.

In the unlikely event that the author did not send a complete manuscript and there are missing pages, these will be noted. Also, if material had to be removed, a note will indicate the deletion.



ProQuest 10701185

Published by ProQuest LLC (2017). Copyright of the Dissertation is held by the Author.

All rights reserved.

This work is protected against unauthorized copying under Title 17, United States Code
Microform Edition © ProQuest LLC.

ProQuest LLC.
789 East Eisenhower Parkway
P.O. Box 1346
Ann Arbor, MI 48106 – 1346

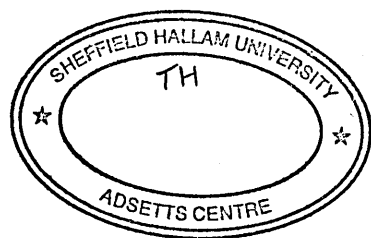
Thin Film Calixresorcinarene Membranes For Chemical Sensing

Thomas Wilkop

A Thesis submitted in partial fulfilment of the requirements of
Sheffield Hallam University
for the degree of Doctor of Philosophy

April 2001

School of Engineering



Copyright © 2001 by Thomas Wilkop

The copyright of this thesis rests with the author. No quotation from it should be published without his prior written consent and information derived from it should be acknowledged.

Declaration

I hereby declare that the work carried out in this thesis has not been previously submitted for any degree and is not currently being submitted in candidature for any other degree.

Signed

Candidate

The work in this thesis was carried out by the candidate.

Signed.....

Signed.....

Directors of Studies

Signed.....

Candidate

Don't panic

Cover Title of the fictitious "Hitchhikers Guide To The Galaxy" by Douglas Adams

Acknowledgements

My research work was conducted in the framework of a joint project between Sheffield Hallam University and the University of Sheffield. This gave me the opportunity to experience the best of two worlds, making it a very educational experience. My thanks go to Sheffield Hallam University which provided the financial support to carry out this study.

I would like to thank my supervisors Professor Asim Ray and Professor Rob Yates for their open mindedness, that gave me the freedom to follow up new developments in the process of the research and for providing the means to carry them out.

Countless hours in and around the cleanroom were excellently supported by the principal technician Geoff France.

The spelling and grammar in my thesis was markedly improved, upon the suggestions and corrections of Brian McQuillin, whom I thank for doing this most boring proof reading.

I have “learned the ropes” for most of the analytical tools and the instrumentation used from Dr. Aseel Hassan, who never tired to assist fixing the odd problem that occurred.

My special thanks goes to Dr. Aleksey Nabok with whom I had countless fruitful discussions, who always made time for this vital brainstorming sessions during which I learned more than from many books.

The chemical side of my work was excellently supported by discussions and active support by Dr. Steffi Krause who further provided the facilities for some of the experiments carried out. It was the chemical part of my work that gave me the greatest understanding of my work in the field of chemical sensors and also provided the most educational part.

Abstract

Novel applications for calix[4]resorcinarene (C[4]RA) sensing membranes have been investigated. A comprehensive deposition study was carried out, encompassing casting, spin coating and Langmuir Blodgett (LB) deposition. The spin coating thickness d depended on the angular velocity ω , following the description of $d = c \cdot \omega^x$ with coefficients of $x = 0.44$ and -0.48 for concentrations of 1mg/ml and 2mg/ml respectively. The analysis of the LB deposited films established a thickness of 0.95 nm for a monolayer. Furthermore the C[4]RA, was successfully employed as a deposition matrix for a non surface active polymer, poly-ortho-methoxy aniline (POMA), which can otherwise not be deposited by LB. The composite film showed good homogeneity and based on thickness and UV measurements a structural model for it was developed, in which two polymer strands aligned themselves per C[4]RA layer, resulting in a monolayer thickness of 2.1 - 2.2 nm.

The response of the C[4]RA and the composite membranes to a variety of organic and inorganic gaseous pollutants was investigated by Surface Plasmon Resonance studies, conductivity and capacitance measurements and UV spectroscopic studies.

The integration of cast films into the gate of a charge flow transistor, is the first application of pure calixarenes in a conduction based sensor. The turn on response of the transistor is modulated by a variety of organic vapours, at the saturation vapour pressure, showing selectivity between polar and non-polar solvents. i.e. chloroform, methanol, acetone and hexane, with no cross sensitivity to water vapour. The modulation lies within factors of 45 for CHCl_3 and 13 for CH_3OH . The conductivity increase is partially attributed to micro-condensation of the vapours inside the micro-porous membrane. A successful application of this implementation as an explosion guard sensor for acetone is demonstrated.

Gold electrodes with and without C[4]RA LB films have been characterised using impedance spectroscopy and cyclic voltammography. The modification of the gold electrodes by the C[4]RA film changes their constant phase element impedance, given

by $\frac{1}{(\omega \cdot Q)^n}$, with ω being the angular velocity. The observed values were from $Q =$

$0.725 \cdot 10^{-5}$ Farad and $n = 0.87$ to $Q = 0.828 \cdot 10^{-6}$ Farad and $n = 0.82$. Organic analytes like, chloroform and acetone in water can be successfully detected with these electrodes. It is shown by cyclic voltammetry, that the permeability of the C[4]RA LB films is modulated by the organic solvents.

Table of Contents

Abstract	I
-----------------	----------

Table of Contents	II
--------------------------	-----------

Chapter one

<i>1 Introduction</i>	<i>1</i>
------------------------------	-----------------

1.1 The structure of this thesis	3
----------------------------------	---

1.2 Bibliography	5
------------------	---

Chapter two

<i>2 Chemical Sensors</i>	<i>6</i>
----------------------------------	-----------------

2.1 The human nose	6
--------------------	---

2.2 Electronic noses	8
----------------------	---

2.3 Multivariate analysis	10
---------------------------	----

2.4 The human tongue	11
----------------------	----

2.5 Electronic Tongues	12
------------------------	----

2.5 Animal chemo-senses	13
-------------------------	----

2.6 Definition of a chemical sensor	14
-------------------------------------	----

2.7 Thermodynamics of sensor analyte interaction	15
--	----

2.8 Intermolecular forces between the analyte and the sensing membrane	17
--	----

2.9 References	17
----------------	----

Chapter three

3	<i>Calixarenes and Resorcinarenes</i>	22
3.1	Synthesis of Resorcinarenes	23
3.2	Conformations	24
3.3	Derivatives of Calixarenes and Resorcinarenes	25
3.4	Calixarenes and Resorcinarenes as Host Molecules	26
3.5	Calixarenes and Resorcinarenes in Sensing Membranes	29
3.5.1	Sensors for Metal Ions	30
3.5.2	Sensors for Organic Analytes	31
3.5.2.1	In aqueous media	31
3.5.2.2	In air	32
3.6	Non-chemical Sensor Orientated Applications for Calixarenes and Resorcinarenes	33
3.7	References	35

Chapter four

4	<i>Materials and film deposition</i>	39
4.1	Calix[4]resorcinareneC ₇ H ₁₅ and Poly-ortho-methoxy aniline	39
4.1.1	Electroactive conjugated polymers and deposition thereof	40
4.2	Thin film deposition principles	42
4.2.1	Casting	42
4.2.2	Spin coating	43
4.2.2.1	Factors influencing the film properties of spun films	45
4.2.3	Langmuir-Blodgett (LB) film deposition	47
4.2.3.1	Factors influencing the film deposition	48
4.3	Deposition details and experimental results	50
4.3.1	LB films	50
4.3.1.1	Deposition details for C[4]RA films	50

4.3.1.2	Film thickness analysis of pure C[4]RA multilayer structures	52
4.3.1.3	Deposition details for C[4]RA/POMA composite films	52
4.3.1.4	Thin film analysis of the composite membranes	55
4.3.1.4.1	Thickness analysis	55
4.3.1.4.2	Homogeneity analysis	57
4.3.2	Spun films	63
4.3.2.1	Deposition details of C[4]RA	63
4.3.3	Casting	65
4.3.4	Absorption spectra analysis of C[4]RA solution, spun and LB films	65
4.4	References	66

Chapter five

5	<i>The detection of gaseous organic and inorganic pollutants with C[4]RA based membranes</i>	69
5.1	Introduction	69
5.2	Spectrophotometer study of the absorption of toluene in LB deposited C[4]RA films	69
5.2.1	Experimental details	70
5.2.2	Results and discussion	70
5.3	DC conductivity modulation of the C[4]RA/POMA membrane upon analyte interaction	73
5.3.1	Response to electroactive gases	73
5.3.1.1	Experimental details	73
5.3.1.2	Results and discussion	74
5.3.2	Response to organic vapours	81
5.3.2.1	Results and discussions	81
5.4	Sensing with the composite membrane using a charge flow capacitor	86
5.4.1	Experimental details	86
5.4.2	Results and discussions	86

5.5	Surface Plasmon Resonance studies upon exposure to electroactive gases and organic solvent vapours	91
5.5.1	Experimental details	91
5.5.2	Results and discussion	92
5.5.2.1	Exposure to organic vapours	93
5.5.2.2	Exposure to NH ₃ vapours	99
5.6	References	102

Chapter six

6	<i>Silicon Device Processing</i>	103
6.1	The planar process	103
6.2	Production process of the CFT	103
6.2.1	Mask generation	104
6.2.2	Wafers	104
6.2.3	Patterning for the p wells	105
6.2.4	Boron doping	106
6.2.5	Patterning of the gate oxide region	107
6.2.6	Growth of the gate oxide	108
6.2.7	Patterning of the source drain contact	108
6.2.8	Metallisation	108
6.2.9	Patterning of the metallisation	109
6.2.10	Patterning of the passivation	110
6.3	Mask layout for a CFT	113
6.4	Standard device characterisation	114
6.5	The Charge Flow Capacitor	117
6.6	References and Bibliography	118

Chapter seven

7 Organic solvent vapour detection with a charge flow

<i>transistor</i>	<i>120</i>
7.1 Introduction	120
7.2 Gas sensitive transistors	121
7.2.1 Field effect transistors without gate electrode	121
7.2.2 Field effect transistors employing work function changes in the gate metal	121
7.2.3 Field effect transistors employing dielectric constant changes or conductivity changes in a sensing membrane	122
7.3 Experimental details	124
7.3.1 Vapour exposure	124
7.3.2 Measuring circuit	126
7.3.3 Explanation of the oscilloscope screen capture	126
7.4 Exposure results and discussions	127
7.4.1 OGFET behaviour	127
7.4.2 Description of the turn-on response modulation upon exposure to saturated vapours of chloroform	127
7.4.3 Process of charge transfer onto the sensing membrane	131
7.4.4 Further saturated vapour exposures to common solvents	132
7.5 Contributions to the charge transport across the membrane	133
7.5.1 Saturated vapour pressures of the solvents	133
7.5.2 Electronic conduction in the C[4]RA membrane	133
7.5.3 Micro-condensation of vapours in the C[4]RA membrane	134
7.5.4 Conductivity of the solvent in the liquid phase	136
7.5.5 Analysis of the charge transfer process	137
7.6 Exposure to dynamic acetone vapours	139
7.7 Turn-on response of the CFT with a cast poly-ortho-methoxy aniline membrane	142
7.8 References	144

Chapter eight

8 The detection of organic solvents in water with

C[4]RA coated electrodes _____ **146**

8.1	Introduction	_____	146
8.2	Experimental details	_____	147
8.2.1	C[4]RA modified electrodes	_____	147
8.2.2	Experimental set-up	_____	148
8.2.3	Electrolyte composition and preparation	_____	149
8.3	Results and discussions	_____	150
8.3.1	Characterisation of the electrode electrolyte electrode system	_____	150
8.3.2	Modulation of the working electrode conductance upon analyte interaction	_____	155
8.3.3	Discussion of the analyte C[4]RA membrane interaction	_____	161
8.4	References	_____	163

Chapter nine

9 Detailed permeability studies on the LB C[4]RA

membrane _____ **164**

9.1	Cyclic voltammetry	_____	164
9.1.1	Potentiostat controlled three electrode system	_____	166
9.1.2	Experimental details	_____	169
9.1.3	Results and discussion	_____	171
9.2	Impedance Spectroscopy	_____	178
9.2.1	Experimental details	_____	178
9.2.2	Results and discussion	_____	179
9.3	SPR analysis of the membrane permeability	_____	189
9.4	References	_____	192

Chapter ten

10 Summary, conclusions and suggestions for further

work _____ 195

Appendix 1

Synthesis and doping procedure of poly-ortho-methoxy aniline

Appendix 2

Description of the Surface Plasmon Resonance principle and measuring set-up

Appendix 3

Production parameters and material details for the Charge Flow Transistor and Charge Flow Capacitor

1 Introduction

The importance of chemical sensors is nowadays well recognised. In many cases sensors are now capable of completing measurements that were once been the domain of analytical chemistry. There are many advantages of the employment of sensors compared to analytical methods such as: portability, price of the instrumentation, speed of data acquisition and the handling by relatively unskilled operators. The large-scale employment of sensors enables an areawide mapping-out of analyte presence over time, a task that is prohibitively expensive with an analytical technique; even when probe sampling is employed.

The determination of the chemical composition of our environment, on the global scale and the microenvironment of our immediate surroundings, has provided the foundations for the description of complex interactions between our ever changing environment and us. Those are used to validate theories about the distribution of pollutants, cause and effect studies, degradation of compounds and toxicological studies.

Myriads of techniques and devices have been used to determine the chemical composition of samples. Comprehensive studies of chemical sensor concepts, their implementation and their fabrication can be found in the literature, in which three works are of outstanding scope and usefulness ^[1-3].

This work focuses on the novel employment of calixresorcinarene macromolecules for sensing membranes. There has been an ever-accelerating development in calixarene/resorcinarene research, with much attention devoted to chemical sensing. A measure for this is the number of publications and patents issued per year with these macro molecules as topics, Table 1.

Year	Patents awarded in the USA	Calixarene Publications
2000	10	151
1999	4	140
1998	14	153
1997	4	115
1996	5	109
1995	4	88

1994	2	62
1993	5	56
1992	3	39
1991	2	29
1990	3	7
1989	2	12
1988	1	5
1987	4	6
1986	2	2
1985	1	2
1984	3	1

Table 1 Overview of calixarene publications and patents (Source: Web of Science & US Patent Office)

One of the enormous potentials of these molecules is the ease with which their molecular structure can be changed by grafting different side chains onto their cyclic core structure or changing the dimensions of the core structure. With this more specific analyte interaction can be achieved. It is expected that calixarene based sensors will be playing a major role in the field of chemical sensors in the future, especially for organic target analytes.

The object of the research presented in this thesis, was the evaluation of novel applications for calixarene and resorcarenes in the field of chemical sensors. The focus was set on the proof of principle, together with an elucidation of the mechanism responsible for the sensor response. As the central element in this study a calix[4]resorcinaren with aliphatic sidechains of C_7H_{15} , (C[4]RA) was employed. Every application of thin film sensing membranes requires extensive knowledge about the deposition possibilities, therefore the different thin film formations were investigated in detail. In addition to the deposition of the pure C[4]RA, it was used to deposit a non-surface active polymer, poly-ortho-methoxy aniline, in a Langmuir Blodgett (LB) composite film. The composite membrane was extensively characterised regarding its structure, homogeneity and the response to organic/inorganic pollutants. The convenience of electrical sensors prompted the quest for a utilisation of the low conductive C[4]RA, in an electrical type sensor. The working concept of the charge

flow transistor (CFT) makes it an excellent transducer to be used with low conducting sensing membranes, therefore CFTs were fabricated and used in conjunction with the C[4]RA for the detection of organic solvent vapours. The detection of organic solvents was further extended into aqueous environments with C[4]RA LB coated electrodes. Extensive literature can be found, utilising calixarenes for the detection of metal ions in water, but only very few studies employing calixarene derivatives for the detection of organic species in water exist. The LB coated electrodes have been characterised and their sensing response was investigated with a two and three electrode system.

1.1 The structure of this thesis

The chapters are self contained, each conclusive in itself and only results spanning two chapters are referenced.

Chapter 1: It contains the present introduction giving an overview of the conducted research and outlines the structure of this thesis.

Chapter 2: The fundamentals of chemical sensors, thermodynamics and intermolecular forces are reviewed. The biological chemo-senses, smell and taste are explained and linked to the electronic equivalents, electronic nose and tongue. Applications and developments of these multi-sensor arrays are discussed and the pattern recognition routines, that emulate the action of the brain are described.

Chapter 3: It reviews calixarenes and resorcinarenes, including their history, synthesis, conformational structures and complexing properties. Sensor and non sensor related applications of calixarenes/resorcinarene are reviewed, with the sensing membrane review structured according to analyte type and environment (gaseous or aquatic).

Chapter 4: Various deposition techniques, casting, spin coating and LB are conceptually reviewed. The experimental details used for the deposition are specified. The results obtained for the various techniques with C[4]RA are presented and discussed. Films are characterised in terms of thickness, homogeneity and structure. Models are developed for the composite LB membrane (C[4]RA/POMA) and the film formation during spin coating.

Chapter 5: A variety of transduction/measuring techniques were used, UV-vis spectroscopy, Surface Plasmon Resonance (SPR), DC conductivity, and capacitance to investigate the response of the C[4]RA and the composite membrane to organic vapours

and/or electroactive gases. The results are presented and discussed in view of the membrane changes and comparative literature values.

Chapter 6: The production process of the charge flow transistor (CFT), together with that of the charge flow capacitor (CFC) is conceptually described. The focus lies on the mechanisms and the concepts of the production techniques used and the device details are presented. The results of the device characterisation prior to the application of the C[4]RA membrane are presented and discussed.

Chapter 7: An overview of transistor type chemo-sensors is given, with a detailed discussion of the working mechanism and applications of the CFT. Experimental details are explained, including the vapour generation and measuring set-up, and the results of the sensing response to a variety of statically generated vapours are presented and discussed. The modulation of the turn-on response of the CFT lies in the range of a factor of 46 for saturated vapours of chloroform and 13 for methanol. Furthermore an application of the CFT as a possible explosion guard sensor for acetone is demonstrated, with a modulation of the turn-on response by a factor of 1.36.

Chapter 8: The response of C[4]RA LB coated electrodes to a variety of organic analytes in water are analysed, in a two electrode continuous flow system with a LCR meter. The system is described; set-up and measuring chamber and the results are presented and discussed. It is shown that organic substances can be discerned based on their polarity (non-polar, polar).

Chapter 9: A detailed permeability study on the LB coated electrodes was carried out in a three electrode system with cyclic voltammography. The three electrode system is described together with the measuring technique and all its components (permeability marker, potentiostat and reference electrode). Further analysis of the modified electrode, within the same system, with impedance spectroscopy was employed to characterise the electrode and to discern any modifications induced during analyte addition.

Chapter 10: In it the obtained results are summarised, conclusions are drawn and suggestions for further work are given.

Appendix 1: Describes the in house synthesis of the poly-ortho-methoxy aniline.

Appendix 2: Contains a description of the Surface Plasmon Resonance phenomena. This tool was extensively used during this thesis but was not a major topic in its own right. It is an accepted analytical tool but the measuring principle is complex and merits therefore an explanation to fully understand the presented results.

Appendix 3: Gives a step by step description of the production process for the CFT, including all the production parameters and the used materials. This format allows for an easy reproduction and frees the Chapter 6 from distracting details.

1.2 Bibliography

[1] Sensors: A Comprehensive Survey Volume 1+2: Chemical and Biochemical Sensors, W. Goepel, J. Hesse, J.N. Zemel, VCH, 1992, ISBN: 3527267689

[2] Principles of Chemical Sensors, J. Janata, Plenum Publisher, 1989, ISBN: 0306431831

[3] Chemical Sensors, T.E. Edmonds, Blackie, 1987, ISBN: 041201601X

2 Chemical Sensors

The first chemical sensors, that have developed were the animal senses followed by the human senses. Recent attempts emulating these senses have resulted in the electronic equivalents, i.e. electronic noses and tongues. An overview of these senses and the transition to their electronic counterparts is illustrated here. For individual sensors a plethora of transduction principles and sensing membranes have been employed to analyse the chemical composition of samples. Not even a brief overview of all these can be given here. Underlying all variety of chemical sensors, are some fundamental principles, i.e. the sensing train, thermodynamics and intermolecular forces, which are briefly reviewed here.

2.1 The human nose

The ability to smell affects our brains and behaviours in many ways. It attracts us to fruits and flowers, adds to the recognition of tastes, warns us of fires and in association with hormone production plays a vital role in our sexual stimulation. The nose, our sensory organ for smelling, is shown in Figure 1.

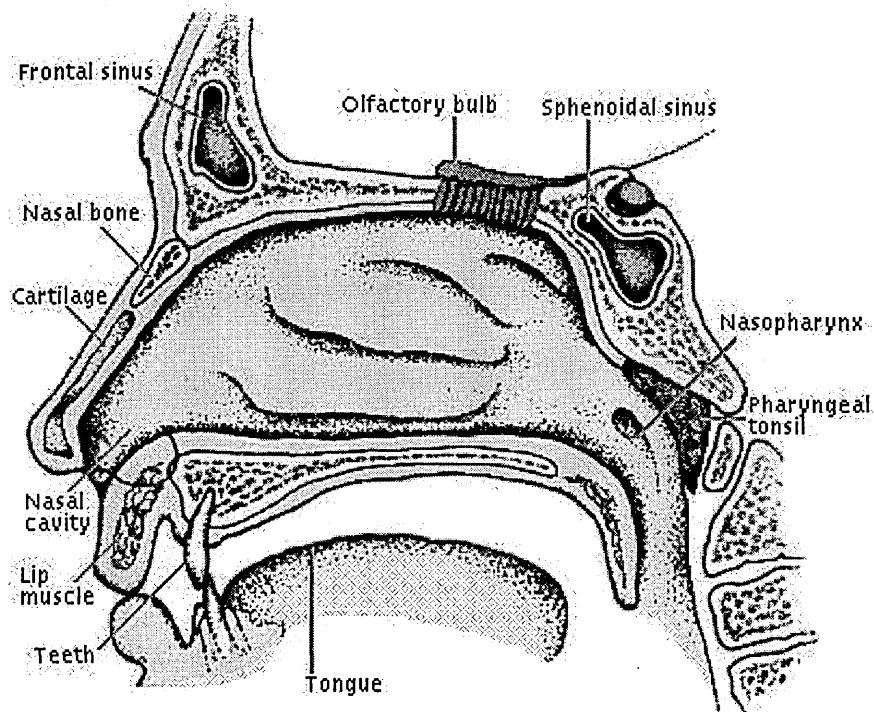


Fig. 1 Cross-section of the human nose, after Microsoft Encarta 95 [1]

When we inhale scent molecules are carried into the nasal cavity and impinge on the olfactory bulb, Figure 1. This is a mucus-lined patch of tissue at the top of the nasal cavity. Water-soluble molecules are captured in the mucus and transported to receptor cells, which identify the molecules and trigger an electric impulse along the nerve endings into the brain. It is the brain that analyses the complex pattern of incoming information and maps it out, generating an “image“ of a scent that can be recalled on repeated encounter. It is the later part of the smelling process that makes out the marvel of analysing complex odours, not the triggering of the receptor cells by individual molecules. On the basis of psychological tests it is believed that humans can detect between 4000 and 10000 odours ^[2]. In certain cases this number can lie higher, as for a professional perfumer. Since there are not that many different receptor cells in the nose, this high number must result from correlations that the brain makes for a complex pattern of cell responses. The nose is very good in determining the absence or presence of a certain scent, it can for example make out methyl mercapton in a concentration of less than 1ppb, but it is often saturated by concentrations of 50 times the odour threshold ^[2]. This makes it difficult for humans to differentiate intensities.

Every human has a different sensitivity to odours, but for some smells, as for methyl mercapton, there exists universally a high sensitivity. The smell resembles that of burning flesh and must have evolved in primordial times as a strong warning signal. Minute quantities are added to the household gas, to alert us in the case of a gas leak. The brain can also filter out certain odours, which is what happens when we become adapted to prevailing smells like the farmer to the typical farmyard smell. Smells can evoke strong emotions and memories as so vividly described in Proust’s “The remembrance of things past ^[3]”. This is accounted for by the fact, that one of the memory-centres in the brain, the hippocampus, is closely connected to the sense of smell. The stimulating effects are also employed in aromatherapy treatment. In many cases the human nose is the ultimate arbiter in the processes of quality control, as in a perfumery, brewery, coffee roastery and in the selection of cooking ingredients. Standards are difficult to establish in odour measurements, the most frequently used method is to employ a panel of several people, who rate smells or notes of smell, on a scale of 1-6 (no perception - overpowering perception) resulting in a smell map ^[4]. Leonardo ^[5] has established the odour threshold for 53 commonly encountered odourants, a selection for some of the chemicals used are reproduced in Table 1.

Odourant	Perceptible odour threshold [ppm]
Acetic acid	1
Acetone	100
Ammonia	46.8
Aniline	1
Carbon disulphide	0.21
Chloride	0.31
Formaldehyde	1
Hydrogen sulphide	0.00047
Methanol	100
Phenol	0.047
Trimethyl amine	0.00021

Table 1 Average odour threshold in air perceptible by humans

2.2 Electronic noses

In recent years there has been increasing interest, research, development, and application of electronic noses. Fundamental to the electronic nose (EN) is the odour characterisation of samples. This deviates from the detailed analysis of the quantitative sample composition. For example the coffee aroma of one particular sample can be described by 1500 peaks in a gas chromatography/mass spectrometer analysis [6], but it is impossible to map this information to the human odour impression describing the aroma in words like, nutty, full, sweet, etc. What is attempted with ENs is chemical imaging, by the detection of a large number of features with chemical sensors, forming a “hyperspace”, with a subsequent feature extraction leading to descriptive information. General attributes are established with ENs formulating the quality of a sample, not the exact composition. The application specific information is spanning medical applications, environmental monitoring, process control and quality control of foodstuff. The pattern recognition of the experimentally recorded and extracted features is of key importance, the methods employed for this are further described in 2.3. An EN consists therefore of a multi-sensor array with overlapping responses, (due to limited specificity) and an analysis performing, patterning recognition routine. There is no limit to the transduction principle employed in electronic noses, below is presented a selection of applications of ENs with details of the used sensor arrays.

- A 14-element conducting polymer sensor array was used for the discrimination of unspoiled milk and milk containing spoiling bacteria and yeast ^[7].
- Different volatile organic compounds have been mapped using a calorimetric multi-sensor arrangement ^[8]. The heat generated by the sorption or desorption of the vapours in a receptor layer was converted into a voltage by silicon thermopile chips and these signals were used as input parameters for the multicomponent analysis.
- A 15-element multi-sensor array, based on differently doped tin oxide sensors, was employed for a study discriminating between grape juice and the different stages in the fermentation of white wine ^[9].
- A novel non-invasive method for the diagnosis of diabetes, based on breath sampling with a tin oxide sensor array, was developed by Ping ^[10]. There selectivity was tailored toward acetone, by mixing catalysts in the Sn powder during the sol gel production process.
- Eight surface acoustic wave sensors (SAW), coated with different polymers formed a multi-sensor array ^[11], which was used to differentiate between organic reagents, different kinds of liquors and several perfume notes. The fact that three types of pattern recognition methods were used, principle component analysis, partial least squares and an artificial neural network, makes the study special in terms of scope and comparability.
- The gas emissions from the leather interior in cars were analysed with an EN, gas-chromatography-mass-spectrometry (GC-MS) and a human sensory panel, seeking for an on-line quality control ^[12]. As a sensor array a combination of 10 metal oxide semiconductor field effect transistors and 5 metal oxide sensors was employed. The EN proved to match the verdict of the human panel whereas the GC-MS data did not allow a discrimination between bad and good samples. A possible reason for this is the presents of chiral volatiles, which are indistinguishable in GC-MS measurements.

Apart form the development of new electronic noses; there has been a proliferation of studies employing commercial ENs to new and interesting fields. Details on commercially available systems can be found in reference ^[13]. Trends that have emerged very recently are the use of module based systems (MOSES), that allow easy configuration of a base system with a variety of pattern recognition algorithm and interchangeable sensor arrays ^[14] or the combination of an EN with an electric tongue ^[15]. So was for example the meat quality from camelids in South America (Alpaca,

Ilama) investigated using the commercial EN Bloodhound BH114 ^[16]. And the aroma changes in the Royal Gala apples, were investigated at harvest and during short-term storage ^[17]. Again the comparison between GC and EN analysis showed that the EN is not only more comfortable to handle but also more sensitive (about 40 times).

2.3 Multivariate analysis

Multivariate analysis methods are used equally for the electronic noses and tongues. They are dealing with two main issues; the search for a structure and correlation in the data or the generation of a model from calibration data, from which predictions based on the test data, can be made.

Principle component analysis (PCA) is used to explain variance in experimental data ^[18]. A number of experiments are combined into a data matrix with n variables. PCA is then used to extract a number of latent variables m , by decomposing the data matrix. Two types of vectors are then specified, the loading vector, which describes the direction of the principle components in relation to the original variables and the score vector which describes the direction of the principle components in relation to the observation. Two types of plot can be generated from these vectors, a loading plot showing the influence of the original variables onto the system and a score plot combining information about the observations and experiments, allowing a grouping of observations to be used for the classification of the system. Since no prior knowledge of the variables is required, this concept has a wide applicability. The most difficult part is to assign a meaning to the components, which are extracted this way.

Another approach is the creation of models from a sufficiently large amount of calibration data and then to predict the sample composition based on this model. Two methods are most frequently used for this, the projections to latent structures (PLS) and artificial neural nets (ANN). During a PLS analysis, a linear model is build on a PCA of the data and on a PCA of the actual component values ^[19] (concentrations, composition). Subsequently a regression model is developed between the two principle components, starting of with a linear regression, which is then further refined.

ANNs possess a multilayer structure, an input layer which is fed by the number of input signals, a number of hidden layers performing the analysis and an output layer, presenting the results in terms of the component concentrations. Both the hidden and the output layer are made up from a number of signal processing nodes, each sprouting

connections to other nodes. This structure is emulating the neural pathways in the human brain, with its myriads of interconnecting neurones. The processing nodes possess a variable connection strength, coupling weight, which is changing during a learning process. The learning process consists of the input of both experimental data and the actual composition of the sample. The coupling weights are adjusted during this process to minimise the sum of the square errors. ANNs are so highly adaptable and powerful, since their non-linear structure can model almost any mathematical transform. A very thorough introduction of ANNs, their design, application strength and their limits can be found in reference [20].

2.4 The human tongue

The human sense of taste developed to allow us to recognise poisonous and spoiled food. It relies on the round 10000 taste buds spread out on the tongue. These taste buds are binding-sites for the flavours and trigger electric impulses to the brain. The tongue is only able to distinguish between four different tastes, namely sweet, bitter, salty and sour. Each taste is most strongly made out with a different part of the tongue as shown in Figure 2.

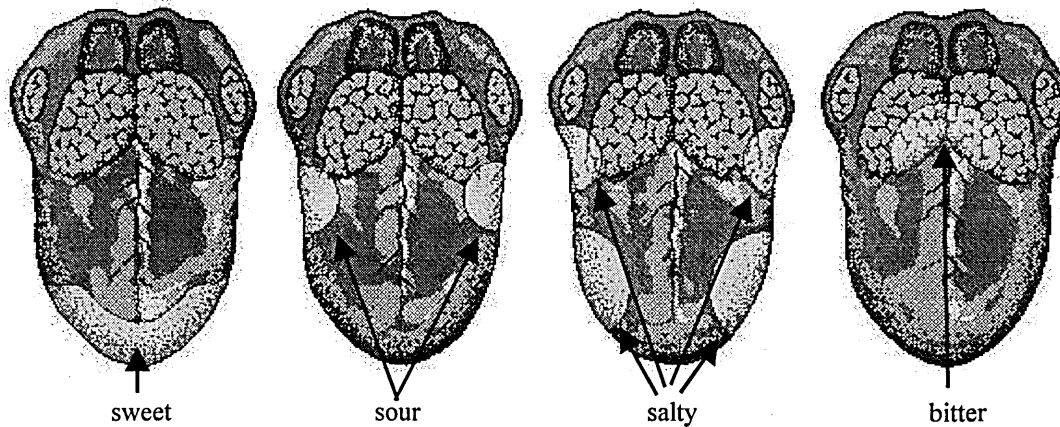


Fig.2 Receptive areas for the different taste sensations on the human tongue, after Microsoft Encarta 95 [1]

The sensitivity for the tastes varies widely, for bitterness it is 2ppm, sourness 6ppm, saltiness 2500 ppm and sweetness 5000ppm [2].

The huge variety of tastes that we can actually make out relies on the supplementary sense of smell. When this one is missing or impaired, as for example during a cold, we

perceive food as less tasty or simply plain. The smell contributes about 80 % to the sense of taste. Temperature and texture strongly influence our taste. Cold chocolate may have very little taste, may taste fine when at room temperature and taste unpleasantly sweet when hot.

2.5 Electronic Tongues

Electronic tongues are the wet chemical counterparts to the electronic noses, attempting to emulate a tasting sensation in liquid samples. There is a distinction between a taste sensor and an electronic tongue (ET).

A taste sensor system is an array of sensors used to classify the different gustatory sensations, sweet, sour, salt and bitter. An electronic tongue is a more general system classifying quality of one or another kind in a variety of samples, food, drinks, water, process fluids, that do not relate to the human tongue. The multi-sensor arrays used for ET can be classified into three groups:

Potentiometric sensor arrays

All ETs based on the potentiometric sensing principle measure the charging of a membrane. This limits the range of detectable compounds to ions or other charged species. Tongues have been build from arrays of chalcogenide glass sensors, coupled with a pattern recognition routine, measuring the metal ion concentrations in river water with possible applications in environmental and process monitoring purposes ^[21, 22]. Lipid/polymer membranes on multi-channel electrodes have also been utilised for ETs ^[23]. They showed low sensitivity to non-electrolytes and weak-electrolytes, but the usage of Langmuir Blodgett membranes improved the sensitivity ^[24].

Voltammetric sensor arrays

Voltammetry measures the electrode current at a fixed potential, its sensitivity is higher then potentiometric methods, but the selectivity is poor since all components in the solution undergoing oxidation/reduction contribute to the signal.

A system consisting of six metal electrodes, (gold, iridium, platinum, palladium, rhenium and rhodium), driven by a series of voltage pulses was employed for the discrimination between fruit juice samples in reference ^[25]. The large amount of

information contained in the generated voltammograms was extracted by multivariate calibration methods. In an explorative study, employing an electronic tongue ^[26], the filter efficiency and intactness of multiple filter stages in a water production process were characterised. A four-element voltammetric sensor array (gold, iridium, platinum, and rhodium) was used in conjunction with PCA. Water qualities could be correctly identified after each stage and this rating of water qualities was successfully used to rate the efficiency of the filters, identifying dysfunctional filters.

Optical sensor arrays

An electronic tongue based on light absorption was built based on a charge-coupled device with chemical indicators embedded in a resin bead. Via colour changes mixtures of Ca^{2+} , Cu^{2+} and simple sugars were analysed ^[27].

The above is only a small selection of the applications of ET, with further research and development many more applications in the environmental and process monitoring will emerge.

2.5 Animal chemo-senses

When compared to the abilities of some animal senses our human senses appear rather crude. One of the most sensitive chemo-senses can be found in butterflies, which are able to recognise a single molecule of a sex hormone, pheromone, with their antenna ^[28]. This allows the attraction of a mate over a distance of several miles.

There exists a long history for the employment of animals as “chemical sensor” of which the canaries for the detection of explosive mixtures of methane in mines are most famous. But there are many more examples utilising the superior senses of animals as in the search for truffle with pigs or the tracing of humans with hounds. Even today the sniffer dogs used for the detection of illicit substances can only be replaced in certain cases and with substantial effort ^[29].

Several hybrid systems have been developed, that use insects who pick up molecules with their antenna and where electronic microelectrodes tap into the nervous system picking up the electric impulse directed to the brain ^[30].

A newly evolved trend is the use of bio-indicators, as for example the presence or absence of fish as an indicator for the overall water pollution ^[31].

2.6 Definition of a chemical sensor

Chemical sensors are devices, which convert a chemical state into an electric signal. The chemical state is determined by the concentration of atoms, molecules or ions in the solid, liquid or gaseous phase. Though it is generally accepted that a sensor must show a reversible action, for many biosensors employing enzyme reactions, the name sensor is also applied despite the irreversibility of the complexation. For other sensors employing irreversible reactions the term dosimeter is used.

There are many different types of chemical sensors; a classification can be undertaken by the properties that are affected by the interaction of the analyte with the sensor. Frequently used properties are conductivity, potential, capacity, heat, mass and refractive index. The principle sensing-train for a chemical sensor is shown in Figure 3. Its key components are sampling, preconcentration, filtering, analyte complexation in the sensing membrane, transduction of membrane changes, feature extraction of the transducer data and a recognition routine based on these features. Some of the elements are optional but the overall performance of the measurement increases with the number of elements and increasing sophistication of every element.

Of all the elements involved in the sensing-train, the sensing membrane, that forms the recognition sites and the transduction mechanism are the most performance determining ones.

Analytical techniques have been partially adopted for employment in portable devices, like for example the detection of carbon dioxide via infrared spectroscopy, these hybrids do not require a sensing membrane, but are not regarded as sensors in the conventional sense.

Traditionally information about the chemical composition of a sample has been provided by analytical chemistry. Today the analytical methods for the chemist comprise tools such as chromatography, mass spectroscopy, nuclear magnetic resonance spectroscopy and so on. These tools have still an unrivalled sensitivity and selectivity but have also many drawbacks attached to it. Those are mainly the cost of the equipment, stationary operation only, extensive sample preparation and long time lags for the analysis results.

The major driving forces responsible for the development of new sensors are:

- Increasingly stringent guidelines and legislations imposed by governments and other stipulating bodies that bring with it the necessity of measurements to prove compliance.
- An increased desire in the understanding of our environment or micro-environment, as our living spaces ^[32], that requires measurements mapping out spatial distributions.
- Replacement of probe taking and subsequent chemical analysis by in-line monitors in production plants.

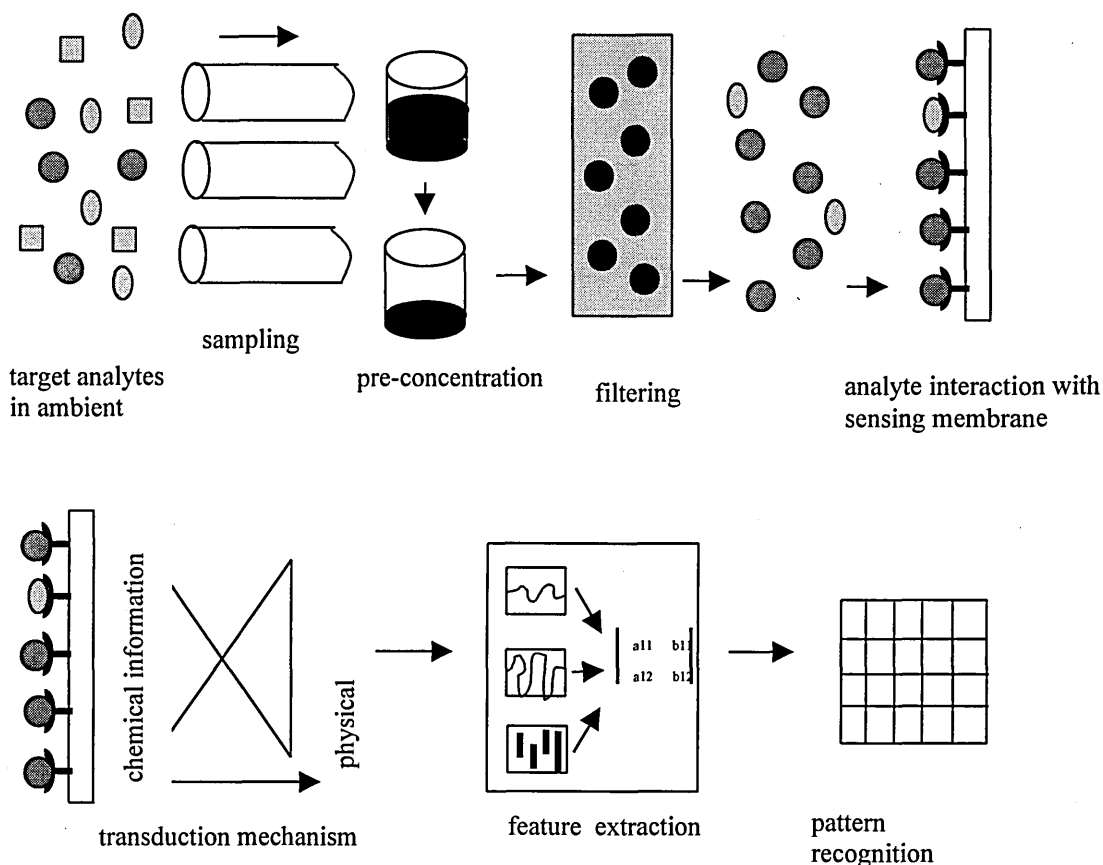


Fig.3 Sensing train with optional steps transferring information from the chemical domain into the physical

2.7 Thermodynamics of sensor analyte interaction

The decrease of the free energy (Gibb's free energy) is the driving force in all sensing processes. For a thermodynamically reversible process a dynamic equilibrium is established between the analyte in the ambient and the analyte sorbed in the sensing

membrane. There are two types of sorption, adsorption refers to sorption taking place at the surface only and absorption includes the migration of analytes from the surface into the bulk of the structure. The dynamic nature of this process means that continuously molecules are exchanged between the ambient and the membrane.

This interaction between the membrane (M) and the analyte (A) can be expressed as in (1) ^[33],



where the equilibrium constant K is defined by (2).

$$K = \frac{\text{Equilibrium constant forward reaction}}{\text{Equilibrium constant reverse reaction}} = \frac{k_f}{k_r} \quad (2)$$

For low to moderate concentrations the activity of a species can be equated with its concentration ^[34], this allows the expression of the equilibrium constant as in (3),

$$K = \frac{a_{MA}}{a_M \cdot a_A} = \frac{k_f}{k_r} \quad (3)$$

with a_{MA} being the activity of the sorbed analyte, a_M the activity of the binding sites, a_A the activity of the analyte in the ambient.

The sorption of species from the liquid or gaseous ambient is nearly always exothermic, since the motional energy of the molecules in the ambient is higher as compared to the energy of the bound species, therefore energy is given off. This means that the heat of adsorption ΔH_a , enthalpy, is negative (4).

$$\Delta H_a < 0 \quad (4)$$

The entropy change, ΔS_a , during the sorption of a species is negative, the entropy being a measure for the orderedness of a system, is increasing since bound molecules are in a more ordered state than freely moving about molecules in the ambient (5).

$$\Delta S_a < 0 \quad (5)$$

The Gibb's free energy, ΔG_a , of the sorption process^[35] is their difference, according to (6),

$$\Delta G_a = \Delta H_a - T\Delta S_a \quad (6)$$

with T being the absolute temperature.

From this, it can be seen that for the sorption to occur, $\Delta G_a < 0$, ΔH_a must be sufficiently negative and T small enough so that the enthalpy term compensates for the entropy term.

2.8 Intermolecular forces between the analyte and the sensing membrane

For a change in the Gibb's free energy upon sorption of the analyte in the sensing membrane, bonds of various nature must be formed between them. These bonds are based on the intermolecular forces between the participating molecules. The strength of these forces defines the reversibility of the reaction, with the energy for the bond breaking stemming from the thermal energy of the molecules. Frequently micro-heaters are therefore integrated into the sensor providing additional energy to improve the reversibility. All binding forces can be ultimately reduced to electrostatic forces between positive and negative charges as described by the Hellman-Feynman theorem [36].

Following is a description of how these electrostatic forces come about and interact between neutral molecules, with a quantitative description of the forces and interaction energies, presented in order of decreasing magnitude in Table 3. Neutral here means, neutral when the whole molecule is considered and that over an extended period of time. Knowledge about the interaction forces and their origin is vital in the understanding of the complexation process, where complexation sites in the membrane can be partially inferred from their electronic structure.

In most molecules the atoms are held together by the shared electron-pair-bond or covalent bond. This bond is so important and universally present in substances that the discoverer of its electronic structure, Lewis, called it simply "The chemical bond". It consists of a pair of electrons shared between two atoms, occupying two stable orbitals, one of each atom. Here the electrostatic attraction between electrons and nuclei balances the mutual repulsion between nuclei-nuclei and electrons-electrons and is the source for

the bond energy. The bond energy can be viewed as the resonance energy for the electrons between positions about the nuclei. The bond can be very strong, as in the case of diamonds, where four covalent bonds per atom are responsible for its hardness. For all sensing applications, the strength of this bond makes it an irreversible process, which can be highly specific, but changes both the make-up of the analyte and that of the sensing membrane permanently. If covalent bonds are formed a chemical reaction takes place, this finds application in colourmetric measurements, like in test stripes.

When two different atoms bond together covalently, there will be an unequal distribution of positive and negative electric charge on the molecule. A measure for the power of an atom to attract electrons to itself is its electronegativity. Pauling who first quantified this concept, assigned a number from 4 to 0.7 to every atom, deriving these values from wave functions calculations ^[37]. The unequal charge distribution in a covalent bond contributes with an additional ionic character to the strengthening of the bond via ionic resonance energy ^[38]. The ionic character can be viewed as two different poles on the molecule, one where the centre of the positive charge lies and one where the centre of the negative charge lies, thus creating an electric dipole. Water is a well-known example of a polar substance with one of the highest dipole moments, due to the large electronegative difference between hydrogen (2.1) and oxygen (3.5). For the intermolecular binding of molecules, which possess dipole moments, the attractive forces between opposite poles are inversely proportional to the third power of the distance between their centres, see Table 3. Molecules or parts of molecules where a large dipole moment exists are referred to as hydrophilic, because their character resembles that of water, in which they are highly soluble.

Even in symmetrical arranged molecules such as carbon dioxide, tetrachloromethane or oxygen there exists an electric dipole moment. In the case of oxygen the dipole comes from a mismatch of the centres of charge at any one time, since the electrons are changing their position within the orbitals, these are termed, instantaneous electric dipole moments. In the case of carbon dioxide, where the oxygen is attached to the right and left of the carbon molecule the dipole moments cancel each other out but only when the whole molecule is considered, there still exists one for each CO segment.

Even for single atomic gases, like helium there exist attractive forces between individual atoms, otherwise it would not liquefy. Though in the case of helium the forces are so small that it only liquefies under pressure at 3 K.

The forces described above are short-range forces so that any interaction between them requires the molecules to be very close together. London developed an initial theoretical model of these forces in 1929. Generally the forces increase with the number of electrons and therefore molecular weight, which is reflected in a correlation of the boiling point and the molecular weight (MW), with the boiling point increasing together with the MW ^[39].

A further possibility for the creation of a temporary dipole is to induce one in a molecule by the presence of either an ion or a strong dipole attracting or repelling the electrons of the passive molecule.

Type of interaction	Quantitative description	Order of magnitude (kcal mol ⁻¹)
Covalent bond	-----	50-200
Hydrogen bond	-----	1-10
Ion-ion	$E \sim z_1 z_2 / Dr$	10-100
London forces	$E \sim C_1 \alpha_2 / r^6$	1-10
Ion-induced dipole	$E \sim z_1^2 \alpha_2 / Dr^4$	0.1-1
Dipole-dipole	$E \sim \mu_1 \mu_2 / Dr^3 kT$	0-1
Hydrophobic bond	CH ₃ CH ₃	0.3

Table 3 Types of intra- and intermolecular interactions, with qualitative description by approximate interaction energies ^[33], with D = dielectric constant, α = polarizability μ = dipole moment, r = distance and z = charge

2.9 References

- ^[1] Microsoft Encyclopaedia Encarta 95, Microsoft, 1995
- ^[2] Marvels and Mysteries of the Human Mind, Readers Digest, 1996, p.140-144
- ^[3] M. Proust, The remembrance of things past, Vintage Books, 1982, ISBN: 0394711823
- ^[4] Experimental Methods For Engineers, J. P. Holman, McGraw-Hill, 1978, p. 452-456
- ^[5] Odour Threshold Determination of 53 Odourant, Leonardos G. D. Kendall and N. Bernard Chemicals, Air Pollution Cont. Assoc V. 24, p. 979, 1974
- ^[6] W. Göpel, Sensors & Actuators B 52, 1998, 125-142

- [7] N. Magan, A. Pavlou, I. Chrysanthakis, *Sensors & Actuators B*, 72, 28-34, 2001
- [8] J. Lerchner, D. Caspary, G. Wolf, *Sensors and Actuators B*, V. 70, 1-3, p. 56-66, 2000
- [9] I. Sayago, M. C. Horrillo, J. Getino, J. Gutiérrez, L. Arés, J. I. Robla, M. J. Fernández, J. Rodrigo, *Sensors & Actuators B*, V. 57, 1-3, p. 249-254, 1999
- [10] W. Ping, I. Yi, X. Huiboo, S. Farong, *Biosensing & Bioelectronics* 12, 9-10, 1031-36, 1997
- [11] Y. Yang, P. Yang, X. Wang, *Sensors & Actuators B*, 66, 1-3, p. 167-170, 2000
- [12] E. Kalman, A. Löfvendahl, F. Winqvist, I. Lundström, *Anly. Chimica Acta* V. 403, 1-2, p. 31-38, 2000
- [13] <http://www.sensors-research.com/links.htm#sensors>
- [14] J. R. Stetter, S. Strathmann, C. McEntegart, M. Decastro, W. R. Penrose, *Sensors and Actuators B*, 3, p. 410-419, 2000
- [15] C. Di Natale, R. Paolesse, A. Macagnano, A. Mantini et al. *Sensors & Actuators B*, V. 64, 1-3, p.15-21, 2000
- [16] K. Neely, C. Taylor, O. Prosser P.F. Hamlyn, *Meat Science*, V.58, 1, 53-58, 2001
- [17] H. Young, K. Rossiter, M. Wang, M. Miller, *Journal of Agricultural and Food Chemistry* 47, 12, 1999
- [18] S. Wald, K. Esbensen, P. Geladi, *Chemomet. Intelligent Laboratory Syst.* 2, 37, 1987
- [19] P. Geladi, B.B. Kowalski, *Anal. Chim. Acta* 185, 1986, 1
- [20] I. A. Basheer, M. Hajmeer, *J. of Microbiological Methods* 43, p. 3-31, 2000
- [21] A. Legin, A. Rudnitskaya, Y. Vasov, C. Di Natale, F. Davide. A. Damico, *Technical digest, EurosensorsX. Leuven, Belgium*, 1996
- [22] A. Legin, A. Rudnitskaya, Y. Vasov, C. Di Natale, F. Davide. A. Damico, *Sensors and Actuators B* 44, 291, 1997
- [23] K. Toko, T. Fukusaka, *Sensors Mater.* 3 171, 1997
- [24] S. Ilyama, T. Miyazaki, K. Hayashi, K. Toko, K. Yamafujii, A. Yamaguchi. *Sensors Materials*. 1, 21, 1992
- [25] F. Winqvist, P. Wide, I. Lundström, *Anal. Chim. Acta* 357, 21, 1997
- [26] C. Krantz-Rülcker, M. Stenberg, F. Winqvist, I. Lundström, *Anal. Chim. Acta* 426, 2001, p. 217-226
- [27] S. Yamakawa, A. Yamaguchi, *Sensors Materials* 4, 271, 1995
- [28] *The Jacobson Organ*, Lyall Watson, Penguin Books, 2000, ISBN: 0140284478
- [29] E. M. A. Hussein E.J. Waller, *Radiation Measurements*, V.29, 6, 1998, p.581-591
- [30] Matti J. Huotari, *Sensors & Actuators B*, V. 71, 3, p. 212-222, 2000

- [31] A. Kosmala, S. Charvet, M.C. Roger, B. Faessel, *Water Research*, V.33, 1, p.266-278, 1999
- [32] Christian Monn, *Atmospheric Environment*, V. 35, 1, p. 1-32, 2001
- [33] J. Janata, *Principles of Chemical Sensors*, Kluwer Academic, 1989, ISBN: 0306431831, p.3
- [34] *Acoustic Wave Sensors*, D.S. Ballantine, R.M. White, S.J. Martin, A. J. Ricco, G. C. Frye, E. T. Zellers, H. Nohltjen, Academic Press, 1993, ISBN: 0-12077460-7, p. 257
- [35] *Surfaces, Interfaces, and Colloids*, Drew Myers, VCH, 1991, ISBN: 1-56081-033-5, p. 125
- [36] The so-called Hellman-Feynman theorem of quantum mechanical forces was originally proven by P. Ehrenfest, *Z. Phys.* 45, 455 (1927), and later discussed by Hellman (1937) and independently rediscovered by Feynman (1939).
- [37] *The Nature of the Chemical Bond*, Third Edition, Linus Pauling, Cornell University Press, 1960, p. 88
- [38] *The Nature of the Chemical Bond*, Third Edition, Linus Pauling, Cornell University Press, 1960, p. 80
- [39] *Chemistry An Experimental Science*, G.M. Bodner, H.L.Pardue, , Wiley, 1995, ISBN: 0471593869, p.146

3 Calixarenes and Resorcinarenes

Calixarenes and resorcinarenes are reaction products from phenols/resorcinarenes and formaldehyde under alkaline conditions. The principle of the condensation reaction is shown in the Figures 1 and 2 for calixarenes and resorcinarenes respectively ^[1, 2, 3].

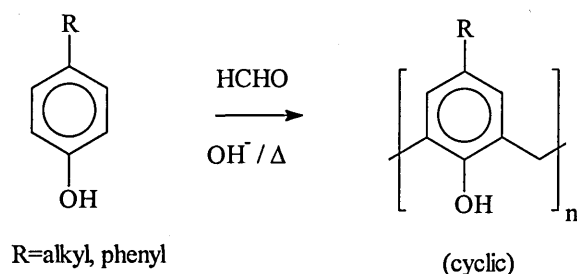


Fig. 1 Condensation reaction for calixarenes

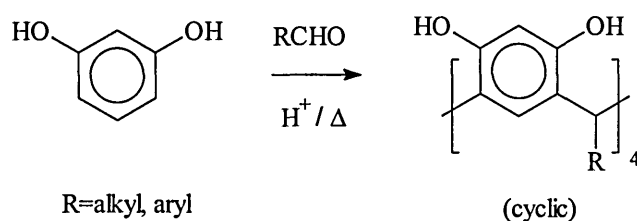


Fig. 2 Condensation reaction for resorcinarenes

The reaction conditions determine if the product is a complex mix of oligomeric molecules or the desired macrocyclic product. The resulting cyclic oligomers are named calix(n)arenes where n specifies the number of phenolic units. Gutsche introduced the name calixarene, based on the resemblance of the molecule to the Greek vase calixcrater. The striking similarity between their shapes can be seen in Figure 3.

The bowl like shape of the oligomer, in Figure 4 is shown a tetramer, makes an inclusion of guest molecules possible, and it is this property that is of fundamental interest for any sensing application.

Resorcinarenes form mostly tetramers ^[4], though pentamers and hexamers have been reported ^[5, 6]. In calixarene chemistry, which is based on phenol derivatives the size of the macrocycle can vary from 4 to 8 units ^[2]. Large amounts of the products can be made in a “one pot” reaction avoiding complex multi-step synthesis. The possibility of

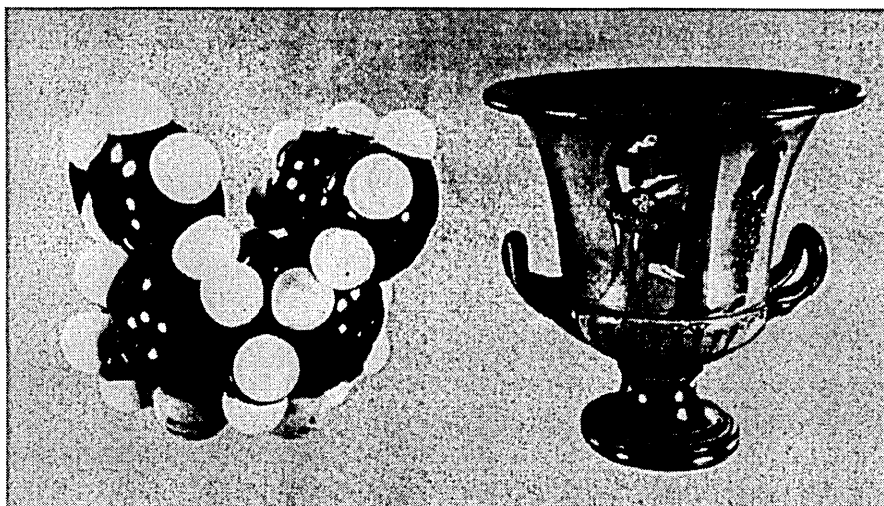


Fig. 3 Comparison between calixcrater and calixarene molecule

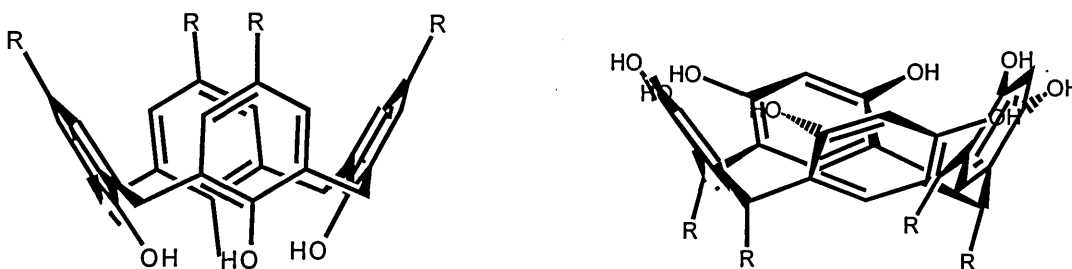


Fig. 4 Bowl structure of calix(4)arene and calix(4)resorcinarene

easy modifications make them an interesting starting material in the design of different types of host molecules. Early phenol-formaldehyde chemistry in the 1870s ^[7] must have resulted in the formation of cyclic oligamers, but it was not until the 1920s ^[8] that first structural predictions were made and not until the 1940s ^[9] that their cyclic structure was understood.

Modern calixarene chemistry has only started in the 1970s with the work of Gutsche and co-workers. Excellent review articles about the history of calixarene chemistry can be found in the references ^[2, 10, 11].

3.1 Synthesis of Resorcinarenes

The reaction of resorcinol and formaldehyde with the catalytic aid of an acid, results in polymers or cyclic tetramers, depending on the reactivity of the aldehydes used ^[12]. The yield for this reaction is high whereas pentamers and hexamers are only produced with

low yields. When compared with the corresponding calixarene synthesis the reaction is more versatile since a larger variety of aldehydes can be used as a starting material. A typical example of such a synthesis is given below.

A solution of resorcinol acetaldehyde and 37 % HCl in ethanol, is heated to 80 °C and held at this temperature for 16 hours resulting in C-methyl resorc(4)arene as the condensation product [13].

Structural proof of the cyclic structure for resorcinol derived tetramers was first obtained in 1968 for octa-O-butyrate [14]. One of the difficulties in getting the structural proof was the necessity of suitable crystals in the x-ray crystallography analysis. It is now accepted that the intramolecular hydrogen bonds between neighbouring resorcinol units are the reason for the formation of a cyclic tetramer [15].

3.2 Conformations

One of the most important features of calixarenes is their ability to recognise organic and inorganic molecules on the basis of their size and shape. For this purpose the conformational properties are relevant.

Calixarenes/resorcinarenes are not completely rigid structures like crystals. Instead their structure is flexible depending on the length and type of substitute attached, temperature and solvent used in their synthesis and their conformation. A great deal of work has been carried out, much with the help of molecular modelling [16], to add to the understanding of these conformations.

The three most likely and stable conformations for resorcinarenes are shown in Figure 5.

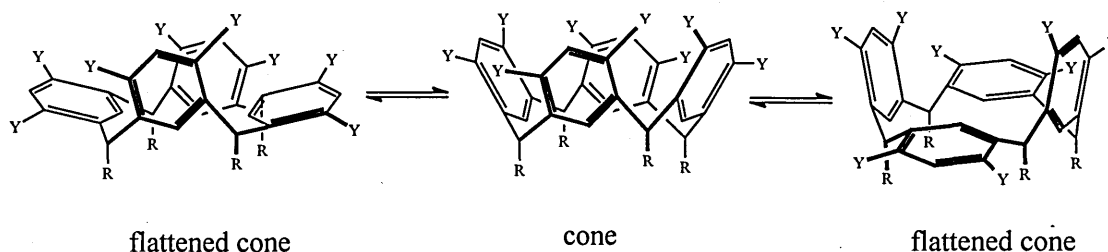


Fig.5 Possible cone formations for calix(4)resorcinarenes

Other structures have been observed in solution and are possible but have so far been of only minor relevance. Further information regarding possible conformations can be found in reference [2].

3.3 Derivatives of Calixarenes and Resorcinarenes

Calixarenes and resorcinarenes are extremely versatile compounds. The chemical modification of the substitutions in the upper and lower rim, Figure 6, allows the tailoring of the conformation and therefore determines the kind of interaction with possible guest molecules.

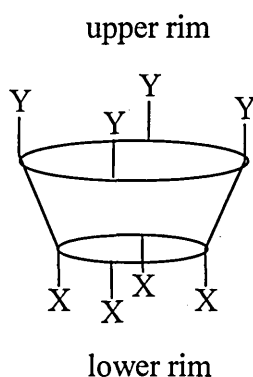


Fig.6 Schematic diagram of a calix(4)arene bowl

Ever larger molecules based on calixarenes and resorcinarenes are appearing and their properties and the ability to be made to measure are far superior to that of other macrocyclic molecules such as crownethers or cyclodextrines [17].

Calixarenes can be modified in mainly two ways, by the introduction of a residue at the phenolic hydroxy group and the substitution of groups in the p-position with respect to the phenolic hydroxy group.

A common way of modifying resorcinarenes is to substitute alkyl and aryl groups on the methylene bridges. Those substitutions determine the conformational properties and guest qualities [2]. In Figure 7 are shown a few of the possible modifications. The size of the molecule increases from 7a, for low n over 7b, with 7c being by far the largest. The bridging of neighbouring resorcinol units has lead to an extension of the cavity, linking up to three molecules together [18].

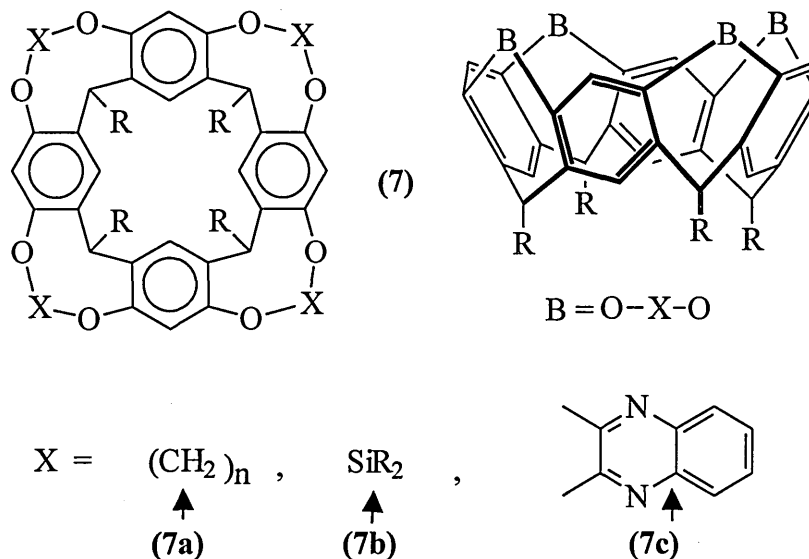


Fig.7 Example of possible resorcinarene modifications

3.4 Calixarenes and Resorcinarenes as Host Molecules

Molecular recognition that can be found in biological systems has evolved over millions of years. These extremely specific reactions, like the antibody antigen reaction, rely on the complexation of molecules that consist of thousands and sometimes millions of atoms. In contrast to this, supramolecular chemistry combined with complexation chemistry is a rather young research field. Starting with Petersen's discovery of crownethers there was and is a steady development in this field. The comprehensive program of host guest chemistry led by Cram, for which he received the Nobel Prize in 1987 ^[19], was a landmark study in this field.

The suitability of the calixarenes/resorcinarenes, as starting blocks, in the design of guest molecules with their ease of functionalisation has been stated earlier.

In the very beginning of the complexation studies, almost all the attention focused on metal ions. Work regarding the complexation with neutral molecules is of much later origin, and has not attracted the same scale attention. Research concentrating on metal ion complexation focuses on three main targets. Firstly, the detection of metal ions in biological environments with the ultimate goal of an in situ, online sensor.

Secondly the extraction of metal and heavy metals out of solutions for the purpose of cleaning up effluents or the extraction of precious metals. So far reports for the extraction of actinides, lanthanides ^[20] and the extraction of caesium out of nuclear waste solutions have emerged ^[21].

The third target is the development of membranes with transport structures for ions, mimicking that of ion channels in cell walls [22].

Izatt discovered that transport properties for cations in calixarenes are strongly pH dependent, where neutral solutions were almost ineffective but strong basic solutions lead to a significant ion transport [22].

An extensive study on the influence of the cavity size on the extraction of ions was performed by Mc Kervey et al. [23]. By using p-tert-butylcalix(4,6,8)arene to extract various alkali ions from the aqueous phase they were able to generalise their findings in the following way.

Calix(4)arene shows the greatest selectivity for Na^+ , calix(6)arene show less affinity for Na^+ than for K^+ with plateau selectivity for Cs^+ and Rb^+ and calix(8)arene showed the least selectivity for the four ions. A universally poor response to Li^+ ions characterised all of them. There is a good correlation between the cavity size and the ionic diameter of the ion included, with the selectivity at its highest where the closest match is found. Apart from the complexation inside the bowl, binding can occur on functional groups in the lower rim. Reports of this type of complexation were made in reference [24]. A combination of both has also been established for calix(5)arenes complexing with acetone, where one acetone molecule is held inside the cavity and another one externally to it. Lately several papers claimed complexation of various analytes between the aliphatic side chains and within the cavity [25]. In general it seems now to be established that the size of the calixarene, the substitutions in the para positions and the rigidity of the molecule all play a part in determining the complexation reaction.

For aromatic organic molecules the CH/π or the CH_3/π interaction between the aromatic ring of the guest molecule and alkyl group/methyl group are responsible for the occurring binding. This behaviour can also be predicted from theoretical calculations [26]. Factors influencing the formation and tenacity of inclusion complexes for neutral molecules were systematically studied for calix(4)arenes in reference [27].

Resorcinarenes seem to have a greater tendency to form complexes with organic molecules compared to calixarenes. Kenichi [21] et al. have carried out detailed studies on resorcinarenes with $\text{C}_{11}\text{H}_{23}$ alkyl chains, in these they found strong interactions for alcohol's, sugars and carboxylic acids. This suggests that the dominant interaction is due to hydrogen bonds involving at least one OH group of the host and one of the guest. The second mechanism contributing to the binding is the CH/π interaction. Table 1

gives some complexation properties for simple calixarenes, all of the type p-tert-butylcalix(n)arene but with varying repeating units of 4-8.

	calix(4)arene	calix(5)arene	calix(6)arene	calix(7)aren	calix(8)aren
Analyte	chloroform ^[28]	isopropyl alcohol ^[31]	chloroform ^[28]	methanol ^[32]	chloroform ^[28]
Analyte	benzene ^[29]	acetone ^[29]	methanol ^[28]		
Analyte	toluene ^[30]				
Analyte	xylene ^[28]				
Analyte	anisole ^[29]				

Table 1 Complexing properties of p-tert-butylcalix(n)arene

One outstanding difference in the complexation, for different combinations, is the permanence of it. Whereas the octamer loses the chloroform in minutes at room temperature and atmospheric pressure, the tetramer and hexamer hold on to some of their guest so tightly that even heating in a vacuum does not remove them completely ^[28]. The close fitting of a benzene molecule inside the p-tert-butylcalix(4)arene was shown by x-ray crystallography ^[30]. Apart from the endo-calix complex that can be formed several types of exo-calix complexes have also been reported, a schematic exo- and endo- complexation is shown in Figure 8. One such exo-calix complex is the 1,1,3,3-tetramethylbutyl-calix(4)arene in which toluene molecules are captured between rather than inside the calixarene molecules. Another complexation mode is found for p-tert-butylcalix(4)aren and anisole, here a single anisole molecule is shared between two, rim to rim aligned calixarene molecules ^[33].

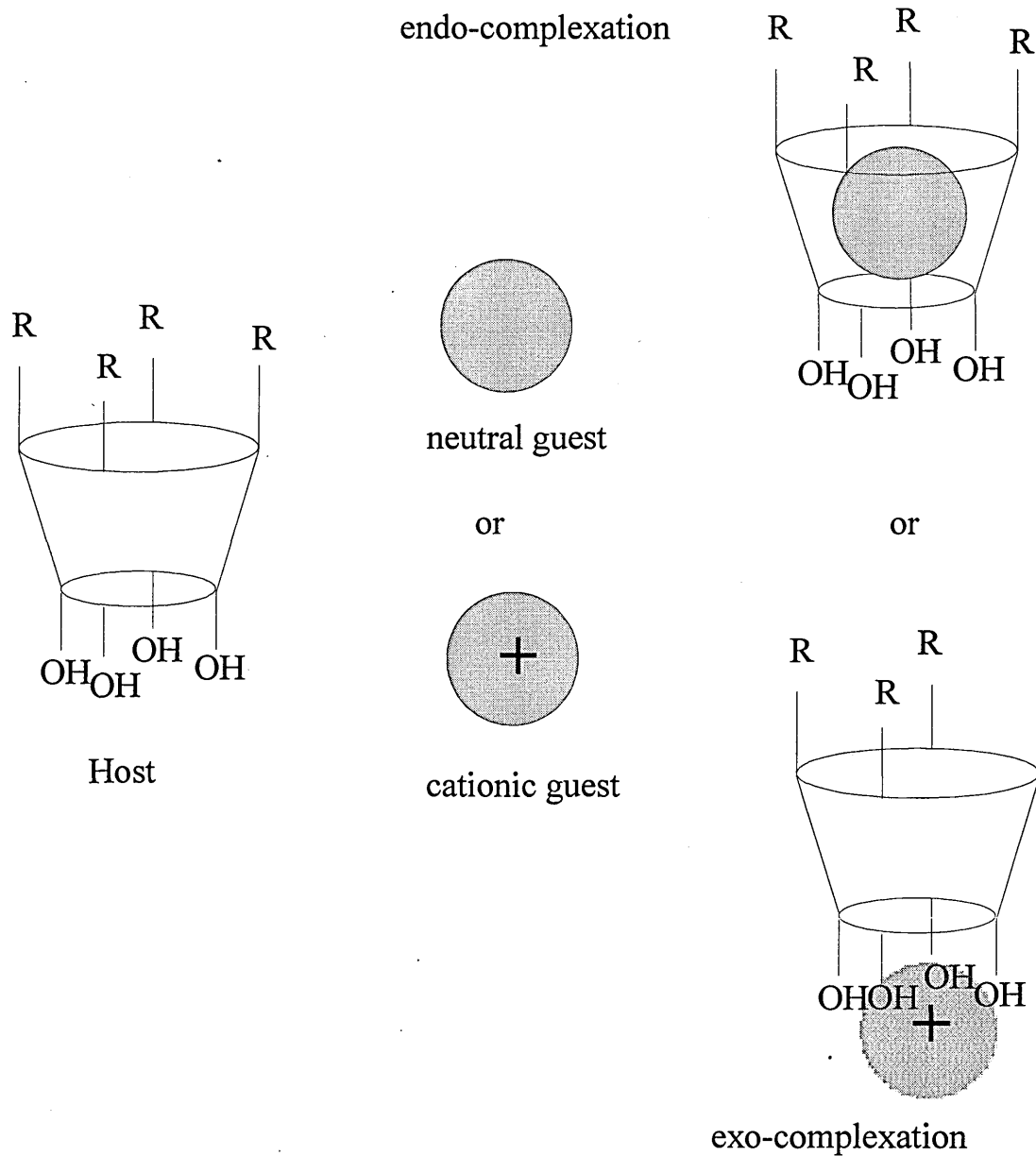


Fig. 8 Schematic of exo- and endo- complexation

3.5 Calixarenes and Resorcinarenes in Sensing Membranes

The ability of calixarenes/resorcinarenes to act as baskets is their most intriguing property. The discussion about synthesis and shaping has only been a prologue to the critical matter of their application in sensing membranes. Since this thesis focuses on novel applications of calixarene sensing membranes, some established sensing techniques are described in the following.

The sensing applications, which use calixarenes/resorcinarenes, can be categorised into metal ion sensors in aqueous media and the detection of organic guest in air and aqueous media.

3.5.1 Sensors for Metal Ions

A variety of optical methods have been used to register the selective binding of metal ions, these are based on the principle of changing the absorption or fluorescence properties of the membrane upon complexation. This is only possible when a chromogenic or fluorescent group is involved in the reaction. The basis of such recognitions is that upon complexation the chemical environment of the molecule is significantly altered to change the UV-vis adsorption spectrum or the fluorescence spectrum. A variety of chromogenic and fluorescent groups have been used including azophenol ^[34], pyrene ^[35] and hexamethyl ^[36]. Other indirect ways involve a mediator ^[37] where lithium ions bind, in the presence of triethylamine in an equilibrium reaction and indicate the extent of the reaction through the appearance of a new band in the visible spectrum.

The operation of the majority of metal ion sensors is based on potentiometric or voltammetric-amperometric principles. These take advantage of the electrostatic forces that accompany the ions. Electrostatic forces are stronger and more easy to register than mass changes and this explains the dominance of this sort of measurements for the ion detection. Ion selective electrodes (ISE) have been developed for a variety of ions, like Na⁺ ^[38, 39], K⁺ ^[40], Cs⁺ ^[41] and uranyl⁺ ^[42]. These ISE follow generally the Nernst equation ^[43], this describes the resulting voltage on an electrode in terms of the ion concentration in the solution. A five times stronger response, as predicted from the Nernst equation, was observed for a thermally evaporated calix(4)arene membrane on electrochemically produced porous silicon as a membrane support ^[44]. The changes upon Na⁺ complexation were measured via capacitance changes. The extremely high sensitivity was attributed to the rather three- than two-dimensional structure of the membrane support.

To improve upon the signal amplitude field effect transistors have been modified to give ion sensitive field effect transistors (ISFETs). A very attractive aspect of this is, that the production costs are reduced, by employing the batch processing techniques from the solid state device fabrication. An inherent problem that has so far hindered the full utilisation of the compact size of the transistor is the necessity for a reference electrode.

Currently, no perfect microdimensional reference electrode has been found, though screen-printed ones from silver-silver chloride ink have shown promising potential. Two FETs, one modified, one blank, working in differential mode have been suggested to overcome this problem. Since 1997 three ISFETs employing a calixarene covering as a gate, have appeared in the literature. In all cases the calixarenes have been thermally evaporated and extensive studies were carried out to show that no decomposition took place during the evaporation.

In accordance with the results for the ISEs, calix(4)arene showed selectivity to sodium ions ^[45], calix(6)arene to nickel ions ^[45], p-tert-butyl-calix[8]arene showed linear sensitivity to Ca²⁺ ions ^[46], p-tert-butyl calix(10)arenes for silver(I) ions ^[47] and p-tert-butyl calix(12)arenes for iron(III) ions ^[47].

Recently microsensors based on an electrolyte-insulator-semiconductor (EIS) structure have been reported ^[48]. Their working principle depends on electrochemical capacity measurements, not unlike that of the ISEs. The membranes were thermally evaporated onto a silicon substrate, with claims being made about an improved membrane lifetime and confirmation of the previously stated complexation predilections, as mentioned for ISEs and ISFETs was obtained.

The behaviour of p-tert-butylcalix(n)arenes monolayers on the air water surface were studied upon complexation with Na⁺, K⁺, CS⁺ and C60 molecules ^[49]. By measuring the pressure area isotherms of monolayers under different complexing conditions it was possible to determine the size of the empty molecules and that of the complexed molecules. The results showed a marked increase of the molecule area upon complexing and this indicates, that filling of the cavity changes the conformation and orientation of the molecules substantially.

3.5.2 Sensors for Organic Analytes

3.5.2.1 In aqueous media

So far very little attention has been given to the detection of organic analytes in aqueous solutions, using calixarenes. The only extensive reported study carried out, concentrated on quartz crystal microbalances (QCMs) as the transduction mechanism. In it Roessler et al. ^[50] compared a variety of polymers, operated below their glass transition temperature and calixarenes as coatings for the QCMs.

The calixarenes were spray-coated onto the QCMs and showed a high sensitivity, down to the ppm region, for aromatic analytes and chlorinated hydrocarbons with good

recovery upon flushing. This study made clear the preferential dispersion properties of calixarenes over that of polymers. For a similar study ^[51] cast and LB membranes, on QCMs were used for the detection of organic amines in water. The reported sensitivities were higher for the more ordered LB films over that of the spun films.

The inclusion of ethanol into different calix(4)arenes from aqueous solutions was confirmed by NMR studies by Arena ^[52].

3.5.2.2 In air

One of the most pressing issues in the field of environmental monitoring is the detection of solvent vapours and other organic compounds in real time, without the employment of cumbersome analytical tools. The concentration ranges of interest vary from a few ppm for the threshold limit value (TLV), to a few percent for the lower explosion limit. Many volatile organic compounds have now been classified as carcinogenic, teratogenic or are suspected carcinogens. One of the early studies on the complexation of organic molecules in thin films of calixresorcinarenes ^[53] showed that LB films of calixresorcinarenes could be employed for the detection of benzene vapours utilising QCMs and ellipsometry.

Dalcanale et al. ^[54, 55] found in their studies two major trends between the molecular structure and the complexing behaviour. Long alkyl chains at the lower rim lead to an increase in the sensitivity by forming more disperse and porous layers and that specific CH- π interactions improve the selectivity for analytes with polarised C-H bonds. These trends were independently confirmed by Dicker ^[56]. Göpel et al. ^[57] found on the basis of QCM measurements that the sensitivity increases with an increasing thickness but also the ageing effects.

Since its inception in 1982 the analytical tool of Surface Plasmon Resonance has become a valuable technique for the study of the complexation reactions in thin films. This analytical tool has so far not emerged in a way that can be described as a sensor, but early signs for this to happen in the near future can be seen in the granting of a patent for a mobile device ^[58] and Texas Instruments efforts ^[59] in developing a handheld set with disposable sensors heads. Unfortunately both devices still rely on an external PC for their data processing.

The first calixarene thin film study based on the SPR technique was carried out by Shirshov et al. ^[60], it investigated the static and dynamic response of a calix(4)resorcinolarene sensing membrane to toluene, natural gas and petrol vapours.

The sensitivity was in the order toluene >> natural gas >> petrol vapours, studies in the same direction continued. The studies carried out have given valuable insights in the observed phenomena of film swelling and changes in the refractive index in the membrane. So far many models have been proposed for the factors influencing the selectivity and sensitivity. In a study on tetra- phosphorylated calix[4]-resorcinolarene LB films ^[61] the selectivity of the SPR response to various hydrocarbons was attributed to the difference in the condensation temperatures of the analytes rather than to the molecular dimensions. Condensation of the vapours in the film, was proposed as a further mechanism, contributing strongly to the response This mechanism was further confirmed in reference ^[62], which added QCMs measurements and SPR studies, expanding the model of condensation to higher vapour concentrations. A variety of tert-butylcalix[n]arene (n=4, 6 and 8) in a combined QCM and ellipsometer study were used in ^[63]. The changes in the optical film parameters were investigated for benzene, toluene and chloroform, concluding that at room temperature, recovery was incomplete and only heating of the film to 160 °C lead to a complete recovery.

Sabot ^[64] carried out an extensive complexation study based on the SPR analysis of spun films and their response to cyclic hydrocarbons using a variety of bridged resorcinarenes with straight and cyclic substitutions on the upper rim. In it the response to a standard concentration of 50 ppm of toluene, benzene and acrylonitrile was investigated for each of the compounds. The study showed a direct correlation between the structural features of the membrane and the selectivity for an analyte, emphasising the importance of the cavity in the process of adsorption for the host guest interaction. So far the exact nature of the complexing reactions has been subject to an inconclusive discussion.

3.6 Non-chemical Sensor Orientated Applications for Calixarenes and Resorcinarenes

The use of calixarenes/resorcinarenes is not only restricted to the field of chemical sensors. Their remarkable properties have been employed for a variety of purposes. Given below are a few outstanding examples of their diverse usage in photolithography, medicine, temperature sensors and glues.

Photolithography: The main challenge in photolithography has been to generate ever-smaller feature sizes in the resist pattern that remain true after developing and etching.

The US patent US5702620 ^[65], was granted for a toner that develops electrostatic images, where the binding resin contains a colouring agent, a calixarene compound and a charge control agent. Here some of the phenolic OH groups of the calixarene are metallized with alkaline and alkaline earth metals.

Such an ultrahigh-resolution negative resist made possible the fabrication of an electrically variable shallow junction metal-oxide-silicon field-effect transistor with a gate length of just 32nm ^[66].

Medicine: Some phenolic compounds are well known to possess physiological properties, as for example the urusthiols with the long chain alkyl-substituted catechols, which are the active ingredients in poison ivy. A method for inhibiting the viral cell infection, that causes herpes, is to administer a therapeutically effective amount of calix(n)arene orally or topically ^[67]. For this the calix(n)arene were functionalised in the meta ring position with carboxylate, phosphate, sulfonate groups, esters and amides all of which are cleavable inside the human body.

Adhesives: The addition of small amounts of calixarenes (0.1%-1%) to cyanoacrylate adhesives has proven to reduce fixture and curing times by deactivating specific substrates such as wood ^[68]. Here simple alkoxy and alkyl substitutions in the para position of the ring suffice, with the calixarenes having 4, 6 or 8 repeating units.

Temperature sensor: Studies driven by the desire to develop more easily operated thermal detectors have employed alternated carboxyl/amide substituted calix(8)arene LB films, exploiting their pyroelectric behaviour ^[69]. The temperature dependent electric polarisation of the membrane can be employed as a dielectric in a capacitor with short-circuited electrodes, connected to an ammeter. Whenever the temperature changes, an electric current can then be registered, indicating changes in their position and with these changes in the temperature. To produce the required non-centrosymmetric structure the carboxyl substituted and the amide substituted calixarenes were alternately deposited. This resulted in a net dipole in the film based on the individual dipoles of the molecules. The influence of pendant chain structure changes, in pyroelectric applications were further studied in same detail in ^[70].

3.7 References

- [1] A. Knop and I. A. Pilato, *Phenolic Resins*, Springer, Berlin, 1985
- [2] C. D. Gutsche, *Calixarenes*, ed. J. F. Stoddart, The Royal Society of Chemistry, Cambridge, Vol. 1, 1989
- [3] J. Vicens and V. Böhmer, *Calixarenes: A Versatile Class Of Macrocyclic Compounds*, Kluwer Academic, Dordercht, 1991
- [4] J. B. Nielder and H. J. Vogel, *J. Am. Chem. Soc.*, 62, 2512, 1940
- [5] H. Konishi, K. Ohata, O. Morikawa, K. Kobayashi, *J. Chem. Soc., Chem. Comm.*, 309, 1995
- [6] H. Konishi, T. Nakamura, K. Ohata, K. Kobayashi, O. Morikawa, *Tetrahedron Lett.*, 41, 7383, 1996
- [7] A. Bayer, *Ber.*, 5, 25, 1872
- [8] F. Rashig, *Z. Angew. Chem.*, 25, 1912, 1939
- [9] J. Niederl, H. J. Vogel, *J. Am. Chem. Soc.*, 62, 2512, 1940
- [10] V. Böhmer, *Angew. Chem., Int. Ed. Engl.*, 34, 713, 1995
- [11] T. Kappe, *J. Inc. Phen. Mol. Recogn. Chem.*, in L. Atwood, J. E. D. Davies, D. D. MacNicol, F. Vögtle (eds.), *Comprehensive Supramolecular Chemistry*, Vol. 2, Elsevier Science Oxford, 1996
- [12] F. Weinelt, H. J. Schneider, *J. Org. Chem.*, 56, 5527, 1991
- [13] A.G. S. Högberg, *J. Org. Chem. Soc.*, 45, 4498, 1980
- [14] Nielsson, *Acta Chem. Scand.*, 22, 732, 1968
- [15] V. Böhmer, *Angew. Chem., Int. Ed. Engl.*, 34, 713, 1995
- [16] P. D. Grootenhuis, P. A. Lollmann, L. C. Groenen, D. N. Reinhoudt, G. J. van Hummel, F. Ugozzoli, G. D. Andreotti, *J. Am. Chem. Soc.*, 112, 4165, 1990
- [17] S. Shinkai, *Adv. Supramol. Chem.*, 3, 1993
- [18] US patent No. 5866087: Calixarene derivatives, their preparation process and their use for extracting actinides and lanthanides
- [19] <http://www.nobel.se/chemistry/laureates/1987/press.html>
- [20] US patent No. 4477377: Recovery of cesium
- [21] Kenichi Yagi, Soo Beng Khoo, Masao Sugawara, Tohru Sakaki, Seiji Shinkai, Kazunori Odashima and Yoshio Umezawa, *Journal of Electroanalytical Chemistry*, V. 401, 1-2, p.65-79, 1996
- [22] S.R. Izatt, R.T. Hawkins, J.J Christensen, R. M. Izatt, *J. Am. Chem. Soc.*, 110, p. 6811, 1985

- [23] M.A. McKervey, E.M.Seward, G.Ferguson, B.Ruhl, S.J. Harris, *J. Chem. Soc., Chem. Commun.*, 388, 1985
- [24] C.D Gutsche, B. Dhawan, K. H. No and R. Muthukrishanan, *J. Am. Chem. Soc.*, 103, 1981
- [25] V.I. Kalchenko, D.A. Rudkevich, D.N. Shivanyuk, I.F. Tsymbal, I.N.Markovskiy, *Zhurnal Obschei Khimii* 64, p. 731-742, 1994
- [26] G. D. Andreetti, O. Ori, F. Ugozzoli, C. Alfieri, A. Pochini, R. Ungaro, *J. Inclusion Phenom.*, 6, 523, 1988
- [27] S. Smirnov, V. Sidorov, E. Pinkassik, J. Havlicek, I. Stibor, *Supramol. Chem.*, 8, 187, 1997
- [28] M. Coruzzi, G. D. Andreetti, V. Bocchi, A.Pochini and R. Ungaro, *J. Chem. Soc., Perkin Trans. 2*, 1133, 1982
- [29] G.D Andeetti, R. Ungaro and A. Pochini *J. Chem. Soc., Chem Commun*, 1005, 1979
- [30] A.Ninagawa, H. Matsuda, *Makromol. Chem., Rapid Commun.*, 3, 65, 1982
- [31] Y.Nakamoto, S.Ishida, *Makromol. Chem., Rapid Commun*, 3, 705, 1982
- [32] M. A. McKervey, E. M. Seward, G. Ferguson and B.L. Ruhl, *J. Org. Chem*, 51, 3581, 1986
- [33] Ungaro R., Pochini G.D., Andretti G.D., Pochini A., *J.Mol.Struct.*, 82, 133, 1982
- [34] J. A. J. Burnik, B. J. R. Haak, J. G. Bomer, D. N. Reinhoudt, M. A. McKervey, S. J. Harris, *Anal. Chim. Acta*, 254, 75, 1991
- [35] H. Shimizu, K. Iwamoto, K. Fujimoto, S. Shinkai, *Chem. Lett.*, 2147, 1991
- [36] US patent No. 599913: Chromoionophores, optical sensors containing them and a method for determining the presence of alkali metal cations or of a base
- [37] Kubinyi M., MohammedZiegler I., Grofcsik A., Bitter I., Jones W.J., *Journal of Molecular Structure*, V.408, p.543-546, 1997
- [38] D. Diamond, G. Svehla, *Trend Anal. Chem. Soc.*, 6, 46, 1987
- [39] US patent No. 5132345: Ion-selective electrodes
- [40] A. Cadogan, D. Diamond, S. Cremin, M. A. McKervey, S. J. Harris, *Anal. Proc.*, 28, 13, 1991
- [41] A. Cadogan, D. Diamond, M. R. Smyth, G. Svehla, M. A. McKervey, E. M. Seward, S. J. Harris, *Analyst*, 115, p. 1207, 1990
- [42] Kaneto K., Bidan G., *Thin Solid Films*, V.331, 1-2, p.272-278, 1998
- [43] W.Göpel, J. Hesse, J.N. Zemel *Sensors A Comprehensive Survey*, ISBN: 3-527-26768-9 Chapter 7.1.2.1 The Nernst Equation and Its Modifications

- [44] M. Ben Ali, R. Mlika, H. Ben Ouada, R. M'ghaieth, H. Maâref, *Sens. & Actua. A: Physical*, V. 74, Issues 1-3, p. 123-125, 1999
- [45] Mlika R., BenOuada H., JaffrezicRenault N., Dumazet I., Lamartine R., Gamoudi M., Guillaud G., *Sens.& Actua.B*, V.47, 1-3, p.43- 47, 1998
- [46] Mlika R., BenOuada H., Hamza MA., Gamoudi M., Guillaud G., JaffrezicRenault N., *Synthetic Metals*, Vol.90, No.3, p.173-179, 1997
- [47] Mlika R., Dumazet I., Gamoudi M., Lamartine R., BenOuada H., JaffrezicRenault N., Guillaud G., *Analytica Chimica Acta*, V.354, No.1-3, p.283-289, 1997
- [48] Mlika R., BenOuada H., BenChaabane R., Gamoudi M., Guillaud G., JaffrezicRenault N., Lamartine R., *Electrochimica Acta*, V.43, 8, p.841-847, 1998
- [49] Nostro P.L., Casnati A., Bossoletti L., Dei L., Baglioni P., *Colloids and Surfaces*, 116, 203-209, 1996
- [50] Steffen Rösler, Ralf Lucklum, Ralf Borngräber, Jens Hartmann and Peter Hauptmann, *Sens. & Actua. B: Chemical*, V. 48, p. 415-424, 1998
- [51] S. F. Y. Li, X. C. Zhou, S. C. Ng and H. S. O. Chan, *Sens. & Actua. B: Chemical*, V. 42, p. 137-144, 1997
- [52] Giuseppe Arena, Alessandro Casnati, Annalinda Contino, Domenico Sciotto and Rocco Ungaro, *Tetrahedron Letters*, V. 38, 26, p. 4685-4688, 1997
- [53] A.V. Naboka, N. V. Lavrika, Z. I. Kazantsevaa, B. A. Nesterenko, L. N. Markovskiyb, V. I. Kalchenkob and A. N. Shivaniukb, *Thin Solid Films*, 259, p. 244-247, 1995
- [54] E. Dalcanale, J. Hartmann, *Sens. & Actua.B*, 24-25, p. 39, 1995
- [55] J. Hartmann, P. Hauptmann, S. Levi, E. Dalcanale, *Sens. & Actua. B*, 35-36, p. 15, 1996
- [56] Dickert F.L., Baeumler U.P.A., Strathopulos H., *Anal. Chem.*, 69, p. 1000-1005, 1997
- [57] Schierbaum K.D., Goepel W., *Syn. Metals*, 62, p.37-45, 1993
- [58] www.biocore.com
- [59] www.ti.com/spr
- [60] Yu. M. Shirshov, S.A. Zynio, E.P. Matsas, G. V. Beketov, A. V. Prokhorovich, E.F. Venger, L.N. Markovskiy, V.I. Kalchenko, A.V. Soloviv, R. Merker, *Supramolecular Science* 4, p. 491-494, 1997
- [61] A. V. Nabok, A. K. Hassan, A. K. Ray, O. Omar and V. I. Kalchenko, *Sens. & Actua. B*, 45, p. 115-121, 1997
- [62] A.V. Nabok, A.K. Hassan, A.K. Ray, *J. Mater. Chem.*, 10, p. 189-194, 2000

- [63] A.V. Nabok, N.V. Lavrik, Z.I. Kazantseva, B.A.Nesterenko, L. N. Markovskiy, V. I. Kachenko, A. N. Shivaniak, , Thin Solid Films, 259, p 244-247, 1995
- [64] A. Sabot, Chemical Sensing with Ultrathin Organic Films using Surface Plasmon Resonance, PhD Thesis, Sheffield University, 1999
- [65] US patent No. 5702620: Ultrafine pattern forming method and ultrafine etching method using calixarene derivative as negative resist
- [66] Kawaura, Hisao; Sakamoto, Toshitsugu; Baba, Toshio; Ochiai, Yukinori; Fujita, Jun'ichi; Matsui, Shinji; Sone, Jun'ichi, IEEE Electron Device Letters, V. 19, 3, p. 74-76, 1998
- [67] US patent No. 5441983: Treatment of infection by enveloped virus with calix(N)arene compounds
- [68] US patent No. 4556700: Instant adhesive composition utilising calixarene accelerators
- [69] McCartney C. M, Richardson T., Greenwood M.B., Cowlam N., Davis F., Stirling C.J.M., Supramolecular Science, V.4, 3-4, p.385-390, 1997
- [70] Richardson T., Greenwood M.B., Davis F., Stirling C.J.M., IEEE Proceedings-Circuits Devices and Systems, 144, 2, 108-110, 1997

4 Materials and film deposition

This chapter describes the material used throughout the studies, outlines different mechanisms of thin film formation and presents an analysis of the resulting film properties.

Thin films are of special interest, for sensor applications since most analyte interaction is restricted to the surface or a very limited region beneath the surface. Diffusion into the bulk of a macromolecular/polymeric membrane is often a complex process that can be described by either Fickian diffusion ^[1], with a linear diffusion coefficient, or for non-Fickian diffusion, with complex diffusion coefficients ^[2]. Thin films by virtue of their large surface to bulk ratio offer faster response times.

4.1 Calix[4]resorcinareneC₇H₁₅ and Poly-ortho-methoxy aniline

The compound that is central to all following studies is the calix[4]resorcinarene C₇H₁₅. Its structural formula is given in Figure 1 and its ball and stick model is presented in Figure 2.

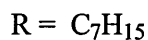
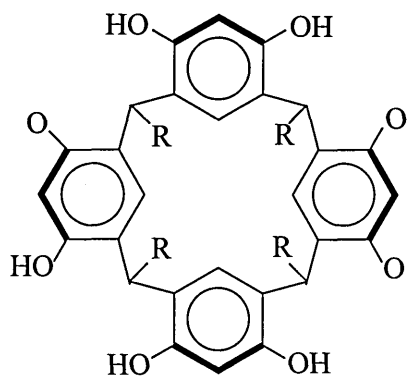


Fig.1 Chemical formula of the calix[4]resorcinareneC₇H₁₅

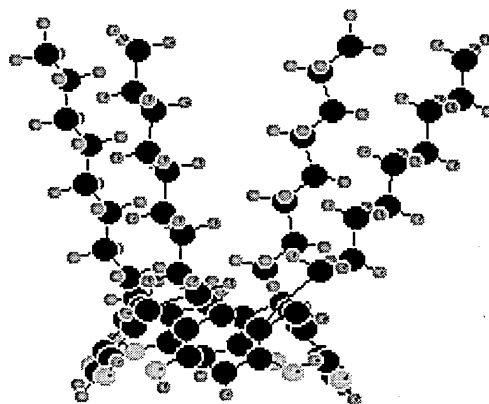


Fig.2 Ball and Stick model calix[4]resorcinareneC₇H₁₅

The compound was synthesised in and obtained from the Academy of Science in Kiev. In addition to it, an in house synthesised polymer was used. A detailed description of the synthesis can be found in the Appendix 1. The chemical formula of the polymer, poly-ortho-methoxy aniline (POMA) is given below in Figure 3a, for the undoped (nonconducting) emeraldine base and Figure 3b, in its doped (conducting) form as an emeraldine salt.

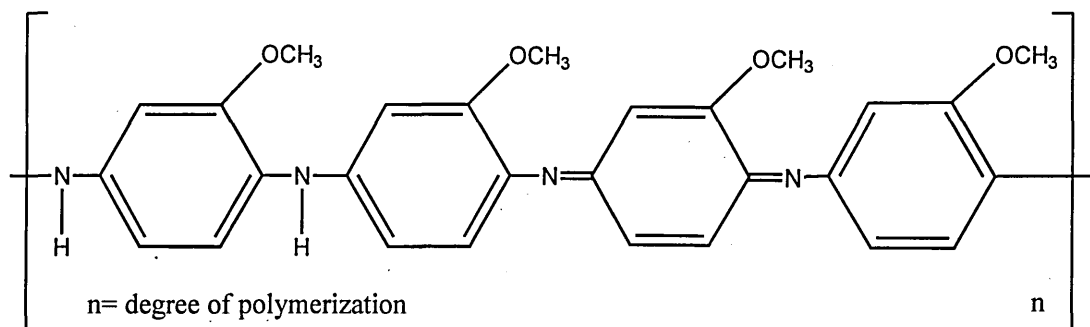


Fig. 3a Poly-ortho-methoxy aniline emeraldine base

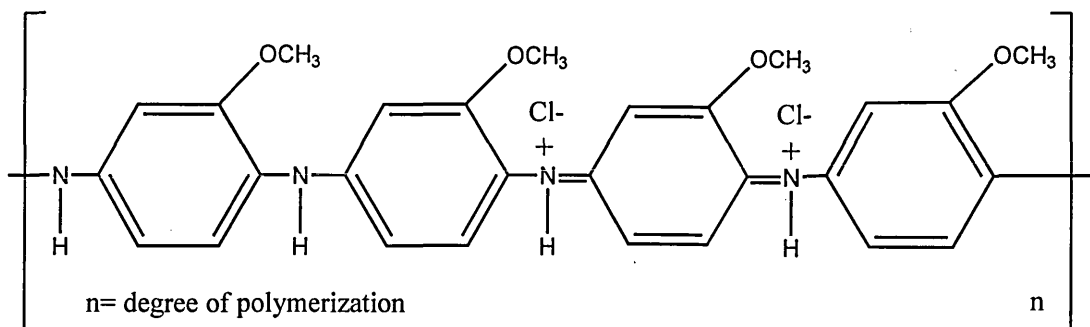


Fig. 3b Poly-ortho-methoxy aniline emeraldine salt

4.1.1 Electroactive conjugated polymers and deposition thereof

Exploitation of electroactive conjugated polymer LB films has attracted much interest in the field of chemical sensors ^[3-5]. Unfortunately many polymers form either unstable monolayer (ML) ^[4] or the layers are too rigid for a transfer onto substrates ^[6]. In order to deposit non-surface active conjugated polymers in the form of LB films, the mixed monolayer approach can be employed. In this the mixing of the polymer with a surface-active agent, provides a mean of rendering the film more flexible, by dispersing the polymer molecules into small domains, which ensures a good transfer of the film onto the substrate. The mixed monolayer film, is a matrix of amphiphilic molecules with the

polymer molecules dispersed in it. The level of mixing that occurs depends on the ratios of the components and their structure. High quality LB films have been reported for very diverse amphiphilic matrix materials, like cadmium stearate ^[7], 3-octadecanoyl pyrrole ^[8], tetra-tert-butyl phthalocyanine ^[9], stearic acid ^[6], vanadium-tetraphenyl porphyrine ^[10] and phosphorylated calixarenes ^[11]. Extensive studies on gas/vapour sensing membranes utilising aniline based polymers have been conducted in the literature ^[12, 13]. Part of their attractiveness stems from the ease of their synthesis, the low cost of the materials, their high environmental stability and an extensive pool of background knowledge that already exists. In line with aniline based sensing membranes POMA was chosen, representing a non-surface active polymer for the incorporation in the C[4]RA matrix. The focus lies here on the matrix for the application in sensoric membranes, not on fundamental studies regarding the polymer per se. No obvious difficulty can be seen, when it comes to replacing the POMA for any other aniline based polymer, with differing sidegroups, like for example ethoxy groups. Main factors, influencing the polymer conductance are its molecular weight and the type of dopant used. Any cited molecular weight is only the average of all the molecular weight fractions contained in the whole sample, making any direct comparison between polymer samples, originating from different synthesis methods, difficult. Recent studies have shown, that the kind of solvent used influences the conductance of the polymer. For m-cresol as a solvent secondary doping for polyaniline was reported ^[14, 15], leading to an increase in the electrical conductivity and an altered film morphology. FTIR spectroscopy has shown that the m-cresol is not incorporated into the polymer ^[16], but influences the polymer structure. The changes have been attributed to conformational changes of the polyaniline chains, from the compact to an expanded coil structure ^[17, 18]. Since no m-cresol is retained, this implies a kind of memory effect ^[14]. These results prompted the use of m-cresol as a solvent, to allow a more homogeneous and better integration in the deposition matrix, despite its high hazard rating ^[19]. In comparison to polyaniline, rather few studies have been carried out on POMA itself and its thin films. Fundamental studies regarding the multitude of synthesis factors influencing the conductivity ^[20, 21] as well as studies on the AC conduction mechanisms have been carried in out in references ^[22, 23].

4.2 Thin film deposition principles

Three different deposition methods have been employed to apply the sensing membranes onto the different transducers. The following is a theoretical description of these techniques.

4.2.1 Casting

One of the simplest methods to coat a substrate is to cast a solution of the dissolved material onto a substrate and let the solvent evaporate leaving a film of the material behind ^[24]. The process is schematically shown in Figure 4. Its advantage is that it is universally applicable and allows the formation of rather thick films, its drawback is the limited homogeneity of the resulting film. The thickness was calculated according to (1), assuming an equal coverage of the substrate.

$$thickness = \frac{\text{volume (of dissolved material)}}{\text{covered area}} \quad (1)$$

Since all solutions were prepared by dissolving a given weight of the material in the solvent, the volume was calculated according to (2).

$$Volume = \frac{\text{concentration (g/ml)}}{\text{density of material}} \cdot \text{volume of solution used} \quad (2)$$

The powder density of the C[4]RA was measured by compressing the powder in a microsyringe, to determine the volume and comparing weights. The powder density was found to be 0.62 kg/dm³. This value is in very good agreement with a theoretical calculation using the densities of n-heptane (0.684 kg/dm³), representing the side chains and benzene (0.8786 kg/dm³), making up the cage, as 0.78 g/ml and allowing for a partially empty cavity. By introducing a factor of 0.8 from geometrical considerations, the theoretical value takes on 0.624 kg/dm³. This geometric factor can be estimated from molecular models.

This method produced films of varying homogeneity, when chloroform was employed as a solvent the high volatility of the chloroform lead to a rapid evaporation and an acceptable film structure. A texture was clearly visible but was uniform over the coated area. The films created by this method were about 250 nm thick. When m-cresol was

used as a solvent for the POMA, the resulting films showed unacceptable structuring. The low volatility (0.1 mmHg vapour pressure) and the high surface tension of the m-cresol (28.47 mN/m) led to the formation of a skin which showed a clear concentration of the solute in the centre of the coated area.

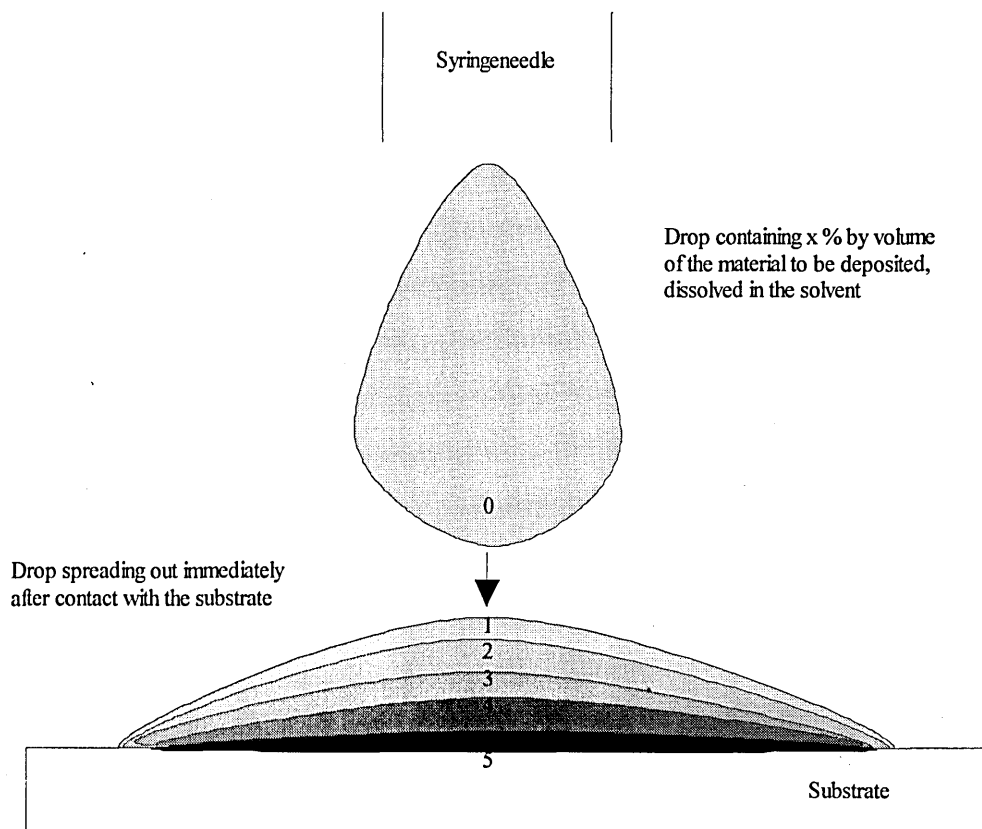


Fig. 4 Schematic of the casting method, evaporation in steps 0-5 illustrating the increasing solute concentration

4.2.2 Spin coating

Spin coating allows the preparation of thin films on a substrate with and without topography. The method offers experimental ease, rapidity of deposition, employment of low-tech equipment and wide applicability for many types of coating. During the spin coating process a solution is pipetted onto a stationary or rotating substrate, which is held in place by the application of a vacuum from the bottom side of the mounting chuck. During rotation the solution spreads out under the influence of the centrifugal forces and is further thinned by the evaporation of the solvent, to leave a solid film

behind. Figure 5 gives a schematic of the spin coating process and Figure 6 compares the film forming mechanisms for a stationary and rotating substrate.

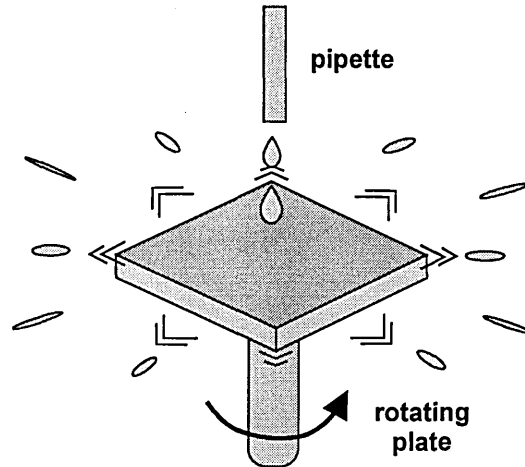


Fig. 5 Schematic of spin coating

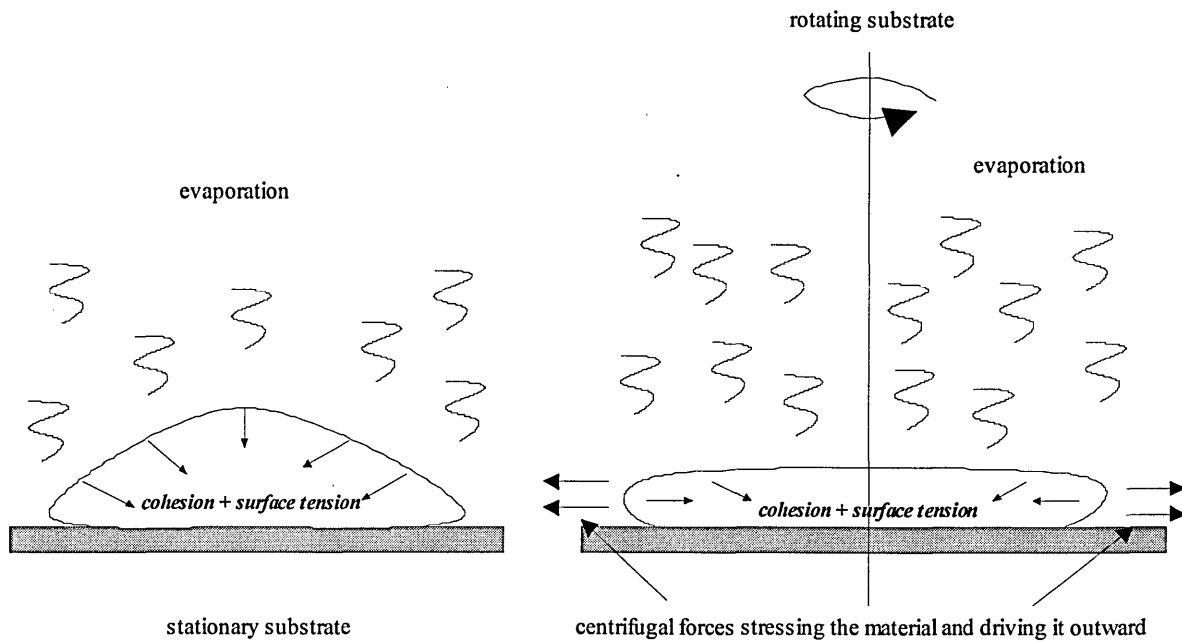


Fig. 6 Film formation on a stationary and on a rotating substrate

Though all spin processes consist of essentially four stages,

- deposition of solution
- spin-up, to wet the substrate surface
- spin-off, to remove excess liquid
- evaporation of solvent

there is a varying degree of overlap in these stages. Three types of solution dispensation are widely used, the dispensing onto the rotating substrate with a single drop ^[25, 26], the dispensation of a stream of solution onto a rotating substrate ^[27] and the deposition onto the stationary substrate ^[28]. The latter two types seem to prevail with photoresist type material. Since the photoresist application is vital for the microelectronics industry, much attention has been focused on assessing the parameters governing the film formation and on the derivation of a model for it ^[29-32]. A detailed look into these, reveals that a multitude of mechanisms contribute to the process. All models are idealised and neglect various contributions, to keep the models manageable. This is a serious shortcoming, when it comes to applying these models to processes that deviate even slightly. All existing models describe the processes shown in Figure 7.

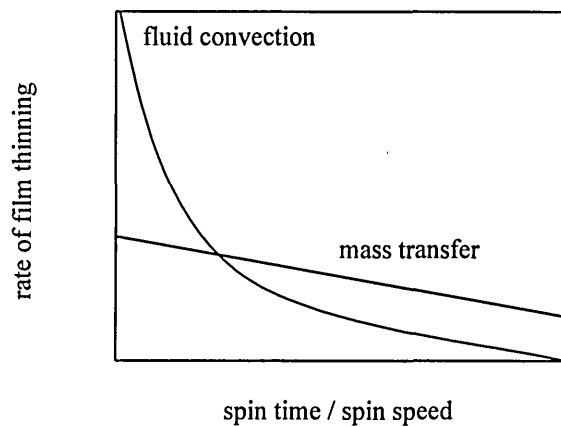


Fig. 7 Schematic illustration of processes contributing to the film formation for spin coating

4.2.2.1 Factors influencing the film properties of spun films

- Washo found that the shape of the substrate does not influence the resulting film, apart from edge effects ^[33].
- Variation of the film thickness d , over the disk radius r is expected to follow a $d = r^{2/3}$ relationship ^[33], but experiments showed that a more asymptotic behaviour, beyond a critical distance, is obtained. Surface tension has been suggested to contribute to this smoothing out of the thickness profile.
- Analysis, employing a one dimensional model, showed that the film thickness is independent of the initial volume of solution dispensed, and further, that the rate of

film thinning by convective flow is proportional to the film thickness ^[34], this is a limiting factor for the maximum attainable thickness.

- Concentration of the solute, in the solvent increases the viscosity and thicker films are obtained ^[35, 36].
- The solvent, depending on its volatility and viscosity changes the film thickness, a well documented phenomena, but with no unequivocal correlation ^[37].
- Spin speed determines the film thickness, though consent is established for the general correlation between higher spin speed and thinner films, the function that the film thickness follows, seems to be strongly material dependent. Generally the function is expressed in terms of ω , the angular velocity as in (3),

$$d = c \cdot \omega^x \quad (3)$$

with varying values for x and c . Vukosik ^[26] reports a linear relation for phthalocyanine with $x = -1$, Hassan ^[36] reports a value of $x = -0.687$ for tetraundecyl-tetra-p-nitrophenylazocalix[4]resorcinarene and Extrand ^[37] reports for natural rubber and polystyrene films an x of -0.5 .

- The formation of a free surface skin, in regions where the solvent evaporation causes the viscosity to increase locally, like on the edges of the convection front, this is particular relevant for highly volatile solvents.
- Temperature variation is regarded as negligible ^[31].

It is believed that many of the proposed models are no longer applicable when the resulting film thickness is reduced to the nm scale. Many model parameters such as the viscosity, evaporation rate, friction, clustering of molecules and stress/strain behaviour are non-linear with respect to concentration. Their characteristic is fundamentally linked to intermolecular forces between the solvent and solute. For film thicknesses in the range of multiple molecule diameters, the spatial orientation of a non-symmetric determined correlations for specific compounds can be considered unique. Though general trends can be a useful aid in undertaking intelligent modifications to the spinning parameters application of one particular model may produce misleading results.

4.2.3 Langmuir-Blodgett (LB) film deposition

Historically the foundations of thin films on the water surface, go back to antiquity where the oil film formation on water, was employed for fortune telling ^[38]. Scientific interests developed over Franklin with his famous teaspoon of oil experiment ^[39], over Rayleighs oil film thickness determination ^[40] and Pockels first trough ^[41].

Studies were developed by Langmuir and Blodgett, starting with initial work on monolayers of amphiphilic molecules at the water-air interface in 1917 ^[42] and continued with the studies on the transformation of these layers onto solid substrates ^[43]. Since then films produced this way have carried the name Langmuir Blodgett (LB). Further background information of the emergence of these monolayer studies can be found in reference ^[44].

The formation of a high quality LB film requires the formation of stable, insoluble layers at the air water surface. For this the material needs to be amphiphilic, possessing a hydrophobic and a hydrophilic part, Figure 8a. The hydrophobic part, consists in many cases of hydrocarbon chains and the polar part of a COOH group. This allows the molecule to orientate itself, according to the affinity of its parts, on the water surface. Such films can be transferred onto a variety of substrates by dipping them through the interface into the subphase while maintaining an intact film. Repeated dipping allows a controlled build up of a multilayer structure, Figure 8b. Of all thin film deposition methods, the LB technique provides the most control over the film thickness, and it is the only technique to provide control of the spatial arrangement of the molecules. The solute is dissolved in a water insoluble solvent, (e.g. chloroform) in concentrations of around 1 % by volume and the solution is spread out onto the water surface. After the solvent is evaporated, the material is randomly orientated on the water surface separated by distances too large for intermolecular forces to be effective. The surface area confining the material is then reduced, with the aid of movable barriers skimming the water surface, Figure 8c. This reduces the distance between molecules so that intermolecular forces start to aid in the orientation of the molecules; this transition is often compared to that from a gas like state to that of a liquid state. Upon further compression the molecules interact so strongly with each other, that they take on the state of a two dimensional solid. A measure for the state of compression, is the surface pressure, which is defined as the surface pressure of the film minus the surface pressure of the uncovered subphase. Once the film has reached the state of a 2D solid, further compression increases its 2D density, but increasing the surface pressure beyond a

critical compression ratio, brings about a collapse of the film by shearing action. The deposition takes place, at a state in which the 2D solid still possesses enough flexibility for a transfer onto the substrate, the most frequently cited surface pressures lie between 20-40 mN/m. Since the transfer of the film onto the substrate reduces the material under compression, the remaining surface needs to be constantly reduced to compensate for this. For the maintenance of a steady surface pressure a negative feedback loop between a surface pressure sensor and the computer controlled movable barriers is used. The computer also allows the programming of the substrate dipping sequence, with respect to the number of cycles and the dipping speed. The analysis of the surface pressure increase under reduction of the surface area allows the determination of the molecule area, A_0 , via extrapolation of the linear part of the pressure area (π/A) isotherm to the x-axis, Figure 8c. This is one of the most vital experiments for any LB deposition, since it describes the packing density and provides information of the molecular arrangement. The formation of the LB layer is performed in a specially designed trough, consisting essentially of a Teflon clad subphase (water) reservoir, with moveable barriers which define the surface area, a dipping mechanism for the substrate and a surface pressure monitor (Wilhelmy plate). Further details on LB trough designs and concepts can be found in reference ^[45].

4.2.3.1 Factors influencing the film deposition

Apart from the dominating influence of the surface pressure at which the deposition takes place there are several more influencing factors:

- dipping speed
- substrate surface properties (hydrophilic, hydrophobic)
- pH of the subphase
- composition of the subphase
- cleanliness of all touching components
- compressions speed of the barriers

The susceptibility of the deposition to any kind of disturbance, from either mechanical vibrations, dust and cleanliness of trough and substrate sets a natural limit to the reproducibility of the films. Furthermore the complexity of the operating procedures and the special equipment required makes it a rather costly technique. It has remained

so far on the fringe of industrial fabrication techniques, and its use is most frequently found in the R&D realm.

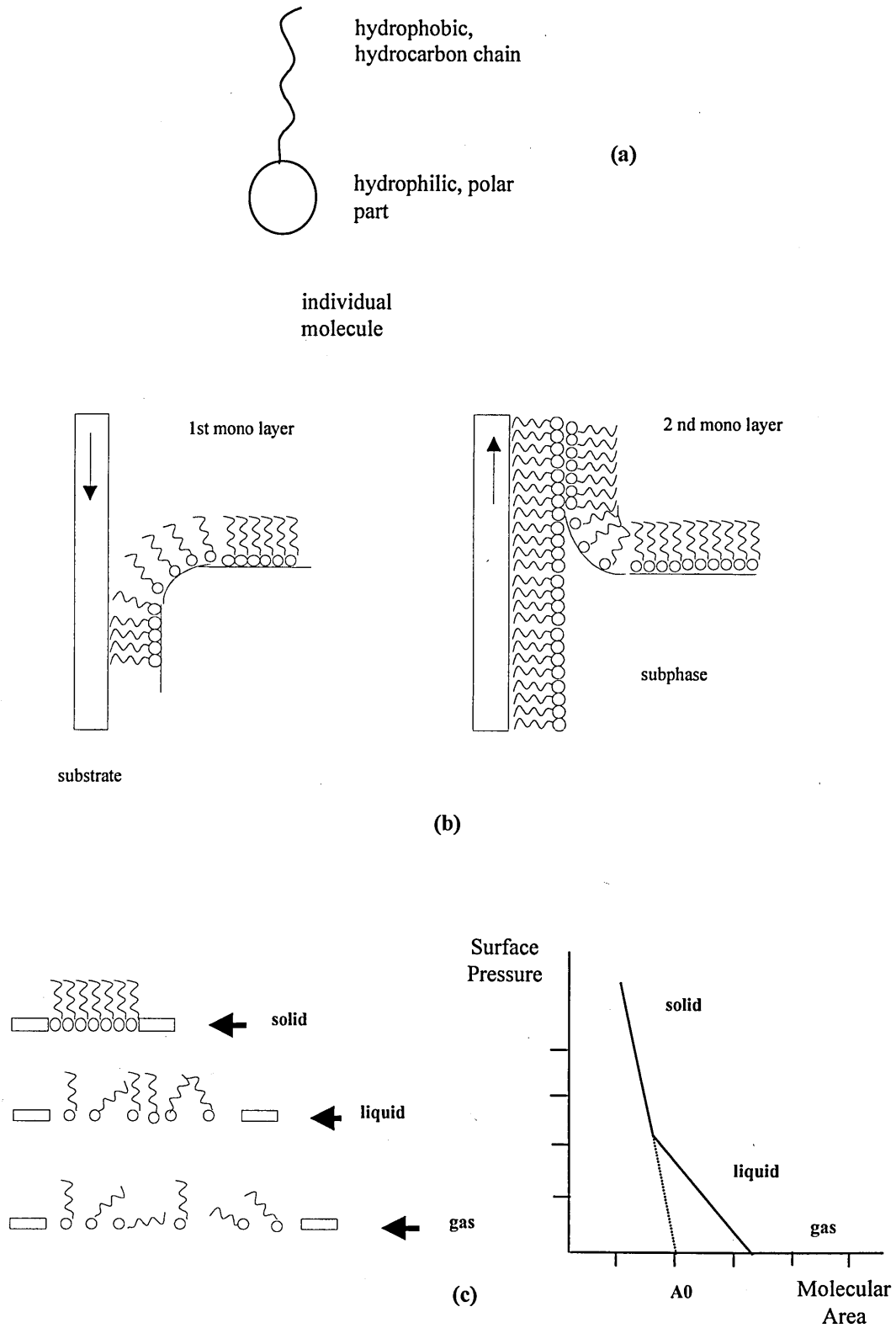


Fig. 8 a-c Illustration of the LB film deposition and the correlation between the different states of the spread molecules

4.3 Deposition details and experimental results

Thin films of C[4]RA and a combination of C[4]RA and POMA have been deposited onto different substrates and a comprehensive analysis of the membranes was carried out with a variety of techniques. The technique SPR is explained in detail in the Appendix 2, we have adopted further techniques that are comprehensively explained in the references ^[46, 47].

4.3.1 LB films

4.3.1.1 Deposition details for C[4]RA films

The C[4]RA was dissolved in chloroform to a concentration of 0.5 mg/ml and then sonicated for 60 seconds, before about 100 μ l of it were spread dropwise onto the water surface (milliq water) of the trough. Enough time was allowed for the chloroform to evaporate before the next drop was spread. The POMA was dissolved to a concentration of 0.5 mg/ml in m-cresol and the solution was sonicated in a sealed vessel for 1 hour to produce a homogeneous solution. After allowing the latter to cool down to room temperature, mixtures were prepared from both solutions and again the solution was sonicated before it was spread on the water surface. The low volatility of the m-cresol made the evaporation time rather large, so to avoid excessive spreading time, drops were placed far apart and only 60 μ l of solution was spread. The layers were trained by compressing and uncompressing the layer repeatedly until the pressure area isotherm stabilised. There was a very marked training effect on the composite layers, very much less so for the pure C[4]RA. Deposition was carried out at a surface pressure of 25 –30 mNm and the dipping speed for the different substrates was adjusted to provide maximum transfer. Table 1 gives the used dipper speeds. Between the up and down stroke a wait cycle of at least 300 seconds was allowed, to facilitate a complete drying of the substrate.

	C[4]RA/POMA mix	C[4]RA
Glass/fused silica substrate	5 down, 5 up	10 down, 10 up
Gold coated glass slide	5 down, 5 up	10 down, 25 up
Silicon substrates	5 down, 20 up	5 down, 25 up

Table 1 Dipping speeds for substrates, all values in mm per minute

The trough was cleaned prior to any usage, employing in-house standard procedures and the substrates were cleaned with a variety of steps to remove any organic contamination. Silicon substrates and fused silica glass slides were left overnight in a solution of sulfochromic acid, extensively rinsed with milliq water and dried under a stream of nitrogen. Gold coated slides were rinsed with chloroform, dried in nitrogen, rinsed with milliq water and again dried in nitrogen.

All substrates used for the LB deposition were then rendered hydrophobic by leaving them over night in a glass jar containing a saturated atmosphere of hexamethyldisilazane, (DMS).

The compression of the floating C[4]RA layer gave the following pressure-area (π/A) isotherm, Figure9. From this the area of the molecule is found to be 1,53 nm². This agrees well with the value found in the literature ^[48] of 1.6nm²

Deposition was carried out at a surface pressure of 25 mNm; the averaged transfer ratios achieved were in the region of unity, within a window of 90-110%, for both upstroke and downstroke, resulting in Y type LB layers. Y type specifies the alignment of the molecules building up the membrane with the heads orientated head to head and the tails, tail to tail.

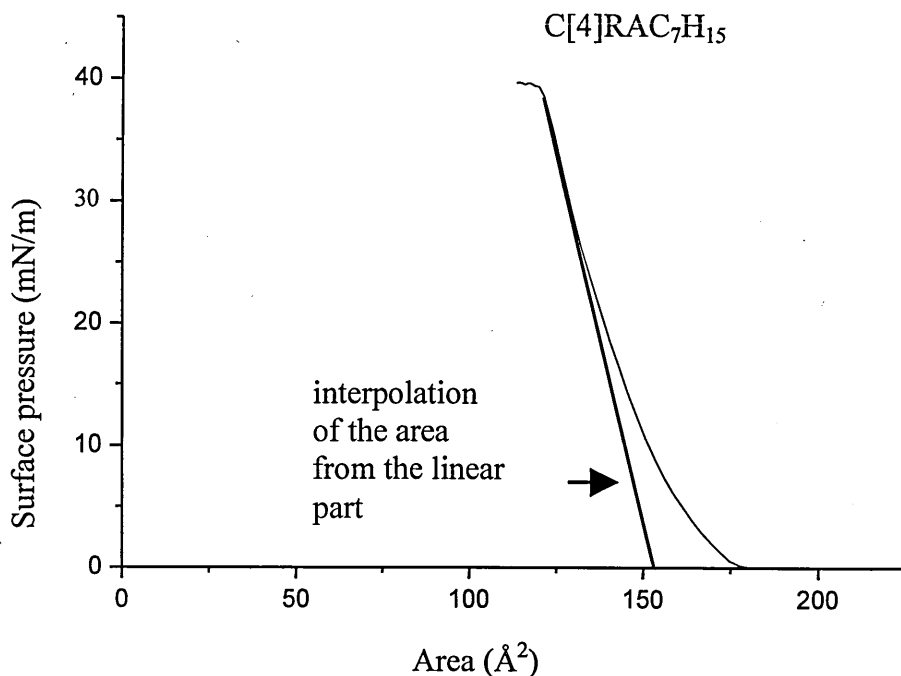


Fig. 9 Pressure area isotherm of C[4]RA

4.3.1.2 Film thickness analysis of pure C[4]RA multilayer structures

The thickness of the resulting membranes was analysed by SPR measurements (individual SPR scans not shown), with step structures of 2&4, 6&8, 10&12 and 16 layers on different Au slides, the thickness was found to increase slightly nonlinearly with the number of monolayers, Figure 10. Since the DMS is contributing to the thickness of the membrane its contribution is proportionally higher for the thinner films. Averaging the thickness results in a value of 0.95 nm for a single monolayer, agreeing well with previously published results ^[48] of 0.9 –1.1 per ML.

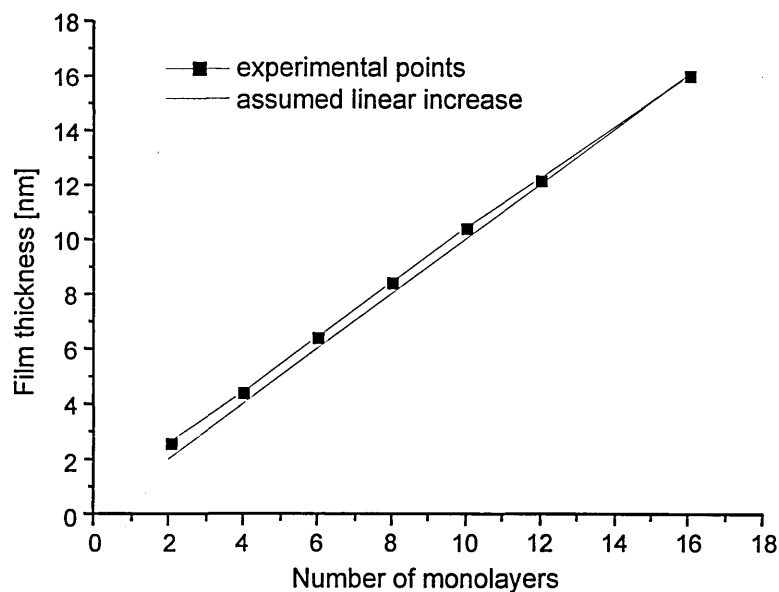


Fig. 10 Thickness of C[4]RA LB step structures

4.3.1.3 Deposition details for C[4]RA/ POMA composite films

Mixed ML of POMA in the C[4]RA matrix have been prepared with different ratios of polymer suspended in it. Solutions in ratios of 1 : 0.5 to 1 : 5 by volume have been prepared, the ML showed varying effects upon multiple compressions (training). The training is responsible for a structural change in the ML, strands of the polymer align themselves with respect to others and the C[4]RA. This behaviour must be considered when it comes to depositing the MLs, only layers that have been trained to the point where stable π/A isotherms are reached, deliver similar film structures. Figure 11 and 12

show the training effects for ratios of 1:1 and 1:2 by weight respectively. In the absence of the exact MW of the polymer, the area per molecule is based on the C[4]RA molecule only. The training effects are more pronounced for the higher polymer ratios, but there is no linear correlation between the molecule area and the mixing ratios. This absence, suggests that the orientation and incorporation into the matrix is very complex. Competing alignment mechanisms between polymer strands, polymer C[4]RA interactions, folding actions of the strands and integration into the C[4]RA basket can all contribute to this complex interplay.

A comparison of the training effects, depending on the mixing ratio and the resulting molecular areas are shown in Figure 13. The molecular area calculated is based on the molecular weight of the C[4]RA only.

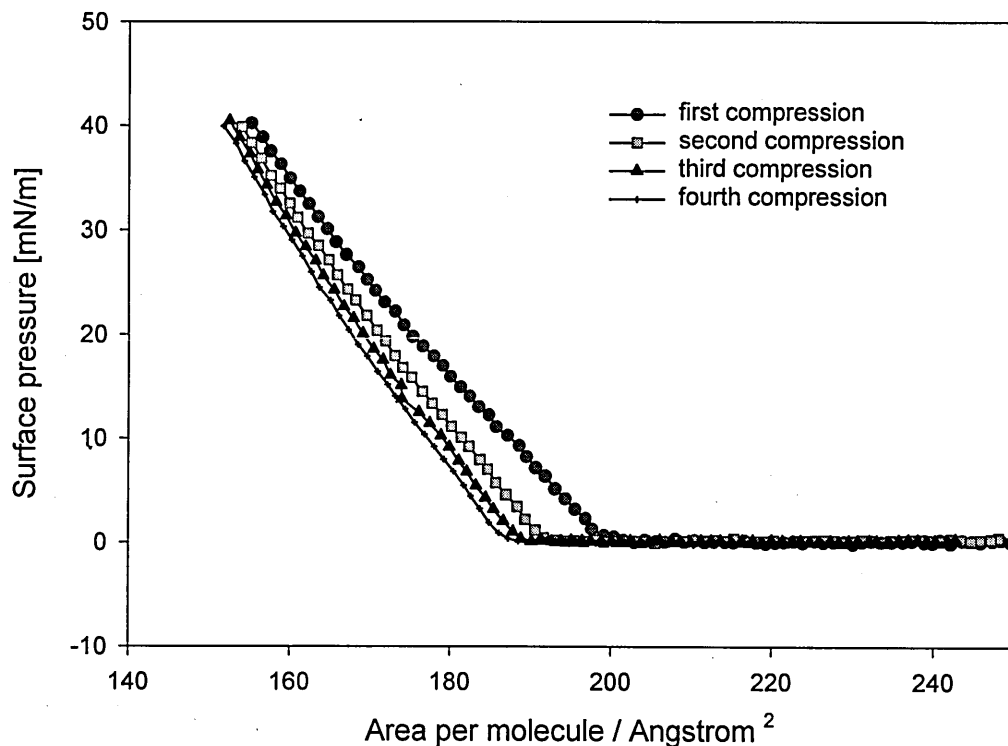


Fig. 11 Training effect on ML 1:1 mixing ratio by weight C[4]RA/POMA

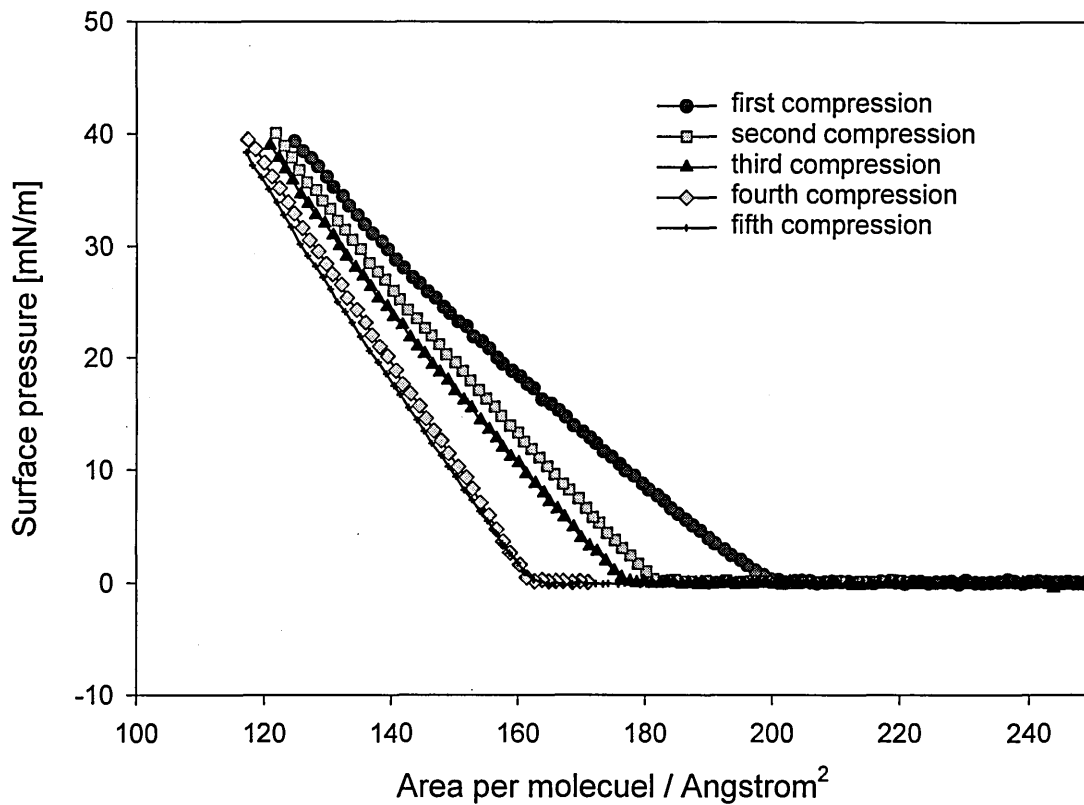


Fig.12 Training effect on ML 1:2 mixing ratio by weight C[4]RA/POMA

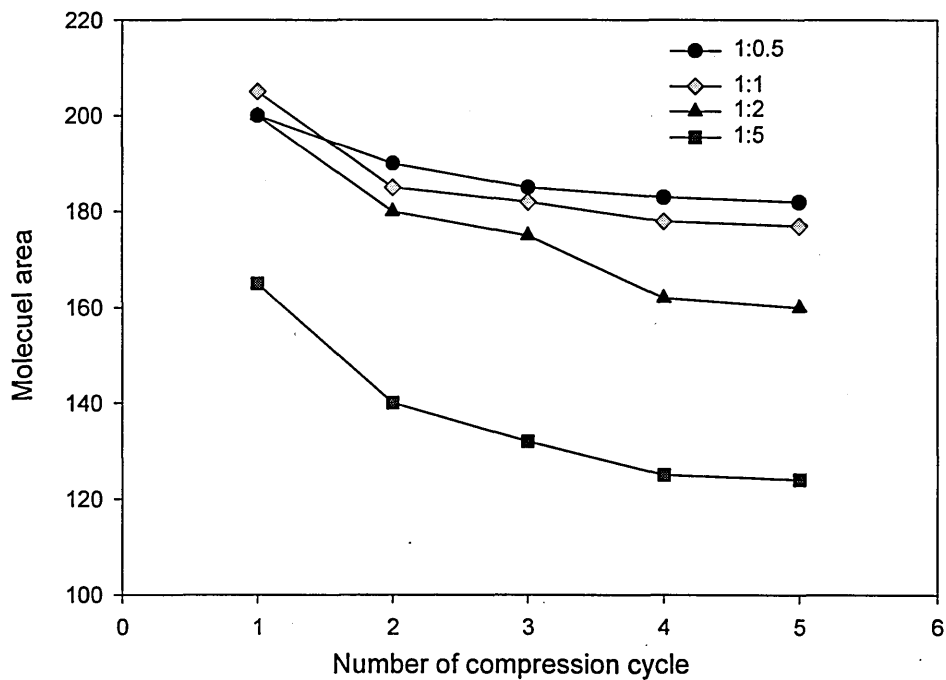


Fig. 13 Reduction in molecular area during training cycles for different C[4]RA/POMA concentrations

4.3.1.4 Thin film analysis of the composite membranes

4.3.1.4.1 Thickness analysis

It was found experimentally that with decreasing polymer ratios the conductivity of the membranes decrease (Chapter 5), therefore for further studies a mixing ratio of 1:1 by volume from 0.5mg/ml by weight solutions was chosen. Thickness measurements were performed in order to elucidate the structure of the membrane. The analysis of SPR and ellipsometry measurements, Figure 14 and 15, resulted in slightly different values for the thickness of a single composite monolayer of 2.1 and 2.2 nm, respectively.

For the ellipsometry measurements the composite matrix was deposited on silicon substrates with a 100 nm silicon oxide on top. The measurements were performed with a nulling ellipsometer. Here the linear polarised light is elliptically polarised upon reflection of the surface, the phase shift Δ between the beams and the tangent of the magnitude ratio of the total reflection Ψ is determined by finding the minimum reflection conditions. From the obtained positions of the analyser and the polariser, used to establish the minimum reflectivity, (values in degrees) the values of Ψ and Δ have been calculated, according to (4).

$$\Delta = P1 + P2 \quad \text{and} \quad \Psi = \frac{(180 - A2) + A1}{2} \quad (4)$$

An analytical determination of both the film thickness d and the refractive index from Ψ and Δ is not possible. Therefore the relationship for Δ and Ψ was plotted for a possible n of 1.3, 1.4 and 1.5, using a simulation-fitting-analysis computer program. Measured values were overlaid to these and where the best fit was obtained the thickness was calculated.

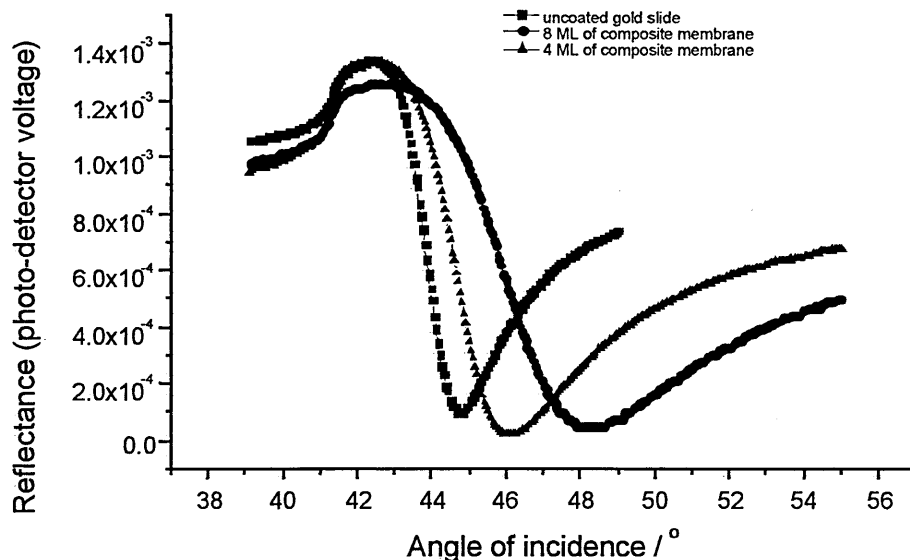


Fig. 14 SPR thickness analysis of 4 and 8 MLs of the composite membrane

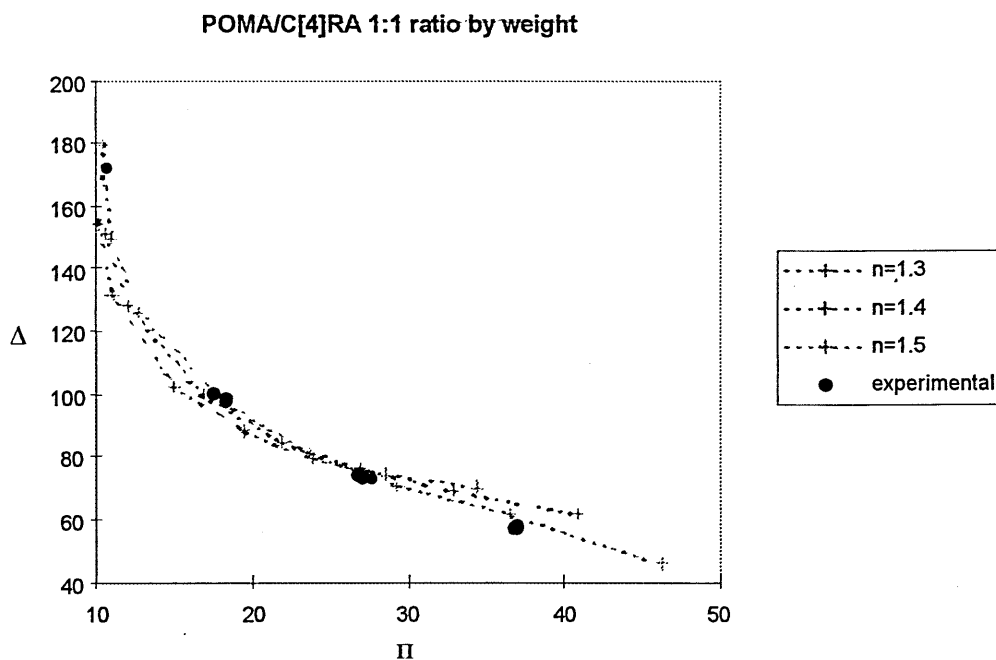


Fig. 15 Ellipsometer thickness analysis of step structures of the composite membrane on silicon

Since the height for a single C[4]RA was determined as 0.95 nm and the height for aniline based polymer backbones is cited as 0.5 nm^[49], this suggests a matrix with two under/over-lying POMA strands per C[4]RA molecule. Therefore an arrangement as shown in Figure 16 is proposed. The POMA strands form a bilayer, based on the

stronger delocalised π - π interaction of the aromatic rings rather than an interwoven structure with the C[4]RA, which sits on top of the POMA. The attractive forces between the POMA are not strong enough to support more than two strands in each transferred layer.

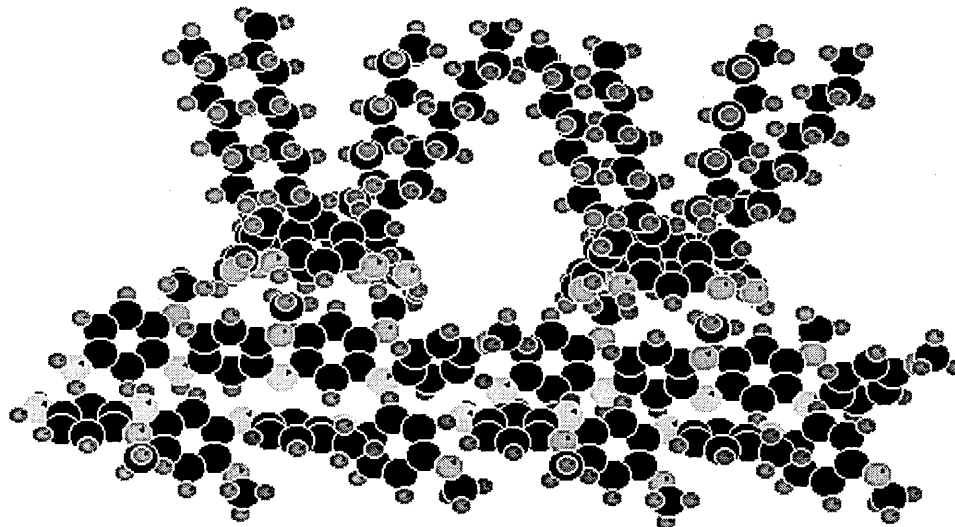


Fig. 16 Proposed molecular arrangement in the composite membrane

It can not be said with certainty, that this is the actual arrangement that is taken up, a variety of arrangements are possible, only scanning atomic force microscopy or nuclear magnetic resonance studies are able to provide more conclusive results.

4.3.1.4.2 Homogeneity analysis

The homogeneity and thickness of the membrane was further evaluated with absorption spectroscopy. For a thickness beyond around 10 mixed ML SPR is no longer suitable, since the evanescent field is completely absorbed (Appendix 2). The colourless C[4]RA, required the use of fused silica as substrates to extend the spectral measurements into the UV region. Figure 17 shows a comparison of the absorption spectra of “pure” C[4]RA and the composite membrane. The C[4]RA has two strong absorption peaks in the ultraviolet at 200 and at 287nm, with the 200nm peak stemming from the π - π electron transition of the ring structure ^[50] and does not show any absorbance beyond 350 nm. The peak at 190 nm increases linearly in height with the steps in the

number of ML. Since the light absorption is directly related to the thickness/concentration of a sample via Beer's law (5) [53], this confirms a linear thickness increase.

$$A = \epsilon \cdot b \cdot c \quad (5)$$

A = absorbance, c = concentration b = pathlength and ϵ = the molar absorptivity

The incorporation of the POMA leads to an increase in the peak heights at 190 nm, 287 nm and the emergence of a new peak at 605 nm. The increase at 200 nm is due to the increase of the aromatic structures whereas the peak at 605 nm is due to the polaronic band in the POMA.

The inset shows that the increase for all three peaks grows linearly with the increase in ML numbers. Since the interrogating beam of the spectrometer has a rather large diameter (0.36cm²), this further indicates a good spatial homogeneity.

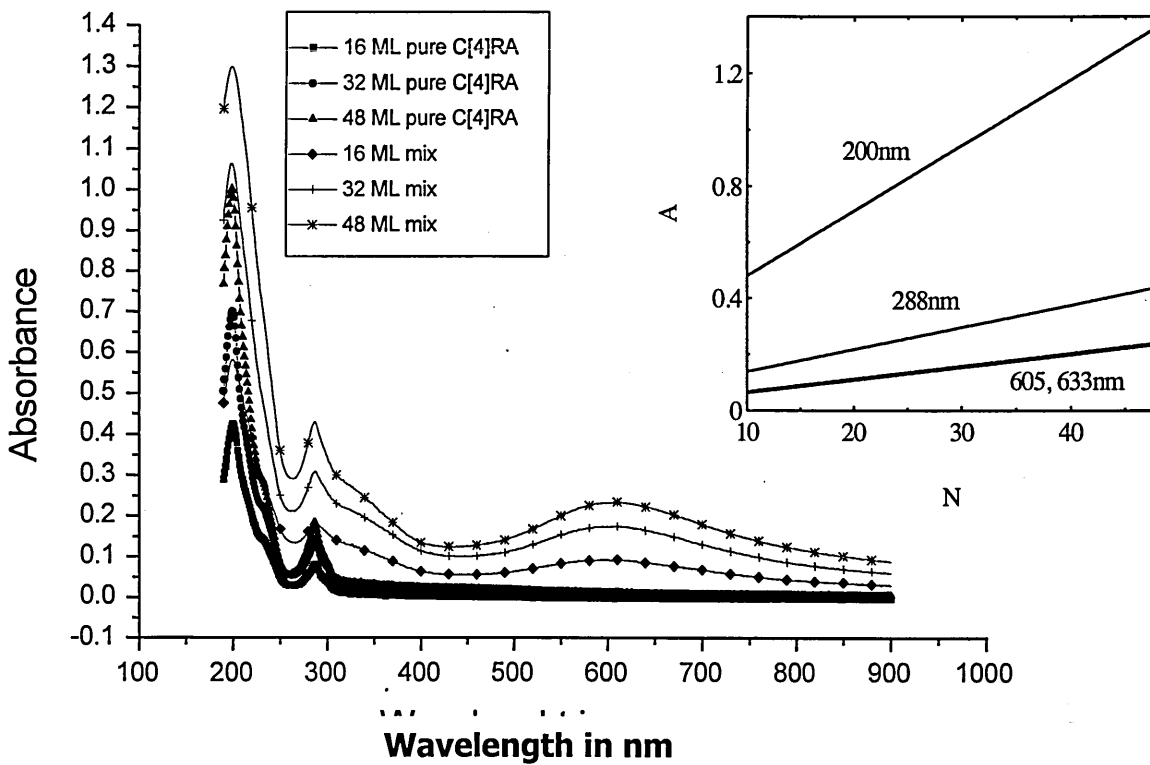


Fig. 17 Absorption spectra of step structures for "pure" C[4]RA, and C[4]RA/POMA membranes

Figure 18 shows a comparison of the absorption spectra of the above mix with a mix of C[4]RA/POMA base (undoped) in the ratio of 1.3 : 1. The inset, magnifies the peak around 600 nm. The peak heights reveal that the higher ratio of the C[4]RA, contributes to an increased absorption at 200 and 287 nm whereas the peak height round 600 nm is slightly reduced and the peak is shifted to lower frequencies. The shift in this polaronic absorbance band is associated with the increase in the concentration of doping level, due to the HCl. This is in line with MacDiarmid findings ^[51, 52], who showed that for polyaniline, sorption bands shift to higher wavelength when the doping state changes from the emeraldine base to the emeraldine salt.

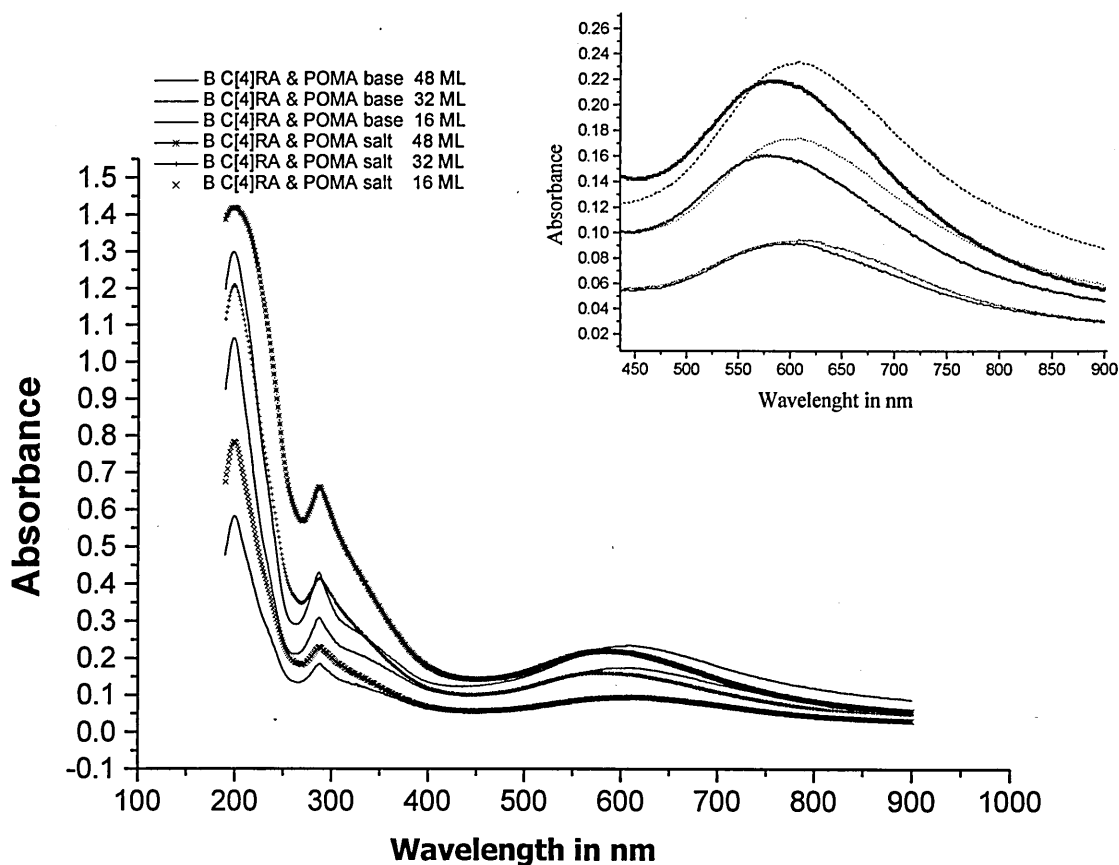
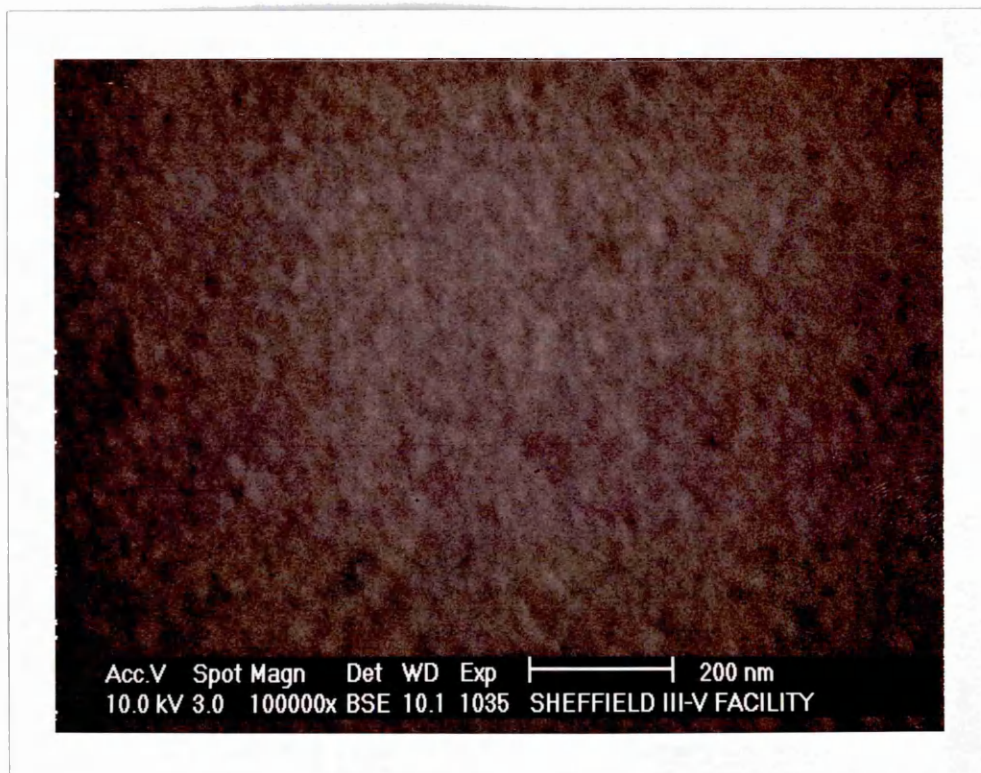


Fig. 18 Comparison between doped and undoped composite membrane

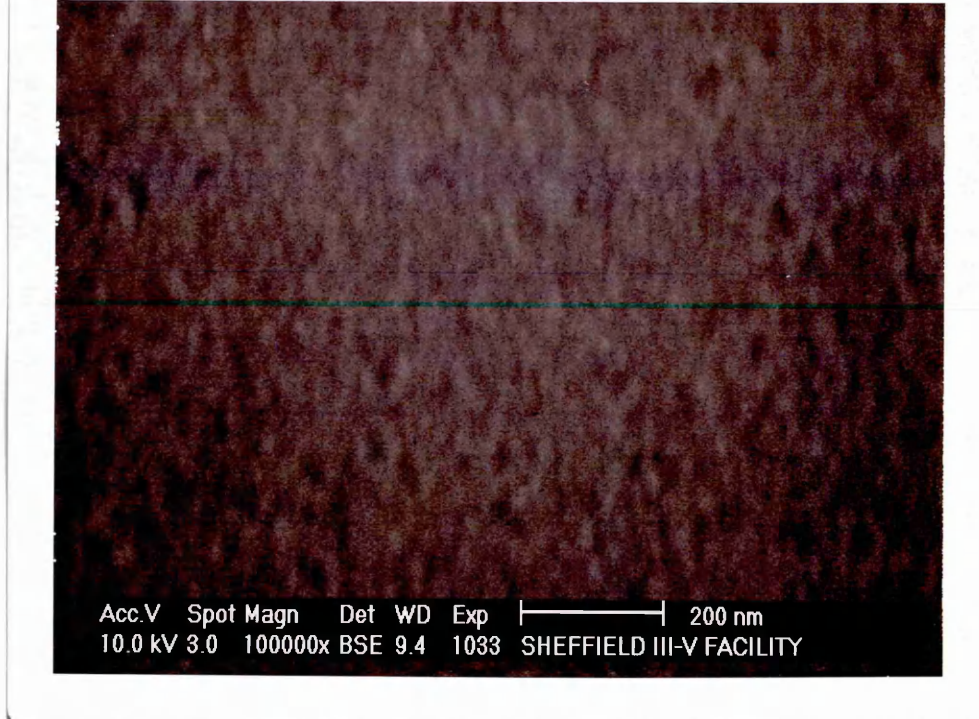
For any composite membrane the homogeneity is absolutely vital. If the materials deposited together, segregate out even partially into islands, its properties become highly anisotropic and there exists only poor reproducibility in the film properties. Optical inspection of the films, with the unaided eye and a light microscope revealed no structure in the film, and it appeared perfectly smooth and homogeneous. Since the resolution of optical microscopes is limited to objects of around 500 nm, these

investigations can only confirm homogeneity up to this limit. In order to investigate any underlying structure with smaller feature sizes, scanning electron microscopy (SEM) was employed. For the analysis, films were deposited onto gold coated glass substrates and these were cut and mounted on sample studs. The effects of organic vapours and electroactive gases on the film structure were investigated by long term exposure (6 hours) on the membrane to saturated vapours of chloroform, representing organic vapours and ammonia representing electroactive gases.

The following two micrographs, Picture 1 and Picture 2, show two different unexposed films 24 hour after deposition. There are no large-scale structures or striations visible. On a scale of 30 nm some film texture becomes recognisable. The textures differ slightly from sample to sample but in general look identical. Since the calixarene is of much smaller size, it must be assumed, that what can be made out are entangled coils of the polymer. Since the texture is dominated by larger flat regions, a possible explanation for this is that the polymer backbone gets mostly 'nicely' incorporated into the calixarene matrix but that to some extent the polymer has not uncoiled into its stretched-out form and was incorporated in its coiled form.



Pic. 1 SEM of composite membrane as deposited

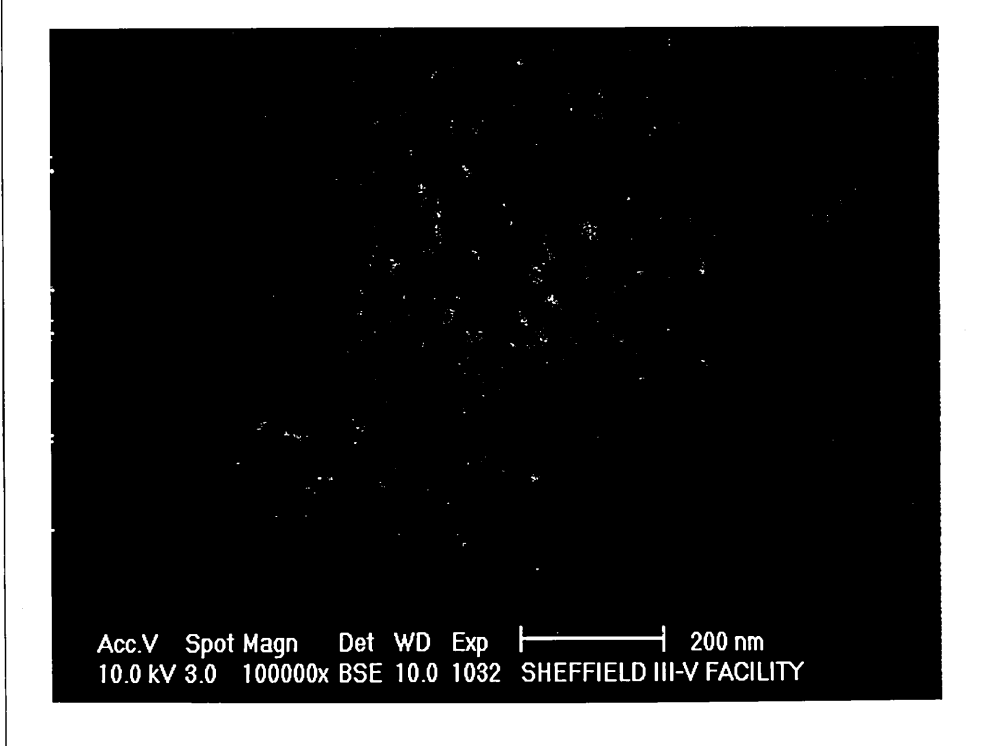


Pic. 2 SEM Picture of a second composite membrane as deposited

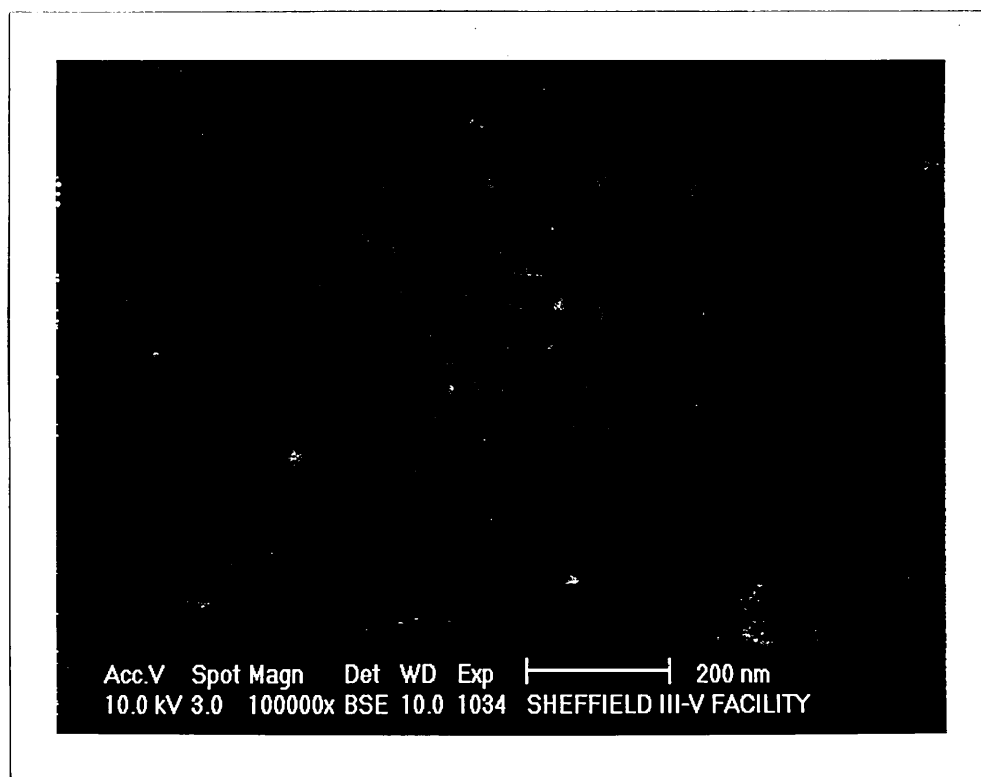
The Pictures 3 and 4 show micrographs of exposed films. The extensive exposure, both concentration wise and timewise have lead to a restructuring of the film. The film with the chloroform exposure, Picture 3, shows a finer microstructure with a higher graininess, whereas the sample treated with the electroactive vapour, Picture 4, shows less microstructure.

In the case of the chloroform it is likely that the vapours have led to a swelling of the film, changing the elasticity of the calixarene matrix, and allowed a resettling in a modified arrangement when the solvent vapour was removed. This implies a partial uncoiling of the polymer chains. The energy that is required for any redistribution and movement of the molecules must stem form the thermal/kinetic energy of the molecules.

The ammonia vapour, should show less effect on the calixarene matrix, with respect to changes in its elastic properties, therefore the low graininess appearance must be due to changes in the polymer itself. When undergoing further doping the density of charged sites increases, due to protonation (Chapter 5), bringing with it stronger electrostatic repulsion, caused by the likewise charge interaction. Since the alkane chains, on the C[4]RA allow for a certain flexibility, this can contribute to a realigning of the polymer strands, in a more separated arrangement.



Pic. 3. SEM of a composite membrane after a 6h exposure to saturated vapours of chloroform



Pic. 4 SEM of a composite membrane after a 6h exposure to saturated ammonia vapours

4.3.2 Spun films

4.3.2.1 Deposition details of C[4]RA

Membranes were deposited onto glass slides and gold coated slides by spin coating, applying the solution to the rotating substrate, as described in reference [26]. This was consistent with the choice of chloroform as a solvent. The high volatility leads to the formation of fringes when the material is deposited onto the stationary substrate and then accelerated. One drop of solution was delivered by pipette onto the rotating substrate, at different speeds from a height of ca 1.5cm. Spinning was then continued for 30 seconds and the thickness and absorption measurements were performed without delay.

4.3.2.2 Film thickness analysis of the spun films

The transparency of the membranes does not allow any comment about the film structure. The results of these measurements are summarised in Figure 19, showing the thickness and absorption dependence on the spin-speed and solution concentration. Mathematically the relationship between the spin-speed, ω , and the film thickness, d , is governed by (3),

$$d = c \cdot \omega^x \quad (3)$$

with c and x being material specific constants. Fitting the SPR scan data as described in the Appendix 2 resulted in the following thickness data. Subsequently the thickness data was fitted to (3), with Figure 19 also showing the theoretical fit. Table 2 gives the values obtained for the fit.

	c	x
Solution concentration 1 mg/ ml	1.16	-0.44
Solution concentration 2 mg/ ml	1.57	-0.48

Table 2 Values obtained for the fitting of the thickness data to (5)

There is a substantial discrepancy between the fitted data and the theoretically derived data. This can only be accounted for by assuming that the c and x values are not truly

constant or that the applied model is only a first order approximation. The obtained values for the exponent are rather close to those reported by Extrand^[37] but there a substantial discrepancy with^[36], where a better agreement with the theoretical $-2/3$ was obtained.

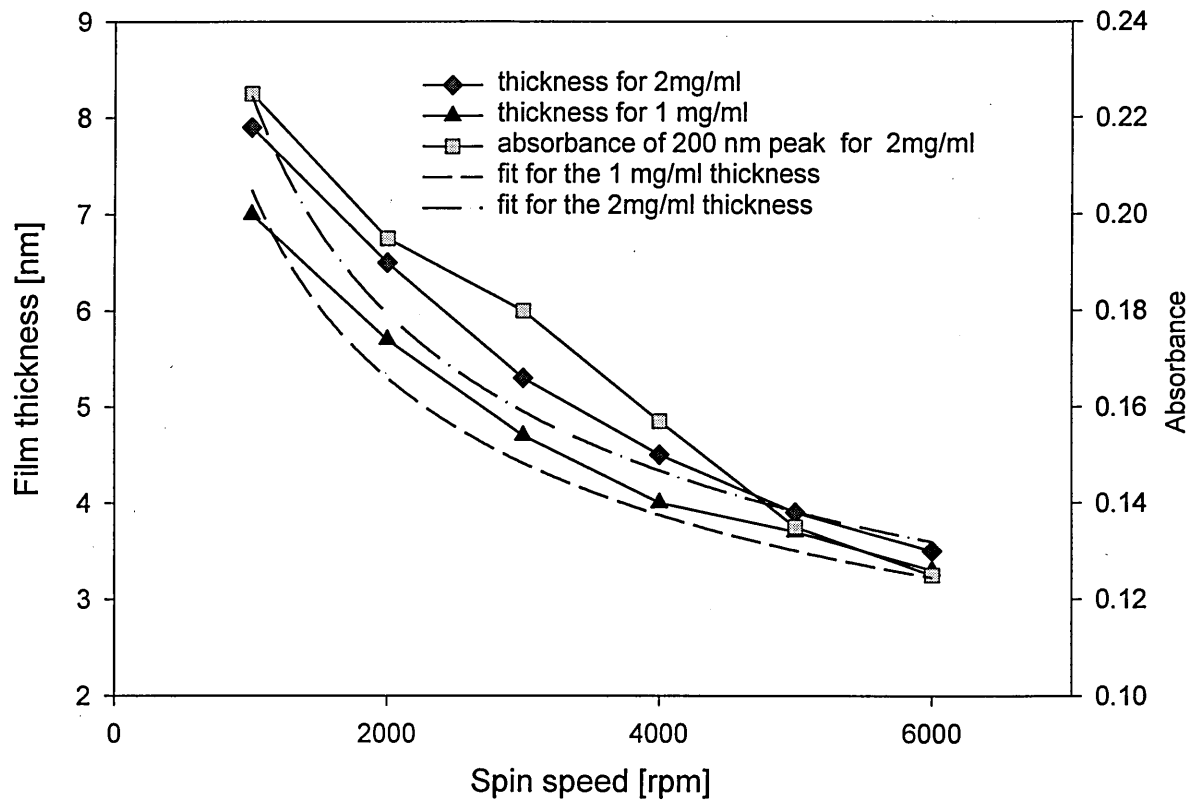


Fig. 19 Thickness dependence of the spun films on spin speed and concentration and absorption peak height dependence of spin speed

According to the theory of hydrodynamics^[54, 55] the thickness of spun films is given in the form of (7),

$$d = \sqrt{\frac{3n\phi}{2\rho^2\omega^2}} \quad (7)$$

ρ is the density of the pure solvent, ω is the angular velocity and ϕ is the mass flux as a result of the evaporation.

It is believed that (7) does not strictly apply to films that are only three or four times the thickness of a molecule. It must be considered that the film thickness will have to show a more asymptotic approach to the single molecule diameter at higher speeds. There is

no thickness possible below that of a single molecule, this is not accounted for by the models. Further the intramolecular forces between solute molecules, forming the friction forces for the convective flow of the solution are unique to a specific compound. In (7) ρ is governing the hydrodynamic flow, but for very thin films the density should contain an element reflecting both the density of the solute as well as the solvent.

It can therefore be said that the experimental results are unique for the C[4]RA, and the discrepancy with the model can be attributed to shortcomings in the model.

The absorbance does not follow exactly the SPR determined curve. Since the SPR measurements are only limited to a spot size of less than a 1mm across, whereas the UV-vis spectroscopy uses beams several times larger (0.36cm^2), fringe effects, might distort the measurements, therefore giving more credibility to the SPR measurements.

Spin coating, allows the generation of films in the region of films with about 10 ML thickness, thicker films are not attainable with this deposition method.

4.3.3 Casting

Membranes from casting were prepared by dissolving 2mg/ml of the C[4]RA in chloroform and casting a volume of 4 μl onto the substrates (CFT- gate region). After the evaporation of the chloroform a film with an area of ca. 0.4 cm^2 had formed. Using the area and solution concentration the thickness was calculated to be ca. 250 nm.

4.3.4 Absorption spectra analysis of C[4]RA solution, spun and LB films

Analysis of the absorption spectra of C[4]RA, in solution, as LB film and spun film reveals that, there is no change in the position of the absorption peaks. Differences in the solution spectra and the spectra of spun films were shown in reference [36], a narrowing of the absorption peak stemming from a nitrophenyl group, whose absorbance centred around 450nm, was reported. No such changes could be observed for the C[4]RA. It is believed that the aromatic structures causing the absorption at 200 nm are not deformed in contrast to the nitrophenyl groups in the chains. The nitrophenyl

groups can show a differing interaction with neighbouring molecules in solution and in a film but hardly any interaction difference between the baskets can be expected.

Summary

In this chapter the theory of several thin film deposition methods have been summarised, and the film properties that are attained for the C[4]RA and a composite of C[4]RA/POMA have been analysed. The desired film thickness dictates the deposition method to use, thin films can be spun, LB films allow thin to medium thick films and truly thick films require casting. The information regarding the membrane properties is fundamental for the application in any type of sensor. Furthermore the suitability of C[4]RA as a matrix for the LB deposition of non surface active polymers, was demonstrated in detail, with poly-ortho-metoxo aniline as a representative of these polymers, covering a wide thickness range.

4.4 References

- [1] J. Crank, G.S. Park, Diffusion in Polymers, J. Crank, G.S. Park, Academic Press Chap. 1, 1968
- [2] V. Stannet in Diffusion in Polymers, J. Crank, G.S. Park, Academic Press Chap. 2, 1968
- [3] C. Jouve, D. Jullien, B. Remaki, Sens. & Actua. B, 28, 75, 1995
- [4] Y. Kungi, K. Nigorikawa, Y. Harima, K. Yamashita, J. Chem. Soc. Chem Comm., 873, 1994
- [5] F.J.G. Monreal, C.M. Mari, Sens. & Actua. 12, 129, 1987
- [6] Z. Chen, S. Ng, S.F.Y. Li, Synthetic Metals 87, 201-204, 1997
- [7] I. Watanabe, K. Hong, M.F. Rubner, Langmuir 6, 1164, 1990
- [8] M. Rikukawa, M.F. Rubner, Abstr. pap. Am. Chem. S. 201, 187-Poly. Part 2, APR 14, 1991
- [9] M. Rikukawa, M.F. Rubner, Thin Solid Films, 210, 274, 1992
- [10] P.S. Barker, J.R. Chen. N.E. Agbor, A.P. Monkman, Sens. & Actua. B, 17, 143-147, 1994
- [11] N.V. Lavrik, D. De Rossi, Z.I. Kazantseva, A.V. Nabok, B. A. Nesterenko, S.A. Piletsky, V.I. Kalchenko, A.N. Shivaniuk, L. N. Markovskiy, Nanotechnology 7, 1-5, 1996

- [12] P.N. Barlett, S.K. Ling-Chung, *Sens. & Actua. B.* 20, 287, 1987
- [13] H.V. Shumer, P. Corcoran, J.W. Garner, *Sens. & Actua. B.*, 4, 29, 1991
- [14] Y. Min, Y. Xia, A.G. Mac Diarmid, A.J. Epstein, *Synthetic metals* 69, 159-160, 1995
- [15] A.Riul Jr., L.H.C. Mattoso, S.V. Mello, G.D. Telles, et al., *Thin Solid Films*, 284-285, 177, 1996
- [16] A. Dhanabalan. A. Riul, D. Conclaves, O.N.Oliveira, *Thin Solid Films*, 327-329, 60-64, 1998
- [17] A.G Macdiarmid, A.J Epstein, *Synthetic Metals* 65, 103, 1994
- [18] A.G. MacDiarmid, A.J.Epstein, *Synthetic Metals* 69, 85, 1995
- [19] R.J. Lewis, *SAX's Dangerous Properties of Industrial Materials*, 9th Edition, Van Nostrand Reinhold, 1996
- [20] S.S. Umare, M.M. Huque, M.C. Gupta, S.G. Viswanath, *Macromolecular Reports A33*, 381-389, 1990
- [21] M.C. Gupta, S.S. Umare, *Macromolecules*, 25, 138-142, 1992
- [22] C.M. Lepienski, R.M. Faria, G.F.L. Fereira, *Appl. Phys.Lett.* 70, 14, 1997
- [23] J.S.Nogueira, L.H.C. Mattoso, C.M. Lepienski, R.M.Faria, *Synthetic Metals* 69, 259-260, 1995
- [24] S. Munoz, T. Nakamoto, T. Moriizumi, *Sensors and Materials*, V11. 7, 427-435, 1999
- [25] M. J. Jory, P. S. Cann, J. R. Sambles, *J. Appl. Phys.*, 27, 169, 1994
- [26] P. S. Vukusic, J. R. Sambles, J. D. Wright, *J. Mater. Chem.*, 2, 1105, 1992
- [27] W.J. Daughton, F.L.Givens, *J. Electrochem. Soc* V 129, 1, 1982
- [28] D. E. Bornside, C. W. Macosko, L. E. Scriven, *J. Electrochem. Soc* V.138, 1991
- [29] R.K. Yonkoski, D.S. Soane *J. Appl. Phys.* 72, 2, 1992
- [30] D.E. Bornside, C.W. Macosko, L.E. Scriven, *J. of Imaging Technology* 13, 122, 1987
- [31] P. C. Sukanek, *J. of Imaging Technology*, 11, 4, 1985
- [32] D. E. Bornside, C. W. Macosko, L. E. Scriven, *J. Appl. Phys.*, 66, 5185, 1989
- [33] B. D. Washo, *IBM J. Res. Dev.*, 21, 190, 1977
- [34] R.K.Yonkoski, D.S.Soane, *J. Appl. Phys.* 72, 2, 1992
- [35] D. E. Bornside, C. W. Macosko, L. E. Scriven, *J. Appl. Phys.*, 66, 5185, 1989
- [36] Hassan AK, Ray AK, Nabok AV, Panigrahi, *IEE Proceedings-Science Measurement and Technology*, 147, 3, p. 137-140, 2000
- [37] C.W. Extrand, *Polymer Engineering and Science*, V.34, 5, 1994
- [38] D. Tabor, *Journal of Colloid and Interface Science*, V. 240, 1, 240-245, 1980

- [39] B. Franklin, *Philosophical Transactions of the Royal Society of London*, 64, 445, 1774
- [40] Lord Rayleigh, *Proceedings of the Royal Society of London*, V. 47, 1890
- [41] A. Pockels, *Nature*, V 46, 419, 1892
- [42] I. Langmuir, *J. Am. Chem. Soc.*, 39, 1848, 1917
- [43] K. A. Blodgett, *J. Am. Chem. Soc.*, 57, 1007, 1935
- [44] M.C. Petty, M.R. Bryce, D. Bloor, *An Introduction To Molecular Electronics*, Edward Arnold, 1995, ISBN: 0-340-58009-7, Chapter 10
- [45] F. Grundfeld, *Review of Scientific Instruments* V. 64, 2, 88-93, 1995
- [46] *Exploring Chemical Analysis* Daniel C. Harris, W.H. Freeman, 1996, ISBN: 0-7167-3042-1
- [47] *Ellipsometry and Polarized Light*, R. M. A. Azzam, North-Holland, 1999, ISBN: 0444870164
- [48] A. V. Nabok, N. V. Lavrik, Z.I. Kazantseva, B.A. Nesterenko, L.N. Markovskiy, V. I. Kalchenko, A.N. Shivaniuk, *Thin Solid Films* 259, p. 244-247, 1995
- [49] N.V. Lavrik, D.De. Rossi, Z.I.Kazantseva, A.V.Nabok, B. A. Nesterenko, S.A. Piletsky, V.I. Kalchenko, A.N. Shivaniuk, L. N. Markovskiy, *Nanotechnology* 7, 1-5, 1996
- [50] G. Schwedt, *The Essential Guide to Analytical Chemistry* ISBN: 0471974129, page 111
- [51] A.G. MacDiarmid, A.J. Epstein, *Brasizilian Conference on Polymers*, Sociedade Brasileira de Polimeros, Sao Paulo, p 544, 1993
- [52] J.G. Masters, Y.Y. Sun, A.G. MacDiarmid, A.J. Epstein, *Synthetic Metals*, 41-43, 715, 1991
- [53] G. Schwedt, *The Essential Guide to Analytical Chemistry*, Wiley, 1997, ISBN: 0471974129, page 106
- [54] P.C. Sukanek, *J. Electrochem. Soc.*, 144, p. 3959-3962, 1997
- [55] A. Patridge, S.L.G. Toussaint, C.F.J. Filipse, *J. Vac. Sci Technol. B*, 14, p. 585-592, 1995

5 The detection of gaseous organic and inorganic pollutants with C[4]RA based membranes

5.1 Introduction

In this chapter will be presented and discussed novel sensing applications for the C[4]RA and C[4]RA/POMA membranes, that are based on well established transduction mechanisms. Results from individual sections will be referred to for the discussion throughout. The inorganic pollutants consist of “electroactive gases“, like NH_3 , NO_2 and HCl whereas the organic pollutants are straight chain and aromatic hydrocarbons. The focus in this work has been on the elucidation of the involved mechanisms and the proof of principle, together with a possible application development, rather than the quest for lower detection thresholds.

5.2 Spectrophotometer study of the absorption of toluene in LB deposited C[4]RA films

UV-vis absorption spectroscopy allows the detection of organic vapours, that absorb in the wavelength range of 190-800 nm. Light energy is absorbed by the molecule to promote an electron transition from the highest occupied to the lowest unoccupied molecular orbital. This absorption of light is detected via the reduction in the transmitted light. C[4]RA itself is non absorbing in the visible range (400-700) nm, as are almost all common solvents. Therefore the spectra in the ultraviolet region were analysed. Of the common solvents toluene is of particular interest since:

- its absorption peak of 200 nm falls into the measurement spectra
- complexation with calixarene derivatives has been proven to be highly reversible
- different theories about the complexation sites exists, i.e. inside the basket or/and between molecules
- the amount of toluene that is incorporated into each host molecule is subject to discussion
- the same points apply to benzene, but toluene was preferred due to its lower toxicity

5.2.1 Experimental details

A 16 ML thick C[4]RA membrane was deposited onto quartz slides, as described in Chapter 4. The slide was then inserted together with a reference slide into a UV-vis spectrometer, which was previously calibrated according to standard procedures. The absorption baseline was recorded and then an open jar filled with toluene was placed inside the tightly sealed measuring chamber of the spectrometer. An equilibration time of 10 minutes was allowed to fill the whole chamber with saturated toluene vapours, before the exposure absorption was recorded. For the smallness of the chamber (Volume ca. 5 l), the vapour concentrations can be assumed to be uniform inside the chamber. Both the reference and the measuring beam pass through an equal amount of toluene, therefore the solvent vapour does not offset the baseline.

5.2.2 Results and discussion

The absorption spectrum of the baseline and the spectrum after toluene sorption is shown in Figure 1.

Calculation of the number of sorbed toluene molecules

Toluene and the C[4]RA have both their maximum absorption peak at 200nm, which corresponds to the π - π^* transition of aromatic structures [1]. The C[4]RA has four aromatic structures, in the basket, the absorption rate of one ring structure can therefore be calculated from the increase of the absorption with the increase in the number of MLs.

The absorption values for 16 ML; 0.43, 32 ML; 0.7 and 48 ML; 1.0 have been established from the characterisation of the film deposition, Figure 17 in Chapter 4.

There is a near linear absorption increase in the region between 16 and 48 ML (inset Figure 17 Chapter 4). Overall absorption increases nonlinearly, individual absorption values per monolayer for each sample yield 0.027 (16ML), 0.022 (32ML) and 0.21 (48ML), therefore an averaging mechanism was adopted, with the baseline being defined by the 16 ML sample. Both 32 and 48 ML are equally weighted in this averaging, details for this are given in (1). For higher layer numbers deposition fluctuations seem to cancel out. Since the measurement is a relative one, the area cancels out in the calculation, giving an averaged absorption rate per ML of 0.0178 .

$$\frac{\frac{1.0-0.7}{16\text{ML}} + \frac{0.7-0.43}{16\text{ML}}}{2} = \frac{0.285}{16\text{ML}} = \frac{1.78 \cdot 10^{-2}}{\text{ML}} \quad (1)$$

Every ring structure has therefore an absorption coefficient of

$$\frac{\frac{1.78 \cdot 10^{-2}}{\text{ML}}}{\frac{4 \text{ ring structures per molecule}}{\text{ML}}} = \frac{4.45 \cdot 10^{-3}}{\text{ring structure}}$$

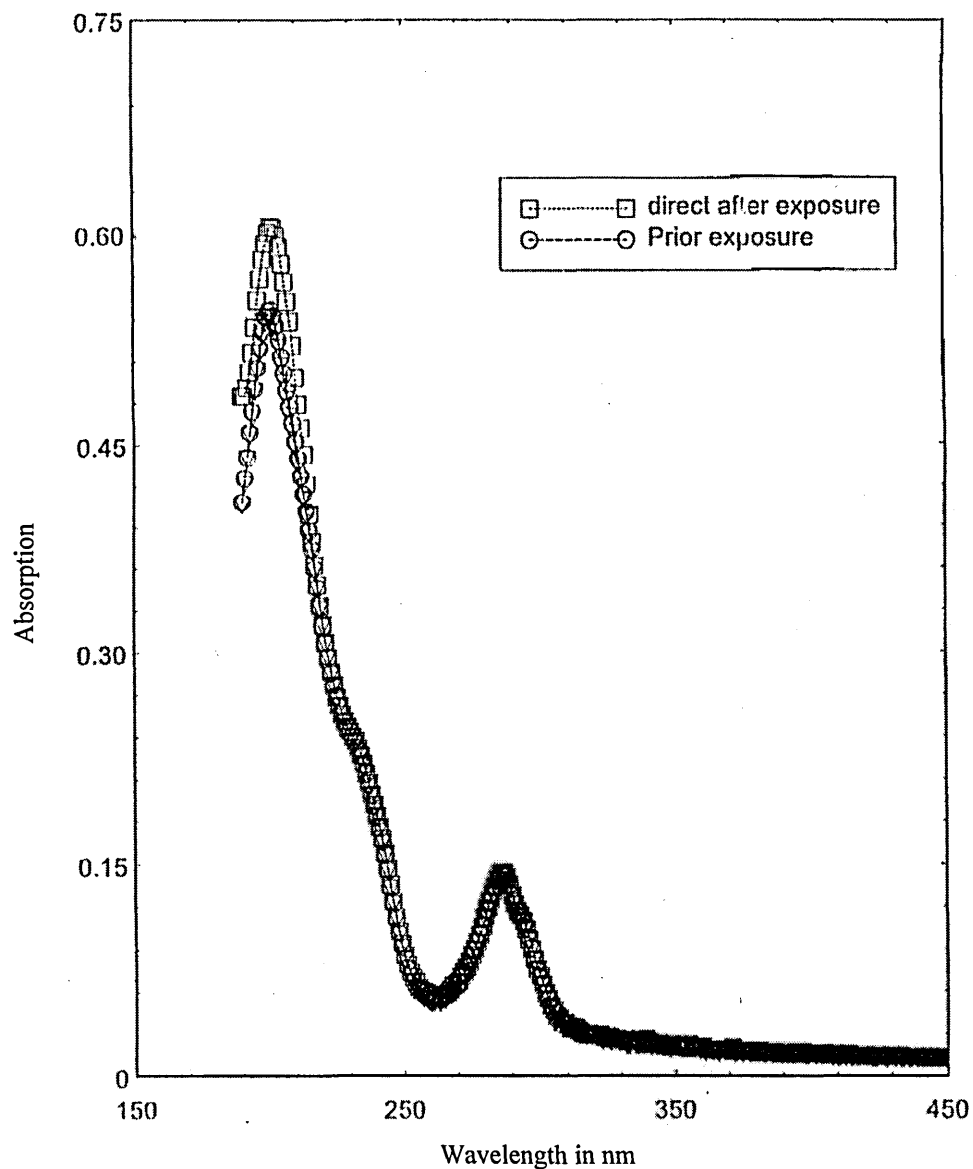


Fig. 1 Absorption spectra of 16 ML of C[4]RA with and without toluene complexation

The absorption increase at 200 nm, as taken from Figure 1, is 0.06. This allows the calculation of the increase in the number of ring structures (2), which equates with the number of toluene molecules absorbed.

$$\frac{6.0 \cdot 10^{-2}}{4.45 \cdot 10^{-3}} = 13.5 \text{ ring structures} \quad (2)$$

ring structure

An increase of 13.5 aromatic structures/toluene molecules in a 16 ML thick film, shows that within the error of the experiment, there exists a complexation ratio of ca. 1:1 toluene per C[4]RA molecule. This result further supports the theory, that for aromatic guest molecules complexation occurs only inside the basket and not between molecules [2]. Since the vapour exposure was conducted at the saturated vapour pressure (22 mbar), it can be assumed that no complexing between molecules takes place in LB films, excluding any micro-condensation of the solvent as was proposed for toluene in reference [3]. For spun films the molecular arrangement of the molecules can be expected to be different, therefore the above may not hold true and complexation might take place between molecules. The molecules in the LB films might be too closely packed for any complexation between adjacent molecules to take place or the π - π interaction between the aromatic structures might provide the only mechanism leading to complexation. A comprehensive comparative study between LB and spun films [4], has shown that spun films possess a higher absorption of organic vapours than LB films. The above further supports this, by showing the number of the complexing molecules to be nearly identical with the number of baskets.

Absorption spectroscopy can be employed in a very selective sensor based on a single wavelength interrogation at 200nm. The enormous benefit of this is, that only aromatic structures will show up at this wavelength. Other hydrocarbons might still complex inside the C[4]RA membrane, but the absorption spectra will not undergo changes at 200 nm.

5.3 DC conductivity modulation of the C[4]RA/POMA membrane upon analyte interaction

The low conductivity of the C[4]RA, (at least 1 order of magnitude lower than the undoped POMA, Chapter 7) makes measurements of the direct thin film conductivity impossible. Neither the powder conductivity (compressed pellet) nor the conductivity of any cast films could be determined within the $G\Omega$ range. It can therefore be assumed that for the following measurements the conduction is dominated by the POMA in the composite membrane and not the C[4]RA. As a first step, work focused on electroactive gases, that provide a sort of doping, via protonation, for the polymer modulating the conductivity. The studies were then further extended to include organic solvent vapours, structural changes in the film contributing to the conductivity changes can be viewed as unique, due to the matrix structure of the membrane.

5.3.1 Response to electroactive gases

Interest in the detection of inorganic gasses, of oxidising and reducing nature, is based mainly on the fact that the emission of these gases occurs as a “by-product” in many industrial processes, like the burning of fossil fuels, smelting of ores, and bleaching of wood pulp.

5.3.1.1 Experimental details

The composite membrane was, as described in Chapter 4, deposited onto interdigitated electrodes (IDE) with 8 finger pairs of 3.125 mm overlap and a separation between fingers of 600 μ m, terminating with 1mm² contact pads at one end. Due to the low conductivity the number of layers making up the membrane was chosen to be 16 layers. The contact was provided by “gluing” connecting wires with silver paste to the contact pads. The IDE were mounted in a 0.3 l Teflon chamber and connected to a Keithly 614 electrometer, using a voltage of 1 V for the conductivity measurements. A computer controlled the electrometer and simultaneously two mass flow controller providing a constant stream of 0.145 l/min of purging gas (N₂) or analyte. The analyte was provided by pre-conditioned gas cylinders for NO₂ (400ppm), NH₃ (300ppm) and by bubbling N₂ through a solution of hydrochloric acid (38%) for HCl.

5.3.1.2 Results and discussion

Though the HCl bath doped form of the POMA was deposited, Appendix 1, the conductivity of the composite membrane, in the as deposited form, was as low as $1 \cdot 10^{-3}$ S/cm for the 1:1 by weight mixing ratio when measured in static air. This value is low compared to the value of 0.1 S/cm published for pure POMA in reference [5]. Three things can account for this; firstly the synthesis methods only yields a polymer with an inherently lower conductivity, secondly part of the HCl dopant leaches out of the polymer during the LB deposition where it is in contact with water and thirdly the dilution by the integration of the C[4]RA. For mixing ratios with a higher C[4]RA contribution a reduction in the conductivity was observed, Table 1. This conductivity decrease is dominated by dilution. Therefore for any subsequent studies the composite membrane with a 1:1 mixing ratio was used.

Mixing ratio by weight [C[4]RA/POMA]	Conductivity [S/cm]
1:1	$1 \cdot 10^{-3}$
2:1	$0.7 \cdot 10^{-3}$
5:1	$0.3 \cdot 10^{-3}$

Table 1 Influence of the mixing ratio on the conductivity of the composite membrane

To increase the conductance, an in situ doping of the membrane was conducted with HCl vapours. The increase in the conductivity during the doping can be seen in Figure 2.

The increase in the conductivity follows a first order exponential decay, according to (3),

$$I = I_0 + A_1 \cdot e^{(-t/\tau)} \quad (3)$$

with a time constant of 1045 seconds. It can be seen that the conductivity increase is reaching asymptotically a plateau value. Upon purging with nitrogen the conductivity decreases rapidly following again a first order exponential decay, as shown in Figure3.

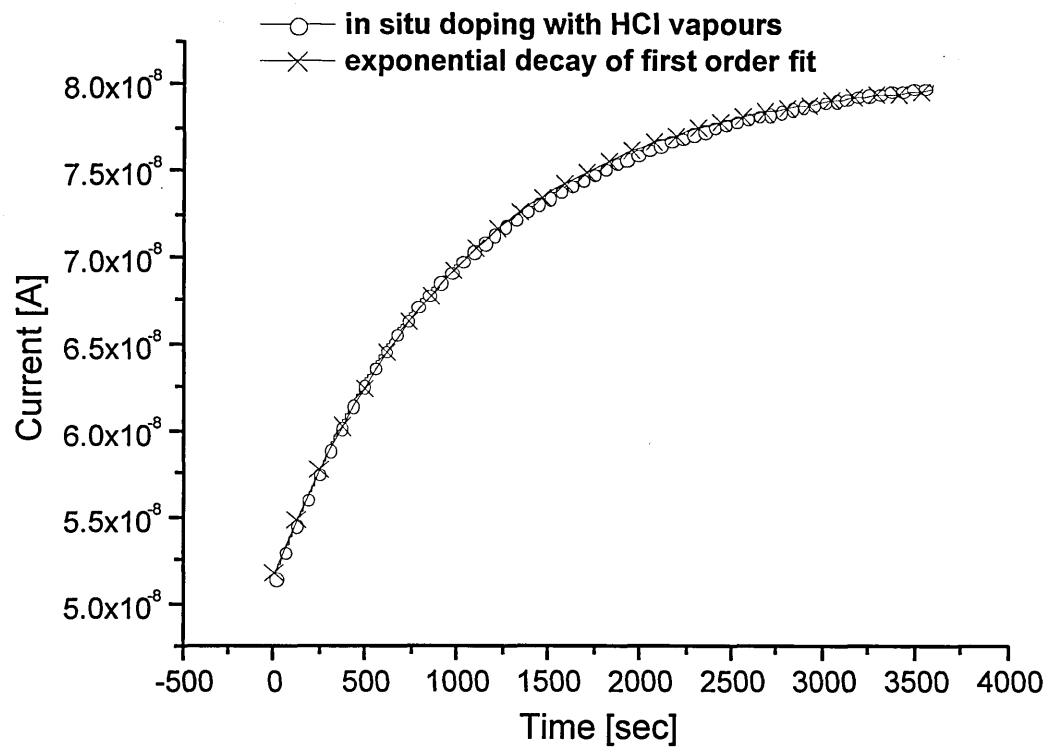


Fig.2 Current increase upon doping with HCl vapours

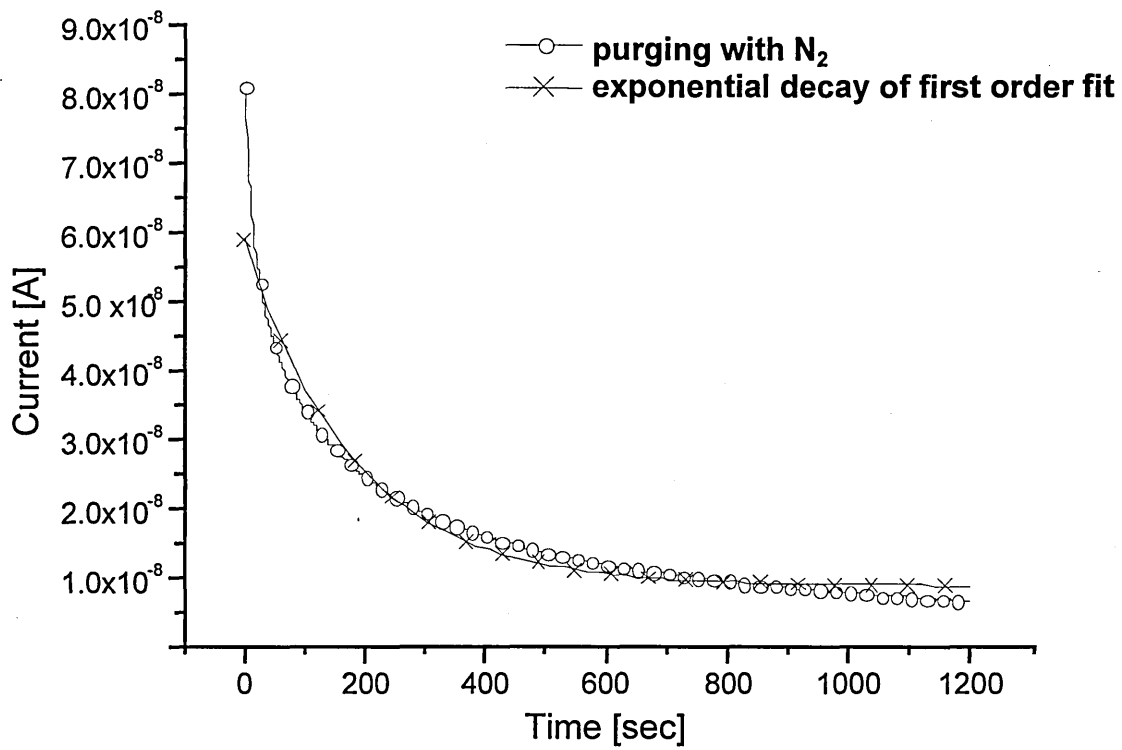


Fig. 3 Current decrease upon purging with nitrogen

The fitted data for the exposure and recovery are summarised in Table 2. The time

	Exposure	Recovery
I_0	$8.05 \cdot 10^{-8}$	$0.83 \cdot 10^{-8}$
A_1	$-2.89 \cdot 10^{-8}$	$1.01 \cdot 10^{-8}$
τ	1045	179

Table 2 Values for (3) describing the exposure and recovery dynamic

constant for the recovery is with 179 seconds 5.9 times faster. The function does not describe a asymptotic approach to a plateau but continues to decrease though with a slow gradient. This behaviour highlights a very important point. The doping with HCl is highly reversible and this makes the conductivity of the membrane strongly history dependent. The as deposited membranes are quite stable, when stored in airtight containers, though they show a similar dedoping behaviour under a constant flow of nitrogen. A similar behaviour of diminishing conductivity was shown to exist for spun film of polyaniline [6], though in that case purging over periods of days stabilised the conductivity. This effect was explained with the removal of surface/bulk trapped water molecules, which may also partially account for the observed behaviour of the POMA. Integration of the POMA in the C[4]RA matrix is most likely responsible for the fast recovery during purging. A microporous structure as, proposed for the matrix in Chapter 4, allows a more unrestricted movement of air into the bulk of the film than in the more condensed pure polymer phase.

The conductivity increase upon exposure to HCl is explained by protonation, that is the addition of a proton to the imine nitrogen in the polymer backbone. This addition of the proton keeps the number of electrons constant. The increase of the conductivity has been explained for polyaniline, by assuming that the addition of a proton removes one of the imine nitrogen lone pair electrons, to form the N-H bond, with the remaining unpaired electron hopping between vacancies, left at these sites. This in effect increases the number of negative charge carriers [7]. Furthermore the protonation will change the geometry of the rings, changing the bond length and with it the wave function overlap to yield a more conducting state. The whole transport mechanisms in aniline based polymers is a complex system, with the nature of the charge carriers and their dynamics still being debated.

The strong difference in the time-constant in the response and recovery, by a factor of 5.9, suggests that the desorption energy of HCl from the imine sites is much lower than the adsorption energy.

The response upon exposure of the same film (aged by 3 days) to a concentration of 400 ppm NO₂ is shown in Figure 4. The oxidising effect of NO₂ again leads to an increase in the conductivity, it can be explained by assuming that NO₂ contact with the π -electron network of the POMA results in the transfer of an electron from the polymer to the NO₂ [6]. This charges the polymer positively, and creates charge carriers, increasing the conductivity. The process is analogous to the protonation by HCl. Again it can be seen that continual purging during the first 600 seconds leads to a decrease in the conductivity. Upon NO₂ exposure these increase again with the notable difference, in comparison to HCl, that the rate of sorption and desorption are about identical. This is indicative of roughly equal sorption/desorption energies of NO₂. The reproducibility is

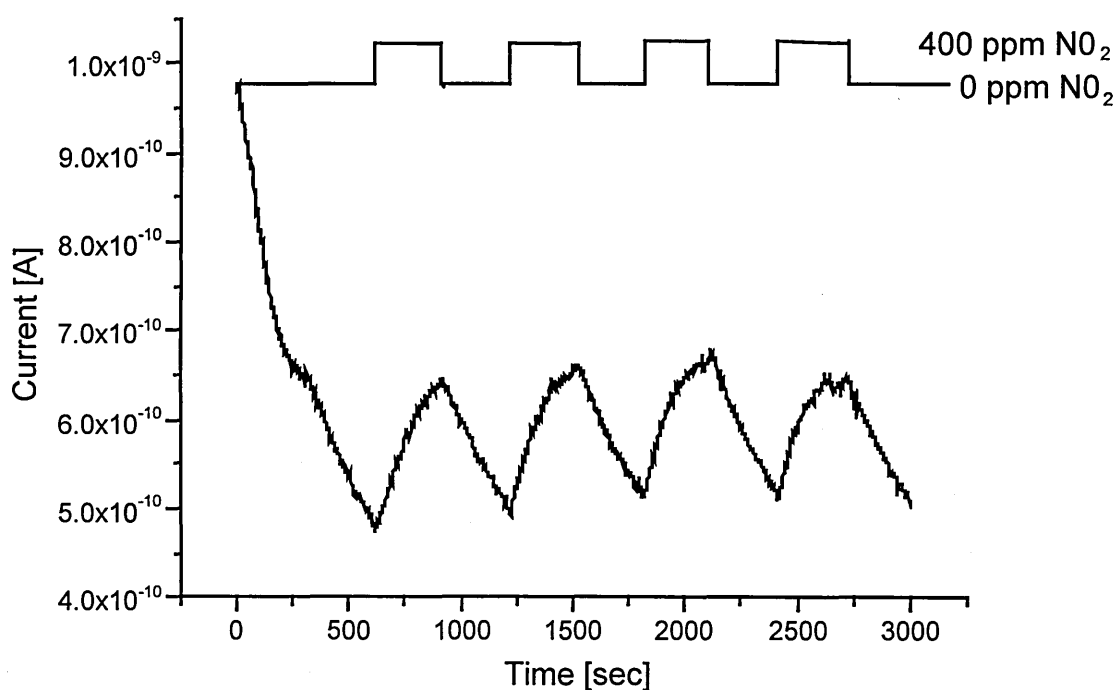


Fig 4 Repeated exposure to the C[4]RA/POMA membrane to NO₂

good with a slight accumulative effect, accounted for by slightly larger desorption times. The current carrying ability is increased 1.4 fold from $4.8 \cdot 10^{-10}$ to $6.3 \cdot 10^{-10}$ ampere.

In order to determine the lower detection threshold the concentration was reduced from 40 to 10 ppm (± 2 ppm). For this the sample was redoped with HCl vapours as described before and then purged with nitrogen until a semi-stable state was reached. Figure 5 shows the induced conductivity changes. Again the effect of a slow but continuous dedoping is visible. Upon exposure to these low concentrations the conductivity increases with respect to the instantaneous baseline but overall the conductivity decreases. This can only be seen as dedoping of HCl dopant with the doping activity of the NO_2 being too low at these concentrations to fully compensate it. Though a lower detection limit of 10 ppm can be defined, the long term drift of the baseline ($>3\text{h}$) makes a comparison of the conductivity modulation with respect to the baseline and concentration difficult. Whereas the 40 ppm concentration shows a stronger conductivity increase the concentrations of 30, 20 and 10 ppm show virtually identical modulations.

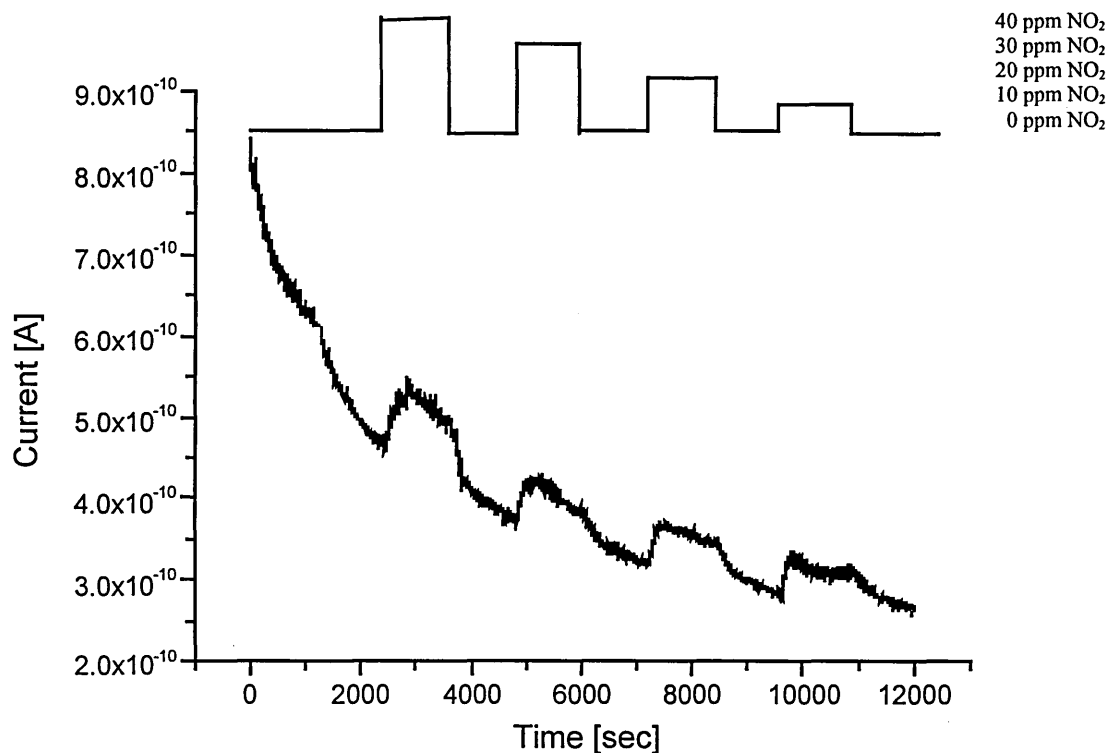


Fig. 5 Response to concentrations of 40, 30, 20 and 10 ppm of NO_2

Conditioning the membrane again, with HCl vapours and subsequent purging with nitrogen it was repeatedly exposed to ammonia with the response shown in Figure 6. The response to ammonia, with a conductivity increase is remarkable. Ammonia is a reducing gas, which should lead to a decrease in the conductivity contrasting the

behaviour of NO₂ and HCl. Instead of compensating the oxidising effect of the HCl, the NH₃ works itself as a dopant. This can be accounted for by assuming that the NH₃, partially dissociates into NH₂⁻ and H⁺, with the H⁺ ion subsequently protonating the polymer according to (4),



with the equilibrium shifting to the right on exposure and to the left on purging. The protonation is again producing positive charge carriers and increases the DC conductivity. Agbor et al. [6] observed a similar conductivity increase for the reducing gas H₂S on polyaniline. The response to exposure and purging are again showing distinctly different time constants, with the doping being about four times faster than the

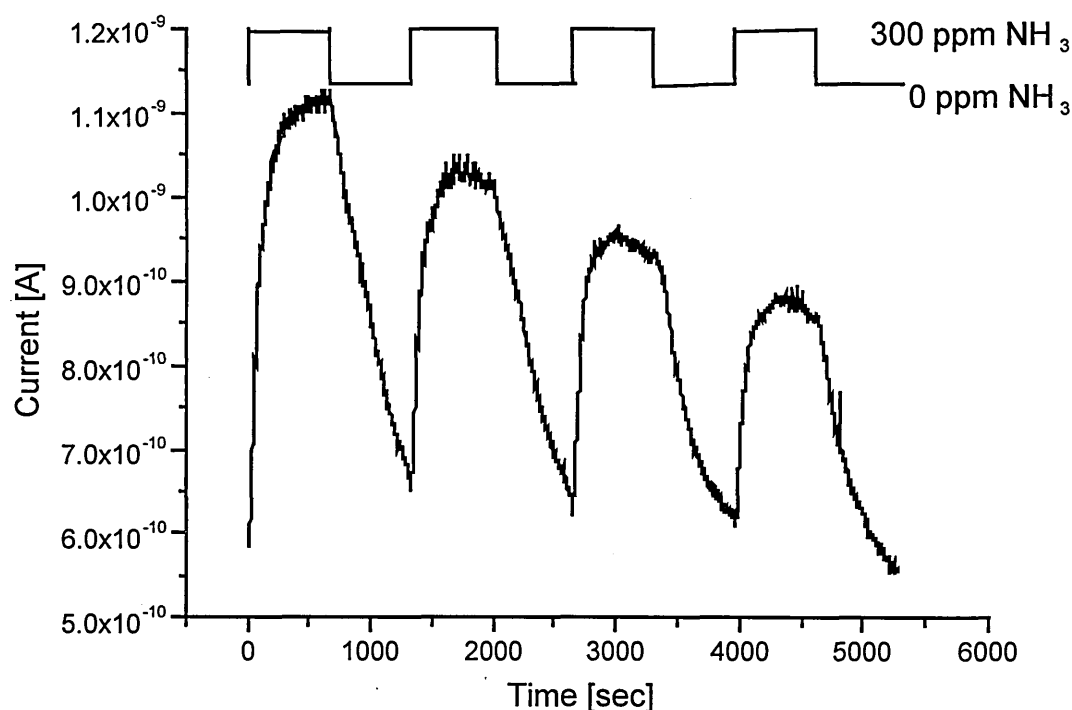


Fig. 6 Repeated exposure of the C[4]RA/POMA membrane to NH₃

dedoping. The current carrying ability is enhanced by a factor of 1.9 from 0.58 nA to 1.1 nA. The repeated exposure results in a decreased modulation of the conductance, with the baseline being rather stable, this implies a sort of memory effect. A possible

explanation for this is structural changes in the membrane, reducing the available reaction/protonation sites, by either affecting the C[4]RA matrix or the POMA itself.

To investigate if this memory effect is a particular feature of the composite membrane, or is an inherent property of the polymer, a film of the polymer was cast from solution onto the IDEs, resulting in an inhomogeneous film, making only a qualitative investigation possible. The response is presented in Figure 7. The response differs markedly from that of the composite matrix. Firstly it must be noticed that the conductivity of the sample decreases upon NH₃ exposure, as was expected from its reducing nature. This is the opposite behaviour to that of the composite membrane. The interaction of the pure POMA and the NH₃ can be explained by deprotonation according to (5),

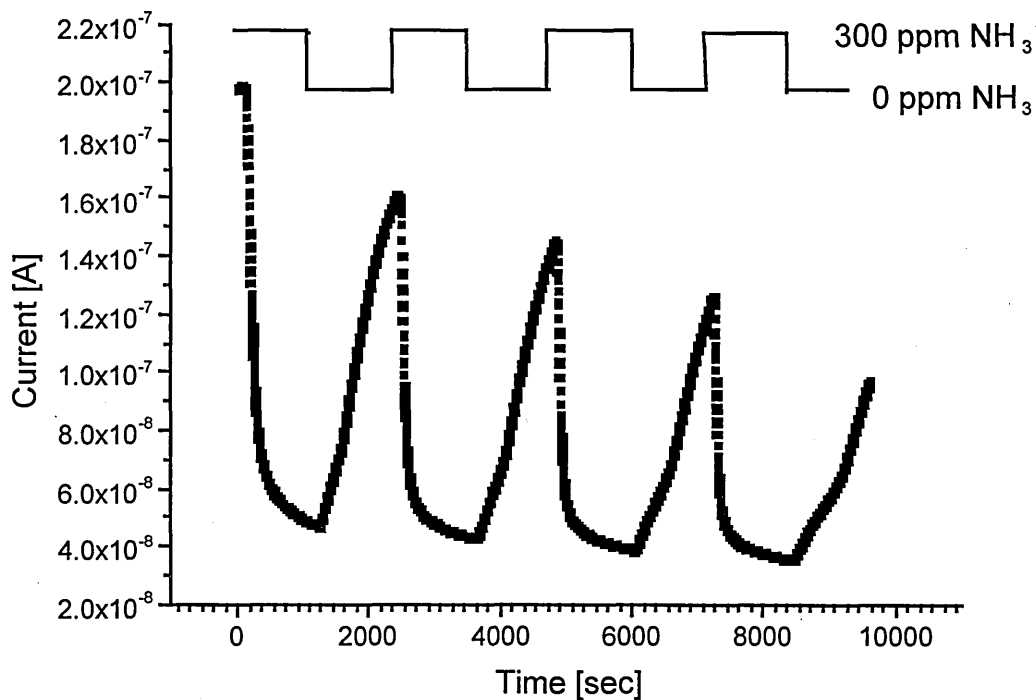


Fig. 7 NH₃ exposure of a POMA cast film

with the direction of the reaction being determined by the presence of ammonia in the air. When no further NH₃ is present in the air, the ammonia can decompose again into protons and ammonia, leading again to a protonation, and henceforth a conductivity increase. A similar mechanism was suggested to contribute to the conductivity

modulation on polyaniline in reference [8]. The difference in the behaviour of the composite and the pure POMA membrane suggests that there exist more than one type of reaction site or that a number of different reactions are possible. It is believed that the C[4]RA, either modifies the direction and equilibrium values of (4) and (5), or does act as a steric hindrance for the different protonating/deprotonating ions to the active sites. The faster sorption over desorption response remains identical to that of the composite film. No longer observable is the “memory effect”, with a reduced response on repeated exposures. Instead the 300 ppm of ammonia is only able to reduce the current carrying ability down to 40 nA. This can be seen as, an removal of all the available protons. With the recovery being slower, the initial current carrying ability is not restored after the flushing and therefore only the relative conductivity decreases upon multiple exposures is observed, not a reduction in the absolute value.

It can therefore be concluded that the memory effect observed and the conductivity increase upon ammonia exposure in the composite structure is a unique feature, stemming from the calixarene matrix in which the polymer is suspended.

5.3.2 Response to organic vapours

Since calixarenes have excellent complexing properties with organic vapours, the influence of these complexed vapours onto the conductivity of the membrane was investigated, using a variety of straight chain and aromatic hydrocarbons.

Experimental details

The same set-up as described above was used, with the vapours being generated by bubbling a nitrogen stream through a solvent filled gas washing bottle, allowing it to saturate with it and then passing it through the chamber. To increase the current height the membrane thickness was doubled to 32 layers, doped with HCl and purged in nitrogen until a semi-stable state was established.

5.3.2.1 Results and discussions

The vapours investigated were branched hydrocarbons, iso-propanol, methanol, acetone, chloroform and hexane, an aromatic hydrocarbon toluene and water.

Below are shown some typical modulations of the conductance upon solvent exposure, for acetone in Figure 8 and for iso-propanol in Figure 9.

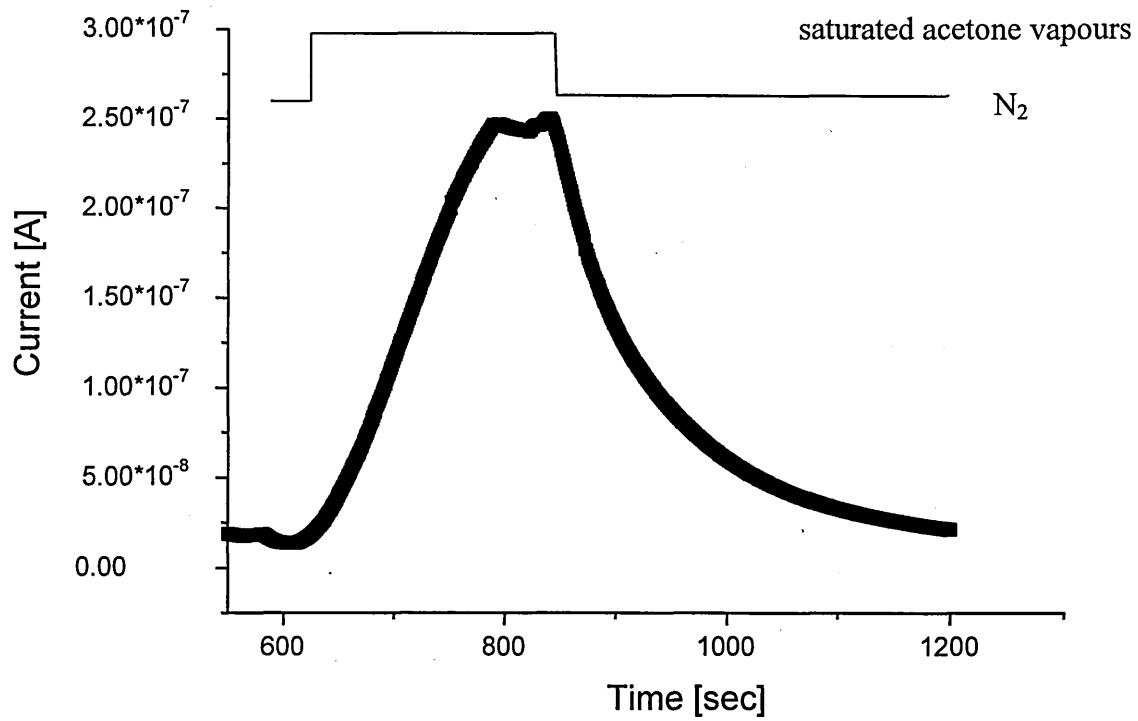


Fig. 8 Response of 32 ML of the composite membrane to saturated acetone vapours

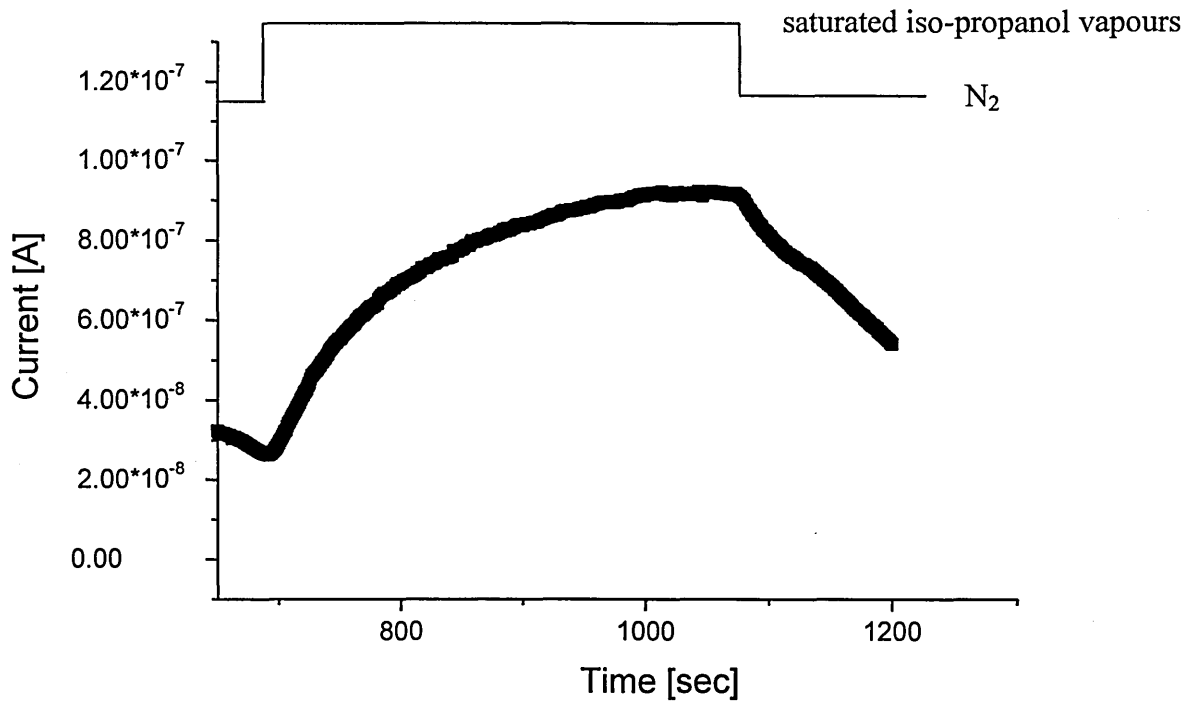


Fig. 9 Response to saturated vapours of iso-propanol

The increase in the current carrying abilities for the different vapours is summarised in Figure 10.

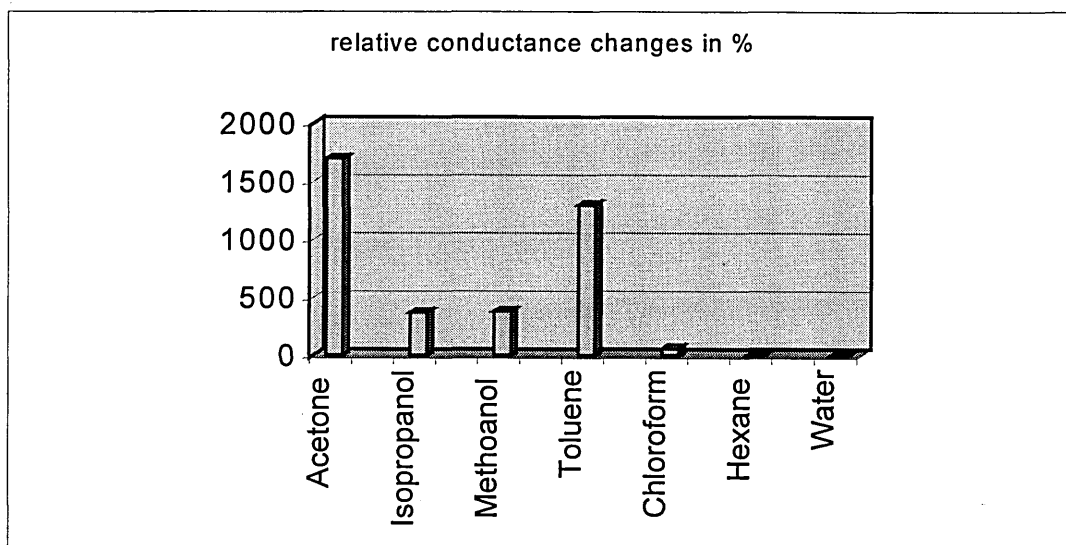


Fig. 10 Summary of conductivity increase upon vapour exposure

There are three possible processes contributing to the increase of the conductivity:

i) Protonation of the polymer according to (6).



This requires a dissociation of the hydrocarbon, the most likely source where it can occur is the site of the counter-ions remaining from the initial protonation.

ii) Absorption of the solvent into the matrix changing the structural arrangement, i.e. the torsion of the polymer strands.

iii) Swelling of the polymer or matrix, bringing strands into closer contact, facilitating a better charge transport between strands and by filling voids enabling a stronger charge hopping.

An analysis can be grouped into three segments, based on the different characters of the response, no or small conductivity increase despite absorption, conductivity increase upon sorption and no absorption taking place.

No absorption taking place

The strong hydrophobicity of the C[4]RA prevents any permeation of water vapour into the membrane, therefore there is no conductivity increase for water vapours. Water has in many cases been cited as a interfering analyte, for polymeric ^[9] or catalytic gas sensors ^[10], the embedding of the polymer in the C[4]RA matrix eliminates this problem.

Sorption but no or very little response

Hexane, C₆H₁₄, has a high vapour pressure (130mbar), it is itself hydrophobic, therefore the most likely complexing sites for it inside the membrane are the alkane chains along the upper brim of the C[4]RA. That hexane is sorbing into the membrane was independently found by means of an SPR analysis. The fact that there is no conductivity increase for hexane, can be explained by assuming that it is not dissociating according to (6), its low dipole moment providing no site where this could be initiated, and that it is not affecting the distances between polymer strands and alignments thereof. Though a swelling of the membrane is taking place, as shown by SPR, it must thus be assumed that the direction of the swelling is different, not leading to closer spaced polymer strands.

For chloroform (CHCl₃), despite having a more polar character the complexation inside the membrane must again not affect the inter strand distances between polymer chains and neither the polymer structure. That the saturated vapours (159mbar) are absorbed into the membrane is again shown by SPR. There is a hydrogen atom in chloroform, that could provide, on splitting up, a protonation of the POMA, since this is not observed it can be assumed that CHCl₃ complexes at sites where no dissociation by counter ions occurs.

Sorption occurring with a strong response

Toluene (C₆H₅CH₃) is the bulkiest of the absorbed molecules, possessing only a saturated vapour pressure of 22 mbar. SPR data revealed that the membrane thickness changes only slightly, implying that only few molecules penetrate into the film, this contrasts with one of the highest conductivity increases observed. Complexation is occurring in the C[4]RA baskets for pure calixarene membranes, according to the proposed model, based on UV spectroscopy. The film swelling is too small to account via structural changes for the high response. Dissociation of the toluene, most likely one hydrogen atom from the CH₃ group, may explain a protonation of the POMA. It

remains unclear what causes the dissociation when the toluene is captured inside the basket, where it will be separated from any counter-ions. It is therefore believed that the complexing behaviour of toluene differs from that in the matrix and the pure POMA, with complexation in the composite membrane occurring, at least partially outside the baskets within the vicinity of counter-ions.

Acetone (CH_3COCH_3) produces the highest conductivity increase, it has a high electric dipole, its saturated vapour pressure is with 181 mbar also the highest of the investigated analytes. This is reflected by a strong absorption, leading to a strong swelling, as shown by SPR. The most likely mechanism behind the exceptionally high conductivity increase is therefore a combination of protonation and structural changes. The high dipole moment, facilitates a strong shift of the equilibrium in (6) to the right, providing hydrogen ions, and the strong swelling brings polymer strands close together. Iso-propanol ($\text{CH}_3\text{CH}_2\text{CH}_2\text{OH}$) and methanol (CH_3OH) show a very similar response. With iso-propanol, being bulkier than methanol, and the saturated vapour pressures being much higher for methanol (96 mbar) than for iso-propanol (15 mbar), it can be expected that the amount of methanol penetrating is higher. This was in essence confirmed, by SPR, with a stronger membrane swelling for methanol. Since the response was found to be roughly similar this means that propanol is shifting the equilibrium in (6) more to the right than is methanol. This compensates for lesser structural changes. Structural changes have been shown to occur in substituted polyaniline derivatives ^[11] upon alcohol vapour exposures. So it was shown that the resistance of compressed pellets changes on exposure to alcohol vapours, with different directions (increase/decrease) for low and high molecular weight alcohols. Whereas methanol and propanol brought a conductivity increase, as observed here, higher alcohols like heptanol decreased the conductivity. It was suggested that the polar molecules can interact with the nitrogen atoms of the polyaniline leading to an expansion of the compacted polymer chains into a more linear form. Further confirmation for structural changes were reported by Svetlicic et al. ^[12] detailing changes in the crystallinity of polyaniline thin films upon exposure to ethanol vapours.

For all saturated solvent vapours it must be noticed that the sorption and desorption times are faster than those observed for the electroactive gases, NH_2 , HCl , and NH_3 . This can be partially accounted for, by the far higher concentrations.

5.4 Sensing with the composite membrane using a charge flow capacitor

Since the low currents that are measured with interdigitated electrodes (10 nA – 0.1 nA), provide a challenge in terms of shielding and require sensitive instrumentation (lowest range 10^{-12} A), an application of the membrane onto charge flow capacitors (CFC) was investigated as an alternative, in order to provide a more practicable method with an inherently better signal to noise ratio. The current carrying ability of the membrane for the IDE measurements can be increased several fold by multiplying the number of layers, but this can achieve only changes within the same order of magnitude. A CFC in contrast provides two major advantages;

i) the area of a capacitor can be easily adjusted till the generated signal is large enough, ii) there exist a variety of low cost capacitance readout chips like that developed in reference ^[13] to which the CFT can be interfaced providing a standard output signal. The readout chips have come of age, being a spin-off from cantilever applications, and provide excellent resolutions ($0.4 \cdot 10^{-18}$ F) and dynamic ranges up to (10^{-8} F). It can be expected that these will be in the future a frequently used interface for chemical sensors.

5.4.1 Experimental details

CFC were fabricated as described in Chapter 6 and Appendix 3, coated according to Chapter 4, with a conditioning performed as described for the DC IDE measurements. The measurements were performed with an HP 4284 LCR meter interfaced to a computer, controlled by a program written by the author. The small signal measuring amplitude was 20 mV, with no bias voltage applied. The CFC was mounted in a chamber, the vapours were generated by injecting the liquid analyte with a syringe and allowing it to evaporate.

5.4.2 Results and discussions

In order to evaluate the most suitable frequency at which to operate the capacitor, the capacitance was measured over the frequency range of 20 Hz – 1 MHz, first for the uncoated device then for the coated, and then for the latter with exposure to NH_3 and HCl vapours. The relation between the capacitance and the frequency is shown in Figure 11. It can be seen that the highest capacitance changes can be found at the lower

end of the spectrum, at 20 Hz. At the upper frequency range the values converge to that of the uncoated device. The application of the coating increases the capacitance, with both ammonia and hydrochloric acid increasing the capacitance further.

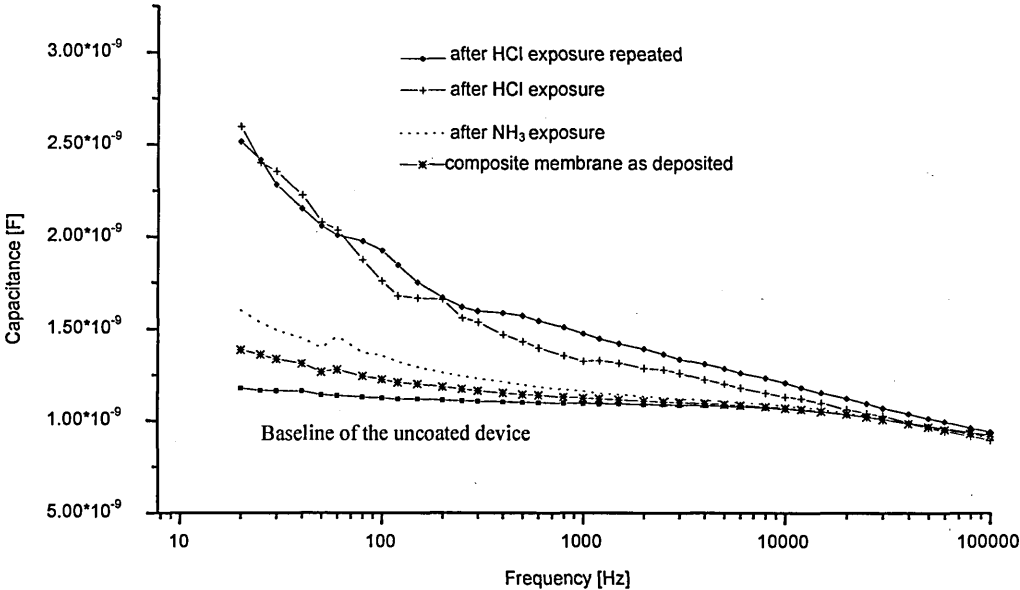


Fig. 11 C-f characteristic of the CFC with different coating states

The shown C-f behaviour of the device can be explained in terms of the equivalent circuit, Figure 12.

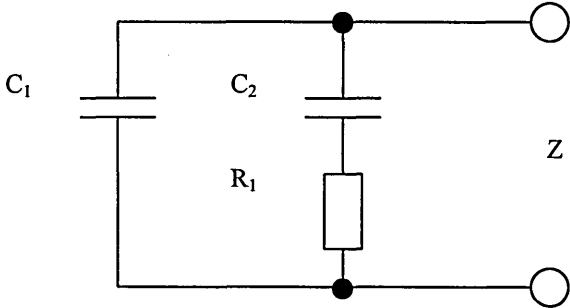


Fig. 12 Simplified equivalent circuit diagram of the coated CFC

C_1 is the capacitance of the metal frame covered area, C_2 is the collective capacitance of the material between the metal mesh, with R_1 being the AC impedance of the membrane over which C_2 is charged.

There exists a maximum capacitance $C_m = C_1 + C_2$ when the AC conductivity is infinity and the capacitance C_2 is fully charged. Since the AC conductivity is never infinity, the

only way C_2 gets close to the maximum, is at low frequencies where the time constant τ for charging C_2 increases ($\tau = 1/f$).

The impedance Z can be expressed as (7),

$$Z = \frac{Z_1 \cdot Z_2}{Z_1 + Z_2} \quad (7)$$

with

$$Z_1 = -\frac{j}{\omega \cdot C_1} \quad (8)$$

and

$$Z_2 = R_1 - \frac{j}{\omega \cdot C_2} \quad (9)$$

The impedance Z can then be separated into its resistance and reactance, which are expressed by R and C .

$$R = \frac{C_1 \cdot R_1 \cdot (C_1 + C_2) - C_1 \cdot C_2 \cdot R_1}{\omega^2 \cdot C_1^2 \cdot C_2^2 \cdot R_1^2 + (C_1 + C_2)^2} \quad (10)$$

$$C = \frac{(C_1 + C_2) - \omega^2 \cdot C_2^2 \cdot C_1 \cdot R_1^2}{\omega^3 \cdot C_1^2 \cdot C_2^2 \cdot R_1^2 + \omega \cdot (C_1 + C_2)^2} \quad (11)$$

The upper and lower limits for R and C can be found by viewing (10) and (11) for the frequency extremes, $\omega = 0$ and $\omega = \infty$.

For $\omega \rightarrow 0$

$$\lim of R = \frac{R_1 \cdot C_1^2}{(C_1 + C_2)^2} \quad \lim of C = \frac{1}{C_1 + C_2}$$

and for $\omega \rightarrow \infty$,

$$\lim of R = 0 \quad \lim of C = \frac{1}{C_1}$$

The limit consideration is confirmed by the highest C values for the 20 Hz frequency and the converging of all C values at 1 MHz to the value of the uncoated capacitor.

The above results confirm, that the composite membrane shows a conductivity increase for both HCl and NH₃ vapours. For further measurements the frequency was set to the lower limit of 20 Hz and the capacitance was measured over time. This is the operational mode that equates to a CFC interfaced to a capacitance readout chip.

A typical capacitance change as a response to acetone and toluene exposure is shown in Figure 13. Representing the electroactive gases the exposure of a new membrane to HCl and ammonia vapours is shown in Figure 14. All recorded signals possess a rather high noise, at 20 Hz (lower range of LCR meter) this can be attributed to some crosstalk from the 50 Hz noise found on the mains supply. A further source for noise, in particular for NH₃ and HCl is the method used for the vapour generation. The injection of the liquid can lead to an inhomogeneous increase in the concentration and dissociated ions can lead to localised conductance changes in the membrane.

The percentile capacitance changes are summarised in Figure 15, in terms of the capacitance basevalue before the injection of the analyte.

There is general qualitative agreement between the DC-IDE response and the capacitor measurements. The variation in the response height can be attributed to i) the different form of vapour generation, ii) the 20 Hz voltage is not equivalent to the DC voltage, iii) the capacitance of C₂, Figure 12, can itself change upon exposure to the analyte. The mechanisms or the induced changes in the membrane are identical to that as explained for the DC measurements. The time constants for the sorption and desorption are greatly changed, so is for example the absorption of HCl and ammonia nearly instantaneously, an effect that is due to the higher concentrations. The recovery for the HCl exposure is erratic, the temporary doping during the desorption process can only be understood from desorbed HCl, not being removed but sorbing again into the membrane.

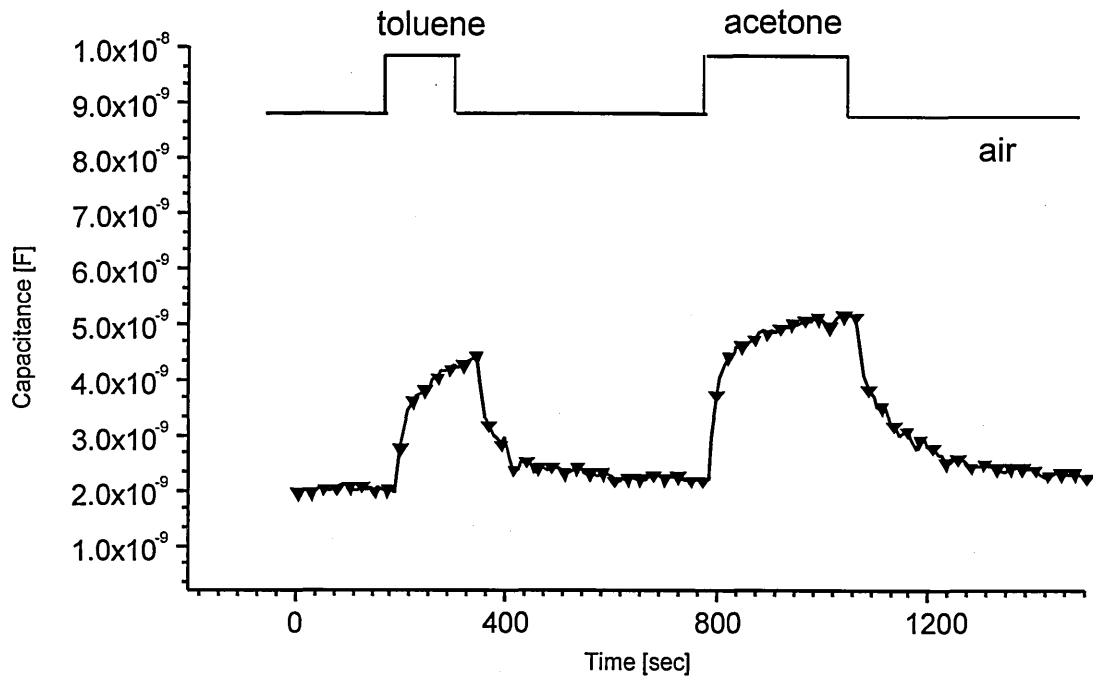


Fig. 13 CFC response to toluene and acetone

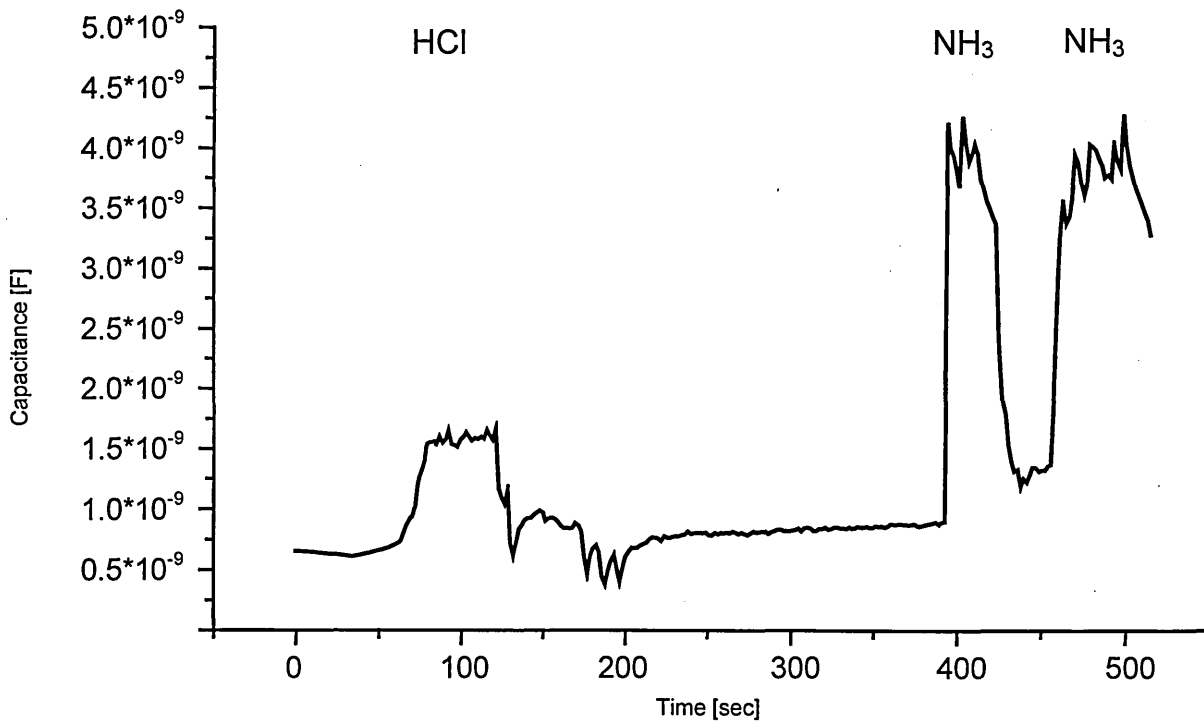


Fig. 14 CFC response to NH₃ and HCl

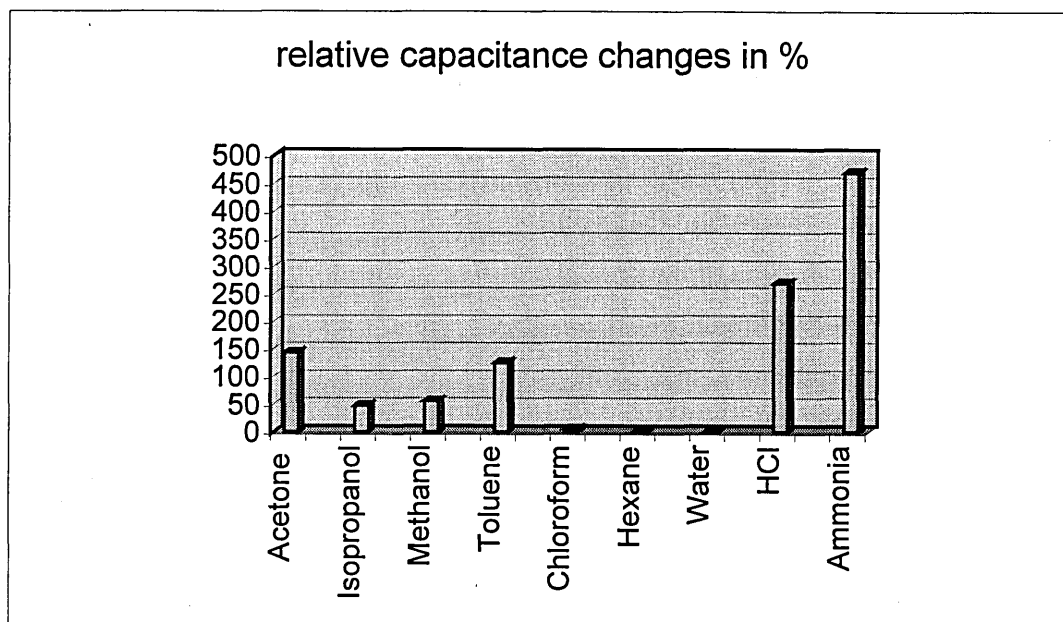


Fig. 15 Induced capacitance changes of the CFC upon exposure to saturated analyte vapours

5.5 Surface Plasmon Resonance studies upon exposure to electroactive gases and organic solvent vapours

SPR studies were carried out in order to investigate that the analyte sorption into the membrane does occur and to relate it to changes in its physical structure, i.e the refractive index and the thickness of the film.

5.5.1 Experimental details

The membrane, consisting of 4 ML of the composite structure, were deposited on gold coated slides, the deposition details are given in Chapter 4. The slides were then mounted via an index matching fluid onto the SPR prism and a gas chamber, with ca. 0.5 cm³ volume, was attached to it. The vapours were injected into the chamber with a 10 cm³ syringe, which was filled from the saturated headspace of a solvent bottle, and then sealed. For the recovery, the chamber was purged with four syringe volumes of air. The measurement scans were conducted immediately after the filling of the chambers. The results were then fitted to the Fresnel equations, to extract the changes in the

refractive index and the film thickness, as described in the Appendix 2. Since every gold coated slide, showed variation in the gold parameters and also variations in the refractive index and thickness of the membranes were found, results are expressed as produced changes to the “basevalues” of the individual film. The samples were only exposed to one solvent, so that no possible accumulative effects distort the results.

5.5.2 Results and discussion

The refractive index n , of a substance is the ratio of the velocity of light in vacuum to that of the velocity inside the substance. The interaction between the light and the substance that causes n to differ from unity is the polarisation of the atoms or molecules by the electric vector of the light. The electric field shifts the electrons from their equilibrium position to induce an electric dipole with the dipole-moment $\mu = \alpha \cdot E$. The relationship between the index of refraction and the molecular polarisation α is described by the Lorenz-Lorentz equation (12) ^[14],

$$\alpha = \frac{3}{4 \cdot \pi \cdot N} \cdot \frac{n^2 - 1}{n^2 + 2} \cdot \frac{M}{d} \quad (12)$$

with M being the molecular weight, d the density and N being Avogadro’s number.

When the film absorbs molecules with a different refractive index and undergoes simultaneously a change in thickness, the refractive index can increase or decrease depending on a combination of factors. To clarify this, let us assume a low refractive index material sorbing into the film, without causing any swelling, there can now be a stronger interaction between the electric vector of the light and the increased number of electrons, with every atom being polarisable, increasing therefore the refractive index. If the film is swelling at the same time the amount of interaction between the light and the polarisable molecules per given volume is increased only, if the swelling is smaller compared to the increased amount of polarisable atoms present. Interaction between the sorbent and adsorbent which influences the polarisability of both, is for simplicity’s sake neglected. For species with a higher refractive index than the film, every sorption is increasing n , apart from the case where the volume increases to such an extent that this offsets the increasing amount of polarisable matter. Since for swelling to occur the

sorbing species must diminish intermolecular forces between molecules making up the membrane, as by shielding van der Waals forces, this is a most unlikely behaviour.

Resorcinarenes and aniline based polymers possess a rather high refractive index, for organic materials, with the literature values of [x]arenes in the range of 1.46^[15]- 1.56^[16] and polyaniline in the range of 1.5^[17]. These high values are explained^[15] with the large number of delocalised electrons, whose displacement enables a high polarisability. It was found that the composite has a refractive index of around 1.68. This is exceptionally high for an organic material, it is believed that the protonated polymer with its mobile charge carriers and the counter-ions are responsible for this together with the delocalised electrons in the four aromatic structures in the C[4]RA. The literature value in^[16] is a value strongly depending on the protonation state and synthesis of the film. In addition to this, the additional methoxy group in the POMA, compared to that in the polyaniline, adds two terms to the electrical polarisability, $C = 1.03 \text{ \AA}^3$, and 3 times $H = 0.4 \text{ \AA}^3$, as taken from reference^[18].

5.5.2.1 Exposure to organic vapours

The chloroform induced changes in the reflectivity curve are shown in Figure 16, which shows only the baseline, the maximum sorption and recovery. The noticeable change occurs around the reflection minimum, Figure 17 magnifies this region, and shows further the absorption over time in intervals of 180 seconds. From these it can be seen that the absorption of the analyte into the membrane has a time constant of about 540 seconds. It can further be observed that the recovery is incomplete, which must be attributed to permanent structural changes. This is in accordance with the SEM investigation, in which a graininess change was observed in the surface morphology of the membrane upon long term exposure to chloroform, Chapter 4. The calculated changes in the refractive index ($\Delta n = 0.089/5.34\%$ change of the initial value) and the thickness ($\Delta d = +1.05\text{nm}/12.8\%$ of the initial value) are summarised in Table 3, which also provides further sorbent properties.

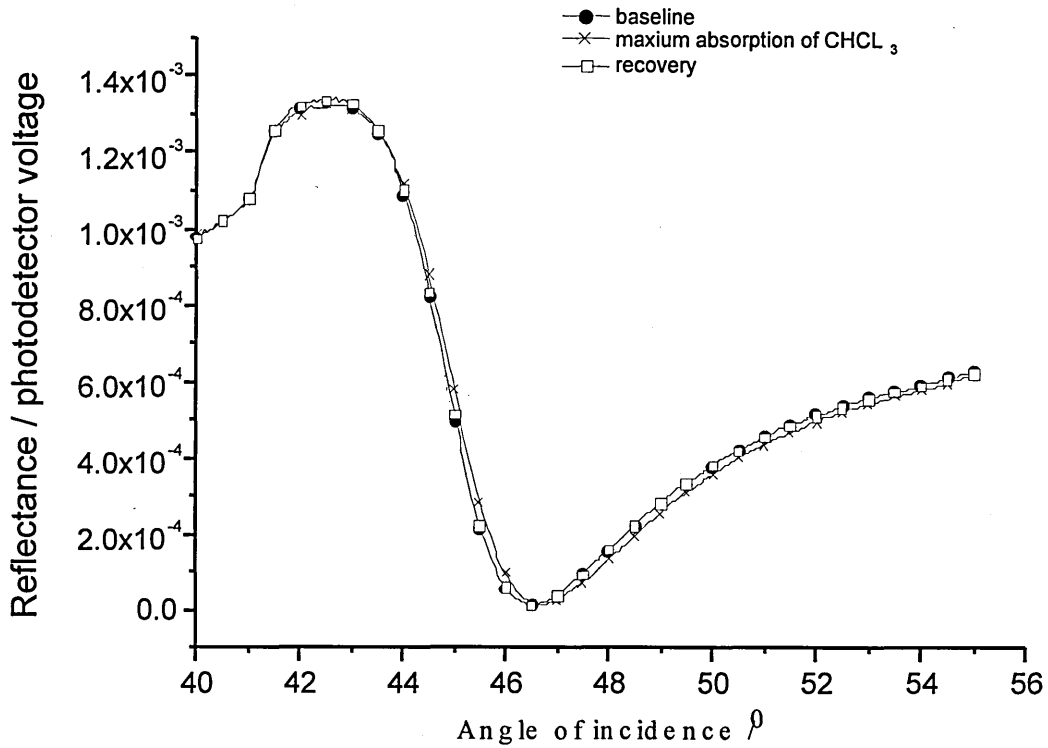


Fig. 16 SPR scan of 4 ML of the composite membrane

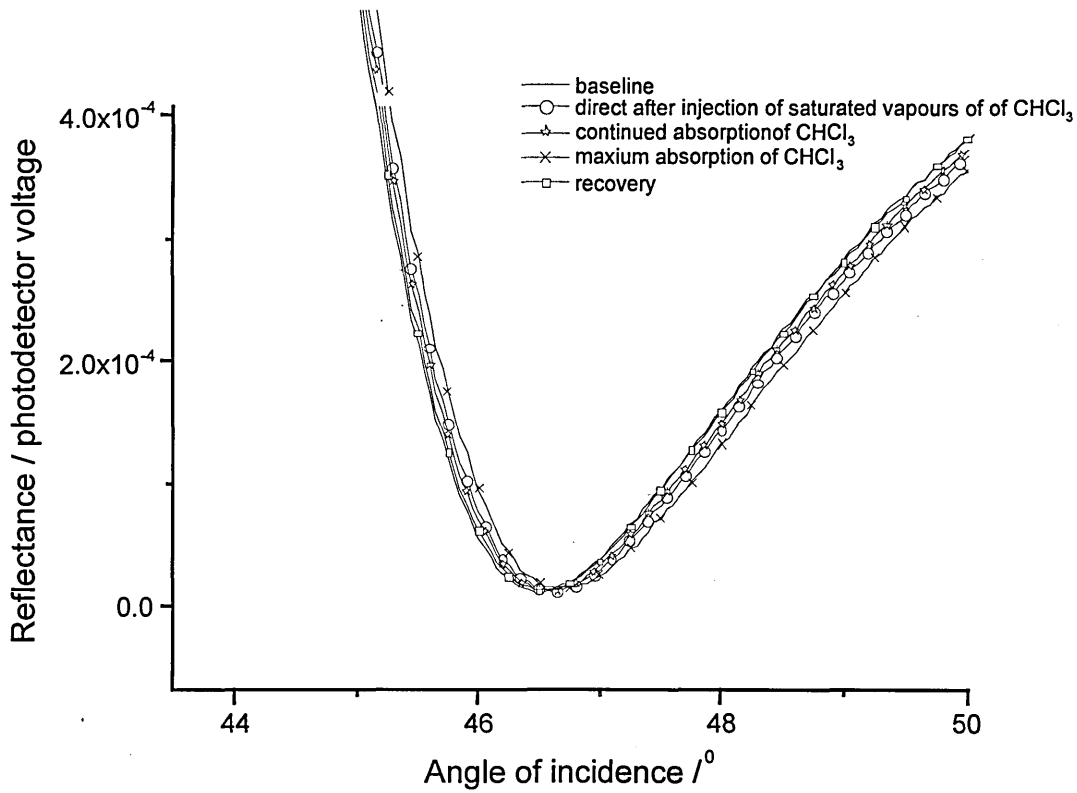


Fig. 17 SPR scan magnifying the reflectivity minimum and showing analyte diffusion

To relate the analyte sorption in the composite membrane to that in the pure C[4]RA membrane, 8 ML of C[4]RA were deposited, which according to the film characterisation, have a film thickness of 7.6 nm compared to that of the composite film of 8.4 nm. The SPR exposure series is shown in Figure 18.

The thickness changes are with $\Delta d = 0.75\text{nm}/9.16\%$ less pronounced compared to that of the composite membrane, but the diffusion process is faster, no further absorbance could be observed after 180 seconds. It is unclear what feature in the POMA is in particular responsible for this increased sensitivity. If the POMA increases the steric hindrance and with it the diffusion time it would not be expected that it can provide simultaneously additional complexing sites.

The conductivity was modulated most strongly by the solvents acetone and toluene. Below in the Figures 19 and 20 are presented the strongly differing modulations of the reflectivity curves for both solvents.

The absorption of acetone allows the film to swell quite considerably, $\Delta d = 0.43\text{nm}/5.31\%$ and the refractive index changes by $\Delta n = 0.037/2.23\%$. Recovery is taking place, though it is not complete, this contrasts with the electrical DC conductivity measurements, where total recovery was observed. It is believed that the purging with air was insufficient to allow a complete recovery. In contrast to the strong structural changes induced by acetone, toluene brings about much less pronounced changes. The change in the refractive index is $\Delta n = 0.014/0.85\%$ and the thickness changes are small as well with $\Delta d = 0.18\text{nm}/2.2\%$. Toluene with its aromatic structure ($\text{C}_6\text{H}_5\text{CH}_3$) is a much larger molecule compared to acetone (CH_3COCH_3). The proposed structure of the composite membrane with two POMA strands per C[4]RA layer, exerts a strong steric hinderance for the diffusion of the toluene into the membrane. Permeation is not completely hindered, as both conductance and SPR study show. The strong increase in the current carrying ability must therefore be attributed to protonation rather than structural changes

The general quality of the fit is exemplified in Figure 21 (for the chloroform exposure) with all the detailed parameters given below. The red line being the fit to the data points presented by the green line.

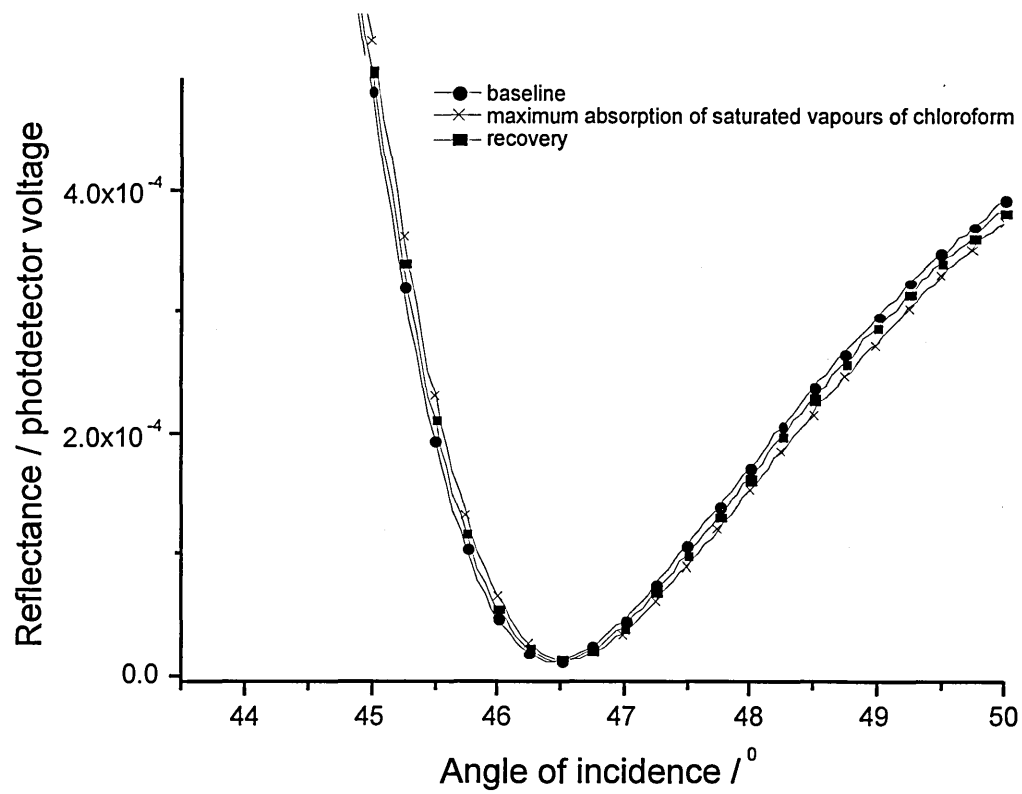


Fig 18 SPR exposure scans for 8ML of C[4]RA to saturated vapours of CHCl₃

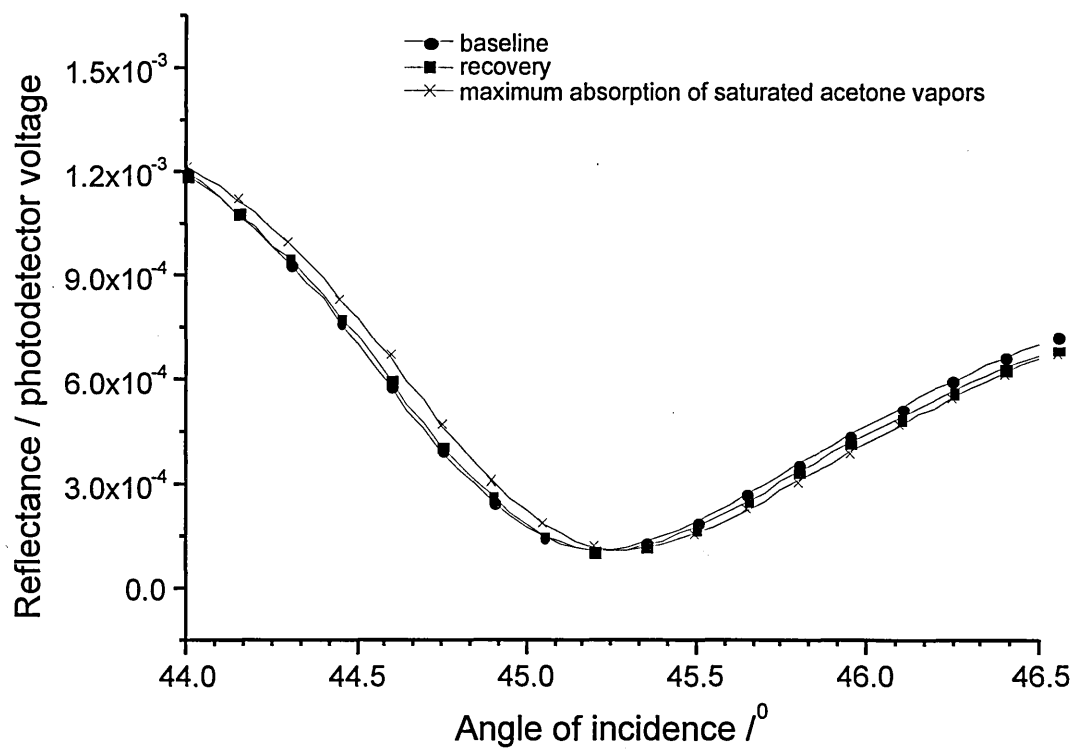


Fig 19 Changes on the SPR reflectivity curves upon acetone sorption

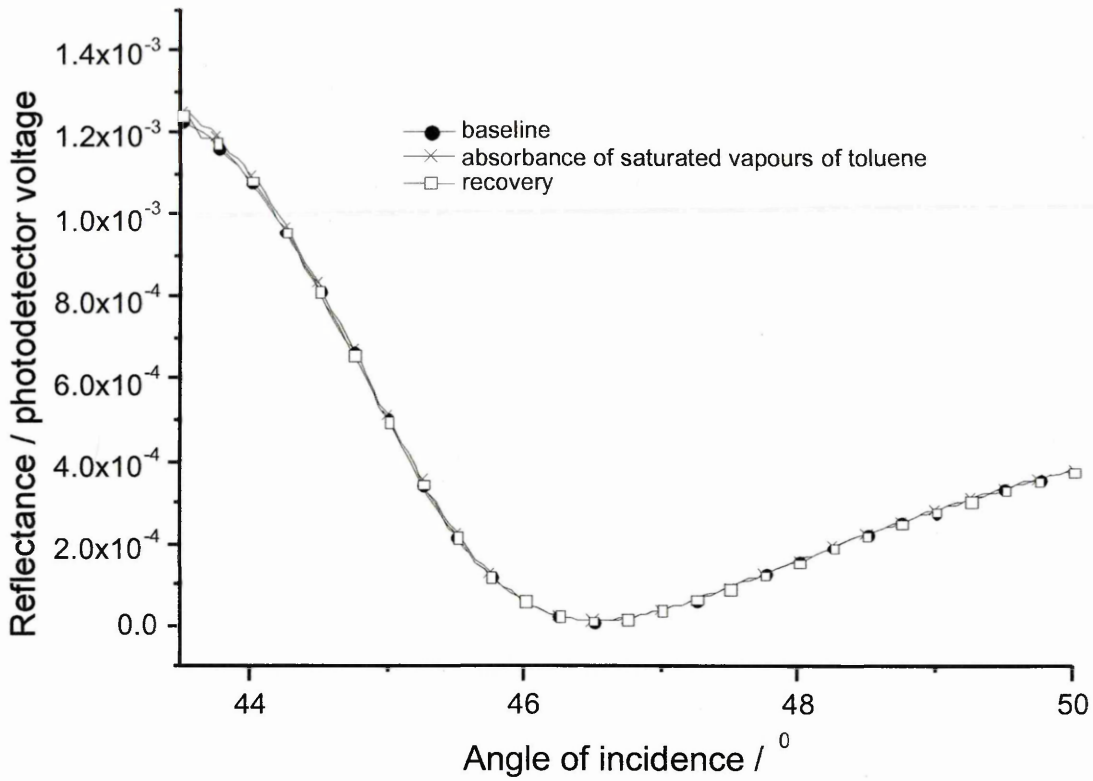


Fig. 20 Membrane exposure to toluene

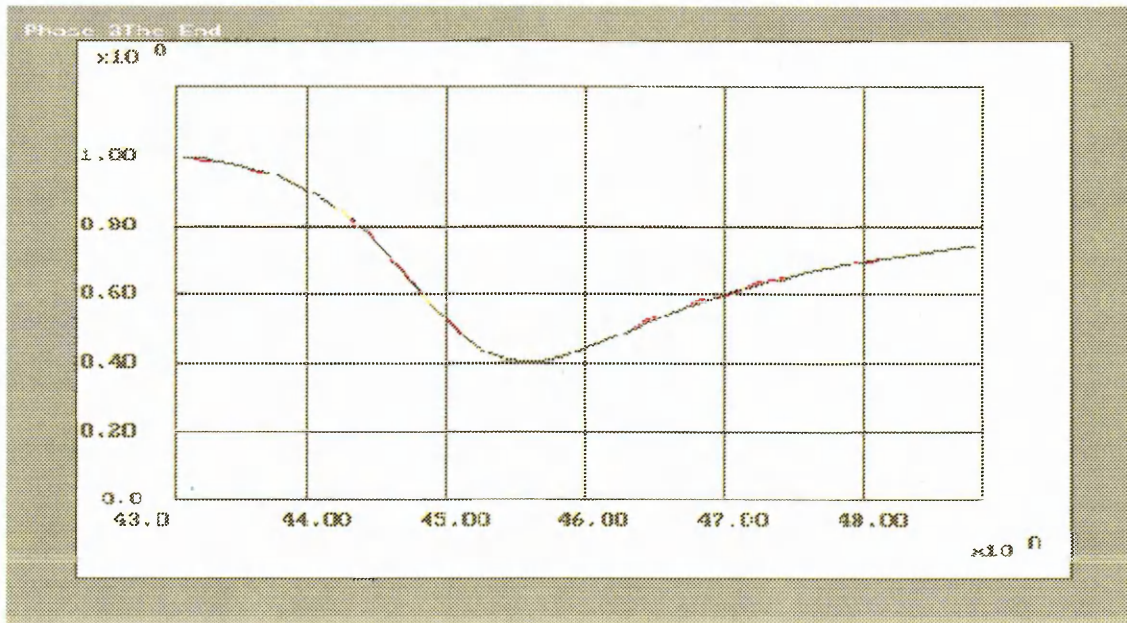


Fig 21. Screen capture of the fitting program, exemplifying the quality of the fit, for the parameters used as follows: gold layer; $n=0.332$, $K=3.457$, $d=56.48$ nm, membrane parameters; $n=1.720$, $K=0.138$, $d=9.298$ nm, error function: 3.1×10^{-2}

In Table 3 are summarised the refractive index and thickness changes of the individual membranes that are induced upon the solvent vapour sorption/desorption. Table 4 lists the MW together with the refractive index of the solvents and their saturated vapour pressure.

Solvent	Δd [nm]	Δd [% of initial value]	Δn	Δn [% of initial value]	averaged recovery of n and d in %
Acetone	0.43	5.31	0.037	2.23	>90
Chloroform/ C[4]RA only	0.75	9.16	0.061	4.22	>95
Chloroform	1.05	12.8	0.089	5.34	>95
Hexane	0.10	1.28	-0.084	-0.50	100
Iso-propanol	0.189	2.11	0.014	0.85	>90
Methanol	0.31	3.76	0.027	1.60	>90
Toluene	0.18	2.20	0.014	0.85	100

Table 3 Summary of the relative membrane change upon saturated vapour exposure

Solvent	Molecular Weight	Refractive Index	Saturated Vapour Pressure /mbar
Acetone	58.08	1.359	181
Chloroform	119.38	1.446	159
Hexane	86.18	1.375	130
Iso-propanol	60.10	1.3836	15
Methanol	32.04	1.329	96
Toluene	92.14	1.497	22

Table 4 Solvent properties

The substantial changes of up to 5.31% that are induced in the refractive index, for acetone and the high swelling of the film in the case of chloroform by over 12 % are easily detectable. Whereas Nabok et al. ^[3] observed an increases in the refractive index in calixarene films for saturated toluene vapours by $\Delta n = 0.035/7.6\%$ and thickness changes of $\Delta d = 1.2\text{nm}/14\%$, the observed changes for the composite membrane are nearly 1 order of magnitude smaller. It was proposed by the authors that micro-

condensation of toluene vapours occurs, this can not be confirmed, neither in pure C[4]RA, see UV spectroscopy, nor for the composite matrix. In contrast to this the results for hexane are more in agreement with the previously documented decrease in the refractive index and increase in thickness. Acetone, methanol, iso-propanol and chloroform, all show similar behaviour, the refractive index is increasing together with a swelling of the film. In reference ^[15] an increase of n with a concurrent decrease in thickness was observed for sputtered arene films upon chloroform exposure. This is not in line with the above, the different deposition method could be responsible for this discrepancy, implying a shrinking of the sputtered film contrasting a swelling for the LB films. There is no unequivocal connection between the physical properties of the solvent and the induced membrane changes but the interaction can be summarised in the following points.

- The nonpolar hexane, upon absorption decreases the refractive index of the membrane.
- For non aromatic polar solvents, the ratio between the increased interaction of light with the matter due to absorption of species and the dilution of matter via swelling is larger than 1, leading to an increase of the effective refractive index.
- The difference in the behaviour can be attributed to distinctly different complexation sites, i.e. hexane along the alkane chains in the C[4]RA, and the polar molecules around/ inside the baskets or around the imine group of the POMA.
- It is believed that the complexation with vapours also changes the polarisability of the molecules making up the membrane, and as was implied by the conductivity changes, creates charge carriers via protonation which also effects the refractive index.

5.5.2.2 Exposure to NH₃ vapours

Electroactive gases, like NH₃ possess smaller molecular dimensions than organic solvent vapours it can therefore be expected that upon sorption effects like swelling are much reduced. The DC measurements showed that NH₃ exposure changes the conductance in opposite direction, when the POMA is embedded into the C[4]RA matrix compared to the pure POMA. It was shown, in Chapter 4, that the structure of the composite membrane changes upon long term exposure to saturated NH₃ vapours.

This is confirmed in Figure 22 where the influence of the saturated vapours of NH_3 on the composite membrane is shown.

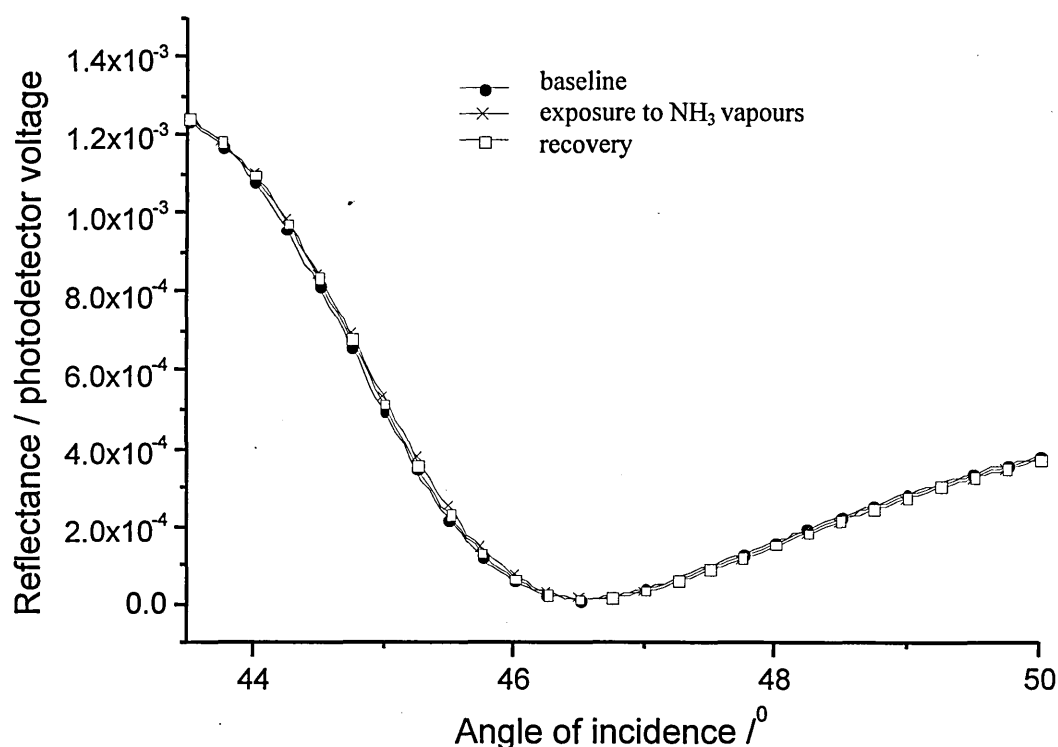


Fig. 22 NH_3 exposure of the composite membrane

It is believed that the interaction is twofold, that the ammonia changes the electric properties of the POMA and that interaction of the NH_3 and the C[4]RA takes place. In reference [19] it was shown via mass spectroscopic measurements, that there is a cation- π binding between calixarenes and ammonia. The magnitude of the response to concentrated vapours of NH_3 is small compared to that observable for monolayers of polyaniline [17], where the exposure to only 600 ppm of NO_2 brought changes in the position of the reflection minima of 0.3° , compared to that observed here of only 0.03° .

The direction of the shift is the same, again suggesting the protonating action of the reducing NH_3 for the composite membrane. Furthermore some solid phase transformations were demonstrated in reference [20], between tert-butyl-calixarenes and chlorine. This can be confirmed by the above SPR based study. The different membrane property changes are presented in Table 5.

Analyte	Δd [nm]	Δd [% of initial value]	Δn	Δn [% of initial value]	averaged recovery of n and d in %
NH ₃	0.30	3.66	0.294	1.75	>90

Table 5 Membrane changes induced by ammonia vapours

Summary

It was found that no micro-condensation of toluene in LB films of pure C[4]RA and the composite membrane takes place; findings support the theory that aromatic molecules complex inside the basket.

Conductivity measurements, determined the conductivity of the as deposited composite membrane to be of the order 0.1 mS/cm for 1:1 by weight ratio. This conductivity is very much history dependent, and continuous purging with nitrogen reduces the conductivity by about two orders of magnitude. The conductivity is modulated by oxidising and reducing gases as well as by solvent vapours. The composite membrane shows a markedly different behaviour to that of the pure POMA with respect to NH₃ exposure, the observed conductivity changes are reversed in direction. This is attributed to structural changes and alterations of the available protonating sites. The solvent induced conductivity changes are a result of protonation, after dissociation of the solvent, and structural changes the film. The response heights lie in the range of 1500 % for saturated acetone vapours and by 450 % for ammonia, this is lower when compared to observations for polyaniline.

The application of the composite membrane to a charge flow capacitor, showed a more practicable approach, with the capacitance in the nanofarad range being more conveniently measured, in comparison to the nanoamperes of the interdigitated electrodes.

Surface Plasmon Resonance studies revealed that different analytes permeate into the membrane and that the membrane swells, in some cases, for example acetone by up to 5.31 %. The possible applications lie rather in the higher than lower concentration ranges.

5.6 References

- [1] Chemical Analysis, F. Rouessac, A Rouessac, Wiley, 2000, ISBN: 0471981370, p. 197, 201
- [2] T.Komoto, I.Ando, Y.Nakamoto, S.I. Ishida, J. Chem. Soc., Chem. Commun., 135, 1988
- [3] A.V.Nabok, A.K. Hassan, A.K. Ray, J. Mater. Chem., 10, 189-194, 2000
- [4] S. Munoz, T. Nakamoto, T. Moriizumi, Sensors & Materials 11, 7, 427-435, 1999
- [5] M. K. Ram, S. Carrara, S. Paddeu, E. Maccioni, C. Nicoline, Langmuir 13, 2760-2765, 1997
- [6] N.E. Agbor, M.C. Petty, A.P. Monkman, Sens. & Act. B 28, 173-179, 1995
- [7] A.P. Monkman, P. Adams, Solid State Comm., 78, 29, 1991
- [8] A.L Kukla, Yu. M. Shirshov, S.A. Piletsky, Sens. & Actua. B37, 135-140, 1996
- [9] H.H.S. Javadi, M. Andelopulos, A.G. MacDiarmid, A.J. Epstein, Synth. Met. 26, 1-8, 1988
- [10] M. Morimitsu, Y. Ozaki, S. Suzuki, M.Matsunaga, Sens. & Actua. B, 67, 1-2, 184-188, 2000
- [11] A. A.Athawale, M.V. Kulkarni, Sens. & Actua. B 67, 173-177, 2000
- [12] V. Svetlicic, A.J. Schmidt, L.L. Miller, Chem. Mater. 10, 3305-3307, 1998
- [13] MICROSENSORS SAMPLING UNIVERSAL CAPACITIVE READOUT CIRCUIT, Readout and Control Chip Being Evaluated by Sensor Manufacturers, www.irvine-sensors.com/ucr_sampling.html
- [14] General Chemistry, L. Pauling, Dover Publications, 1988, ISBN: 0-486-65622-5, p. 396
- [15] A.V. Nabok, A.K. Hassan, A.K. Ray, O. Omar, V.I. Kalchenko, Sens. & Actua. B 45, 115-121, 1997
- [16] Y. M. Shirshov S.A. Zynio, E.P. Matas, G.V. Beketov, A.V. Prkhorovich, E.F.Venger, Supramolecular Science 4, 491-494, 1997
- [17] N.E.Agbor, J.P.Cresswell, M.C.Petty, A.P. Monkman, Sens.& Actua. B 41, 137-141, 1997
- [18] General Chemistry, L.Pauling, Dover Publications, 1988, ISBN: 0486656225, p. 397
- [19] F. Inokuchi, K. Araki, S. Shinkai, Chem. Letter., 1383, 1994
- [20] R. Lamartine, R. Perrine M. Perrine S. Lecocq, C. Duchamp, Mol. Cryst. Liq. Cryst., 248, 61, 1994

6 Silicon Device Processing

This chapter describes the techniques used for the fabrication of the CFT and the CFC and gives details of the device dimensions. In the Appendix 3, the specific process parameters are presented in a format of a recipe, allowing the straightforward reproduction of the process. This splitting avoids the distraction from the principles presented here by too many fabrication details, which are specific to the used equipment and material. More detailed information regarding silicon device processing can be found in the literature ^[1-6].

6.1 The planar process

Since the birth of the solid state industry in 1947, with the invention of the contact transistor by Bardeen, Schokley and Brattain ^[7], the production processes have been constantly undergoing changes. The introduction of the integrated circuit by Kilby ^[8] in 1959 has led to the development of the planar process in 1960 by Noyce ^[9]. The planar process allows the build up of individual layers, plane by plane and makes interconnections between individual elements in one plane possible. Modifications in the planar process, allowing the production of elements above each other with lateral and vertical connections, made the growing complexity of the modern circuit layouts possible. The desire for shrinking feature sizes has always brought with it the introduction of new techniques that allowed more control over the process together with lower tolerance margins. The processes used in this work, are still a cornerstone in the semiconductor fabrication, but in some cases they have been superseded by more complex and precise techniques, as for example the substitution of diffusion doping by ion implantation and the thermal oxide growth by chemical vapour deposition.

6.2 Production process of the CFT

The following production process is schematically illustrated in a separate series of sketches, Figure 1. In it, a profile of the wafer is shown focusing on the core steps and omitting repeating steps. The numbering throughout the text refers to the individual

pictures. A segment of the mask design is also presented, showing an overlay of the masks used for one transistor.

6.2.1 Mask generation

The fabrication process started with the design of the photolithographic masks. The required five masks were designed with the aid of the CAD package AutoCAD 10. The graphic files were then converted into a format that can be used on an Electromask pattern generator (PG). The conversion consisted of a fracturing of the image into an array of rectangles, with a minimum feature size of 10 by 10 μm . The masks were then produced by loading photosensitive, emulsion coated glass planes into the PG and exposing the defined rectangles to the UV radiation. The rectangles and squares are defined by a pair of knife-edges set at right angles to each other. The image can then be projected onto the plate and by flushing a number of these, a complex image can be build up. The masks were then developed with the aid of a developer, in a similar fashion to that of a normal black and white photographic film and then washed and fixed. Afterwards the masks were thoroughly cleaned and inspected for errors and opacity.

Two types of mask were produced in this way, clear-field and dark-field masks, for use in conjunction with positive and negative resist, respectively. Emulsion masks were used for the production process since they are, by a factor of ten, more economical than the more robust chromium masks. Their greatest drawback is that their mechanical durability is not as high as that of chromium ones and therefore no rigorous scouring cleaning is possible. This limits their reuseage to about 10 times before accumulated debris from the contact print process leads to irreparable scratches and smudged edges.

6.2.2 Wafers

The silicon wafers for the transistor productions were from the lightly doped n-type, having a resistivity of 1-10 Ωcm . Wafers with a precisely defined resistivity would have improved upon the reproducibility of the device characteristic, but would have raised the cost substantially.

The wafers were used as received from the manufacture. Tests have shown that further cleaning is not necessary, providing the wafers are opened within a clean environment i.e. class 100 cleanroom. The native oxide that is present on all silicon surfaces was accepted since it does not interfere with the following steps.

6.2.3 Patterning for the p wells

A dopant impervious layer of silicon dioxide was grown by thermal oxidation on top of this virgin wafer (1). This was performed, using the technique of wet oxidation, which has the advantage over dry oxidation to allow a higher growth rate, though this results in a less homogenous and slightly porous oxide. Nitrogen is bubbled through pure water and the resultant saturated vapour is passed down the process tube. The high temperature lets the water dissociate into hydrogen and oxygen, the oxygen combines with the silicon to form the silicon dioxide, growing from the silicon-silicon dioxide interface. The growth time for a certain oxide thickness is taken from the calibration charts according to the Deal & Grove model [10]. The resulting thickness of the oxide is checked with the aid of colour charts, which correlates the corresponding thicknesses to the different colour shades of SiO₂.

For the creation of the strongly doped p⁺ wells, windows must be defined in the SiO₂ to allow diffusion of the dopant, boron, into the silicon substrate. The selective removal of the SiO₂ is performed by first patterning it photolithographically and then selectively etching it. A light sensitive photoresist is spun onto the wafer (2), which is then softbacked, to drive off any remaining solvent and to start the adhesion process between the resist and the substrate. The wafer is then exposed through a mask (mask 1) to UV light (3). During this step a negative resist is used and the parts of the resist that are exposed to UV light are transformed from a monomer into a polymer by cross-linking the monomer units (4). This treatment renders these areas insoluble in the developer.

The UV-light exposure is performed in a mask aligner, which brings the mask in direct contact with the wafer and irradiates the mask. A mask aligner is needed to position the mask correctly over the wafer, to aid the positioning alignment marks are used on the masks. The three dimensional positioning of the wafer with respect to the mask is performed under a low magnification stereo microscope with micrometer type screws acting on a positioning table.

The photoresist then requires developing, for this a tank method was employed as opposed to a spraying technique. It is a three-stage process involving different immersions.

The photoresist that is left undeveloped, and henceforth remains on the wafer (5), is hardbacked to remove any remaining solvent and to finalise the adhesion process. The uncovered silicon dioxide is etched away in a bath of hydrochloric acid (6) stabilised with an ammonium buffer. To avoid any underetching of the pattern, the etching has to be precisely timed. For this purpose a test wafer onto which the same oxide was grown, is etched together with the device wafer as a reference. The easily observable transition in the wetting properties, from the hydrophilic SiO_2 to the hydrophobic Si indicates the completeness of the oxide etch on the both wafers. After this the wafer was washed again in a bath of deionised water, until the water in the recirculating system indicated a value of $25\mu\text{S}/\text{cm}$, which is the in-house pass for cleaning wafers. This procedure ensures that all residual HF acid has been removed. The hardbacked photoresist presents an extremely robust coating that is inert to most solvents and acids, which needs to be removed before the fabrication can continue. The resist can be removed either with a hazardous chemical process or with a plasma in a plasma asher (PA). In the PA a radiofrequency coil, produces very reactive oxygen plasma, that is elementary oxygen, this oxidises the resist into gaseous components, which are then exhausted.

During the removal of the photoresist, the reactive oxygen combines with the silicon and a thin layer of SiO_2 growth again (7). This required removal, it is removed in a short contact etch in a weak HF solution (8).

6.2.4 Boron doping

So far only the windows through which the dopants are introduced are fabricated. The following doping procedure must invert the n-type silicon, that has a surplus of electrons in its lattice due to the inclusion of phosphorus atoms, to a p-type silicon, with a deficit of electrons in its lattice. This is achieved by introducing an excess of boron atoms; first to compensate for the phosphorus atoms electron surplus and then to render the whole exposed crystal structure electron deficient.

There are two types of process that allow the introduction of foreign atoms into a crystal, ion implantation and diffusion. During ion implantation, atoms that form the

dopant are ionised and accelerated in a strong electric field. The stream of highly energetic particles is then directed onto the substrate and the ions are driven into it by virtue of their kinetic energy. This method provides excellent control over the implantation but is unfortunately very costly.

For the device fabrication in this work diffusion implantation was used as a means of introducing the dopant atoms. The wafers together with boron trioxide wafers are loaded into a diffusion oven and heated up in a stream of nitrogen. The high temperature of about 1000 degrees leads to a migration of the boron trioxide to the surface of the wafer and a subsequent sublimation into the nitrogen stream. The nitrogen stream then carries them onto the silicon wafers on which surface they are deposited, forming a glassy oxide layer on top of it. From there the boron migrates into the top layer of the silicon (9). The diffusion process is described by the gas diffusion equations and these are used to calculate the junction depth and concentration [11].

After completion of the diffusion process the wafers are slowly removed from the oven to avoid warping due to temperature stresses.

Now a combination of SiO₂ and borontrioxide glaze is covering the whole wafer, they are removed with a HF etch (10).

After the dopant atoms are introduced in the crystal lattice an annealing process is required to ensure an equal distribution in the lattice and the “healing out” of some introduced defects. This process brings with it a lateral and perpendicular spreading out of the diffusion zone. It is combined with the growth of the thick field oxide (11). The field oxide is about 1 μm thick, which is about ten times thicker than the gate oxide. It provides an insulating layer and due to its thickness prohibits the formation of an inversion layer underneath the metal contacts. The oxide is grown with a wet oxidation process since marginal inhomogeneities in it can be tolerated and it is much quicker process as compared to dry oxidation.

6.2.5 Patterning of the gate oxide region

The next process defines the gate region on the wafer, for this a window is etched in the field oxide and subsequently the gate oxide is grown inside this window. Patterning of the field oxide is done via the mask 2, including the same steps for

spinning on the photoresist, softbake, exposure, hardbake (12), etch (13) and cleaning as described previously.

6.2.6 Growth of the gate oxide

The quality of the gate oxide is important, with respect to the homogeneity of its dielectric properties and complete coverage, for the performance of the transistor. Since the electric field that exists between the substrate and the electrode on top of the gate oxide needs to penetrate the oxide, bringing about the formation of the conducting channel between source and drain, a thin oxide layer is required in the order of 100 nm. Any contamination seriously alters the dielectric properties of the oxide, forming the starting point for defects in the oxide layer i.e. pinholes. It was found that pinholes in the gate oxide formed a major source of defect. The dimensions of the gate oxide is $0.4 \mu\text{m}^2$, since the likelihood of encountering a pinhole grows with the area it was found that many devices were short-circuited by metal bridges between the gate metalisation and the substrate.

To fulfil the high quality demands of the gate oxide, it was grown in a dry oxidation process (14). The wafers were loaded into the oxidation furnace and the oxide was grown in a stream of nitrogen and oxygen, at a rate of about 60 nm per hour, with a simultaneous growth on top of the field oxide.

Being of such vital importance for the performance of the transistor the thickness was verified with ellipsometer measurements to be 120 nm.

6.2.7 Patterning of the source drain contact

In a further step the p-type wells are made accessible by etching contact windows through the field oxide above them (16). This requires patterning with the mask 3 (15). The steps for the patterning process are the same as for the patterning with masks 1 and 2.

6.2.8 Metalisation

After cleaning the wafers, they are ready for the metalisation. Two types of contact are needed, the back contact on n-type silicon, and the contacts for the source, drain

and gate (17). Different metals were used for the contacts, since the back contact is not exposed to any analyte, it is only bonded to the holder, for its chemical stability is not an issue. The requirement that both contacts need to fulfil is that they are not forming a Schottky contact with the substrate. Aluminium was chosen for the back contact and because of its chemical inertness, gold for the source, drain and gate contacts. Since gold does not adhere well to silicon oxide, a seed-layer of chromium, of roughly 3 nm, is needed to provide an adhesive support for the gold.

The metal is deposited in a thermal evaporator, at a high vacuum of about 10^{-6} bar. The metal is loaded in a boat or coil and an electric current is passed through the filament, to heat it up to the evaporation temperature of the metal. In the case of the chromium-gold metalisation rotatable filaments must be used since maintenance of the vacuum between the evaporation steps is crucial, to avoid the formation of an oxide on the chromium, interfering with the adhesion of the gold. The evaporation rate and the final thickness of the metal layer are monitored with a quartz crystal microbalance positioned next to the wafers.

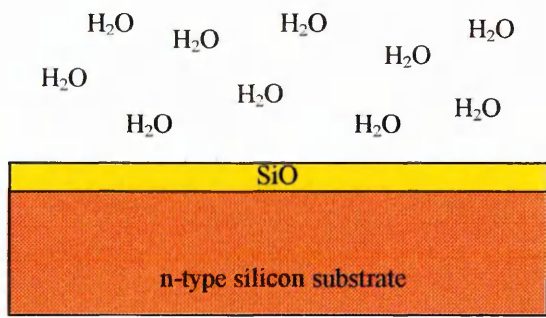
6.2.9 Patterning of the metalisation

The gold top layer needed to be patterned to form the metal contacts for the three terminals of the transistor, this is done with the mask 4 (18). A positive photoresist is used for this patterning process. The resist is again spun on, softbacked, exposed to UV light through mask 4 and developed in a two stage process. First the gold is removed with an in-house prepared gold etch and then the chromium is removed with a commercial chromium etch (19). The etch completeness is verified under an optical microscope. This etch process was employed instead of the otherwise frequently described “lift-off process”, due to its simplicity. Tests on wafers with a gate oxide on top have shown, that the two etchants do not attack the silicon oxide, even over an immersion period of an hour. The remainder of the photoresist is then removed by washing with a solvent. For the backcontact, the native oxide, that grows on all silicon surfaces, was removed by wiping it repeatedly with a cotton bud soaked in HF, until the surface transition from hydrophilic to hydrophobic is complete. The wafer is then, without washing immediately loaded into the vacuum evaporator and the aluminium deposited.

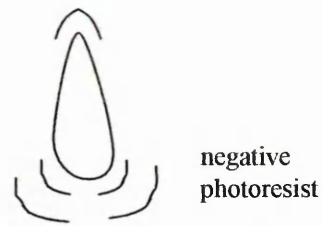
The metalisation of the wafer is completed with a further heat treatment in an oven at a moderate temperature under a nitrogen atmosphere. This treatment allows the metal to diffuse into the substrate improving the ohmic contact and the adhesion.

6.2.10 Patterning of the passivation

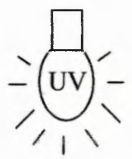
To avoid the need for a patterning of the sensing membrane, a passivation layer, eliminating the possibility of short-circuiting the three contacts was introduced. The contact to the drain and source were then made by “piercing” through the passivation. Negative resist was spun on exposed through mask 5 and developed (20). Hardbaking of the resist rendered it solvent resistant and ensures good adhesion, completing the production process.



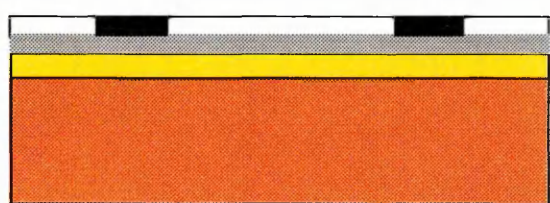
1



2

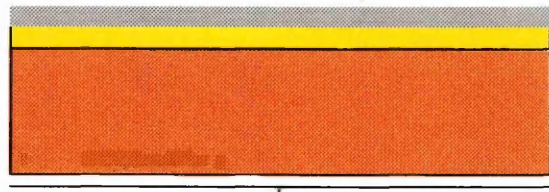


dark field mask 1



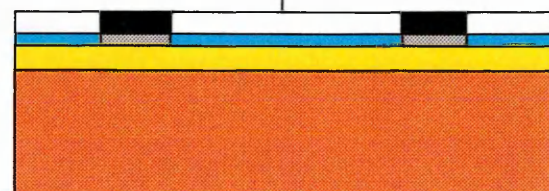
3

resist developed



4

photochemical reaction



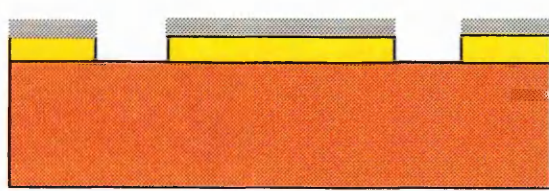
5

SiO₂ etch



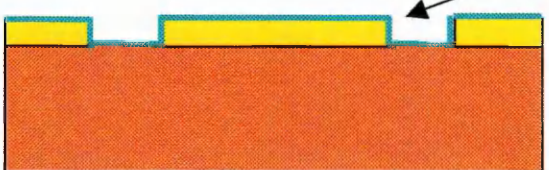
6

resist removed in barrel asher



7

contact etched



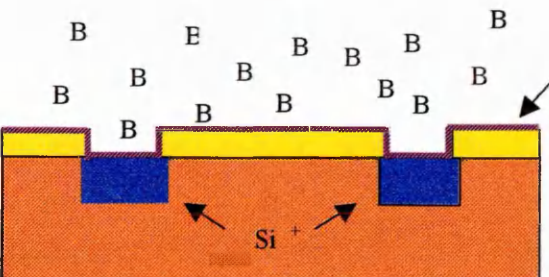
8

thin oxide



9

p type diffusion doping



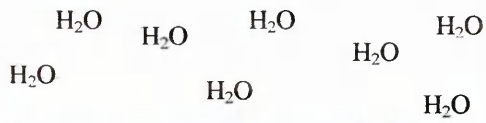
10

boron glaze

oxide and glaze removed



annealing redistribution of the dopant



11

after etch and removal of the resist an opening in the field oxide for the gate oxide is prepared



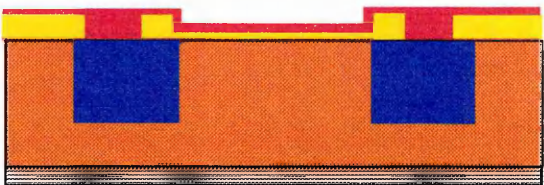
13

patterning and developing with mask 3



15 "front and back" metalisation

Cr + Au metalisation



17

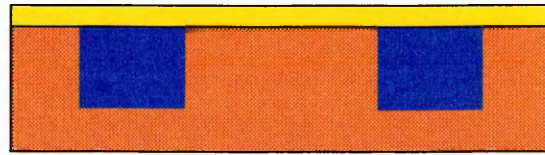
aluminium back contact

two stage metal etch



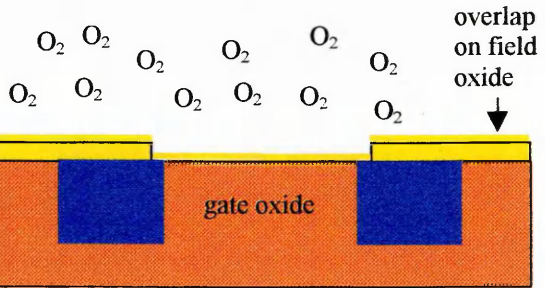
19

patterning and developing with mask 2



12

dry growth of gate oxide



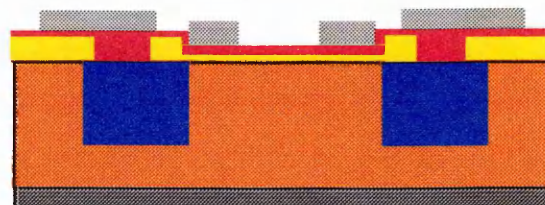
14

source and drain contact holes etched



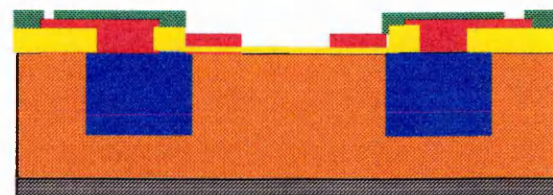
16

patterning and developing with mask 4



18

passivation of hardbacked photoresist applied with mask 5



20

Fig. 1 CFT production process illustration

6.3 Mask layout for a CFT

Below are presented the masks as used, with a magnified set of masks for the 50 μm gate gap device. The masks can be identified according to the colour coding, mask 1= yellow, mask 2 = pink, mask 3= green, mask4 =blue, mask 5 is a negative the blue mask over the gate (not shown).

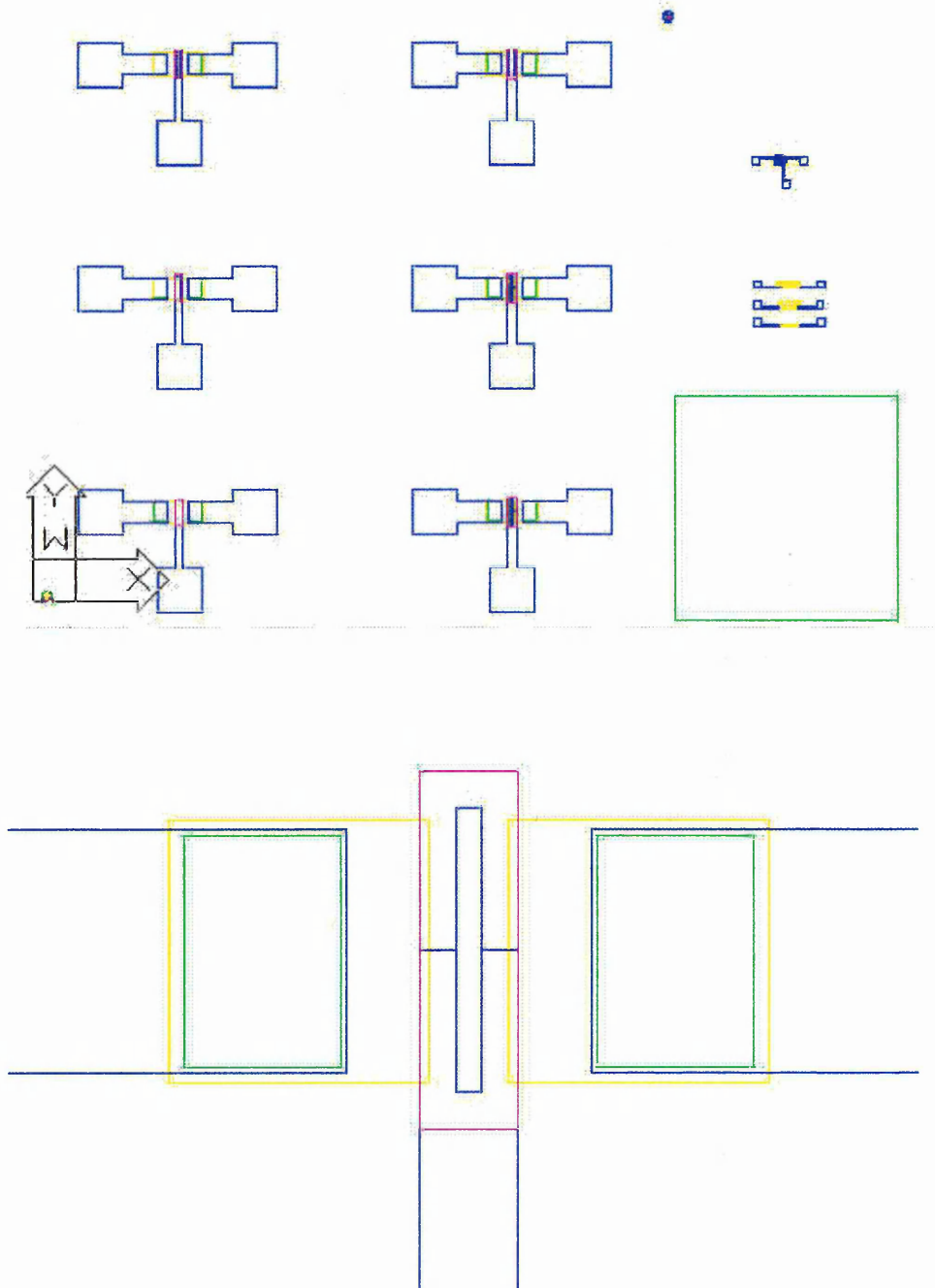


Fig. 2 Top view of the photolithography masks with a magnified individual set

The exact physical device specification is given in Table 1.

Substrate Resistivity (n-type)	1-10 Ωcm
Channel Length	200 μm
Channel Width	180 μm
P-type Doping (Surface)	$4 \cdot 10^{20}$ Atoms/ cm^{-3}
Field Oxide Thickness	1000nm
Gate Oxide Thickness	120 nm
Metal frame Thickness	150 nm
Width Of Gate Hole	0,50 μm

Table 1 Device specifications

6.4 Standard device characterisation

With the aid of a semiconductor analyser a standard characterisation of the devices was carried out, to select the working devices from the faulty ones. This step was required since the large area of the gate area, with 0.04mm^2 and the large size of the contact pads with ca. 4mm^2 , led to a high proportion of the devices suffering from short circuits, through pinholes in the silicon dioxide.

Barker showed that a CFT with a 25 μm air gap in the gate electrode switches completely on after only 6 minutes ^[12], even in an atmosphere of water free nitrogen. This implies that the gate charge creeps over the silicon; no such effects could be observed for the 50 μm devices, indicating that no continuous charge layer is formed when a threshold length for the gate opening is exceeded. This threshold must therefore lie between 25 and 50 μm . In order to create a temporary, electrically conducting layer in the gate opening, the wafer surface was saturated with water vapour, by blowing on it. The water vapour film is easily recognised and remains in place for ca. 12 seconds. Any lasting contamination from salts present in the breath are avoided by rinsing the wafer in milliq water and drying in a stream of nitrogen. The response of these “gated “ transistors is similar to a reference device with a metal gate. A typical behaviour of a device tested in such a way is shown in the Figures 3 and 4.

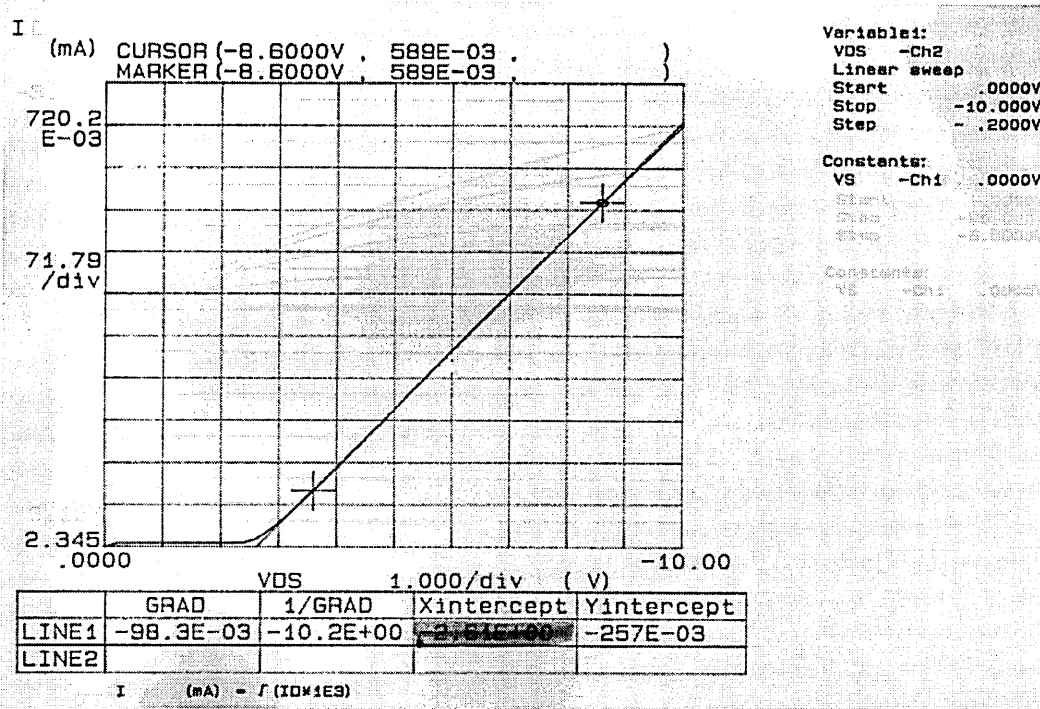


Fig.3 Determination of the gate voltage at a fixed Vds of 10 V, recording Ids over Vg

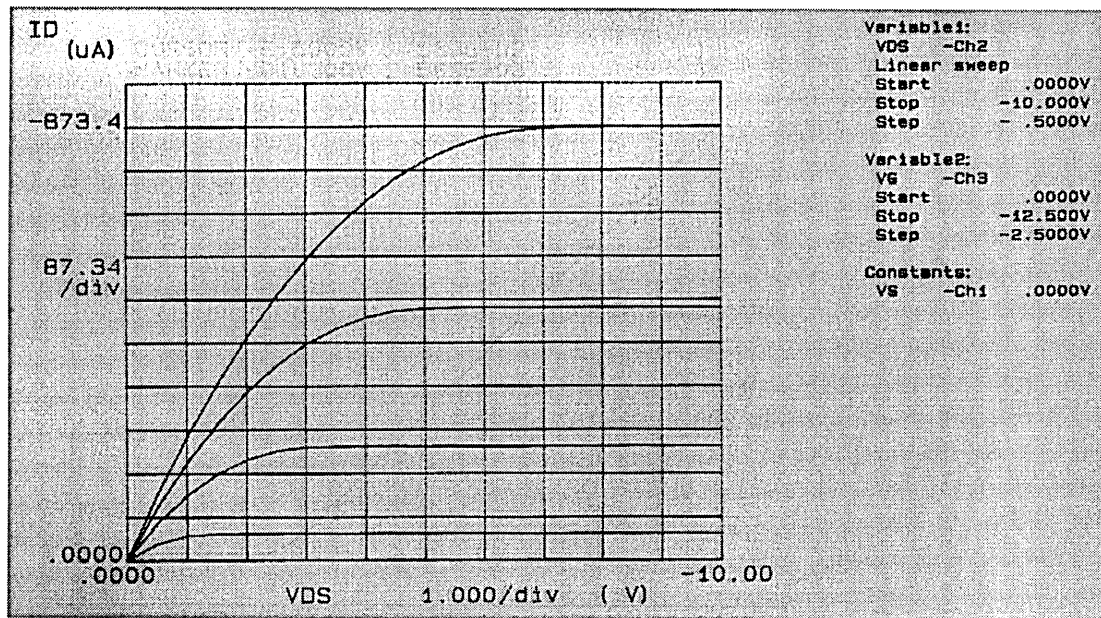


Fig. 4 Transfer characteristic of the “gated” device for different gate voltages

The devices showed a large spread in the observed threshold voltage and current carrying capability. This can in part be attributed to the varying sheet resistive of the used wafers and to a larger extend to the varying quality of the gate oxide. The

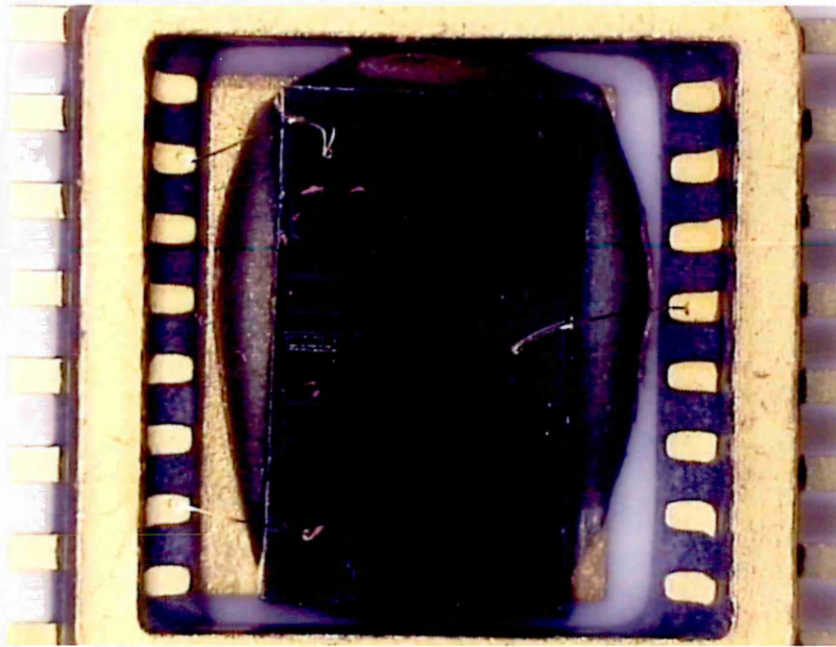
threshold voltage V_t of a conventional p-channel MOSFET for a zero bulk source polarisation is calculated according to reference ^[13] by (1).

$$V_t = \Phi_{GB} - \frac{Q_{ox}}{C_{ox}} + 2\Phi_F - \frac{Q_D}{C_{ox}} \quad (1)$$

Φ_{GB} being the work function difference between the gate and the bulk material, Q_{ox} represents the positive charges at the silicon oxide interface, C_{ox} is the capacitance of the silicon oxide, $2\Phi_F$ is the surface potential at the source side of the channel under strong inversion, which is the distance of the Fermi level in the middle and in the bulk of the energy bandgap of the semiconductor material, Q_D is the charge in the inversion layer

The first two terms in (1) describe the flatband voltage V_{FB} . Whereas the work function of the bulk is depending on the doping concentration, which can be calculated using textbook equations ^[14], the work function of the water layer forming the gate material or the C[4]RA is not known which leaves the term undetermined. In production processing techniques attempts are made to minimise the charges inside the oxide forming Q_{ox} ; this aim was not completely realised in this production. The absence of these parameters makes a comparison between the experimental and the theoretical threshold voltage impossible. The threshold is high when compared with textbook values in the region of around -3 V for conventional FET devices ^[15]. This is attributed to large terms for Q_{ox} and Φ_{GB} . The observed large spread in the threshold voltage prompted the use of a $V_t = -12.5$ V, ensuring a maximum transconductance for all transistors.

Picture 1 shows a 14-fold magnification of a device mounted and wire bonded onto a header.



Pic. 1 Header mounted and bonded CFT

6.5 The Charge Flow Capacitor

For the production of the CFC the same processes were employed, as described earlier. The fabrication order is a different one, the limitation to a single mask for the patterning of the structure is the main difference. The silicon substrate employed was from the lightly doped n-type variety, with a gate oxide thickness of 100nm, grown by dry oxidation. The Al back contact was identical to the one used for the CFT. The meshed front pattern, was for reasons of chemical stability again fabricated from gold with a chromium seedlayer providing adhesive support. The Cr and Au were thermally evaporated in one process and photolithographic patterning was carried out with a clear field mask and positive resist. After developing and fixation of the resist the double metal layer was etched in the two stage process as described earlier and then the remaining resist was removed. A schematic cross-section and top-view of the CFC, with the unpatterned sensing membrane in place, is show in Figure 5. The wafer was finally diced to yield individual devices; a patterning of the membrane was not required since fringe effects make only a negligible contribution to the capacitance. An area of 25 mm^2 forms the capacitor, with a mesh size of $100 \mu\text{m}$ by $100 \mu\text{m}$. The

membrane extending beyond the frame can be calculated by allowing for a 100 μm extension of the area beyond the outer frame along its 20mm circumference this makes only a contribution of 2mm^2 , or 8% of the capacitor's area. It can further be assumed that this extension is universally present in a similar manner for all devices.

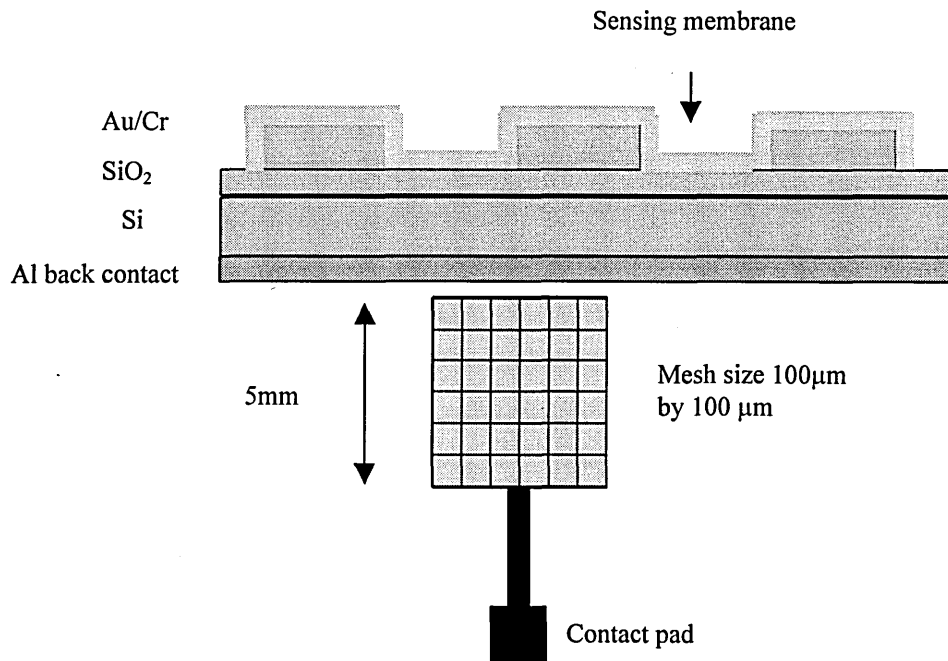


Fig. 5 Cross section and top-view of the CFC with the sensing membrane in place

6.6 References and Bibliography

- [1] An introduction to Semiconductor Microelectronics, V. Morgan, K. Board, Wiley, 1983, ISBN: 0471924784
- [2] Microchip Fabrication A Practical Guide To Semiconductor Processing, P.V. Zant, McGraw Hill, 1990, ISBN:007067194X
- [3] Principles of Growth and Processing Semiconductors, S. Mahajan, McGraw Hill, 1997, ISBN: 0071165525
- [4] Materials Science and Technology: A Comprehensive Treatment Vol. 16, Processing of Semiconductors, K.A. Jackson, VCH, 1992, ISBN: 3527268294

- [5] Semiconductor and integrated circuit fabrication techniques, P.E. Gise, R. Blanchard, Reston Publisher, 1979, ISBN: 0879096683
- [6] Introduction to Integrated Circuit Engineering, D.K. Reinhard, ISBN: 039537068X
- [7] The solid state Century, Scientific American, Scientific American, 1997, ISSN: 1048-0943, p. 10
- [8] <http://www.ti.com/corp/docs/kilbyctr/jackstclair.shtml>
- [9] <http://www.cnn.com/TECH/computing/9905/19/1958.idg/>
- [10] S.M. Sze, VLSI Technology, McGraw Hill, 1988, ISBN: 0071003479, p. 103
- [11] Reinhard, Introduction to Integrated Circuit Engineering, ISBN: 039537068X, p. 34
- [12] P.S. Barker, Gas sensing using an organic/silicon hybrid field effect transistor, Ph.D. Thesis, University of Durham, 1996, p.100-101
- [13] Design of Analog Integrated Circuits and Systems, K.R.Laker, W.M. C.Sansen, McGraw Hill, 1994, ISBN: 0-07-113458-1, p. 9
- [14] Design of Analog Integrated Circuits and Systems, K.R.Laker, W.M. C.Sansen, McGraw Hill, 1994, ISBN: 0-07-113458-1, p. 10
- [15] Design of Analog Integrated Circuits and Systems, K.R.Laker, W.M. C.Sansen, McGraw Hill, 1994, ISBN: 0-07-113458-1, p. 12

7 Organic solvent vapour detection with a charge flow transistor

7.1 Introduction

Sensors that are probing electric properties such as permeability and conductance have a major advantage over optical ones. They can be easily interfaced with a plethora of existing signal conditioning systems and offer therefore the possibility of designing embedded systems.

Among the most basic measurements that can be performed in a chemical sensor are transconductance measurements on chemoresistor type sensors. The changing resistance of a material under investigation is determined by ohmic measurements involving a voltage source and an ammeter. The lower current range for electrometers/ammeters is currently extending down to the picoampere level. This sets a natural limit to the resistivity of the chemoresistor type material that can be utilised in this way. Furthermore the signal to noise ratio is very poor for measurements conducted at the bottom end of this range and require elaborate measurement conditions, involving heavy electromagnetic shielding. Materials with a low conductivity require therefore a different approach.

The transistor provides with its built in signal amplification, a device that is very versatile and allows the utilisation of highly ohmic materials as chemically sensitive membranes. Its amplifying properties also greatly enhance the signal to noise ratio.

Calixarenes possess due to their organic nature a very low DC conductivity. So far no type of gas/vapour sensor probing the electrical properties of calixarene has been reported in the literature. AC conductivity studies on very thin calixarene membranes sandwiched between metal electrodes have been conducted by Chaabane ^[1]. The electronic transport mechanism inside the membrane has been explained in terms of Mott hopping ^[1]. Unfortunately the sandwich structure employed with an impervious top electrode prohibits any vapour sensing application.

7.2 Gas sensitive transistors

Gas and vapour sensing requires the material to be exposed to the atmosphere, therefore only field effect type transistors and not bipolar ones can be used. An in depth analysis of conventional MOSFET technology can be found in many studies [2, 3, 4], and is therefore not repeated here.

Gas sensitive transistors have been designed in a variety of ways, which can be grouped into four categories depending on the mechanism that is utilised to register the presence of the analyte. The following brief overview illustrates the main working principles of ChemFETs. It is by far not complete, but all existing developments are based on modifications of the described principles, tailored to specific applications using novel materials.

7.2.1 Field effect transistors without gate electrode

In 1970 Johannessen [5] introduced the Open Gate Field Effect Transistor (OGFET), which is a conventional field effect transistor (FET) without a gate electrode. The adsorption of polarised vapours on the insulator surface, like water and methanol, modulate the drain current.

A variant of the OGFET is the Adsorption Field Effect Transistor (ADFET) [6], which possesses an extremely thin gate insulator ($< 5\text{nm}$). The adsorption of any kind of gas with a permanent dipole moment like, H_2O , NH_3 , HCl , CO , NO , NO_2 and SO_2 modulate via their stray fields, the drain current.

In both devices the mechanism used for the signal generation is the modulation of the source drain channel by the electric field of the adsorbed species. Non selectivity and diffusion of the analyte into the substrate or the gate insulator seriously compromise the stability of such devices.

7.2.2 Field effect transistors employing work function changes in the gate metal

Lundström pioneered the Palladium Gate Field Effect Transistor (Pd-FET) in 1975 [7]. In it the gate electrode is fabricated from Pd, which has the characteristic property of absorbing large amounts of hydrogen and allowing easy diffusion of it into its bulk.

During the process of adsorption, hydrogen molecules at the surface dissociate into atomic hydrogen and diffuse into the Pd gate. A dipole layer is formed at the Pd/SiO₂ interface which changes the work function of the gate electrode, this in turn modulates the drain current. Replacing the Pd with Pt in a similar structure leads to a higher sensitivity for ammonia ^[8]. Though the modification of the gate metal, including changes in the morphology ^[9] allows a partial tailoring towards different target analytes, this type of device requires hydrogen to be part of the target molecule, since only it can migrate through the metal.

The introduction of a thin, perforated gate as in ^[10], allows the detection of other hydrogen-free gases like CO. Here the perforation allows contact between the gas and the gate insulator metal boundary where again a dielectric layer is formed, modulating the work function of the metal.

Though all hydrogen containing gases interfere with the measurement of the target analyte, compromising the selectivity, Pd-MOSFETS have proven to be very reliable in the detection of hydrogen leaks ^[11] over periods of more than 10 years.

One interesting modification of the Pd-FET is its use as a biosensor, where the Pd gate is covered by a gas permeable membrane with an immobilised enzyme on top of it. Hydrogen gas evolving as a consequence of a biochemical reaction of the target analyte with the enzyme, diffuses through the membrane and then into the gate, changing its workfunction. This principle was successfully employed for the detection of urea down to concentrations of 10 µmol/l, using urease as the enzyme ^[12].

7.2.3 Field effect transistors employing dielectric constant changes or conductivity changes in a sensing membrane

In the Oxide-Semiconductor-Field Effect Transistor (OSFET), an organic thin film, whose charge carrier density changes upon exposure to electroactive gases, replaces the metal gate. These transistors work mostly in the depletion mode and changes in the threshold voltage are used to register the presence of gases. A variety of compounds have been utilised for the gate, with most of the attention focusing on phthalocyanine derivatives ^[13, 14] and porphyrin ^[15] with NO₂, Cl₂ and SO₂/SO₃ as target analytes. Sensitivities are usually in the ppm region but detection thresholds in the ppb range have also been reported ^[6].

Siemens introduced a gas sensor, where the gate insulator is formed by a layered system of SiO_2 , Si_3N_4 and an organic gas sensitive membrane ^[16]. The gate consists of an extremely thin layer of gold, which is highly perforated and allows the permeation of gaseous species. The absorption of gas into the organic layer modifies its dielectric constant and modulates henceforth the drain current by changing the penetration of the electric field emanating from the gate electrode. Solvent vapours in higher concentrations almost invariably lead to a swelling of the organic layer, therefore the gate is stretched as a result and the adhesion of the metal can deteriorate with continued exposure cycles.

Senturia developed the principle of the Charge Flow Transistor (CFT) in 1977 ^[17]. The CFT consists in essence of a charge-flow capacitor [CFC] within the gate electrode of an enhancement MOSFET. The CFC consists of a metal frame filled with a low conductivity material. Upon application of a gate voltage, the charge present on the metal frame is transferred onto the filling material and when enough charge is transferred, an inversion channel is formed in the substrate underneath the gate insulator connecting the source and drain. The time required for the charge to spread out and the channel to form is directly dependent on the charge transport properties of the filling material. The time required for the channel formation is usually referred to as the turn-on response. Initial studies were focused on the determination of the curing behaviour of resins ^[18] and the detection of water vapours ^[19]. Barker then pioneered the development of the CFT for gas sensing applications, by using polyaniline for the reversible detection of NO_2 and $\text{NO}_2 + \text{SO}_2$ ^[20, 21] and later octa-substituted metal free phthalocyanine for the detection of NO_x ^[22]. Throughout these studies the cross sensitivity of polyaniline to water vapour was noticed and this effect was exploited in a moisture sensor ^[23], now of course suffering from a cross sensitivity to NO_2 .

Modifications of the gate structure lead to the Interdigitated Gate Electrode Field Effect Transistor (IGEFET). Here the gate electrode consists of two comb like structures, separated from the source-drain region, with the sensing membrane connecting the two combs ^[24]. Charge is transferred between the two combs and is lead to the “normal gate” connecting source and drain. This separation allows the placement of a heating element underneath the combs, which enhances desorption without affecting the transistor characteristic. The complexity of this arrangement in comparison to a gap in the gate does not lend itself to prototyping.

7.3 Experimental details

The production process of the CFT is covered in detail in Chapter 6, in which are also presented the exact physical and electrical dimensions of the device. The coating of the device with the membranes, is described in Chapter 4.

Extensive characterisation of the CFT concept was conducted in previous work ^[25]. The MOSFET itself is a standard electronic element described in most semiconductor text books, therefore here is presented only the material that is relevant for its specific application as a vapour sensor.

7.3.1 Vapour exposure

The exposure experiments were conducted, by mounting the devices under a bell-jar and the vapour was generated in two ways, static and dynamic. For the static vapour generation, the analyte was injected with a syringe into the bell-jar, allowed to evaporate freely and the measurements were taken in equally spaced time intervals throughout. The first measurement taken prior to the injection, provided the baseline. For the dynamic exposure measurements, the baseline was recorded in air and then a constant stream of vapour in nitrogen was used to purge the chamber. The purging was continued, until 4 times the volume of the chamber had flown through, reaching equilibrium, after which the recovery was recorded by removing the bell-jar.

The bell-jar volume of 2.4 litre and the used flow rate of 100 ml/min resulted in a purging time of 1.5 hours. A vapour generator was used to provide this constant vapour stream of know concentration. In it a vessel containing the solvent (diffusion tube) is heated in a chamber through which a stream of nitrogen flows. The vapour concentration was calculated according to (1).

$$\text{ppm} = 22.4 \cdot \frac{\text{diffusion rate}[\text{mg} / \text{min}]}{\text{MW} \cdot \text{flowrate}[\text{ml} / \text{min}]} \cdot 10^6 \quad (1)$$

With 22.4 being the volume, in ml, of one mmole of gas, the diffusion rate is the rate at which the diffusion tube loses weight, MW is the molecular weight of the compound

and the flow rate is the total flow controlled by the flowmeters and 10^6 , is a factor to convert the concentration to the ppm level.

The diffusion rate is calculated by the weight loss of the diffusion tube over time with the vapour generator running at constant flow and temperature. The latter requires long equilibration times and several configurations of the diffusion vessel have been tested. The vessel finally used had a volume of 70ml, with a neck-opening diameter of 13mm, and a neck length of 21 mm. Table 1 shows the calibration data used for the calculations. Dilution of the vapour stream with nitrogen allowed a final adjustment of the concentration.

Time	net weight
t_0	55.3 g
$t_0 + 532 \text{ min}$	41.8 g
$t_0 + 1040 \text{ min}$	27.9 g
$t_0 + 1750 \text{ min}$	0.79 g

Table 1 Vapour generator calibration with acetone at a temperature of 50 °C

A schematic cross section of the device, with the sensing membrane in place, is shown in Figure 2.

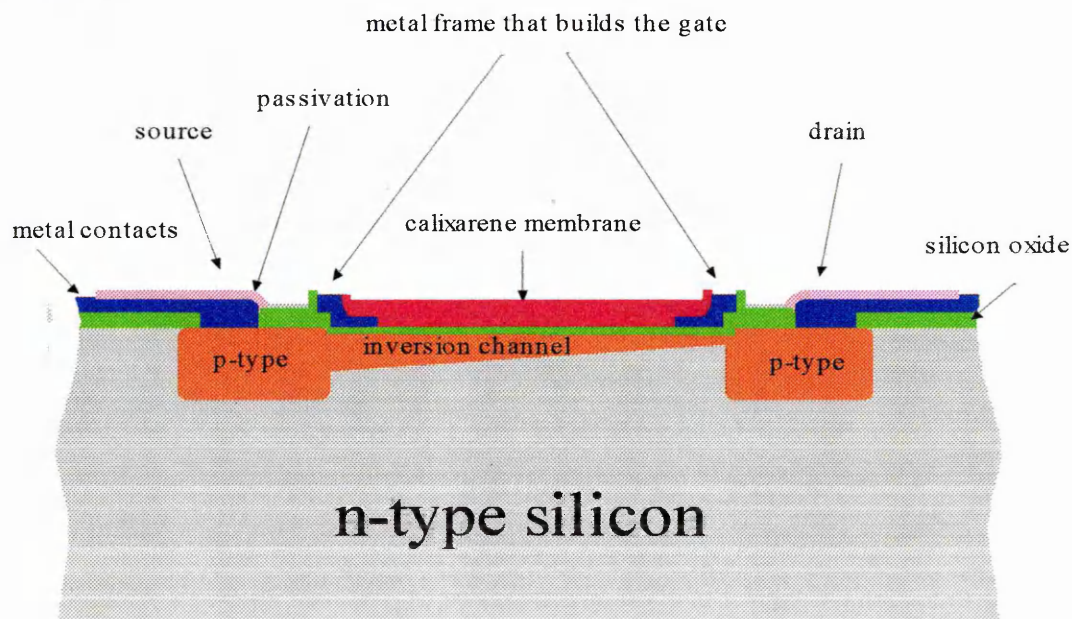


Fig. 2 Cross section of the turned on CFT with the C[4]RA membrane filling the gate

7.3.2 Measuring circuit

A schematic diagram of the circuit used to register the turn-on response is presented in Figure 3. The storage oscilloscope used, could have been replaced with a very fast computer controlled ammeter with an external trigger, and the square wave generator could have been replaced by a computer controlled voltage source. This would have allowed a plotting of data points for comparison instead of relying on the screencapture of the oscilloscope. The attractiveness of the used set-up is its simplicity, there is no need for computer controlled components and no programming is required.

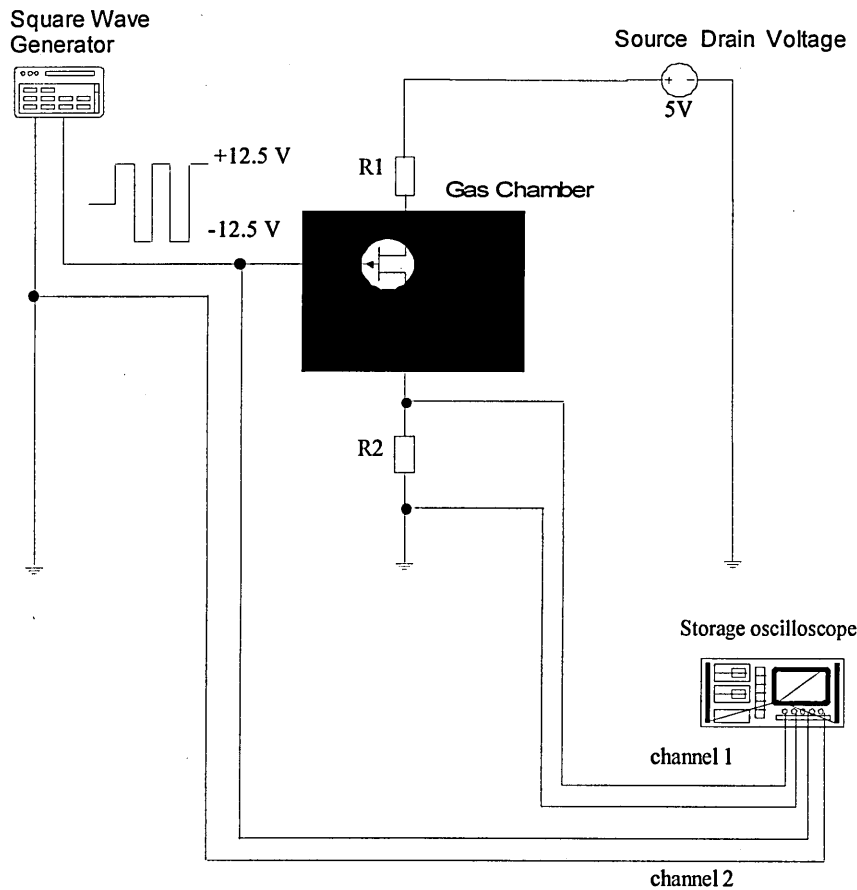


Fig. 3 Schematic of the measuring circuit used

7.3.3 Explanation of the oscilloscope screen capture

In order to explain the following screencaptures, in Figure 4 an annotated screencapture is shown. Following screencaptures show only the top left quadrant.

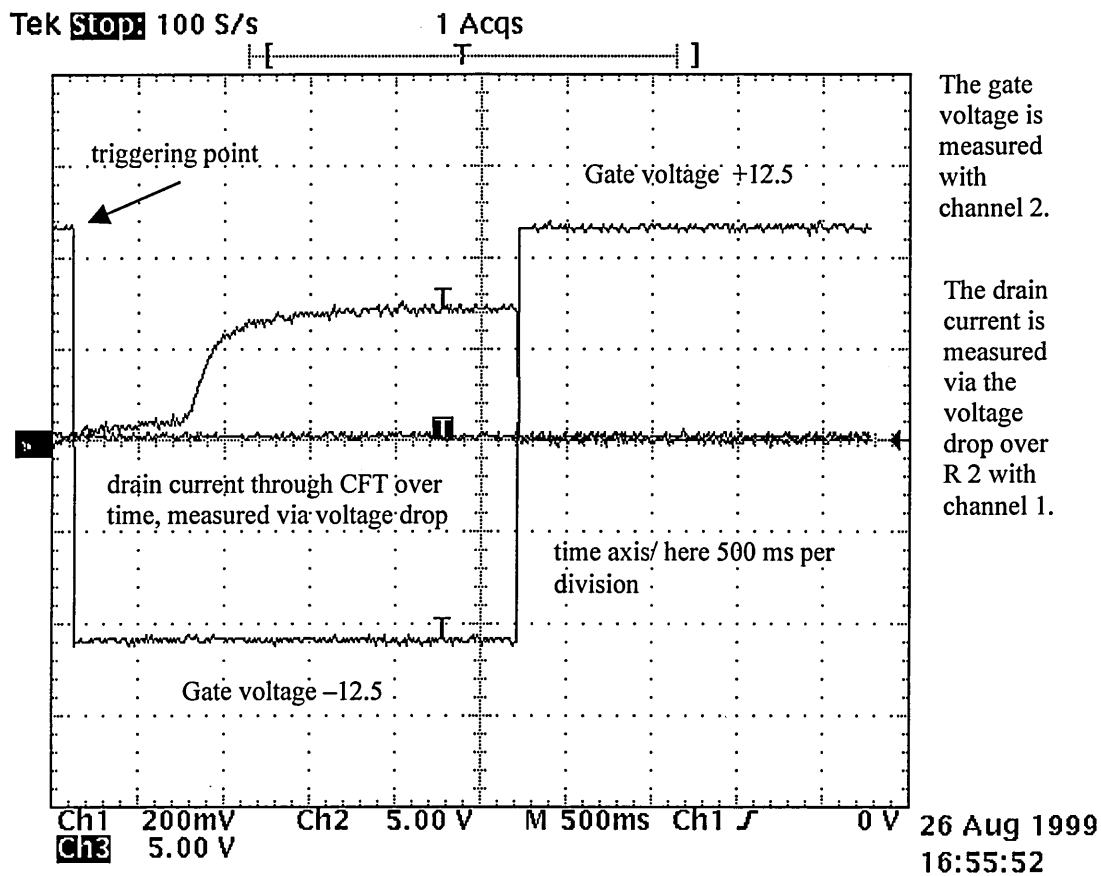


Fig. 4 Annotated oscilloscope screenshot

7.4 Exposure results and discussions

7.4.1 OGFET behaviour

To clarify the contributions of the exposure response, it was first established that the CFT does not work as an AGFET, by creating an inversion layer upon sorption of the analyte without the application of any gate voltage. No measurable increase in the drain current could be observed upon exposure to saturated vapours of hexane, acetone, chloroform, methanol and water, without any gate voltage applied.

7.4.2 Description of the turn-on response modulation upon exposure to saturated vapours of chloroform

A typical data series, showing the modulation of the turn-on response upon the static exposure to saturated chloroform vapours is presented in the Figures 5a to 5g. The T

marks the trigger point when the gate voltage changes from + 12.5 to - 12.5 volt at channel 2, and the drain current is measured via the voltage drop across a resistor with the channel 1, Figure 3. The time intervals between triggers are marked in terms of time passed from the baseline measurement t_0 . For the sake of comparison the time scale is kept constant over the whole series, at 10 seconds per division.

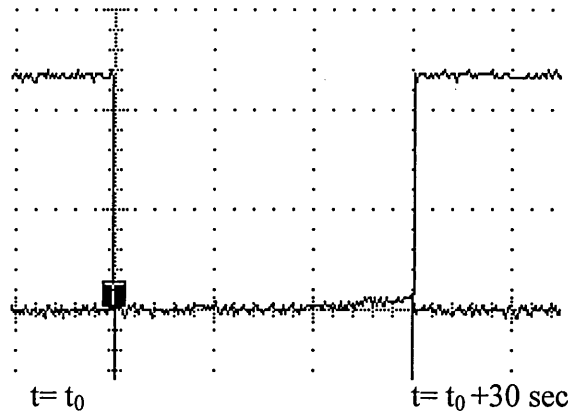


Fig. 5a Baseline, on the very right, the onset of the turn-on is visible

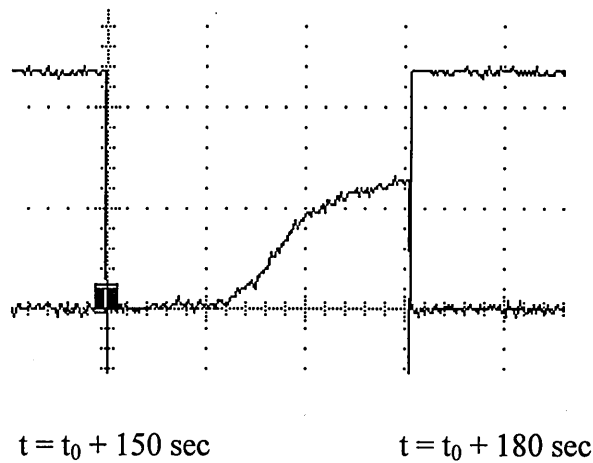


Fig. 5b Injection of chloroform at $t=60$ sec, onset of evaporation and therefore absorption in the membrane, the deadtime before the threshold voltage is exceeded, is reduced and the shallow slope in I corresponds to $V_g < V_t$.

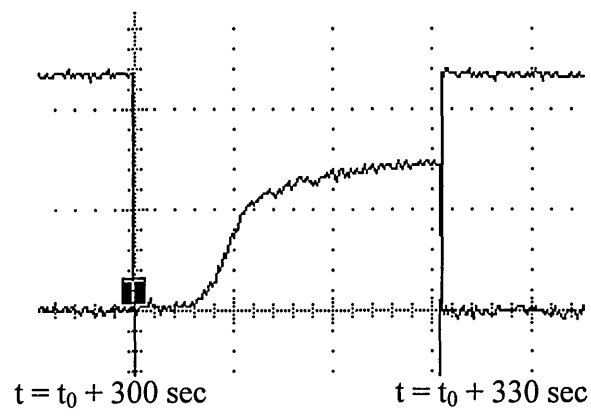


Fig. 5c The turn-on time is further reduced, with an onset of saturation at the end of the 30-second measuring interval

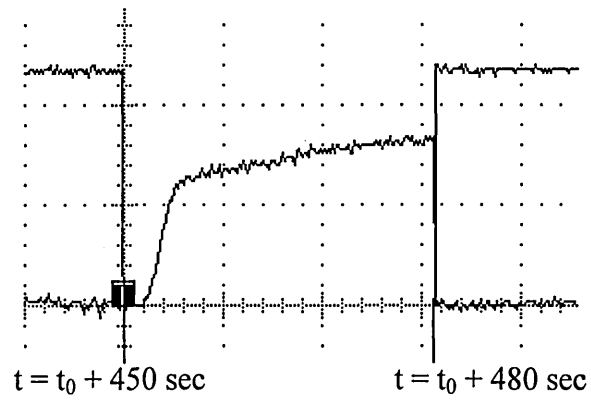


Fig. 5d Further decrease of the turn-on delay

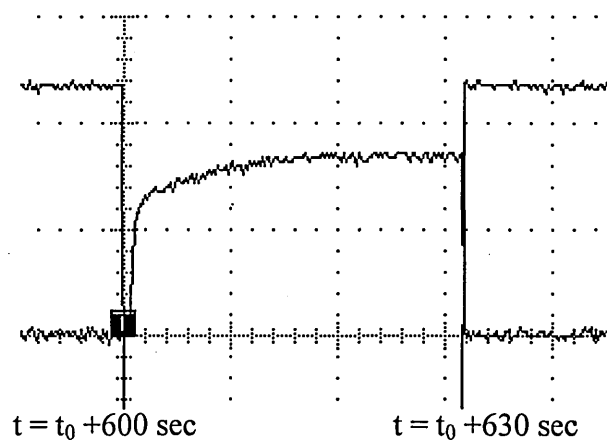


Fig. 5e Further decrease in the turn-on time, with true saturation reached after 20 seconds

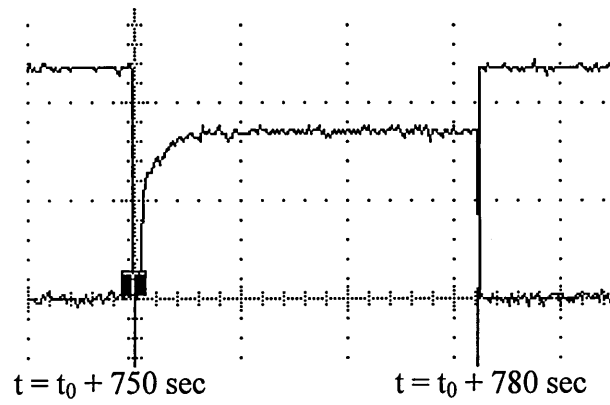


Fig 5f Saturation is complete after 6 seconds

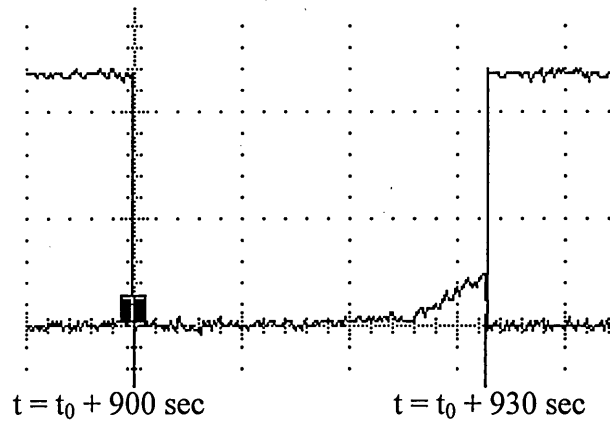


Fig. 5 g Recovery after removing the bell-jar at $t = t_0 + 800$

The above series covers the whole concentration spectrum, from zero up to the saturation vapour pressure of 159 mbar. Recovery was only 100 % complete after 40 minutes.

For sake of comparison, a modulation factor was introduced to compare CFTs with different baselines. This eliminates the influence of the coating quality, with respect to the contact resistance between the gate and the membrane, membrane morphology and thickness. The modulation factor is defined as in (2).

$$\text{modulation factor} = \frac{\text{delay time of the baseline}}{\text{delay time on exposure}} = \frac{t_b}{t_e} \quad (2)$$

With the delay time defined as, the time that is marked by the intercept from the extrapolation of the linear part of the current increase to the time axis (as marked in Figures 10a to 10e). For the above chloroform exposure this results in a modulation factor of,

$$\text{modulation factor} = \frac{t_b}{t_e} = \frac{30 \text{ sec}}{0.66 \text{ sec}} = 45,5.$$

7.4.3 Process of charge transfer onto the sensing membrane

For an inversion layer to form underneath the gate, charge must be transferred onto the sensing membrane. This process is shown schematically in Figure 6, with the corresponding steps shown in the turn-on response, Figure 7.

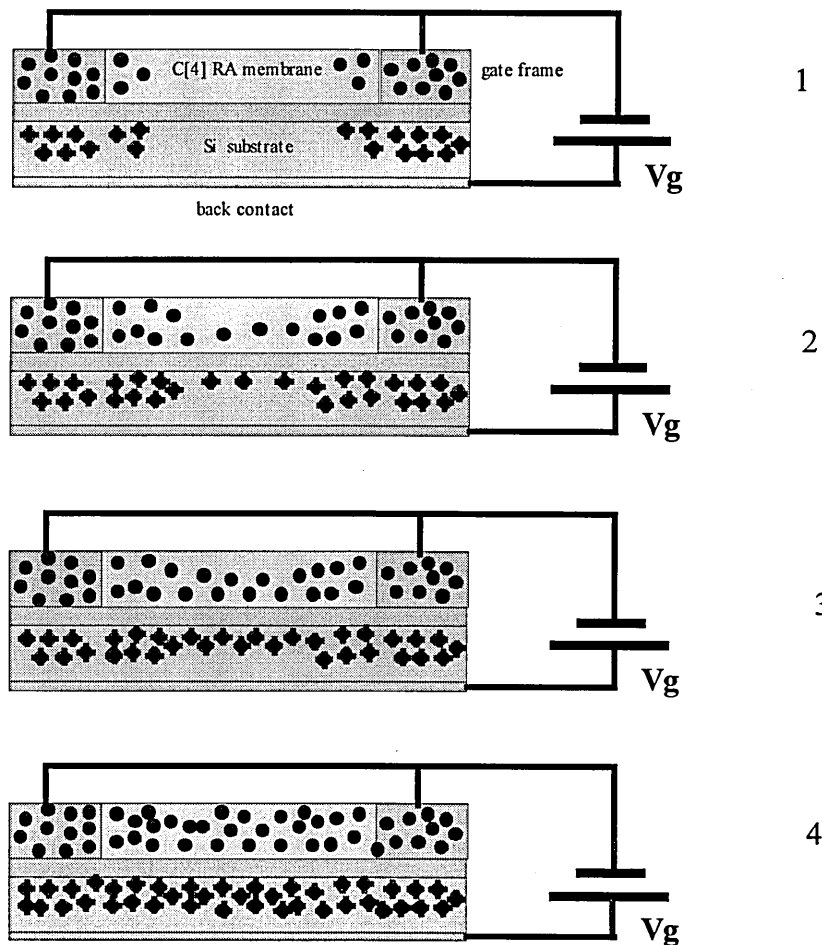


Fig. 6 Charge transfer from the gate electrode onto the sensing membrane in steps 1 to 4

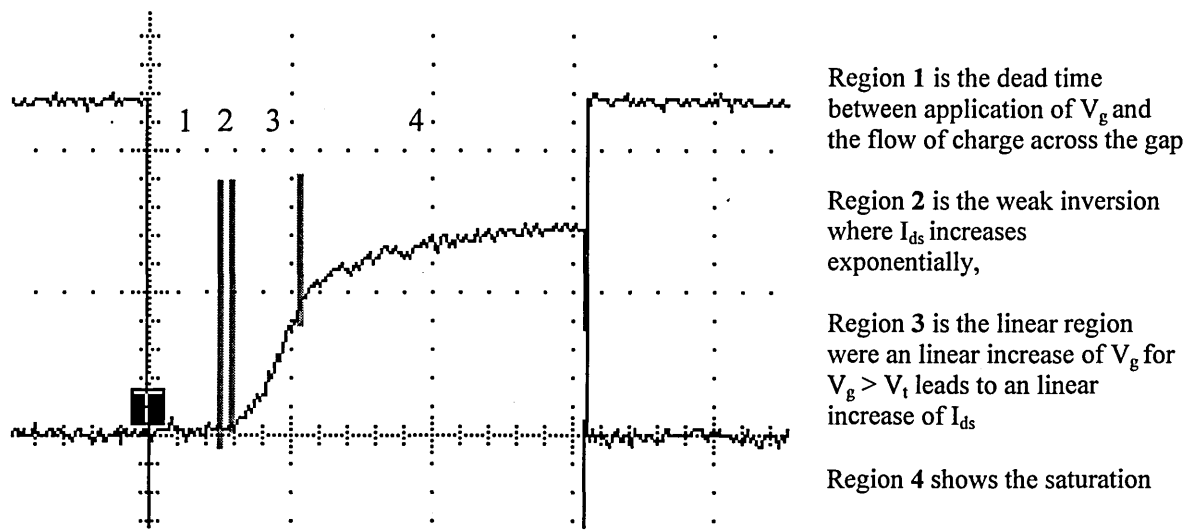
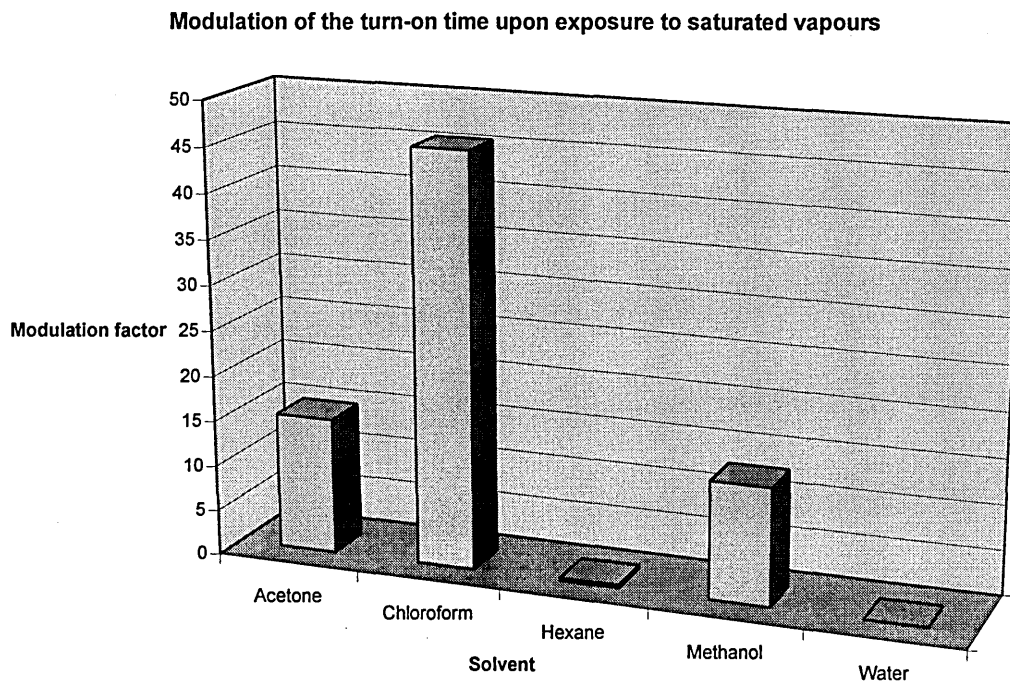


Fig. 7 Changing charge distribution of the CFC in the gate of the CFT over time, after the application of the gate voltage and corresponding I_{ds} over time

7.4.4 Further saturated vapour exposures to common solvents

The response to different saturated vapours was determined in identical ways. Since the baseline for every transistor differed, the response to the vapours in air was normalised to the turn-on modulation factor. Figure 8 shows this normalised response in terms of the decrease of the turn-on response by the modulation factor.



Acetone	Chloroform	Hexane	Methanol	Water
15	45.6	0.3	13	0

Fig. 8 Normalised decrease in the turn-on time of the CFT for saturated solvent vapours

7.5 Contributions to the charge transport across the membrane

The charge transport modulation across the membrane is dependent on a variety of factors, which are analysed below.

7.5.1 Saturated vapour pressures of the solvents

The saturated vapour pressures of the solvents as taken from reference ^[26] at 20 °C are given in Table 2, together with their molecular weight. The saturated vapour pressure defines the number of molecules in the sample space.

Solvent:	Saturated vapour pressure in mbar:	Molecular weight
Acetone	181	59
Chloroform	159	115
Hexane	130	86
Methanol	96	32
Water	27	18

Table 2 Saturated vapour pressures of solvents at 20 °C and molecular weight

7.5.2 Electronic conduction in the C[4]RA membrane

In disordered systems with delocalised electronic states the electronic conduction does not follow the diffusion process, but can be described by a process of variable range hopping. The theory describing this hopping process was developed by Mott and Davis ^[27, 28]. According to this theory electrons are apparently intelligent, they hop from one initial site A to another site B with the energy hop being as low as possible. For the C[4]RA the four aromatic structures per molecule form the delocalised electronic states. The hopping behaviour can be modulated by three process taking place on absorption:

- The swelling of the film changes the distances between hopping sites, since the film is highly unordered and swelling does not take place in one well defined plane, distance changes between sites are rather random.
- Filling of “voids” between adjacent hopping sites with polar molecules provides a bridging function for the hopping electrons.

- The conduction activation energy for the hopping is modulated by altering the state of the delocalised π electrons due to van der Waals bond formation with the analyte.

It is therefore believed that the charge transport across the C[4]RA membrane, must progress along the basket and/or hydrophilic part of the molecule at the brim of the basket. The alkane chains can be regarded as nearly perfect insulators. Upon the complexation with polar vapours the electron distribution in the molecule is modified, based on the formation of weak intermolecular bonds. The polar molecules can polarise parts of the C[4]RA due to induced dipole interactions as described in detail in reference [29]. Table 3 [30] gives the polarity of the solvents used, characterised by the dipole moment, which is defined as: The distance between centres of charge in the molecule multiplied by the magnitude of charge.

Solvent	Dipole moment [Debey]
Acetone	2.69
Chloroform	1.15
Hexane	0.08
Methanol	2.87
Water	1.87

Table 3 Dipole moments of the solvents

7.5.3 Micro-condensation of vapours in the C[4]RA membrane

Nabok et al. [31], showed that nonporous calixarene LB films allow the micro-condensation of organic solvents below the saturation vapour pressure. QCM measurements showed a strong nonlinearity in the absorbed mass on increase of the solvent vapour pressure, indicating the onset of condensation as early as 0.1 times the saturated vapour pressure for hexane. Condensation in small pores occurs at a lower partial pressure, as compared to the partial pressure required for condensation on a flat surface. A concave surface provides more sites at which the condensing liquid can interact. This relationship is described for hemispherical menisci by the Kelvin equation (3) [32].

$$\ln \frac{p_r}{p_0} = -\frac{2\sigma V_m}{r_c RT} \quad (3)$$

p_0 = the partial pressure at which capillary condensation occurs, σ is the surface tension, V_m is the molar volume, R is the gas constant, T is the absolute temperature, r_c is the radius of the hemispherical meniscus

Though the equation is valid only for hemispherical menisci, the basket shaped C[4]RA can at a first approximation be treated as two oppositely stacked hemispheres, Figure 9.

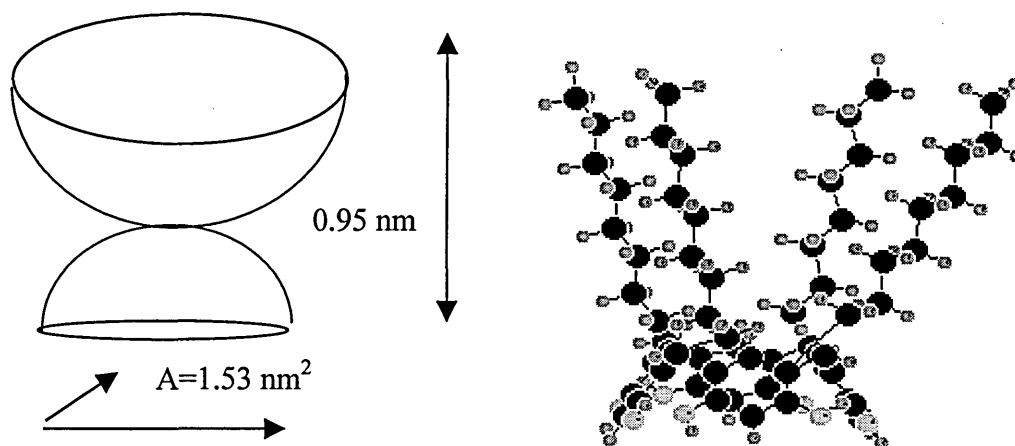


Fig. 9 Simplified model of the C[4]RA molecule based on two hemispheres

From the height as determined experimentally of 0.95 nm and the area of the molecule at 1.53 nm^2 , the model can be described by two hemispheres with an radius of ca. 0.7 nm for the hemisphere formed by the alkane chains and a radius of 0.3 nm for the hemisphere made up by the ring structures. Other models are possible like a cylindrical treatment of the capillaries as in ^[31], particular when intermolecular spaces are considered. A further complication introduced, is the swelling of the membrane changing r_c by filling of pores. There are also other adsorption models according to Dubinin/Radushkevich ^[33], which again are based on the theory of micropore filling in combination with the Polanyi adsorption potential concept ^[34].

In Table 4 are presented the data used for the calculation of the pressure at which microcondensation at room temperature can occur, and the results of these calculations with a separate treatment of the two hemispheres.

It was shown in ^[31], based on QCM measurements, that the mass gained during the absorption of vapours with respect to the relative vapour pressure (p/p saturation) is not varying over more than 50 % over a range of 4 orders of magnitude, for the solvents hexane, chloroform, benzene and toluene. The molecular weight for these compounds (Table 2) differs by not more than a factor of 0.5 (benzene MW = 78, chloroform MW =

115). It was therefore proposed that at high concentrations the condensation of vapours is rather independent of the presence of specific absorption sites.

Solvent	Surface Tension [dyne/cm]	Molar Volume [cm ³ /mol]	Micro-condensation $r_c = 0.3 \text{ nm}$ [p _r /p _s]	Micro-condensation $r_c = 0.7 \text{ nm}$ [p _r /p _s]
Acetone	23.32	73.52	$9.57 \cdot 10^{-2}$	$3.66 \cdot 10^{-1}$
Chloroform	27.16	80.16	$5.08 \cdot 10^{-2}$	$2.79 \cdot 10^{-1}$
Hexane	17.91	130.69	$4.06 \cdot 10^{-2}$	$2.54 \cdot 10^{-1}$
Methanol	22.55	40.49	$2.86 \cdot 10^{-2}$	$5.35 \cdot 10^{-1}$
Water	72.8	18.02	$1.66 \cdot 10^{-1}$	$7.69 \cdot 10^{-1}$

Table 4 Calculated micro-condensation pressure ratios

7.5.4 Conductivity of the solvent in the liquid phase

To ascertain the relative conductivity of the solvents, as used, measurements were performed on interdigitated electrodes, covered with a drop of the solvent, to completely cover the fingers. The measurements were carried out with an electrometer at a DC voltage of 10 V, measuring the current between adjacent fingers of the IDEs, the stray current through the meniscus above the fingers can be neglected, due to the high resistivity of the material. The measuring voltage was chosen to be 10 V, in line with the gate voltage of - 12.5V. It is believed, from a test conducted at a lower voltage (1.5V), that at this high voltage level, dissociation of the solvent molecules contributes to the increases of the conductivity of the liquid phase. The results for the 10V measurements are presented in Table 5.

Solvent	Current
Acetone	2.3 μA
Chloroform	1.5 nA
Methanol	2.2 μA
Hexane	23 pA
Water	> 2 mA

Table 5 Current through solvent covered IDEs at a DC voltage of 10 V

7.5.5 Analysis of the charge transfer process

There is no direct correlation between the modulation of the turn-on response and a single criterion like, the vapour pressure, conductivity of the solvent or the polarity of the solvent. It is believed that the reduction of the turn-on time is dominated by the charge transfer through the condensed phase of the solvent inside the membrane, ionic conduction, with a secondary contribution stemming from an enhancement of the electron hopping.

The conductivity of the solvent in the condensed phase must not be directly reflected by the conductivity of the solvent in the liquid phase. There are several factors that can account for a difference:

- Separation of molecules, in the truly liquid phase intermolecular distances are smaller as in the condensed phase, with C[4]RA molecules dispersed in-between.
- Solvation of ions, which stem from the dissociation, influence their propagation speed.
- The mobility of molecules in the two phases takes on a different form.

Water vapour

The zero response to water can be explained with the fact that the hydrophobic alkane chains prohibit any water vapour permeation into the sensing membrane, therefore making any conduction modulation impossible.

Hexane vapours

The poor response to hexane can be well understood, when the complexation of the hexane is assumed to be primarily along the alkane chains. The hydrophobic-hydrophobic binding would therefore not affect the charge transfer properties along the cage structure. The deduction of the turn-on response by a factor of 0.3, can be attributed to the swelling of the membrane decreasing the contact resistance between the membrane and the gate or the conduction across the condensed phase. With hexane having the lowest solution conductivity this contribution can be expected to be very small.

Acetone and methanol vapours

Acetone and methanol provide similar turn-on response modulations. Both their solvent conductivity as well as their dipole moments are very similar, they differ by only 5% and 7 % respectively. The higher response to acetone seems to be stemming from its slightly larger contribution of the condensed phase. Furthermore the calculated micro-condensation vapour pressure is lower for acetone than for methanol. Both solvents possess a highly polar character. They can change the electron distribution alongside the basket, possibly via the formation of bonds between delocalised π -electrons in the aromatic rings and the solvents or induced dipole dipole bonds with the hydrogen atoms terminating the baskets at the lower rim. This is strongly affecting the conduction activation energy required for charge hopping.

Chloroform vapours

The high reduction in the turn-on time upon chloroform absorption is at the moment difficult to interpret. Its solvent conductivity is lower than that of acetone and methanol, so is its dipole moment. There are two possible explanations that can account for this. Firstly the complexation of the chloroform is taking place in a different position at the basket, exerting a stronger influence on its π -electrons particular to the spatial arrangement that they take up. Secondly the conductivity of the condensed solvent is disproportionately higher than that of the liquid phase. Dissociation of the solvents results in ions, the strong electrostatic forces between the ion and the solvent molecule bind a shell of molecules around the ion. This process of solvation increases the effective radius and slows the charges down. In the condensed phase this effect might be less marked than in the liquid phase. Acetone, methanol and chloroform might have very different solvation effects. Acetone and methanol with their higher dipole moment might show stronger solvation, resulting in a larger radius and therefore slower movement. This would mask the effective ion mobility and therefore the conductivity. At the moment no definitive explanation can be provided for the very strong response to chloroform.

7.6 Exposure to dynamic acetone vapours

The detection of saturated solvent vapours is proof that low conductive C[4]RA membranes can be utilised in a conduction based sensor. It can have its application in closed storage facilities, where the detection of one or more leaks in the containers can be provided. However there is a much wider interest in sensors that can detect lower solvent concentration, as for example around the concentration level equivalent to that of the lower explosion limit (LEL). Therefore attention was focused on this, with the choice of the target analyte acetone being conclusive with the facts that it is:

- the 44th highest volume produced in the US (1991) of all chemicals ^[35]
- its LEL is 10.9% of that of the saturation vapour pressure ^[26] (this falls into the region were microcondensation according to (3) is predicted)
- frequently used as a common solvent

The vapour concentration of the LEL was generated as described above and the same measuring circuit was employed as previously. The baseline was again recorded in air and the exposure was recorded in intervals of 24 minutes throughout the purging process of the chamber. Figures 10a to 10e show the modulation of the turn-on response throughout the measurement, with the arrow marking the turn-on time, and 10a providing the baseline.

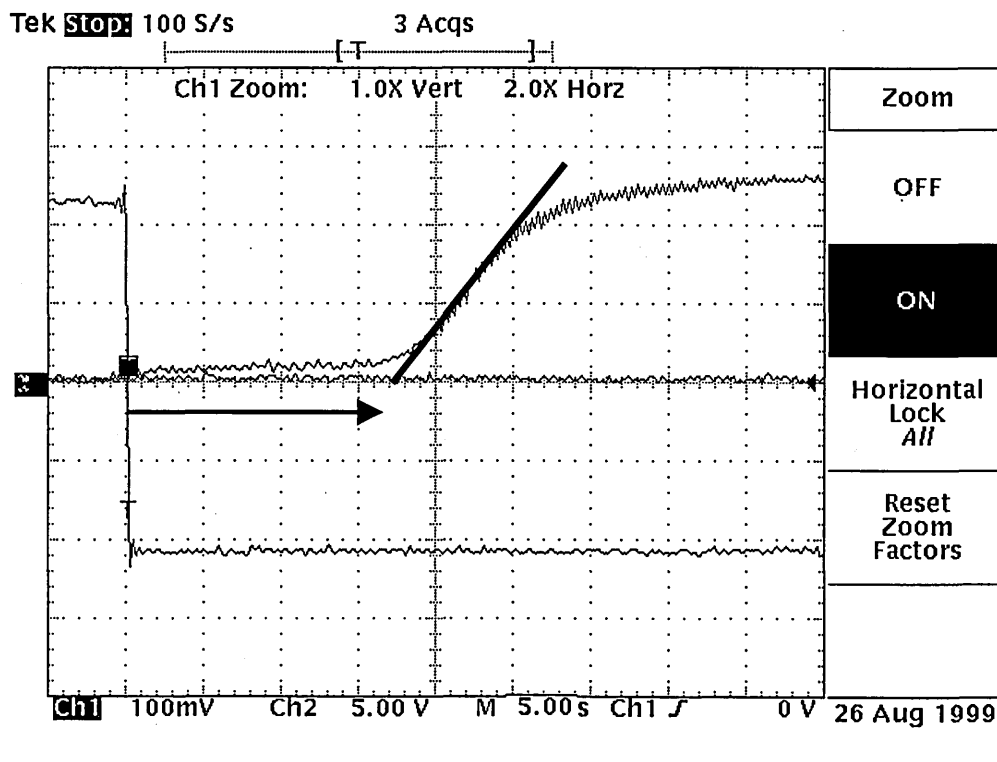


Fig.10 a baseline

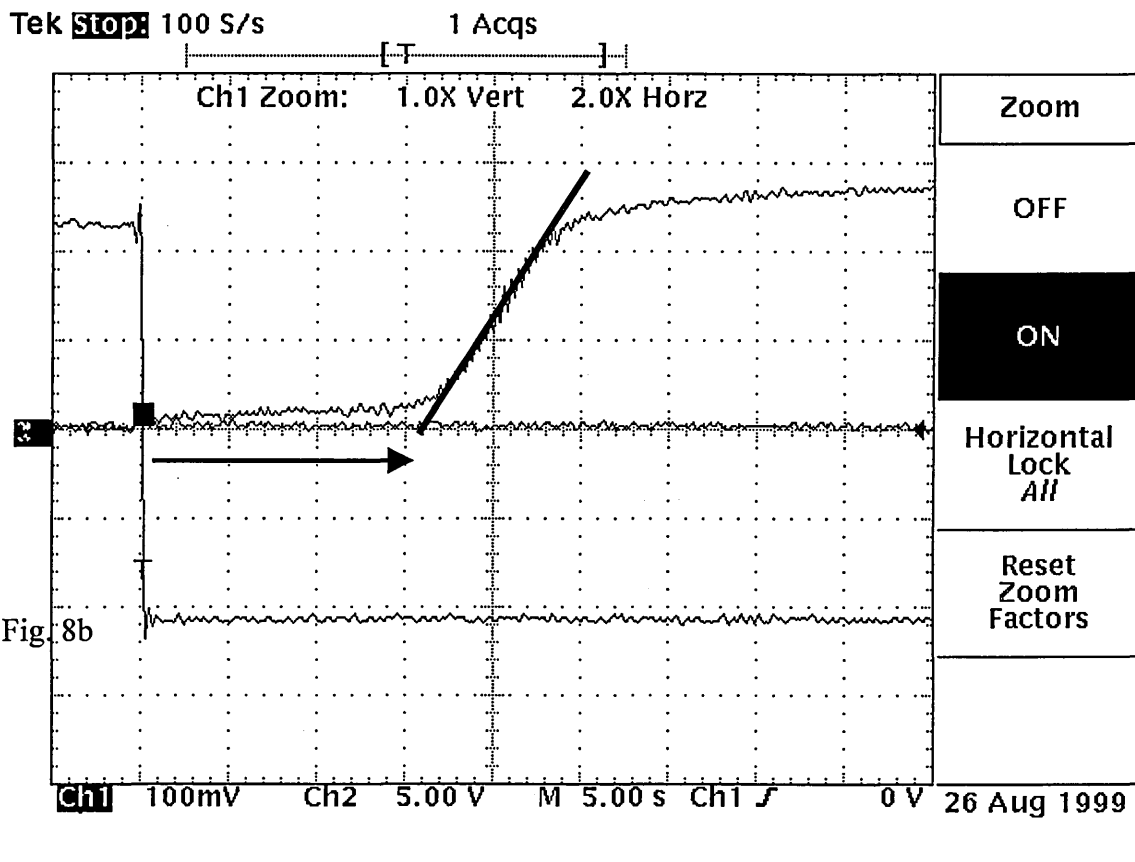


Fig. 10b $t = t_0 + 24 \text{ min}$

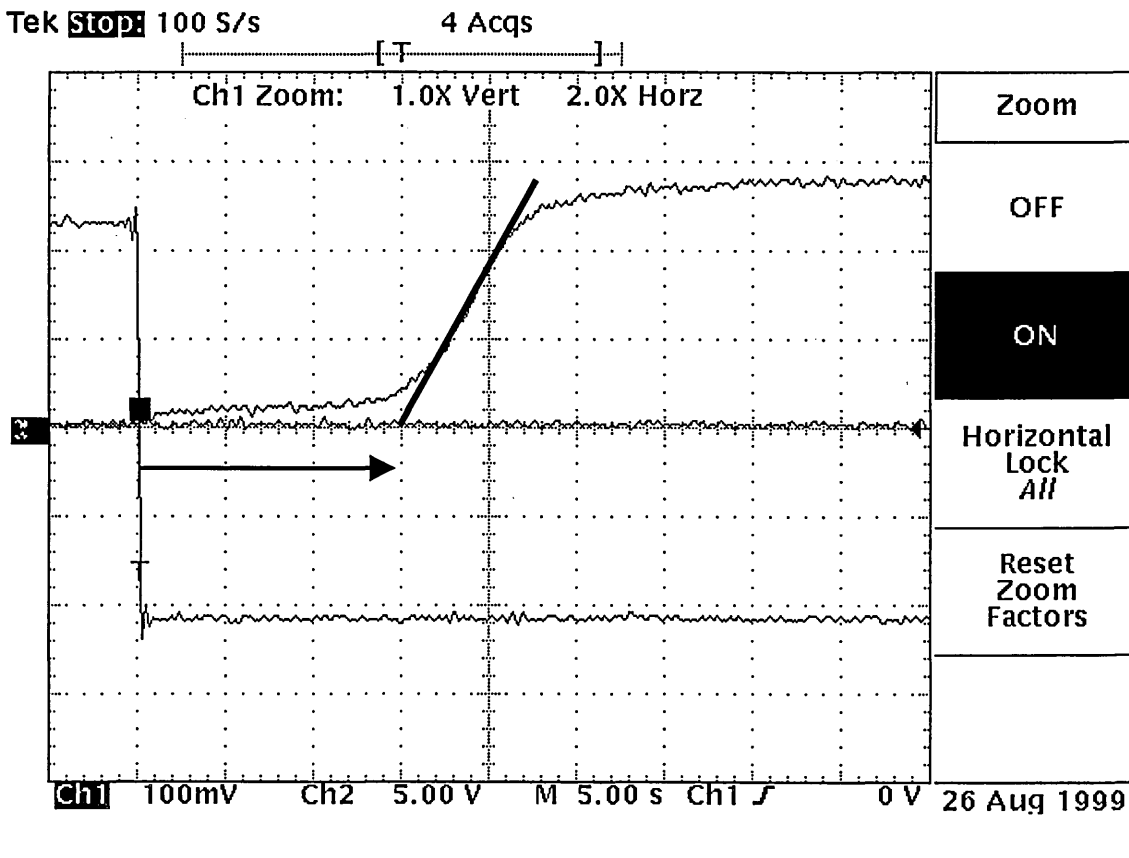


Fig. 10c $t = t_0 + 48 \text{ min}$

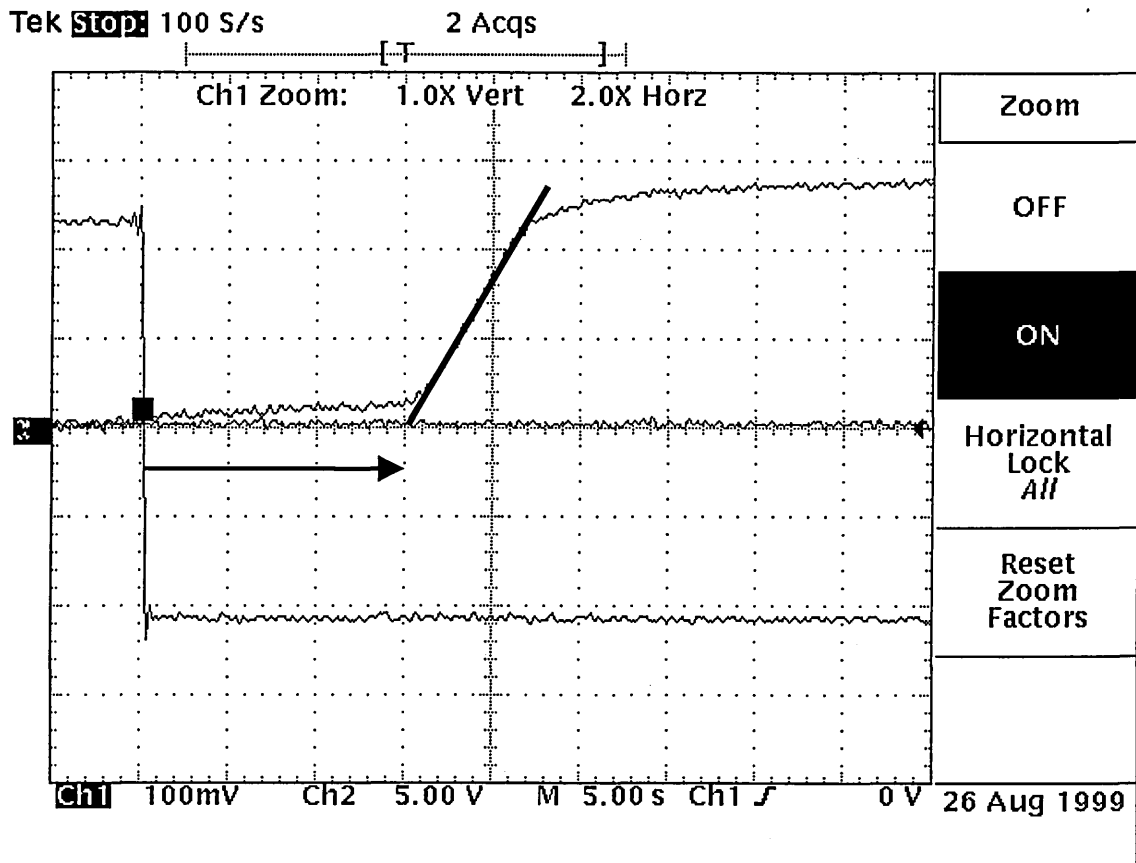


Fig. 10d $t = t_0 + 112\text{min}$

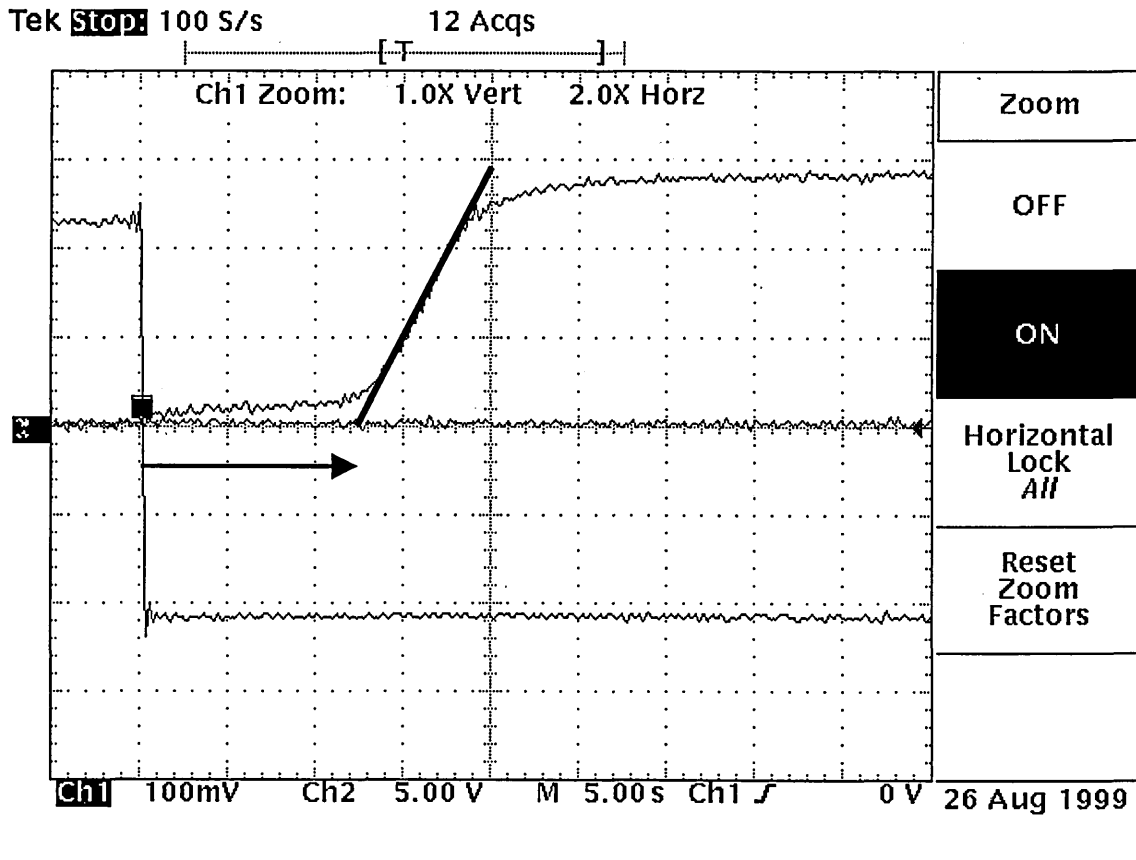


Fig. 10e $t = t_0 + 136\text{ min}$

From the above measurements the modulation factor can be calculated as,

$$\text{modulation factor} = \frac{t_b}{t_e} = \frac{17 \text{ sec}}{12.5 \text{ sec}} = 1.36.$$

This is less than the percentile fraction of the saturated vapour pressure response of 1.5, which could be interpolated from a linear response. It must therefore be assumed that the modulation is a non-linear function of the solvent concentration, with a stronger modulation at higher concentrations.

Based on the calculation carried out in 7.4.3, it can be stated that the condensation starts at the lower hemisphere of the C[4]RA because this is the only part where at a vapour pressure ratio of $p_r/p_o = 0.1$ condensation is predicted. For the upper hemisphere a required p_r/p_o ratio of 0.36 is predicted for acetone. The swelling of the membrane after the onset of the evaporation can contribute to the reduction of intermolecular spaces thus generating further voids and structures for the micro-condensation.

The above proves successfully, that calixresorcinarane membranes can be employed in an electronic explosion guard type sensor.

7.7 Turn-on response of the CFT with a cast poly-ortho-methoxy aniline membrane

To put the conductivity of the calixarene into perspective, the CFT was cast coated with the undoped POMA, the difficulty of this coating procedure, required the coating of several devices from which the one with the most acceptable coating was selected for the measurement. The thickness was calculated to be 200nm, with a tolerance of at least 20% due to the high inhomogeneity of the film. The turn-on response of the CFT in air was determined to be 1 second, see Figure 11.

It can therefore be inferred that the conductivity of the C[4]RA is lower in comparison to that of the undoped POMA, by more than one order of magnitude. After doping the POMA, in situ, with saturated HCl vapours of for 1 hour, this turn-on response decreased to such extent that no turn-on delay could be any longer observed. The device turn-on behaviour equalled that of a reference device having a complete metal gate.

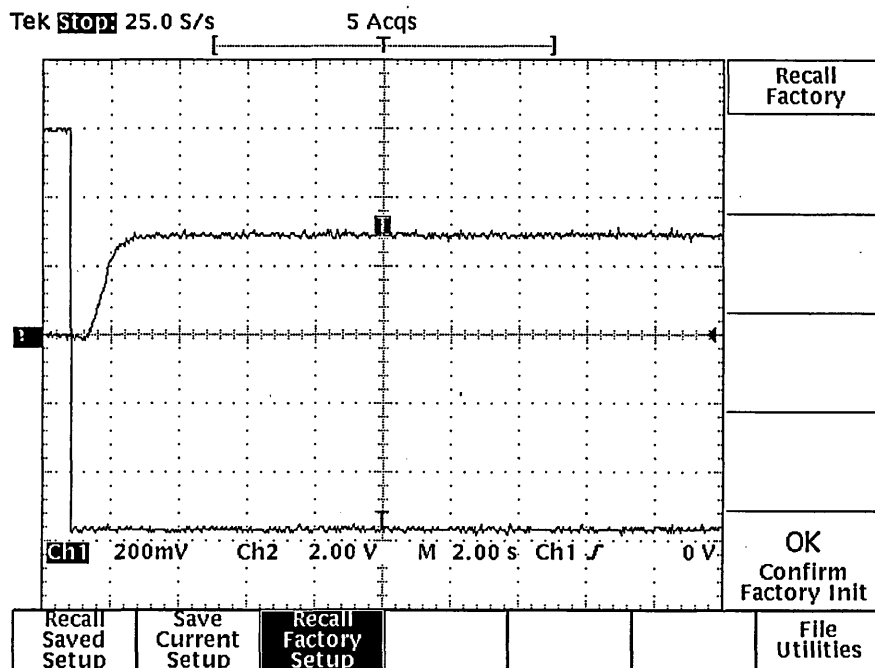


Fig. 11 Turn-on response of undoped POMA

Summary

The novel application of calixarene membranes in a conduction type sensor was demonstrated. The CFT in combination with calixarene membranes can be used for the detection of organic solvent vapours in the concentration range of the lower explosion limit. Usage as a threshold monitor in storage spaces, degreasing stations and processing plants are possible applications. The presented application offers several advantages over existing concepts:

- the immunity to water vapours, due to the hydrophobic nature of the membrane
- no observed poisoning of the membrane as commonly observed for doped SnO_2 (catalytic poisoning)
- no accumulative effects are observed, as are responsible for the baseline drift in QCMs
- no porous metal layer is needed on top of the membrane, whose adhesion is subject to degradation

The reproducible coating of the CFC with membranes of ca. 250 nm thickness remains a challenge. LB deposition is a possible way for providing better control of the thickness and leading to a more reproducible membrane gate contact. The major drawback of this is that the application of hundreds of layers becomes a very lengthy

procedure, depending on the deposition conditions, Chapter 4, this can take up to 18 hours plus additional spreading time.

7.8 References

- [1] R.B. Chaabane, M. Gamoudi, G. Guiland, *Synthetic Metals* 67, 231-233, 1994
- [2] S.M. Sze, *Physics of Semiconductor Devices*, Wiley, 1981, ISBN: 0471056618, Chapter 8
- [3] R.M. Warner, B.L. Grung, *MOSFET Theory and Design*, Oxford University Press, 1999, ISBN: 0195116429
- [4] P. Reinhold, *MOS Feldeffekt Transistoren*, Springer Verlag, 1994, ISBN: 3540558675
- [5] B. Thorstensen: Field effect studies of gas adsorption on oxidised silicon surfaces, Thesis, University of Trondheim Norway, 1981, Report no. SFT 44A81118
- [6] Z. Gergintschew, *Zweidimensionale Simulation, Entwicklung und Optimierung von Gassensoren auf der Basis von Feldeffekttransistoren*, Verlag fuer Wissenschaft und Forschung, 1996, ISBN: 3-930324-88-1, p.7
- [7] I. Lundstroem, M.S. Shivaraman, C.S. Svensson, L. Lundkvist, *Applied. Phys. Letters*, 26, 55-57, 1995
- [8] A. Spetz, M. Armgarth, I. Lundstroem, *Sensors and Actuators B*, 11, 349-365, 1987
- [9] J.F. Ross, I. Robins, B. c. Webb, *Sensors and Actuators B*, 11, 73-90, 1987
- [10] G.J. MacClay, K.W. Jelley, S. Nowrooziesfahani, M. Formosa, *Sensors and Actuators B* 14, 331-348, 1988
- [11] I. Lundstroem, *Sensors and Actuators A*, 56, 75-82, 1996
- [12] F. Winquist, A. Spetz, M. Armgarth, I. Lundstroem, *Sensors and Actuators*, 8, 91-100, 1985
- [13] P.M. Burr, P.D. Jeffery, J.D. Benjamin, M.J. Uren, *Thin Solid Films* 151, 111-113, 1987
- [14] C. Changzhi, L. Sun, T. Zhang, T.Li, X. Zhang, *Thin Solid Films*, 327-329, 383-386, 1998
- [15] L. Sun, C. Gu, k. Wen C. Xizhang et.al., *Thin Solid Films* 210-211, 486-488, 1992
- [16] Siemens Ag, *Gebrauchsmuster*, DE 88G 8525, 1989
- [17] S.D. Senturia , C.M. Sechen and J.A. Wishneusky, *Appl. Phys.Lett.*, 30, 106, 1977
- [18] S.D. Senturia, N.F. Sheppard, S.Y. Poh, H.R. Appelman, *Polymer Engineering and Science* 21, 113-118, 1981

- [19] S.D. Senturia, S.L. Garverick, K. Togashi, *Sensor and Actuator*, 59-71 1981
- [20] P.S. Barker, A.P. Monkman, M.C. Petty, R. Pride, *IEE Proceedings: Circuits, Devices and Systems*, 144, p. 111-116, 1997
- [21] P.S. Barker, B. Di, C. Monkman, A.P. Petty, R. Pride, *Sensors and Actuators B*, B25, 1-3, 451-453, 1995
- [22] P.S. Barker, M.C. Petty, A.P. Monkman, J. McMurdo, M.J. Cook, R. Pride, *Thin Solid Film* 285, 94-97, 1996
- [23] P.S. Barker, A.P. Monkman, M.C. Petty, R. Pride, *Synthetic Metals* 85, 1-3, 1365-1366, 1997
- [24] E.S. Kolesar, J.M. Wiseman, *Analytical Chemistry*, 61, 2355-2361, 1989
- [25] P.S. Barker, *Gas sensing using an organic/silicon hybrid field effect transistor*, Ph.D. Thesis, University of Durham, 1996
- [26] D.R. Lide, *CRC Handbook of Chemistry and Physics*, CRC Press, 1975, ISBN: 0849304784
- [27] N.F. Mott, *Phil. Mag.* 19, 1969, 835
- [28] N.F. Mott, E.A. Davis, *Electronic Processes in Non-Crystalline Materials*, Clarendon Press, 1979, ISBN: 0198512880
- [29] *Surface, interface and Colloids*, D. Meyers, VCH, 1991, ISBN: 1560810335, p. 46-48
- [30] Product Information as taken from the Honeywell Burdick & Jackson catalogue, <http://www.bandj.com/BJProduct/SolProperties/Dipole.html>
- [31] A.V. Nabok, A.K. Hassan, A.K. Ray, *Journal of Materials Chemistry*, 10, 2000, 189-194
- [32] S.J. Gregg, K.S.W. Sing, *Adsorption, Surface Area and Porosity*, Academic Press 1982
- [33] M.M. Dubini, *Prog. Surf. Memb. Sci.*, 1, 97, 1985
- [34] J.J. HacsKayolo, M.D. Levan, *Langmuir*, 1, 97, 1985
- [35] R.J. Lewis, *Hawleys Condensed Chemical Dictionary*, Van Nostrand Reinhold, 1996

8 The detection of organic solvents in water with C[4]RA coated electrodes

8.1 Introduction

Whereas already a variety of applications for calixarene derivatives were found and developed for sensing gaseous analytes, see Chapter 3, only very few studies have dealt so far with the detection of organic species in aqueous environments. Organic pollutants form a major source of contamination in water ^[1, 2]. There are several sources for these organics; the effluents of various production plants of the chemical industry, oil refineries and oil drilling stations. A further, at times catastrophic source is the accidental spillage in and around the transport and storage chain of these materials. The latter can take on tremendous dimensions, as happened in 1998 ^[3], when large areas of central Europe were flooded around the Danube and Rhein. Heating oil storage tanks were damaged resulting in their contents being dispersed throughout the whole waterlogged area. Existing sensors of organic pollutants in water are mostly based on optical or mass sensitive methods. A variety of fibre optic sensors based on different principles as reflectometric interference spectrometry ^[4], evanescent fiberoptic measurements ^[5] or a combination of solid-phase micro-extraction with infrared attenuated total reflection spectroscopic methods ^[6] have been developed. This complex optical system is now available as a prototype device. Further techniques that have been employed are mass sensitive techniques, that are dependent on the precise determination of changes in the resonant frequency of quartz crystal microbalances ^[7], coated with a variety of materials like polymers and calixarenes. Recently the use of bio-tests ^[8] employed the reaction mechanisms of algae and bacteria to pollution. The QCM systems showed some promising potential, whereas the bio-test requires further research and development before it can become a quantitative broad spectrum analytical tool.

In many cases the accumulative effect of the contamination is of interest rather than its exact analytical composition, as for example in the analysis of the flow and diffusion directions of heating oil in the 1998 flooding. For this a broad spectrum sensors is required.

Nabok et al. have shown that the capacitance of a Ta₂O₅ semiconductor electrode coated with LB films of calix[4]resorcinarene in an aqueous solutions, can be controlled by the

presence of small amounts of aniline ^[9]. However, this effect was not studied in detail and results were only obtained for aniline with no other solvents investigated. It is well known that amphiphilic calixarene derivatives are extremely hydrophobic and that their hydrophobicity can be controlled by the presence of small additives of organic solvents to aqueous solutions ^[10].

According to an account from Dr. A. Nabok ^[11] this was demonstrated by Professor C.J. Sterling in a most ingenious way. A cotton wool ball was coated with amphiphilic calixarene and dropped into a water bath, where it floated on the water surface. Upon the addition of an organic solvent to the water, the cotton ball sank into the water.

This principle forms the basis of using calixarene thin films for the detection of organic species in water, with an extension of the analyte range as studied in ^[9] and the development of a model for the analyte membrane interaction.

A more detailed investigation regarding the membrane permeability changes, is carried out in Chapter 9 with the aid of an electrochemical method i.e. cyclic voltammetry. It must be stated that the experimental conditions for these investigations differ from the ones adopted here, to suit the different technique. Among the most influential changes are, the usage of a potentiostat controlled three electrode system, a different electrolyte composition containing a permeability marker, an extended frequency range and a static electrolyte compared to a flowing electrolyte adopted here.

8.2 Experimental details

8.2.1 C[4]RA modified electrodes

The electrodes used were fabricated, by thermally evaporating a seed layer of 3 nm of chromium, followed by a 70 nm thick layer of gold under vacuum onto standard microscope glass-slides (BDH) and coating them with 12 ML of Langmuir Blodgett C[4]RA films. The evaporation rate was about 0.2 nm second⁻¹ for the chromium and 1nm second⁻¹ for gold, the vacuum, which was maintained during the hole evaporation cycle was between 10⁻⁵ and 10⁻⁴ mbar. The metals were of standard semiconductor technology purity. The details for the membrane deposition are given in Chapter 4. Twelve monolayers were chosen, after initial test were conducted with thinner (2 ML) and thicker membranes (20 ML), where the thinner membranes provided a too pronounced permeability and the thicker membranes showed too little response. All the electrodes were used only once, to avoid cross contamination and to allow any

structural changes in the membrane to occur without respect to the history of possible previous changes. All electrodes have a unique structure, with respect to the number of pinholes, molecular arrangement and other defects, despite identical deposition conditions. This required the normalising of the values to the relative basevalue for every electrode. In the case of irreversible changes occurring in the process of an exposure series, values were normalised to the base value directly before the analyte exposure.

8.2.2 Experimental set-up

Figure 1 shows the experimental set-up that was used. The flow chamber was designed by the author and fabricated in house. All pipes and the body of the chamber were made from PTFE to avoid any cross contamination between analytes. The electrodes were mounted beneath the chamber head, as indicated in Figure 1, which was sealed via a rubber O-ring. A spring mechanism applied the required sealing pressure. Care was taken when the spring pressure was adjusted so as not to damage the film. The counter electrode above the C[4]RA coated one, was made of gold wire (1mm diameter) coiled up in the shape of a “snails house” resulting in an electrode surface of ca. 1,2 cm². The effective area of the C[4]RA electrode was 0.45 cm². Both electrodes were separated by about 2.8 cm. Through the chamber a continuous flow of 0.45 l/min of electrolyte was maintained, which was adjusted by the position of manual outlet valves. The recordings were taken with a HP 4284 LCR meter, which was interfaced to a PC and controlled by a program written by the author. The operating mode was set for a parallel circuit measurement, with no biasing voltage applied and the measuring signal amplitude was set to 20mV peak to peak, with the automatic integration interval being set to long. The latter function smoothes the recorded signal. For the exposure scans the measuring frequency was chosen to be 60 Hz. This was in line with the observed frequency dispersion of the system, revealing the most pronounced difference between the coated and uncoated electrode at the lower end of the measuring spectrum of 20 Hz – 1 MHz. Recordings were simultaneously the conductance and capacitance of the working electrode (C[4]RA coated or uncoated), electrolyte, counter electrode system over time. The times when the electrolyte composition was changed, was manually recorded.

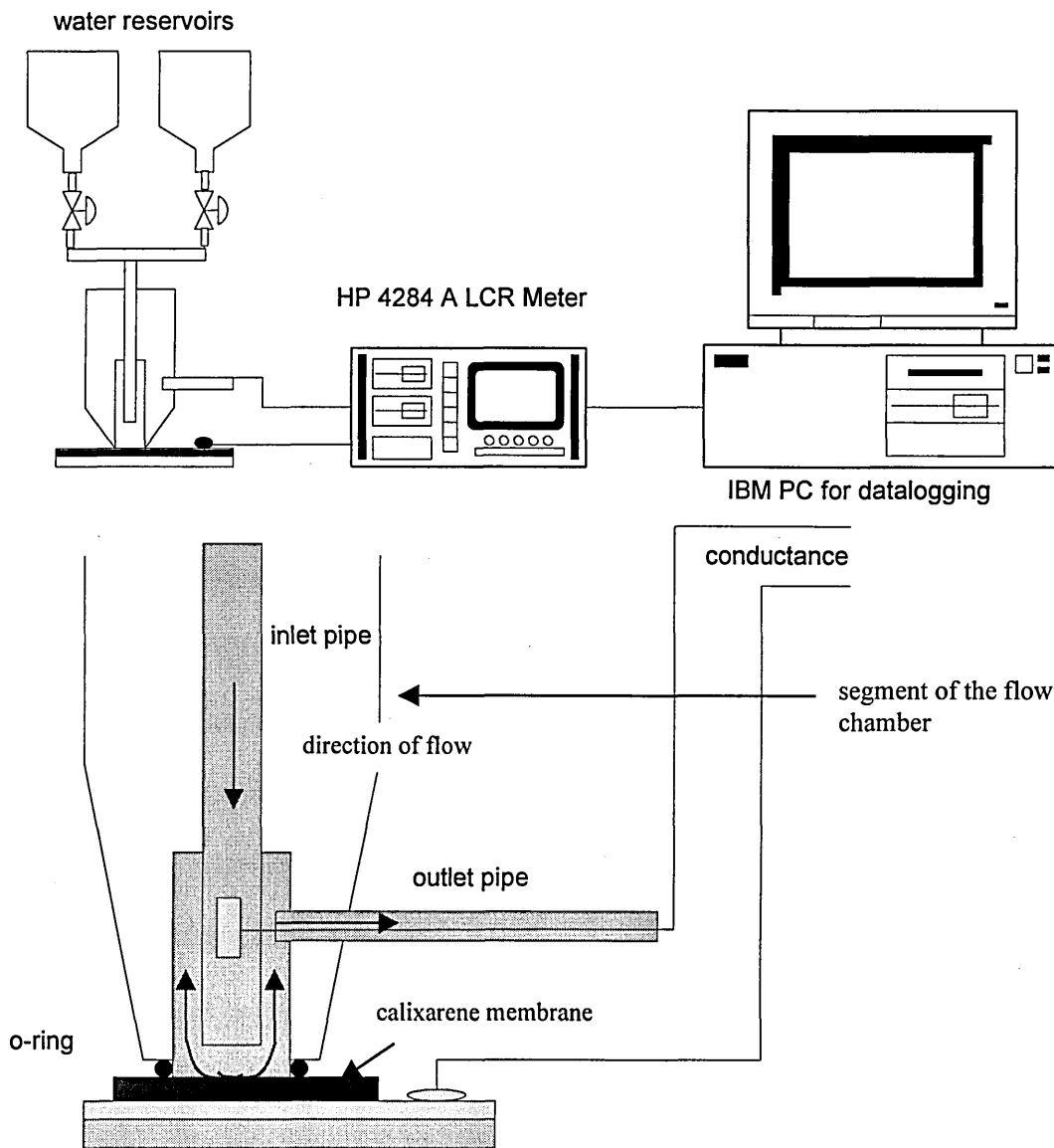


Fig. 1 Experimental set-up and flow chamber

Before every measurement a standard volume of 1 litre of pure electrolyte was flushed through the system to allow for any initial film structure changes, occurring at the first transition from the dry to the wet environment to settle and also for any sodium ion membrane interaction to equilibrate.

8.2.3 Electrolyte composition and preparation

The electrolyte was prepared by dissolving 1g/l NaCl in Millipore water (resistance > 18M Ω) resulting in a concentration of 0.017 mol. Only freshly prepared electrolyte, not

older than 180 minutes, was used and it was kept in a sealed bottle for this period to avoid any contamination through airborne particles. Different organic analytes were mixed into this mother solution, Table 1 gives some of the analytes properties.

Group	Analyte	Formula	Solubility in water in % (by weight)	Density:	MW:
A	Methyl alcohol	CH ₃ OH	miscible with water	0.7924	32.04
A	Acetone	CH ₃ COCH ₃	miscible with water	0.792	58.08
A	Ethanol (ethyl alcohol, grain alcohol)	C ₂ H ₅ OH	miscible with water	0.816	46.07
A	Phenol	C ₆ H ₅ OH	soluble in water	1.07	94.11
B	Aniline	C ₆ H ₅ NH ₂	3.38	1.0235	93.13
B	4methyl2pentanone	(CH ₃) ₂ CHCH ₂ COCH ₃	1.7	0.8042	100.16
B	Chloroform	CHCl ₃	0.8	1.485	119.4
C	Trichloroethylene	CHCl:CCl ₂	0.11	1.456	131.34
C	Benzene	C ₆ H ₆	0.178	0.879	78.12
C	1-Hexane	CH ₃ CH ₂ CH ₂ CH ₂ CH ₂ CH ₃	0.0053	0.6734	84.16
C	Tetrachloroethylene	Cl ₂ C:CCl ₂	0.026	1.625	165.82

Table 1 Selected properties of the analytes investigated

Some of the analytes, those with limited solubility, required a rigorous stirring procedure to produce a homogeneous solution. The solvents were added to the solution, stirred for periods of up to 5 minutes and then sonicated up to 15 minutes in an ultrasonic bath. The solution was then allowed to cool down to room temperature and was inspected with respect to the formation of micelles. Light was shone through the solution, and the mixing procedure was repeated when any light scattering was observed. This test is based on the Tyndall theory ^[12] that particles/micelles with a size of the wavelength of light scatter light. This sets the lower observable particle size to about 350 nm. The electrolyte composition was prepared by mixing the analyte by weight or volume, these concentration values were then converted to the ppm concentration format. All analytes used for the electrolyte preparation were of the analar grade quality.

8.3 Results and discussions

8.3.1 Characterisation of the electrode electrolyte electrode system

The system of the working electrode, electrolyte, counter electrode (WEC) was characterised with respect to the frequency dispersion and the difference that the coating of the C[4]RA LB film has on the working electrode. The conductance and capacitance changes over frequency, for both the coated and uncoated working electrode are shown in the Figure 2 and 3 respectively.

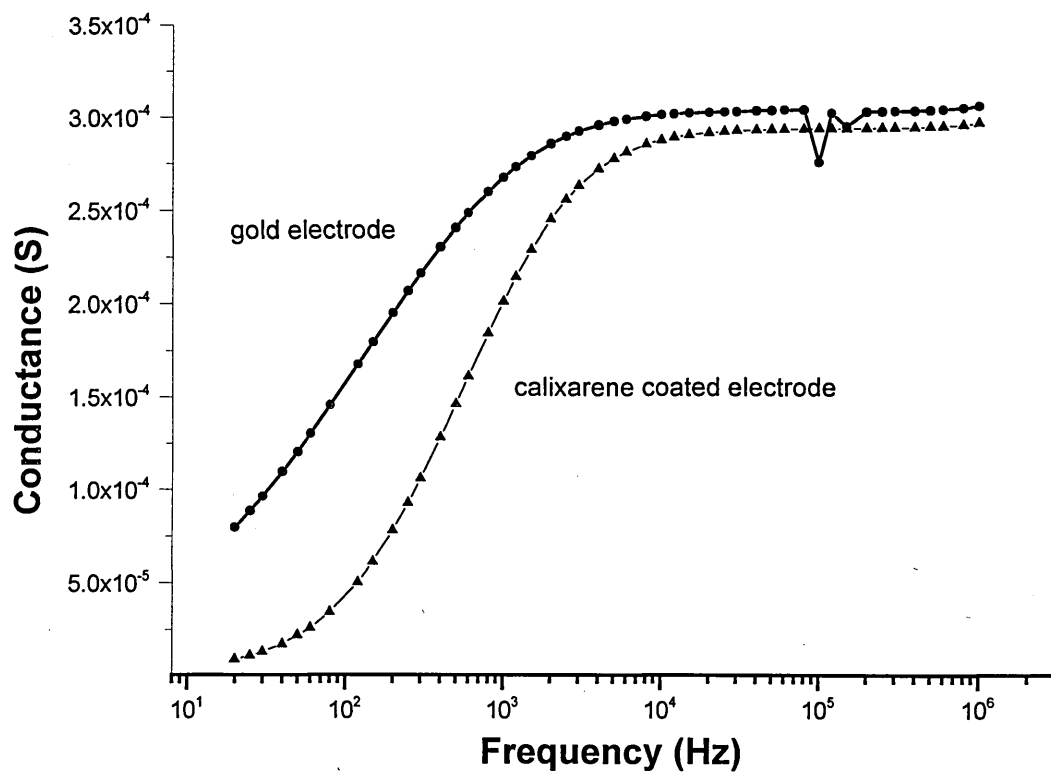


Fig. 2 Conductance changes over frequency for the WEC system with a coated and uncoated working electrode

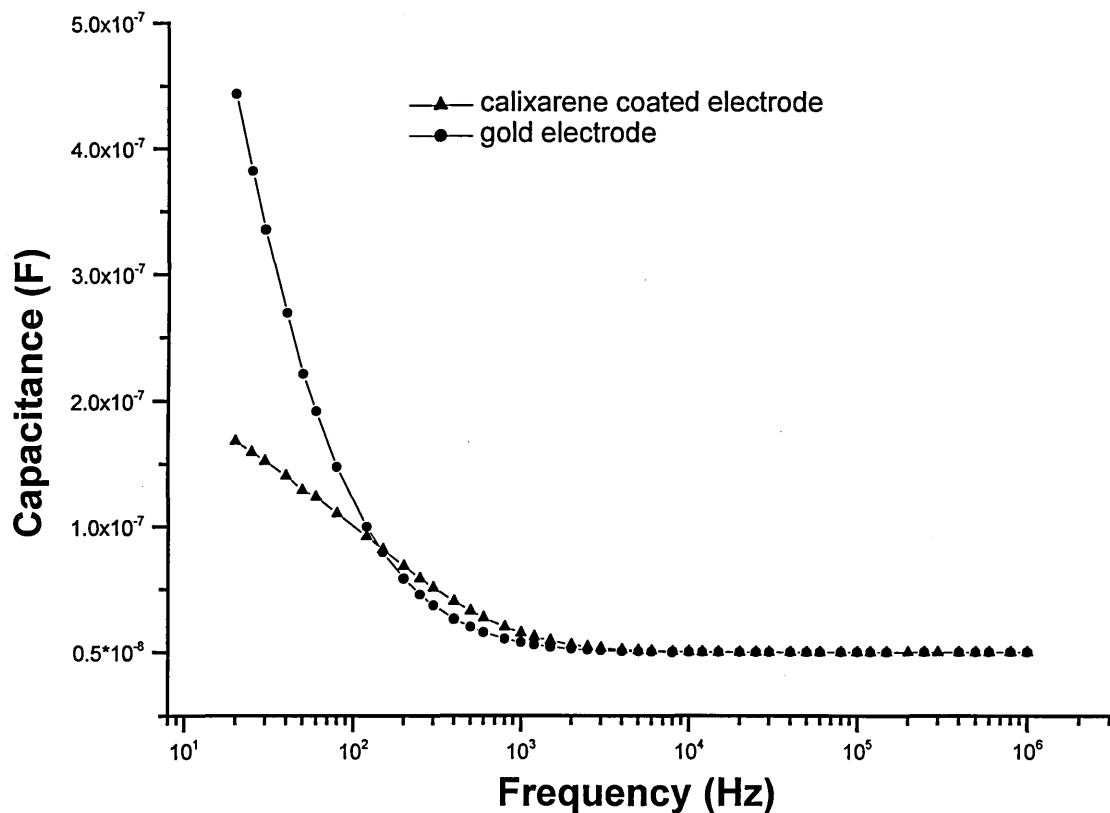


Fig. 3 Capacitance changes over frequency for the WEC system with the coated and uncoated working electrode

The WEC system can be described by the detailed equivalent circuit shown in Figure 4, in the case of the uncoated working electrode C_3 and R_3 become zero.

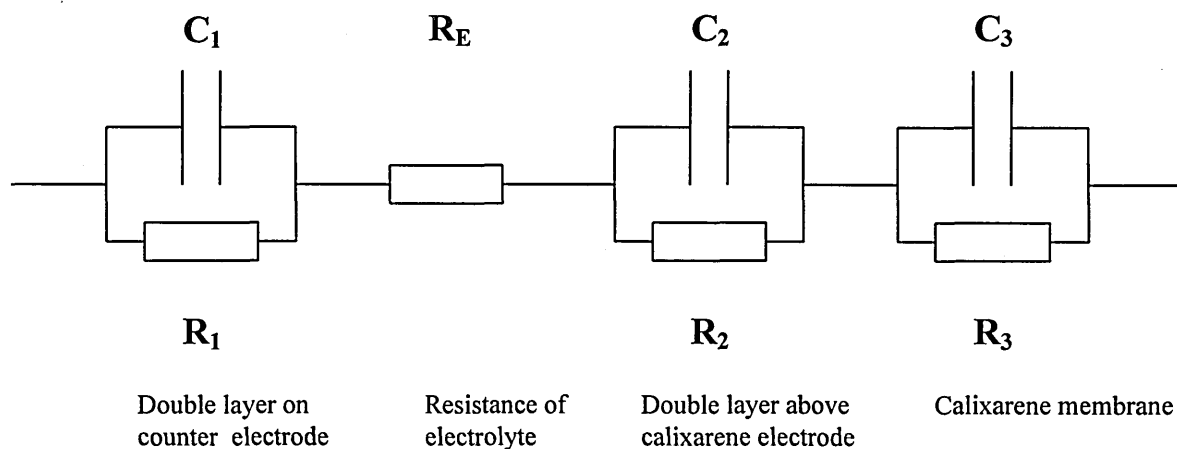


Fig. 4 Detailed equivalent circuit of the coated working electrode electrolyte counter electrode system

The overall impedance of the circuit can be written in the form of (1).

$$Z = \sum_{i=1}^3 \frac{R_i}{1 + j\omega R_i C_i} + R_E \quad (1)$$

The real and imaginary parts can then be separated in the forms of (2) and (3) respectively.

$$\text{Re}(Z) = \sum_{i=1}^3 \frac{R_i}{1 + \omega^2 R_i^2 C_i^2} + R_E \quad (2)$$

$$\text{Im}(Z) = \sum_{i=1}^3 \frac{\omega R_i^2 C_i}{1 - \omega^2 R_i^2 C_i^2} + R_E \quad (3)$$

For a parallel circuit measurement, the conductance G and capacitance C can be given in the form (4),

$$G = \frac{1}{\text{Re}(Z)} \quad \text{and} \quad C = \frac{\omega}{\text{Im}(Z)} \quad (4)$$

with (5) defining Re for the limit of $\omega \rightarrow 0$.

$$\text{Re}(Z) = R_1 + R_2 + R_3 + R_E \quad (7)$$

On the other hand, (6) gives the limit for $\omega \rightarrow \infty$.

$$\frac{1}{C_{total}} = \frac{1}{C_1} + \frac{1}{C_2} + \frac{1}{C_3} \quad (6)$$

Equations (5) and (6) establish the validity of the equivalent circuit. The observed non-linear frequency dependencies of G and C are apparent from Equations (2) and (3). Because of the inclusion of R_E , equation (4) implies that G is higher for the uncoated electrode than the coated electrode. A similar inference can be made about the behaviour of the capacitance.

The proposed detailed equivalent circuit above can be simplified by assuming that not all impedance elements have a significant influence on the impedance spectra. The impedance spectra in the form of Z and Φ over f was calculated from the above (Fig. 2 and 3) and is shown in Figure 5.

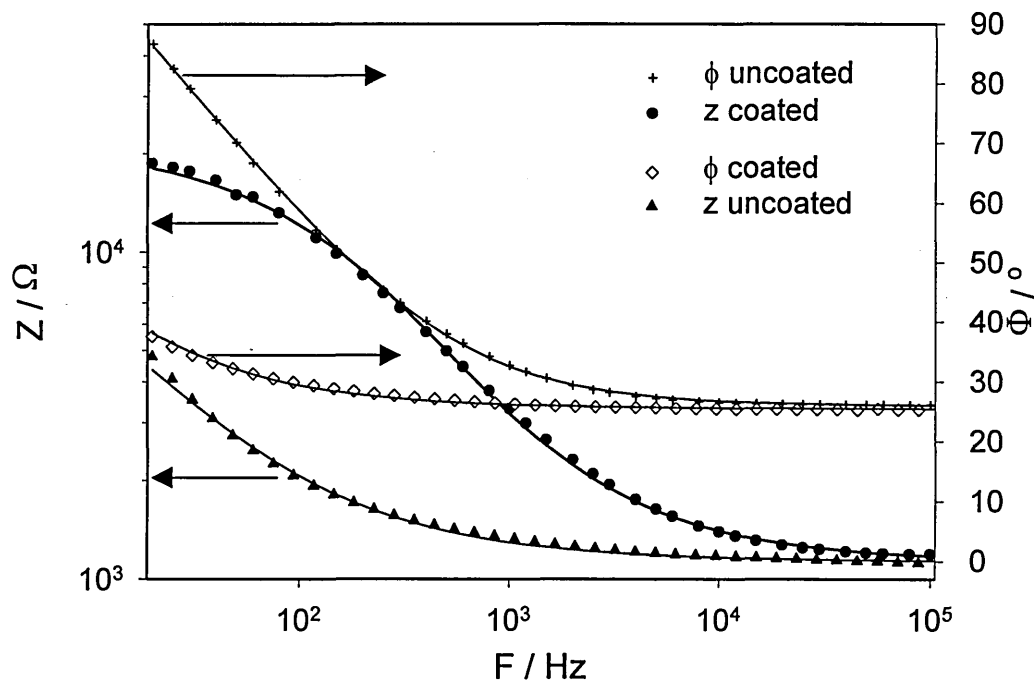


Fig. 5 Bode diagram of the system with coated and uncoated working electrode

For example, the charge transfer resistors R_1 and R_3 are expected to be nearly infinitely large since there are no redox-active species present in the solution, and the double layers of the working and reference electrodes cannot be resolved. Hence, the equivalent circuit can be simplified to the one shown in Figure 6.

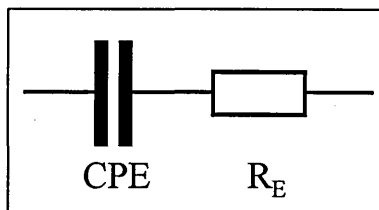


Fig. 6 Simplified equivalent circuit for the WEC system

The resistor represents the resistance of the electrolyte solution between working and counter electrode. The Constant Phase Element (CPE) represents both electrodes. More detailed information about the constant phase element can be found in Chapter 9.

Table 2 shows the results of the mathematical fit. The fairly

Impedance element		uncoated electrode	calixarene coated electrode
Resistance	R_E in $k\Omega$	3.31	3.37
CPE defined as:	Y_o in nF	84.4	9.26
$Z_{CPE} = \frac{1}{(2\pi f Y_o)^\alpha}$	α	0.708	0.778

Table 2 Values derived for the CPE for the different systems under constant flow of electrolyte

large electrolyte resistance dominates the high frequency behaviour, while the capacitive behaviour of the electrode surface and the calixarene film dominates the impedance spectrum at low frequencies. The calixarene film lowers the capacitance of the electrode, i.e. the films appear to be mostly insulating since the nanoporous calixarene matrix restricts the mobility of solvated ions. The proposed simplified model is only an approximation, and does not allow the correlation of the observed conductance changes to any parameter in the CPE, therefore for further discussions the detailed model is considered.

8.3.2 Modulation of the working electrode conductance upon analyte interaction

In order to investigate the response of the working electrode to the analyte, the electrolyte composition was changed with intermittent cycles of “pure” electrolyte between exposures. A constant flow had to be maintained throughout, to avoid any distortion of the results by air bubbles. Some typical exposure responses are presented in the Figures 7 to 10.

The exposure to trichloroethylene, shown in Figure 7, exemplifies the response of the electrode to non or very weakly polar substances. Interaction with the membrane brings about a decrease in the conductance. Sorption and desorption are fast with the sorption being the slightly faster process.

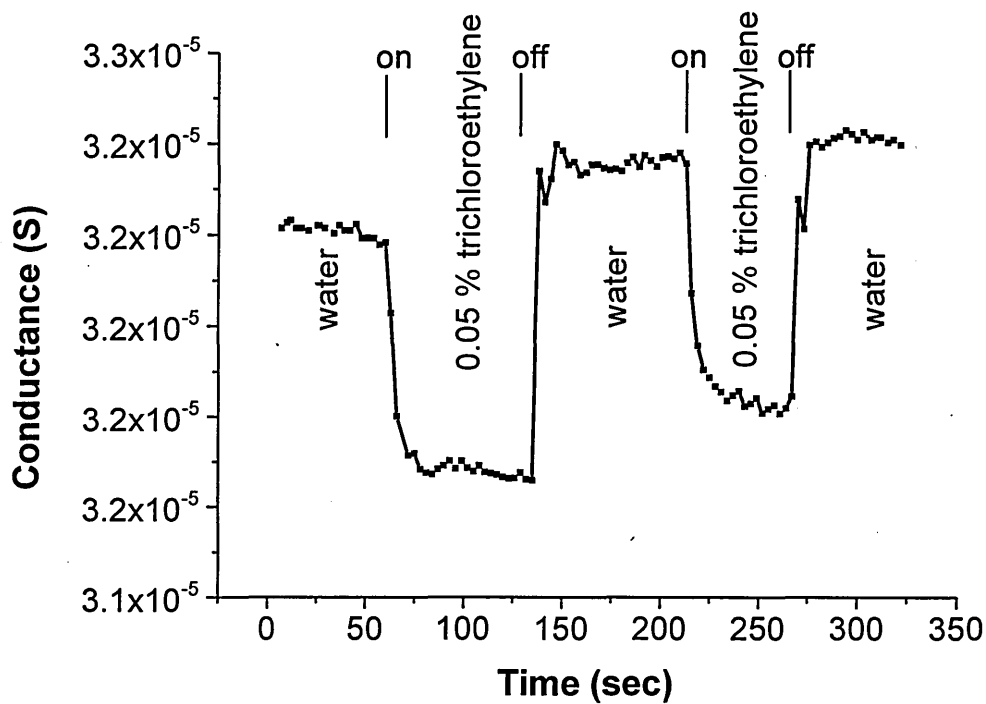


Fig. 7 Electrode response to 100 ppm (0.05%) of trichloroethylene

The group of analytes that have a polar to weakly polar character and whose solubility therefore lies over that of the non polar ones but is still limited to the range of 0.8 % for chloroform and 3.7 % for phenol is represented in the Figures 8 and 9. Phenol is the only analyte that is a solid (powder) at room temperature and it was included in the analysis since its highly toxic nature, makes its detection of particular interest in the monitoring of water qualities. The conductance is increasing with the analyte interaction, the recovery upon flushing is slower than the sorption, most pronounced for the 0.4g/100ml concentration.

As in the case of the phenol interaction the exposure to chloroform increases the conductivity, the response shows a markedly different time constant for the exposure and recovery. The interaction with chloroform highlights one important aspect of the electrode with respect to its stability. When the solubility limit is exceeded, a dramatic increase in the conductivity occurs, most probably due to an irreversible damage in the film. Vesicles of the solvent, which can form at concentration higher than the solubility limit, may dissolve the film partially and this may contribute to the observed increase in conductivity. The strength of the reaction thus depends on the quality of the analyte as a solvent for calixarene. In the case of chloroform this reaction is very strong, even for solutions just exceeding the solubility limit.

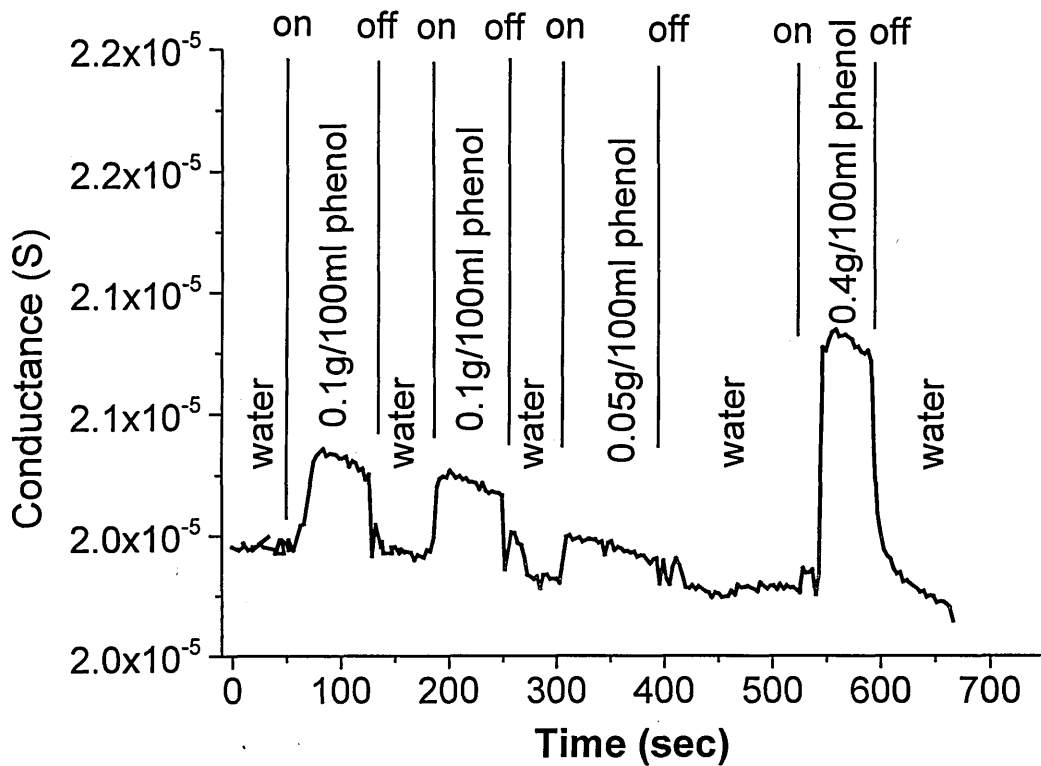


Fig. 8 Phenol exposure series

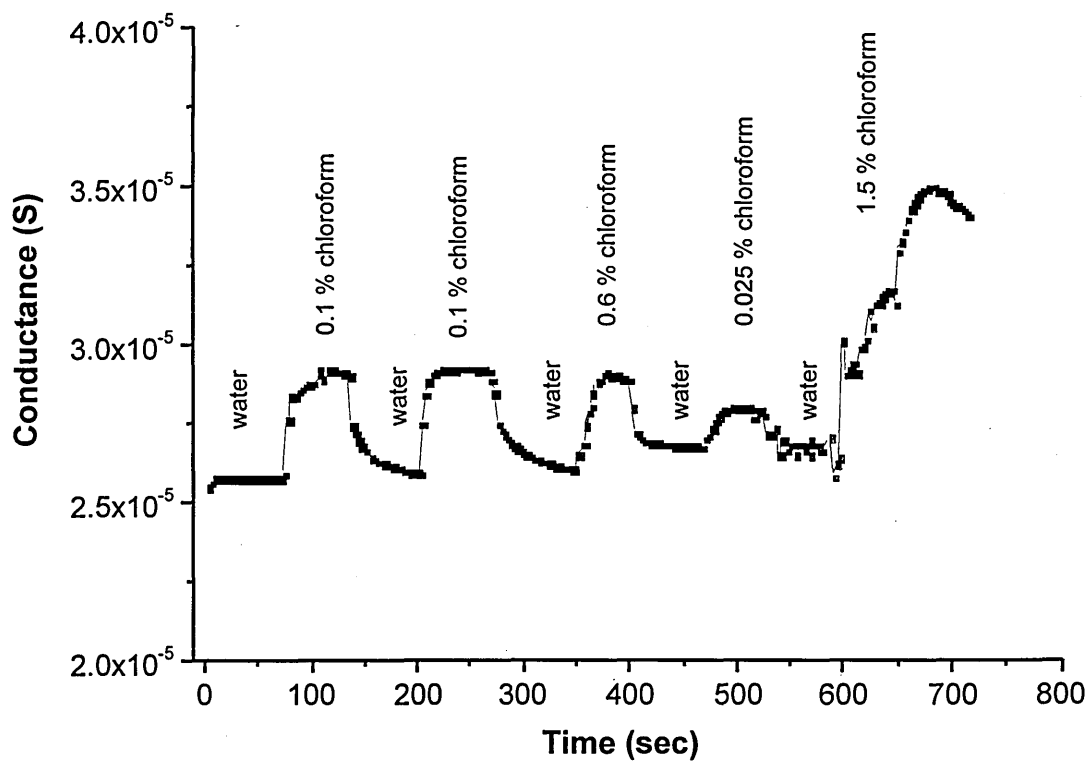


Fig. 9 Chloroform exposure within and above the solubility limit

The third group of analytes consists of organics which have unlimited solubility in water, they are polar and the response to them is exemplified by the response to grain alcohol in Figure 10.

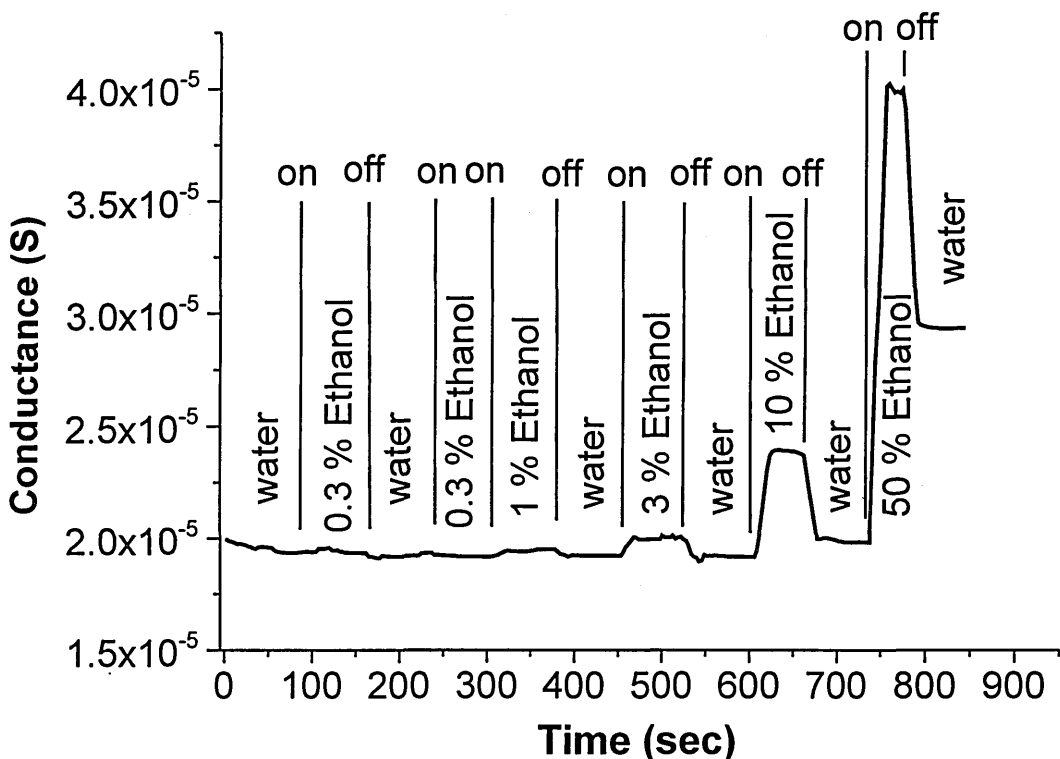


Fig. 10 Exposure series to different concentrations of ethanol

Similar to the behaviour of chloroform and phenol the conductance increases upon analyte membrane interaction. As already observed for higher chloroform concentrations, permanent membrane changes occur for concentrations over 10 %. Since ethanol is a solvent for calixarenes, again partial film removal can be proposed as the responsible mechanism. For concentrations as high as 50 %, it must be said that the electrolyte composition is substantially changed with respect to the sodium ion concentration. This reduces the observed response.

To ensure that the observed responses can be correctly attributed to changes in the coated working electrode and not to changes in the electrolyte resistance or changes at the counter electrode, exposure series were carried out with an uncoated gold working electrode. Figure 11 exemplifies the analyte induced response, showing that there is no specific reaction to the analyte and therefore the changes observed are attributed to the C[4]RA LB film covering the electrode.

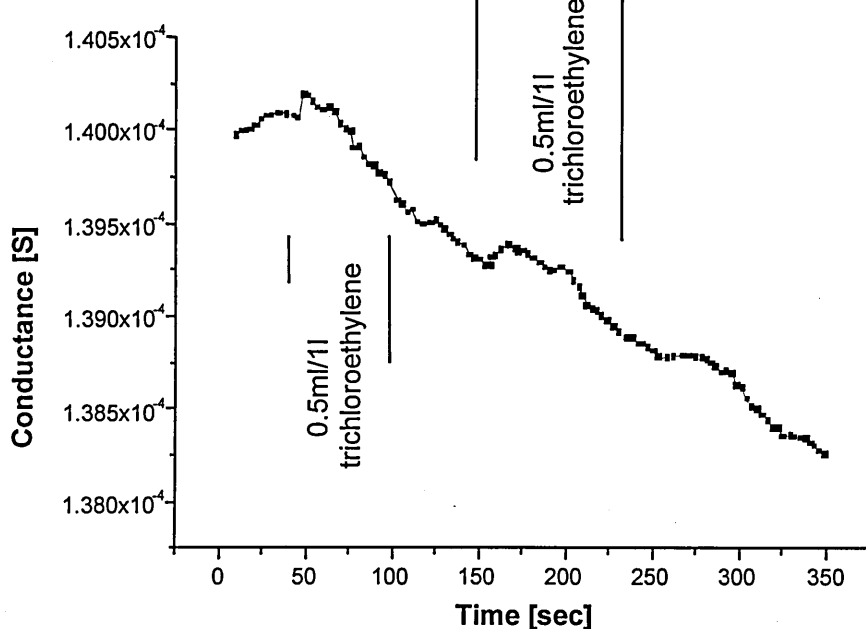


Fig. 11 Response of the CWE system with an uncoated working electrode upon exposure to trichloroethylene

There is some fluctuation in the conductance value, which was also observed for a gold slide with pure electrolyte, Figure 12. The variations observed can be attributed to the dynamic of the constant flow system and further some drift in the baseline.

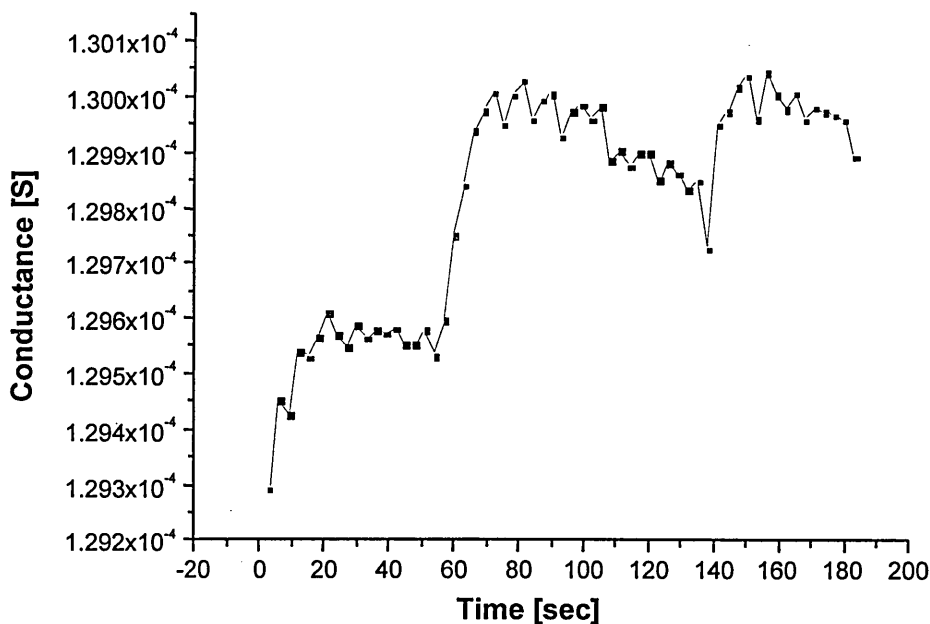


Fig. 12 Fluctuations of the conductance over time of a gold slide in pure electrolyte

Further experiments were carried out (individual plots not shown) the results of which are summarised in Table 3. Though generally the observations follow a the trend of

continuous increase or decrease in conductance, there are some fluctuations of unknown origin in the observed data for chloroform and trichloroethylene.

Analyte	Concentration (ppm)	Changes in conductance (S)	Relative changes in conductance (%)
Methanol	22	negligible	0
	1346	3.00×10^{-7}	1.16
	4497	5.00×10^{-7}	1.86
	13768	7.50×10^{-7}	2.86
Phenol	1	negligible	0
	1028	4.00×10^{-7}	0.98
	2067	2.00×10^{-7}	1.92
	4176	1.05×10^{-6}	5.15
Acetone	1	negligible	0
	246	8.00×10^{-8}	0.3
	1979	7.4×10^{-7}	3.41
	4499	1.42×10^{-6}	6.51
Ethanol	1	negligible	0
	959	5.00×10^{-8}	0.16
	3220	3.10×10^{-7}	1.59
	9860	7.40×10^{-7}	3.7
	35424	4.66×10^{-6}	19.48
	318819	2.09×10^{-5}	51.18
Chloroform	1	negligible	0
	56	1.24×10^{-6}	4.43
	224	3.37×10^{-6}	11.57
	674	2.50×10^{-6}	8.47
	1351	3.00×10^{-6}	10.4
	3409	5.98×10^{-6}	20
Benzene	51	-2.00×10^{-7}	-0.0172
	203	-1.60×10^{-7}	-0.63
Hexane	7	1.20×10^{-7}	0.4
	143	-4.60×10^{-7}	-1.65
	865	-6.00×10^{-6}	-22.7
Tetrachloroethylene	7	6.50×10^{-8}	7.86
4methyl2pentanone	29	6.00×10^{-7}	2.05
	145	1.20×10^{-6}	2.72
Aniline	40	3.50×10^{-6}	9.58
	79	5.00×10^{-6}	13.45
Trichloroethylene	100	-6.00×10^{-7}	-1.83
	200	-3.30×10^{-6}	-9.82
	400	-1.50×10^{-6}	-5.41

Table 3 Summary of various analyte induced changes on the C[4]RA LB coated working electrode

In Figure 13 a selection of some modulations of the relative conductance changes are plotted over the investigated concentration range. These plots are highlighting the

discrimination between polar and nonpolar analytes by positive or negative conductance changes.

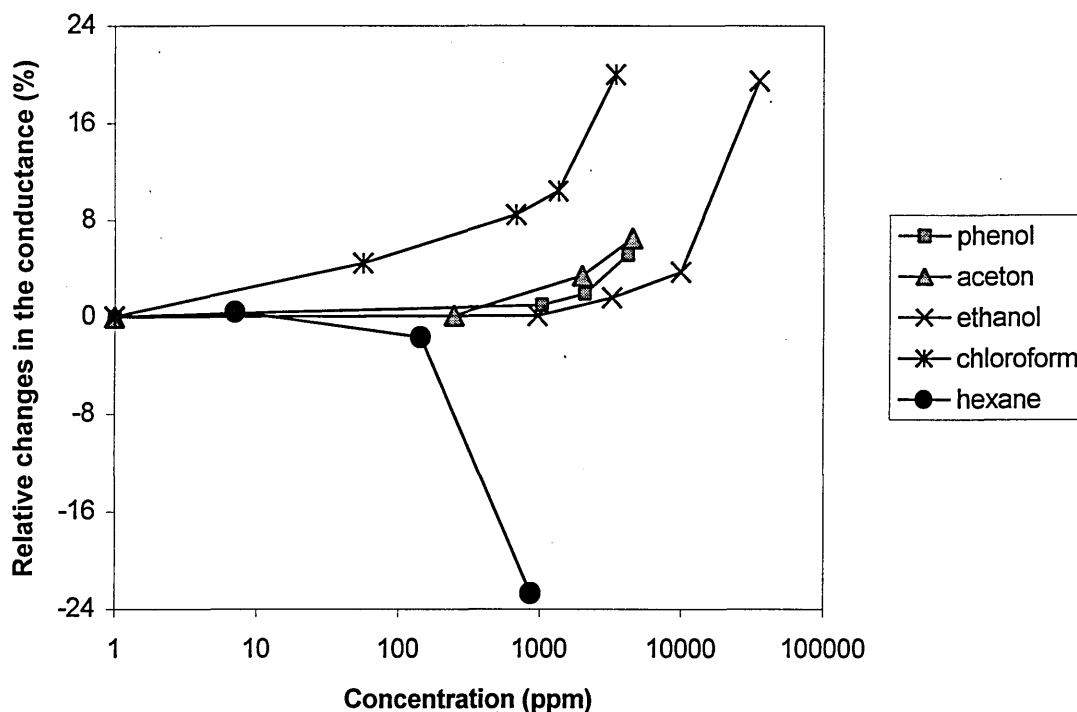


Fig. 13 Analyte responses in terms of relative conductance changes, plotted for selected compounds from Table 3

8.3.3 Discussion of the analyte C[4]RA membrane interaction

As indicated in Table 1, the analytes under investigation can be classified into three separate groups depending on their solubility in water and polarity. The first group A, comprises analytes which are infinitely miscible with water and are strongly polar. The conductivity of the membrane is increased upon analyte interaction. The next group B comprises aniline, chloroform and 4methyl2pentanone which are soluble in water by a factor of between 0.8 and 3.1 % by volume, these molecules still possess a polar character. Similar to group A, the presence of these compounds increases the electrical conductivity. However, when the solubility limit is exceeded, a permanent increase in the conductivity occurs. This is most probably due to an irreversible damage of the membrane coverage on the gold electrode. Vesicles of the solvent, which form at this concentration, may dissolve the film partially contributing to the observed increase in conductivity. The strength of the reaction thus depends on the quality of the analyte as a solvent for the calixresorcinarane. The analytes with very low water solubility, for example benzene, hexane and trichloroethylene, belong to the third group C. These

compounds are either non polar or very weakly polar. As highlighted in Figure 11, their induced response is opposite to that displayed by the polar molecules, thus decreasing the conductivity.

Mechanisms contributing to the membrane changes

With the absence of any redox active species in the electrolyte and the measuring voltage below the oxidising or reducing potential of the membrane, the measured increase in the conductance can not be simply attributed to the increase in the charge transfer through the electrolyte. There are several mechanisms contributing to the increased conductance:

- The permeability of the membrane changes, this lets the coated electrode behave more like the uncoated one (This point is investigated in detail in Chapter 9). In terms of the detailed equivalent circuit this influences the values C_2, C_3, R_2 and R_3 .
- The accumulation of the species in the membrane changes its dielectric constant, changing C_3 and R_3 .
- Organic species on the top of electrode compete with the conventional double layer formed by the sodium cations, modifying C_2 and R_2 .
- A modulation of the π electrons network in the C[4]RA basket can change its conductance, which is represented by R_3

It is believed that the permeability changes are dominating the observed effects. It is therefore proposed that the difference in the direction of the conductivity changes are stemming from the changes in the hydrophobicity of the membrane. Upon complexing with polar molecules the permeability is increased whereas the complexation with non polar molecules increases the hydrophobicity. That organic species complex in calixarene membranes in aquatic environments, was unequivocally shown with the aid of nuclear magnetic resonance studies in reference ^[13].

Summary

A sensing system consisting of gold coated microscope slides covered with Langmuir Blodgett C[4]RA films, was characterised and a detailed and simplified equivalent circuit model was derived. The working electrode allowed the discrimination between polar and non polar species in water, covering a concentration range up to the solubility

limit, at which point the membrane is etched away. The relation between the analyte concentration and the observed conductivity increase/decrease is non-linear for the analysed species. The system offers the possibility to be integrated into a dipstick like, one shot sensor as a broad spectrum sensor determining the overall content of organic solvents in water. Of particular interest is that the system response to phenol and hexane, with the latter being a major component in fuels.

8.4 References

- [¹] Organic pollutants in water: sampling, analysis and toxicity testing, I.H. Suffet, M. Malaiyandi, American Chemical Society, 1987, ISBN: 0841209510
- [²] Industrial water pollution control, W. W. Eckenfelder, McGraw-Hill, 1989, ISBN: 007018903X
- [³] Report of the European Environment Agency, No. 16,
http://reports.eea.eu.int/Environmental_issue_series_16/en/envissue16.pdf
- [⁴] H.M Yan, G. Kraus, G. Gauglitz, *Analytica Chimica Acta*, V. 1.312, 1, p.1-8, 1995
- [⁵] D.S. Blair, L.W. Burgess, A.M. Brodsky, *Analytical Chemistry*, V.69, 13, p.2238-2246, 1997
- [⁶] H.M. Yan, G. Kraus, G. Gauglitz, *Analytica Chimica Acta*, V.312, 1, p.1-8, 1995
- [⁷] S. Rosler, R. Lucklum, R. Borngraber, J. Hartmann., P. Hauptmann, *Sensors & Actuators B*, Vol.48, 1-3, p.415- 424, 1998
- [⁸] P. Schmitz; F. Krebs; U. Irmer, Proceedings of the international conference on rehabilitation of the river Rhine; MAR 15-19, Arnheim, Netherlands, 1993
- [⁹] A.V.Nabok, N.V. Lavrik, Z.I. Kazantseva, B.A. Nesterenko, L.N. Markovski, V.I. Kalchenko, A.N. Shivaniuk, Conference Proceedings of LB 9, Ancona, Italy , 1995, P1.2
- [¹⁰] F. Davis, and C. J. M Stirling , U.K. Patent. No. 9607886.0
- [¹¹] Dr. Aleksey Nabok, Sheffield Hallam University, Sheffield S1 1WB, Pond Street, A.Nabok@shu.ac.uk, referring to a "Calixarene" Seminar at the Sheffield University in 1998 organised by C.J.M. Stirling
- [¹²] The Tyndall, or better Faraday-Tyndall effect, was proposed and used by both scientists but first proven by H.F.W. Siedentopf, R. Zsigmondy, *Annalen der Physik*, Leipzig, 10, 1-39, 1903
- [¹³] G. Arena, A. Casnati, A. Contino, D. Sciotto, R. Ungaro, *Tetrahedron Letters* Vol 38, 26, pp. 4685-4688, 1997

9 Detailed permeability studies on the LB C[4]RA membrane

The results of the previous chapter strongly suggested that the permeability of the LB membrane is modulated by the presence of organic analytes. In this chapter, these permeability modulations are investigated in detail, mainly with the aid of an electroactive permeability marker, employing cyclic voltammetry, impedance spectroscopy and SPR. The permeability of the membrane is correlated to the oxidising and/or reducing current that is flowing when the permeability marker undergoes oxidation and/or reduction.

Permeability control of membranes can be found in a most sophisticated way in biomembranes, controlling the molecular exchange on a cellular level. These most intriguing systems have been comprehensively studied for artificial [1-5] and biological systems [6-9]. As far as the artificial systems are concerned, channel mimetic sensing membranes of orientated layers of valinomycin and anionic phospholipid [1, 2], macrocyclic polyamine [3] and cyclodextrine [5] were investigated. Similarly biological membranes of polypeptides [10, 11] and DNA [12, 13] were investigated. Monolayers of substituted calixarene esters, at the air water interface and on carbon electrodes, have shown to possess the quality of changing their permeability on complexation with alkali metal ions [14]. This study revealed that depending on the nature of the permeability marker, cationic, anionic or neutral varying effects can be obtained.

9.1 Cyclic voltammetry

Voltammetry is an amperometric electrochemical analyse technique, that is widely applied for the detection of analytes in solution which undergo electrolysis [15, 16]. Cyclic voltammetry is very similar to linear sweep voltammetry, the major difference is that the voltage is swept in a cyclic mode between two values. The following describes the very basics of this technique, using the frequently cited example of the redox reaction of the $\text{Fe}^{3+}/\text{Fe}^{2+}$ ion pair. The potential of the working electrode is swept over time between V_1 and V_2 as shown in Figure 1.

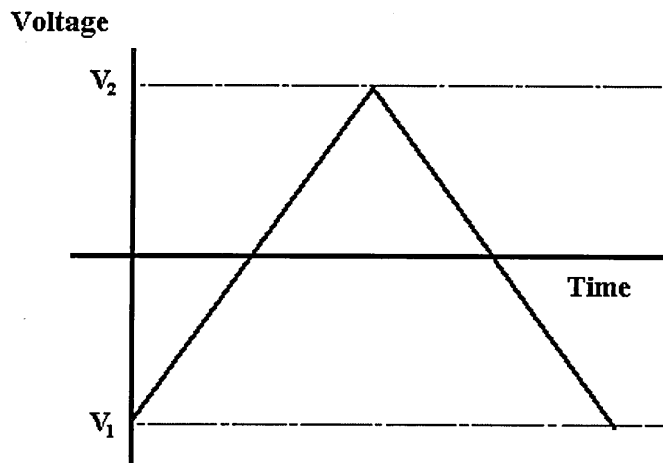


Fig.1 Cyclic voltage sweep of the working electrode

This results in the corresponding voltammogram, Figure 2, which shows the current over the electrode potential.

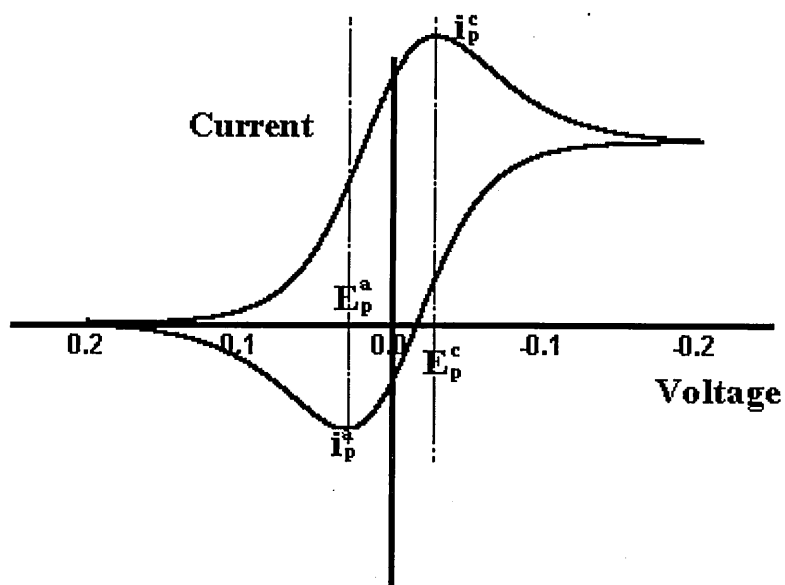


Fig. 2 Cyclic voltammogram of the Fe^{3+}/Fe^{2+} ion pair ^[16]

The forward sweep from 0.2 V to -0.2 V (V_1 to V_2) oxidises the Fe^{2+} species in the solution according to (1).



This transfer of charge, corresponds to the current peak i_p^c , on reversing the voltage back to 0.2 V, the Fe^{3+} is reduced back to Fe^{2+} according to (2).



The reduction current corresponds to the trough i_p^a . The electron transfer takes place at the electrode and its dynamic depends on the scan rate and the concentration of the species undergoing electrolysis. Increasing the concentration and the scan rate increases the current flow. A membrane covering the electrode with a modulated permeability for the marker leads in turn to a modulated current.

9.1.1 Potentiostat controlled three electrode system

All measurements employing amperometric techniques, require the use of a potentiostat controlled three electrode system. The function and workings of a potentiostat in a three electrode system are not immediately obvious. The following explanation highlights the principle of operation and shows why its use is required. Detailed technical aspects and an advanced theoretical treatment regarding potentiostats can be found in reference [17].

For a two electrode system with no DC current flowing, the applied voltage E is split, equally or unequally, between the two electric double layers forming on top of the electrodes. There exists no voltage across the bulk of the solution. The potential gradients for such a system are shown in Figure 3a. Appropriate design measures in the construction of the counter electrode, like a large area to minimise the current density and selecting a material that establishes a fixed half cell potential with the electrolyte, like colomel with chloride ions in the electrolyte, makes it possible to keep the potential Φ_c constant.

If the potential at the working electrode is exceeding the one required for the oxidation or reduction of the electroactive species, the resultant current flowing across the solution, is giving rise to a voltage drop across the solution resistance. This voltage drop ϕ_s across the solution causes the potential ϕ_w to be reduced since ϕ_c and E remain constant. The potential gradients for this case are given by Figure 3b. In its extreme case ϕ_w changes so much, that the oxidation or reduction stops, which reduces the voltage drop across the solution to zero and ϕ_w starts then to oscillate. This process is shown

schematically in Figure 4. To maintain a constant potential ϕ_w , E has to be increased to E_c , as shown in Figure 3c. Since any variation in E is also changing the voltage drop across the solution, controlling ϕ_w is very indirect and leaves a rather large unknown potential ϕ_s in the feedback loop.

In a two electrode system the counter electrode fulfils thus two functions, it completes the circuit allowing a charge transfer across the cell and it is supposed to keep a constant interfacial potential.

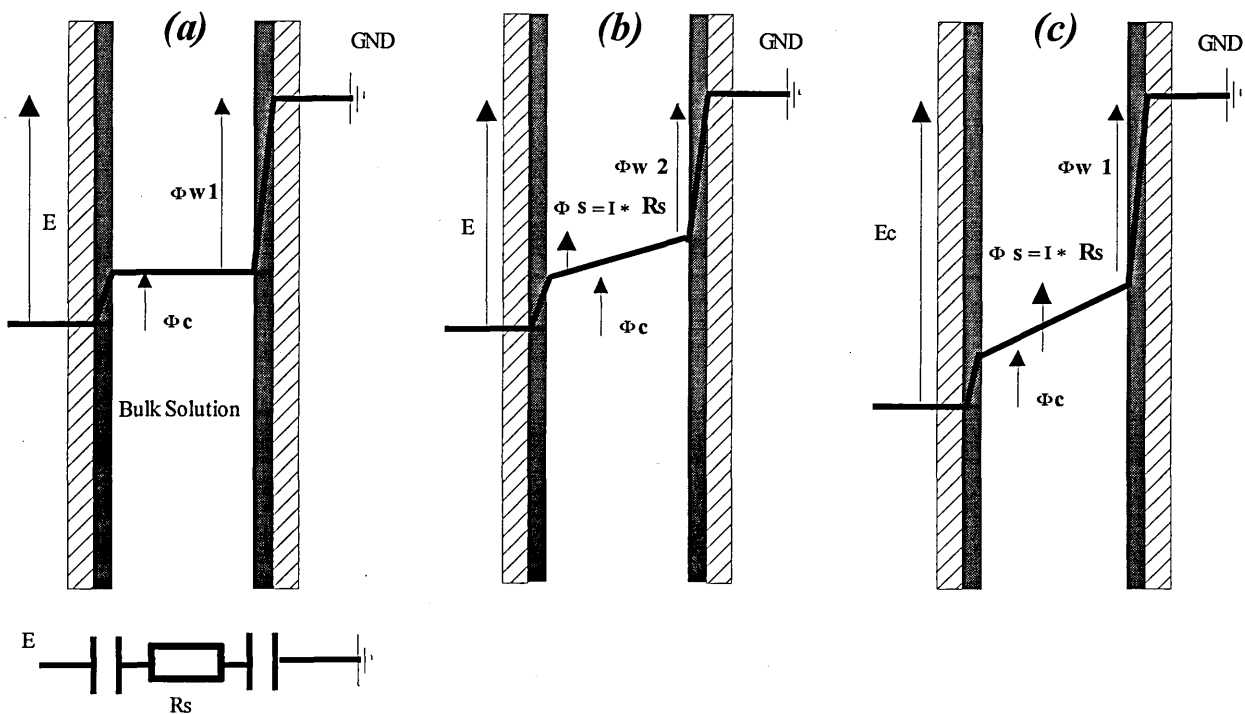


Fig. 3a, 3b, 3c Electrode potentials in a two electrode system with and without DC current flowing

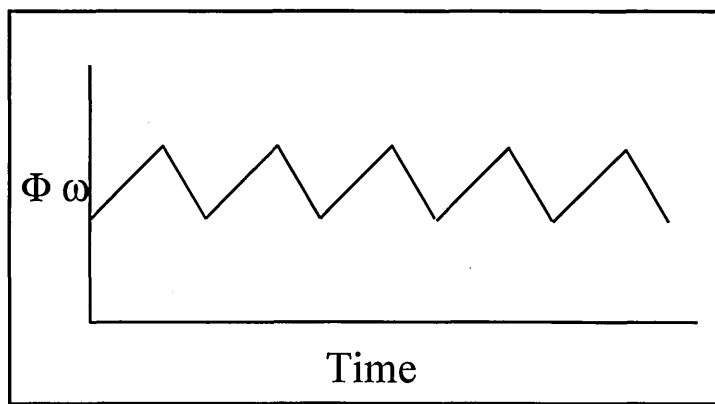


Fig. 4 Schematic representation of the variation in ϕ_w over time in an uncontrolled two electrode system

A potentiostat with its three electrode system splits these two functions between the counter and reference electrode. A schematic of a primitive three electrode system is given in Figure 5, which also represents the electrode arrangement used.

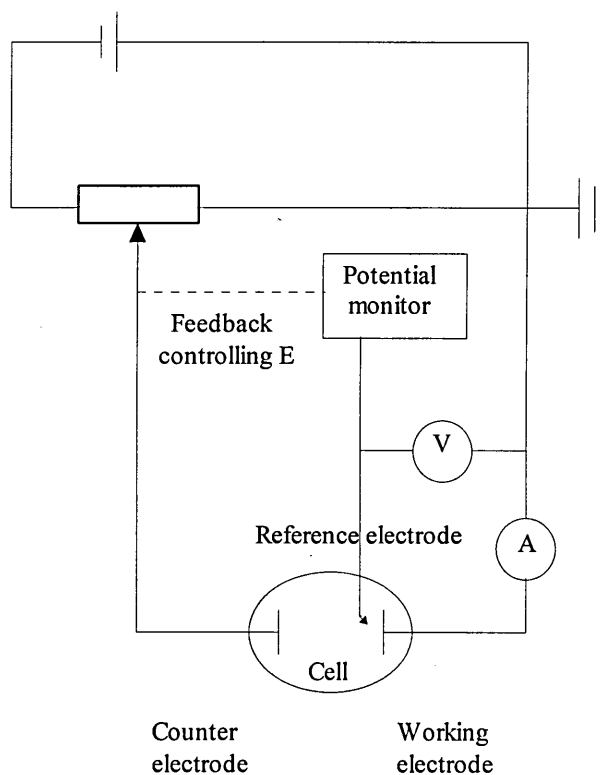


Fig. 5 Electrode arrangement and schematic of a primitive potentiostat

The reference electrode is used as a potentiometric probe to measure ϕ_w with respect to its own potential ϕ_r . The potential ϕ_r is established by the half cell potential of the electrode according to the chemical equilibrium reaction taking place at it. Any current drawn from the reference electrode would alter ϕ_r , therefore a zero current measurement must be used. This is nowadays virtually achieved with the aid of extremely high input resistance operational amplifiers. Figure 6a shows the potential gradients in a three electrode system, with no DC current flowing and in 6b when there is a flow of direct current across the electrolyte.

Since the position of the reference electrode is much closer to the working electrode than the counter electrode, the voltage drop across the solution, given by $I \cdot R_{s2}$ is also smaller than the drop across the whole of the solution, given by $I \cdot (R_{s1} + R_{s2})$. By constantly comparing the potential of $\phi_r + I \cdot R_{s2} + \theta_w$ with a reference and adjusting the

voltage E applied to the cell, ϕ_w is kept constant independent of ϕ_c and with a much reduced influence of any voltage drop across the solution.

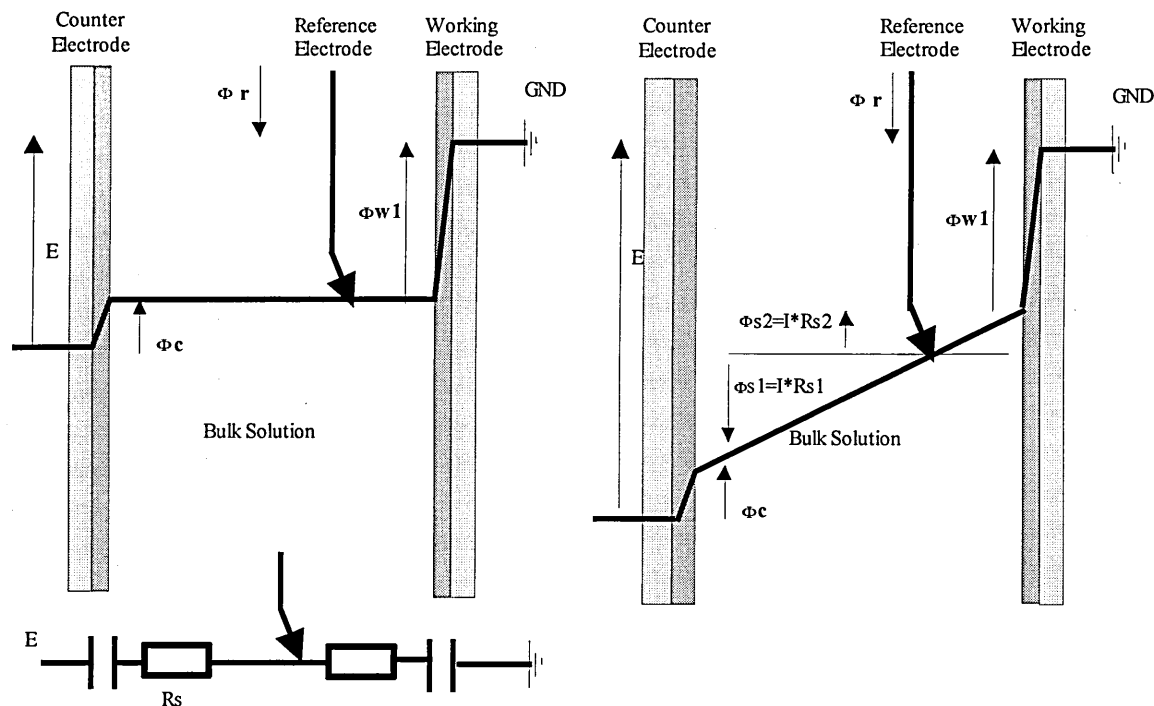
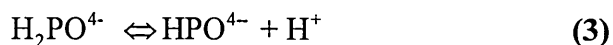


Fig. 6a, 6b Electrode potentials for a potentiostat controlled three electrode system

9.1.2 Experimental details

The neutral electroactive hydroquinone (HQ) was used as the permeability marker to avoid complications with electrostatic repulsion. The redox reaction of the hydroquinone is pH dependent, therefore a buffer is required to keep the pH of the electrolyte constant. The buffer consisted of a phosphoric acid NaH_2PO_4 and its conjugated base Na_2HPO_4 , the equilibrium reaction of interest stabilising the pH is given by (3).



The concentrations of the acid and its conjugated base determine the pH value, with a pH of 6.4 a slightly acidic character of the electrolyte was chosen. The background electrolyte concentration was 0.1 M NaCl.

In Figure 7 is shown the principle of the redox reaction for the hydroquinone.

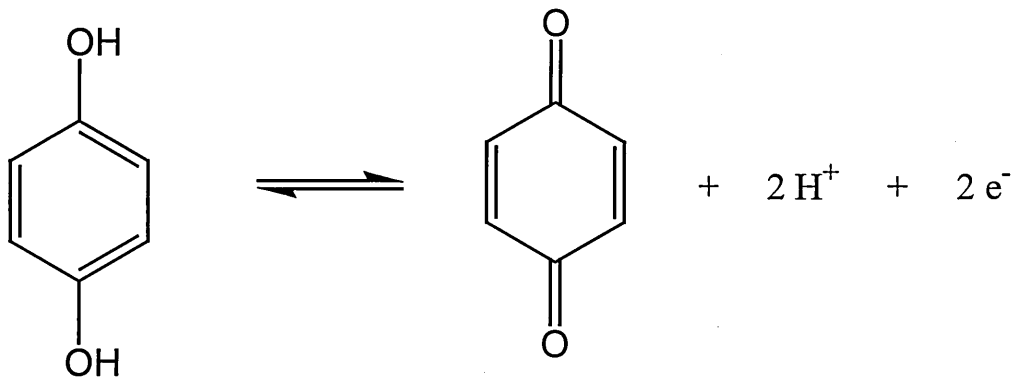
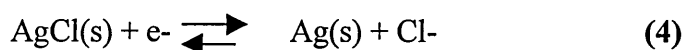


Fig. 7 Redox reaction of hydroquinone

For the third electrode needed by the potentiostat, a silver-silver chloride (Ag | AgCl) reference electrode was used. The equilibrium reaction that establishes the potential of the Ag | AgCl is given by (4),



the chloride ion stems from the electrolyte. The potential that the electrode in solution assumes, is dependent on the concentration of the Cl^- . It is quantitatively related to the standard potential for a 1 mol concentration (E_0) of chloride ions, by the Nerst equation (5). n denotes the number of electrons transferred in the reaction and E_0 is 0.222V for AgCl.

$$E = E_0 - \frac{0.05916}{n} \cdot \log \text{Cl}^- \quad (5)$$

The used 0.1 M concentration establishes according to (5) a half cell potential E of -0.013V, with respect to the hydrogen electrode, a standard against all others half cell potentials are measured.

The measurements were performed using an Autolab potentiostat PG STAT 10 connected and controlled by a computer running the software package General Purpose Electrochemical Systems (GPES) 4.7. The Ag | AgCl electrode was fabricated by preanodising a 0.25 mm diameter silver wire in a saturated NaCl solution at 3 V for 1 minute. For the electrolyte 5.844 g/l NaCl was dissolved in Millipore water giving a 0.1

M solution. To this was added the buffer consisting of 0.00528 M Na₂HPO₄ (7.5 g/l) and 0.01 M NaH₂PO₄ (2.02 g/l), buffering the electrolyte to pH 6.4, as confirmed by a pH electrode measurement. This formed the mother solution to which the permeability marker hydroquinone was added to give a concentration of 10mM (1.1g/l). The solution was vigorously mixed and when analyte was added to it, the solution was sonicated until a micelle free solution was obtained.

The potential scan rate for the cyclic voltammograms was set to 50 mV/s, each scan was started from 0 V and underwent 2 complete scans of which the last one was recorded and evaluated. The cyclic voltammograms (CVs) were analysed on the basis of the redox current peak heights, with respect to a baseline. This baseline was drawn, to follow the most linear part of the background scan without any analyte present. All the voltages cited and plotted are with respect to the potential of the Ag | AgCl electrode. A volume of 200 ml of electrolyte solution was flushed through the chamber and a settling time of ten minutes was allowed before each measurement was undertaken under static flow conditions. The used LB calixresorcinarene coated electrodes were prepared as described in Chapter 8.

9.1.3 Results and discussion

A cyclic voltammogram of an uncoated gold electrode in the buffered solution, containing no marker, results in a nearly linear increase of the current with respect to the voltage, Figure 8. This current is the result of the charging of the electrode. The electrode forms one part of a parallel plate capacitor, the opposite plate consisting of the charged species, Na⁺ or Cl⁻ ions, migrating to it under the influence of the applied field. This is commonly termed the electric double layer. The slight hysteresis for the up and down sweep, is based on a certain affinity of the ions for the Au electrode, and a competing action of charged species for the same place when the polarity of the electrode changes. The magnitude of the current at $6 \cdot 10^{-7}$ A so small that for any further considerations its contribution to the CV is neglected.

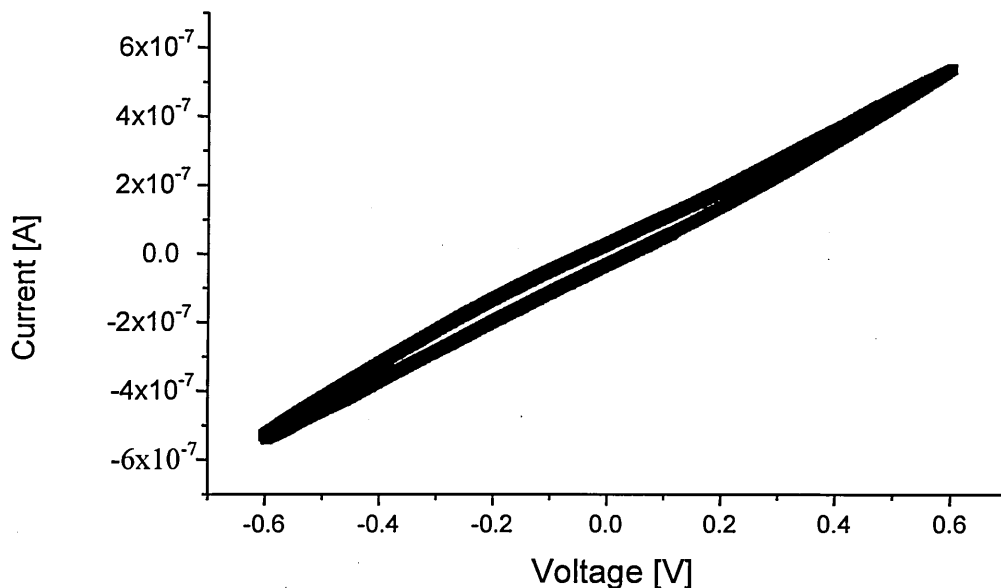


Fig. 8 CV of a gold electrode in buffered NaCl electrolyte

The CV of the calixarene coated electrode in the buffered solution, without the marker, shows a markedly different form, Figure 9. Whereas the voltage forward sweep to the first vortex potential has a shallow slope, indicating a capacitive current, its magnitude is about 10 times higher, then that for the uncoated electrode. For the reverse sweep there is a rather steep increase in the current, at voltages below -0.15 V, it is believed that this is due to some reducing action on the membrane. When the voltage sweep window is reduced to -0.15 to $+0.6$ V (as shown in the inset of Figure 9) the current follows the voltage sweep with a near linear current increase, indicating again capacitive behaviour, and perfect stability.

Figure 10 shows the CV of the hydroquinone on an uncoated gold electrode. The current flow due to the oxidation of the hydroquinone peaks at $+0.22$ V and the current flowing for the reduction peaks at -0.11 V. For a diffusion controlled reversible reaction, redox peaks would be expected to show a $59/n$ mV separation according to (6)^[18], with n being the number of electrons that are transferred during the redox process. The found separation of 0.33 V is larger than expected.

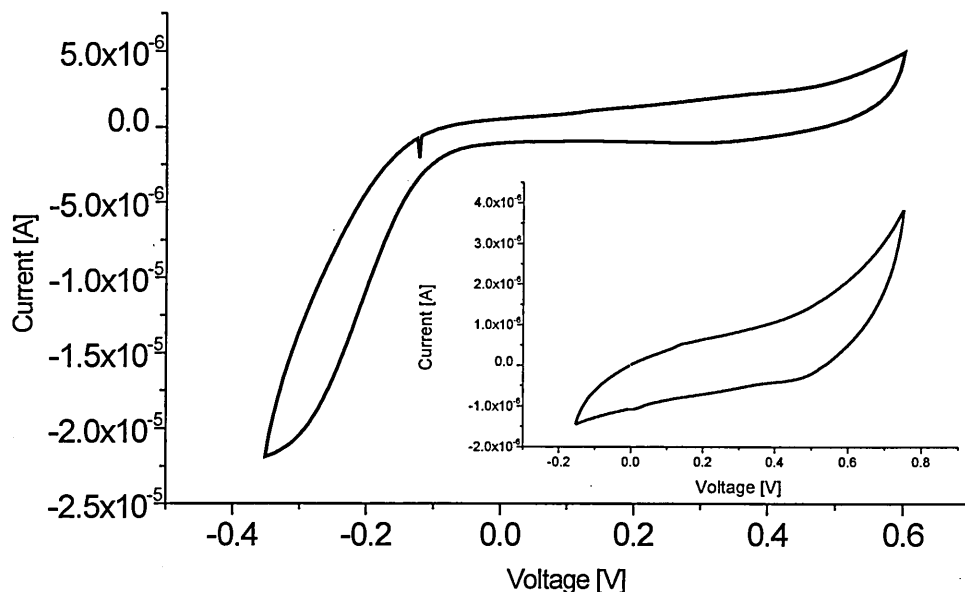


Fig. 9 CV of C[4]RA coated membrane in buffered electrolyte, for two different voltage ranges, with the inset showing the CV over the linear voltage range

$$\Delta E = E_p^a - E_p^c = \frac{59\text{mV}}{n} \quad (6)$$

Gold electrode surfaces are known to frequently only permit quasi-reversible oxidation and reduction kinetics for many redox couples, that might otherwise exhibit reversible behaviour as for example on platinum [19].

Figure 11 shows three CVs for three different electrolyte compositions for the same membrane. The baseline recorded with the marker in the electrolyte, shows that there is a considerable background permeability of the membrane. This is attributed to:

- i) pin holes and voids in the membrane
- ii) a certain permeability of the marker through intermolecular spaces of the C[4]RA
- iii) possible intramolecular penetration of the hydroquinone of the C[4]RA

The size of the HQ is, with ca. 0.65 nm diameter, similar to that of the electroactive species methylviologen²⁺ for which this type of inclusion/ intramolecular permeability was advocated for calix[6]arenes [20]. This rather high background permeability, was a

determining criteria for the usage of a membrane with 12 monolayers over thinner and therefore more permeable membranes.

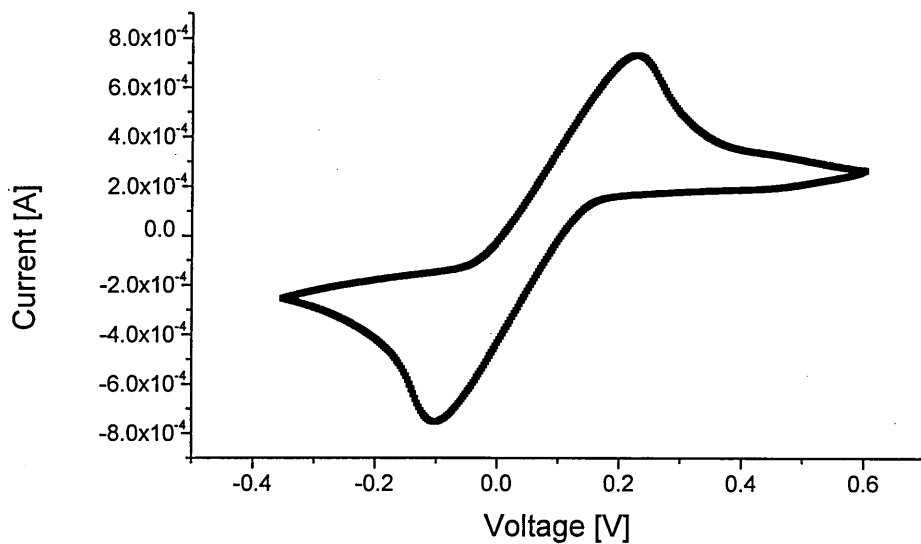


Fig. 10 CV of hydroquinone on an uncoated gold electrode

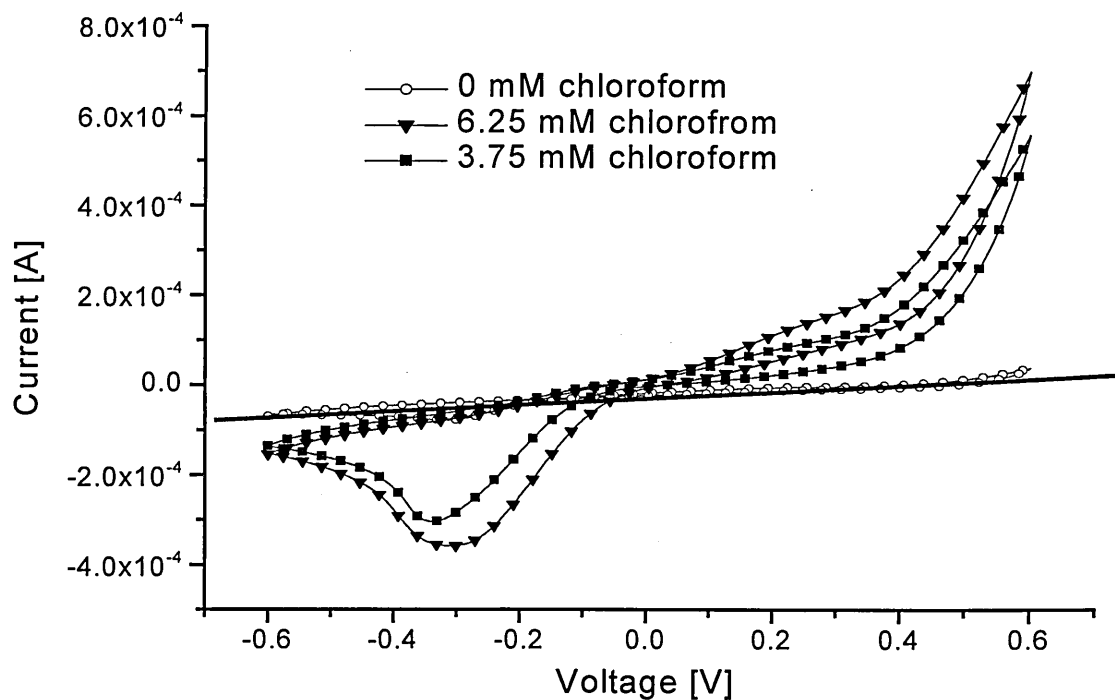


Fig. 11 CVs of C[4]RA coated electrodes, showing an increase in permeability under CHCl_3 addition

The oxidation peak of the hydroquinone appears at + 0.2 V vs. Ag | AgCl, corresponding well with the oxidation peak on the uncoated electrode, the reduction peak is shifted to – 0.33V vs. Ag |AgCl. A possible reason for this shift is an increased irreversibility of the hydroquinone redox-reaction and/or an alteration of the charge transfer characteristic. The latter alteration can be substantial depending on the position of the hydroquinone with respect to the electrode surface. The Intersecting State theory [21] or Marcus theory [22] for charge transfer mechanisms shows that molecular or ionic coupling, and therefore electron transfer rates decrease exponentially with distance (7).

$$V_R^2 = V_O^2 \exp(-\beta R) \quad (7)$$

V_O^2 represents the maximum electric coupling, R is the distance and β is the exponential electron tunnelling coefficient

The distance of the HQ from the electrode in turn depends on the position of it in the membrane. It can take up several positions, like suspension in the basket, partial attachment to membrane molecules and free contact with the electrode. Since no separate peaks are discernible, no further differentiation is possible and the shift must be lumped up under a modified charge transfer characteristic.

An analysis of the peak heights with respect to the drawn baseline for the oxidation and reduction peaks results in an average relative increase of the current and therefore the permeability of 900 % for 3.75 mM CHCl_3 and 1500 % for 6.75 mM CHCl_3 .

Upon flushing with electrolyte, without the marker, recovery was substantial but imperfect. A likely reason for this is the strong difference in the solubility of the hydroquinone and the benzoquinone. The former has a solubility of 70g/l and the latter is essentially insoluble.

Figure 12 shows the induced permeability changes for a different membrane, upon the addition of 13mM of acetone to the electrolyte. The oxidation peak is again found at + 0.22V vs. Ag | AgCl and the reduction peak is shifted to – 0.27 V vs. Ag | AgCl. As in the case for chloroform the permeability is increased under analyte addition. An analysis of the peak heights with respect to the drawn baseline gives a current and therefore a permeability increase of 260 % for the addition of 13 mM of acetone.

The inset in Figure 12 shows the induced permeability changes for the same analyte concentration on a different electrode. The resulting current increase is 80 percent. This is a substantially different value for a principally identical case. Deriving the baseline

for the most linear part, introduces an uncertainty for the determination of the peak heights. But this rather poor reproducibility can be mainly attributed to the nature of the LB films. Two LB films are never exactly the same with respect to their structure and the amount of pinholes present. Since these factors determine the background permeability this varies with it. A given background permeability can only be modulated to a certain degree, and this causes deviation for results obtained from different electrodes.

The reaction to acetone is considerably smaller than that for chloroform, clearly indicating a stronger complexation with stronger structural modulation in the case of the latter. The recovery upon flushing, is as in the case of chloroform, substantial but imperfect.

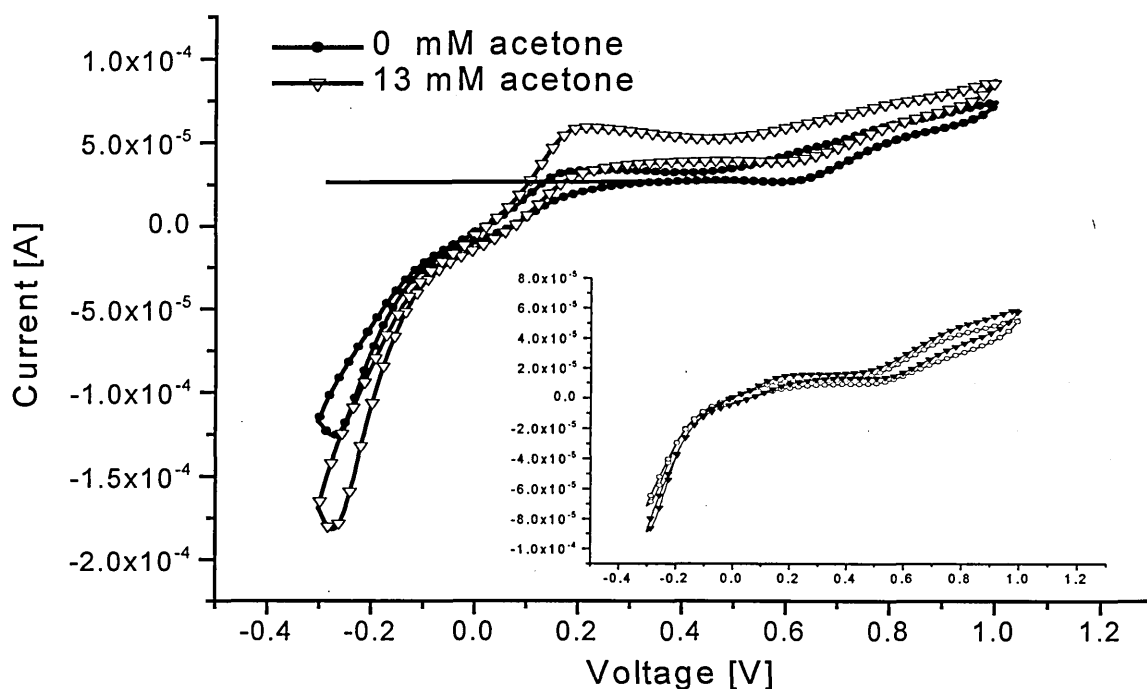


Fig. 12 CVs of a C[4]RA coated electrode, showing an increase in permeability upon C_3H_6O addition, the inset shows the same reaction for a different sample

When the voltage window is reduced to the range of -0.1 V to $+0.6$ V, in which the oxidation of the HQ takes place, the peak heights can be compared without any relative peak shift. Figure 13 shows the CVs for a membrane with and without acetone in the electrolyte. Evaluation of the peak heights gives an increase of 33 % for 6.5 mM, 80 % for 13mM and 125 % for 19.5 mM of acetone.

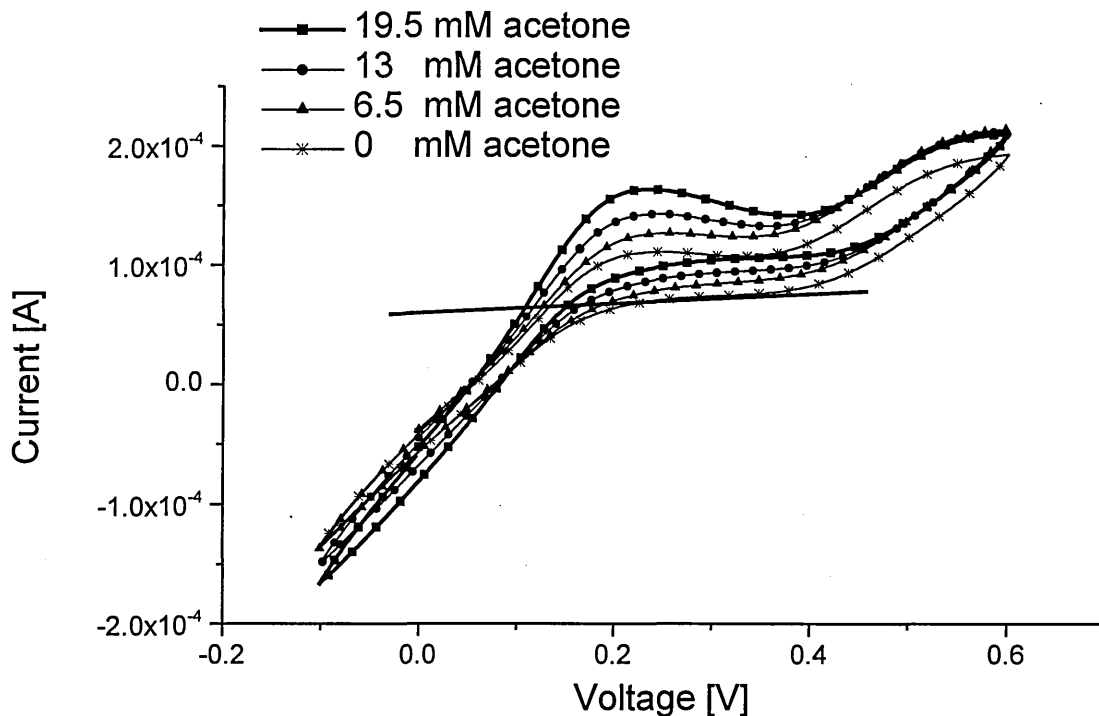


Fig. 13 Cyclic voltammogram for a C[4]RA coated electrode, showing the increase in the oxidation peak height under acetone addition

The above results have show that the relative permeability of the LB C[4]RA membrane is controlled by the presence of organic analytes like chloroform and acetone. These permeability changes are attributed to changes in the conformational structure of the film. Any complexation with the organic analyte is changing the intermolecular voids, altering the arrangement of the aliphatic side chains and generally changes the hydrophobicity of the film. The aliphatic C_7H_{15} side chains are strongly hydrophobic, due to their nonpolar character. An estimate of the polarity can be taken from the permittivity ϵ (dielectric constant) of a substance. For 1 heptene, C_7H_{14} , ϵ is 2.092, chloroform has an ϵ of 4.8 and acetone has an ϵ of 6.18, all values taken from reference [23]. A complexation with acetone and chloroform can therefore alter the overall hydrophobicity of the membrane. Since the experimental results contradict the trend for the polarity of the molecule, which is higher for acetone than it is for chloroform, this effect is only part of the overall contribution.

The results obtained, broaden the spectrum of analytes that show a permeability control on macrocyclic membranes by adding organic analytes to them. Previously only the

permeability changes of membranes upon complexation with alkali metal cations was shown with anionic and neutral markers, like $\text{Fe}(\text{CN})_6^{4-}$ and hydroquinone in reference [14].

9.2 Impedance Spectroscopy

The electrodes were further analysed with the aid of impedance spectroscopy in the range of 0.1 - 10^5 Hz.

Impedance spectroscopy (IS) provides a non-invasive means of characterising the electrical properties of many systems. The systems can be a solid multilayer structure, a solid electrolyte or even an electrolyte solid electrolyte structure. IS has initially been applied to membrane studies of living cells, showing that these possess a low permeability for ions [24], and providing an estimate of their thickness [25]. Low frequency IS, probing bilayers achieved spacial resolutions in the order of 0.1 nm [26, 27]. It has further been an instrument in studying the various transport mechanisms of proteins across biological membranes [28]. Apart from biological membranes, IS is extensively used in corrosion studies, where organic coatings (membranes) protect a metal body [29, 30]. Models have been developed for the quality characterisation and intactness of these protective coatings [31, 32, 33]. Impedance measurements are carried out by applying a small AC voltage of frequency ω across the system under investigation and measuring simultaneously the amplitude of the current across the system and the phase shift between the voltage and current. For IS the frequency ω of the signal is varied across several orders of magnitude. In a multilayer system it is possible with this to discern the contributing elements, each of which has its characteristic frequency response. This is only an outline of IS, as applied to membrane studies, a detailed theoretical treatment and much more details can be found in the references [34, 35, 36].

9.2.1 Experimental details

The measurements were performed, using the afore described Autolab potentiostat PG STAT 10, in connection with the Frequency Response Analyser FRA2. The whole set-up was controlled by a computer running the software FRA 4.7. The electrode configuration and the electrolyte preparation was identical to the one used for the CV

measurements. Each spectrum was recorded after the system was allowed to equilibrate for 10 minutes. The spectra were fitted to equivalent circuits, employing algorithms described in the references [37,38].

9.2.2 Results and discussion

For comparative reasons, the impedance spectra of the Au and the C[4]RA coated electrode were recorded in the buffered electrolyte, without the marker added. The spectra are shown in Figure 15. A mathematical fit of the experimental data, employing the equivalent circuit shown in Figure 14, was carried out. The theoretical response as derived from the equivalent circuit is also presented in Figure 15.

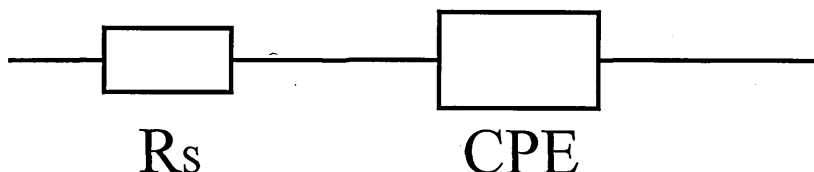


Fig. 14 Equivalent circuit used to represent the working electrode electrolyte system, without marker in the electrolyte

At high frequencies, the impedance is nearly frequency independent, while at low frequencies, an increase of the impedance is observed. The system impedance shows increasing dispersion for frequencies below 100 Hz, increases at the lower end of the spectrum. The solution resistance R_s determines the high-frequency behaviour, while the capacitive behaviour of the membrane dominates at the lower frequencies. A constant phase element (CPE) was chosen to represent the capacitive structure formed by the double layer and the calixarene membrane, the impedance of a constant phase element is given by (8). With f being the frequency, Q the admittance at $\omega = 1 \text{ rad/s}$, and n an expression for the degree of resemblance to a capacitor. A value for n of 1 results in a similar behaviour to a capacitor, with a somewhat lower phase angle than 90 degrees.

$$Z_{CPE} = \frac{1}{(2\pi f Q)^n} \quad (8)$$

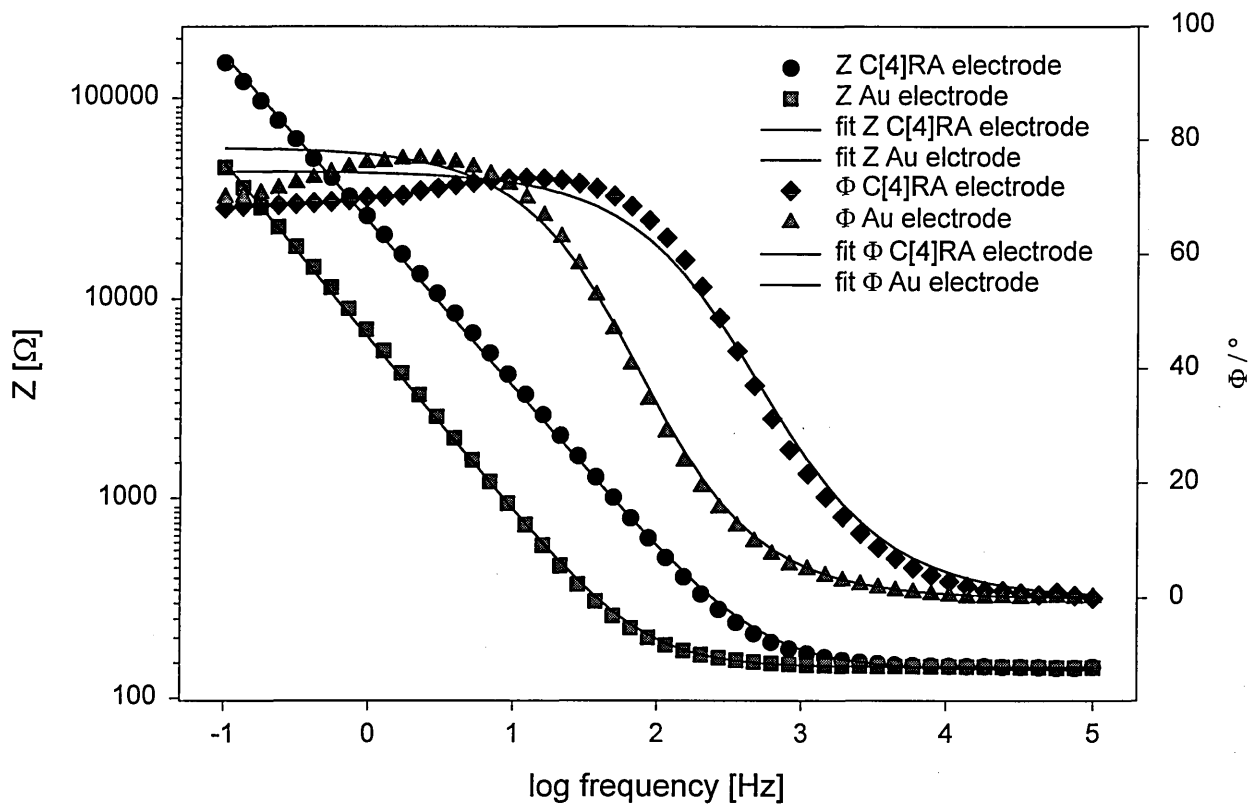


Fig. 15 Bode plot of the spectra of the coated and uncoated Au electrode, with fitted equivalent circuit values

A CPE was chosen, instead of a capacitive structure, since it better represents real world structures. Fundamentally its origin can be traced to the complex double layer structure, forming in/on the electrode. Various theories have been advanced describing the double layer, in terms of ions directly located on the electrode surface, Stern layer, the diffused layer adjacent to it, Gouy-Chapman layer and ions in the bulk of the solution ^[36], Figure 16. A layered structure of even higher order has been suggested in reference ^[39]. Complicating things further is the electrode roughness. If a fractal surface is assumed, the fractal dimension (D) of the surface is between 2 and 3. This means that the surface fills between 2 dimensions (perfectly flat) and 3 dimensions, (branching every which way through space resembling a porous cube). It was shown by Mulder ^[40], that for such electrodes the interfacial impedance is modified by an exponent, $n=1/(D-1)$. For a smooth fractal dimension ($d=2$) n is therefore 1, and for a highly three-dimensional surface ($D=3$) n is 0.5.

Additionally, inhomogeneous reaction rates and varying thickness or composition of the coating have been cited as contributions to the CPE ^[41].

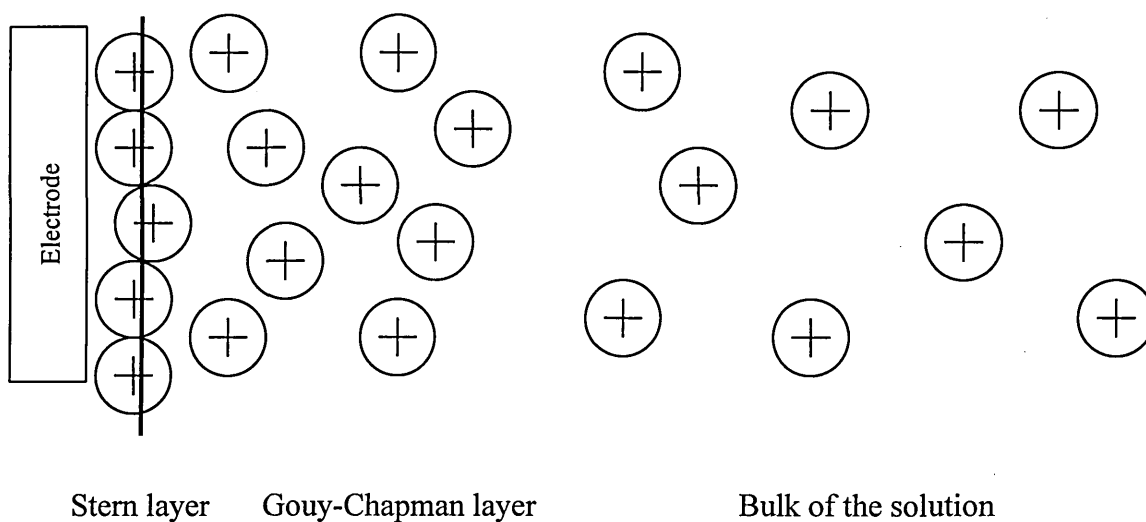


Fig. 16 Approximated model of an electric double layer

Values of $Q_{\text{calix}} = 0.8208 \times 10^{-6} \text{ F}$ and $n_{\text{calix}} = 0.820$ were obtained for the CPE in case of the coated electrode and $Q_{\text{Au}} = 0.7258 \times 10^{-5} \text{ F}$ and $n_{\text{Au}} = 0.875$ in case of the uncoated electrode, with a constant electrolyte resistance. This shows a substantial change in the three-dimensional character of the electrode surface upon coating with the C[4]RA.

Whereas two identically prepared gold slides result in more or less identical spectra, the C[4]RA coated electrodes show some deviation. Similar behaviour was observed for the CVs of different electrodes. Figure 17 shows the spectra of two identically prepared electrodes. The fitted equivalent circuit result in a $Q_{\text{calix1}} = 0.82 \times 10^{-6} \text{ F}$ and $n_{\text{calix1}} = 0.82$ $Q_{\text{calix2}} = 0.49 \times 10^{-6} \text{ F}$ and $n_{\text{calix2}} = 0.81$, with the solution resistance of 138Ω being constant

To illustrate the influence of the hydroquinone on the coated and uncoated electrode both impedance spectra are presented for comparison in Figure 18. The working electrode is biased to $+ 0.22\text{V}$, to facilitate the oxidation of the marker. The charge transfer during this process can be represented by a resistance (charge transfer resistance), parallel to the capacitive dominated element of the membrane. The charge transfer resistance, is a direct measure of the accessibility and kinetic behaviour of the marker with the electrode. The charge transfer resistance decreases the impedance by more than two orders of magnitude and changes the phase shift to a less capacitive character.

For the C[4]RA coated electrode the introduction of the charge transfer resistance has a less pronounced effect on both the reduction in Z and the changes in the phaseshift. The

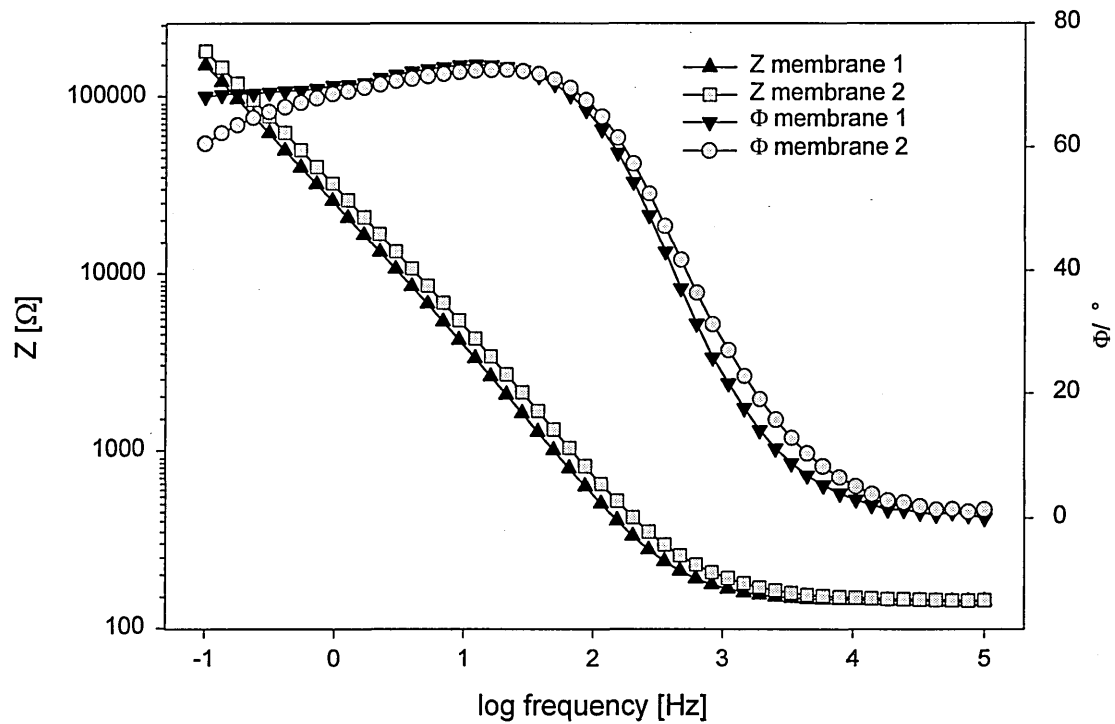


Fig. 17 Comparison of impedance spectra for two "identical" C[4]RA coated electrodes

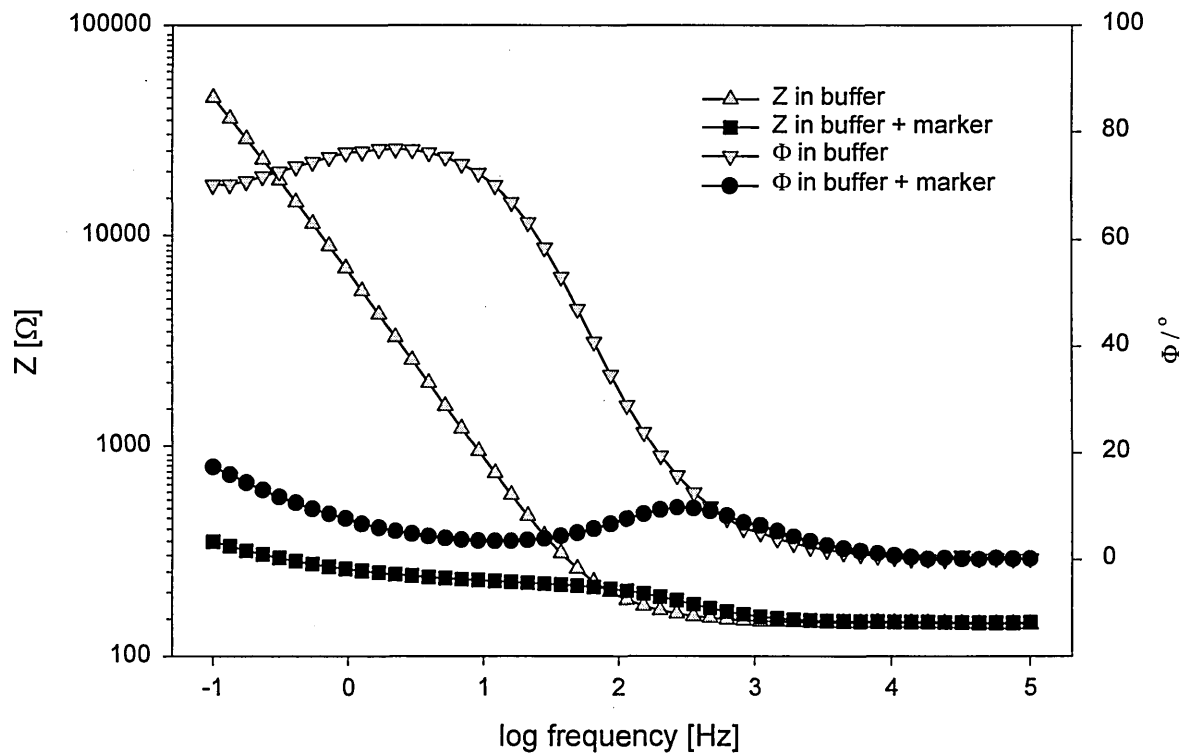


Fig. 18 Au electrode in buffered electrolyte and in buffered electrolyte with marker

amount of material undergoing oxidation is greatly reduced with the membrane in place. Figure 19, compares the Bodeplot for the different electrolyte compositions with and without marker.

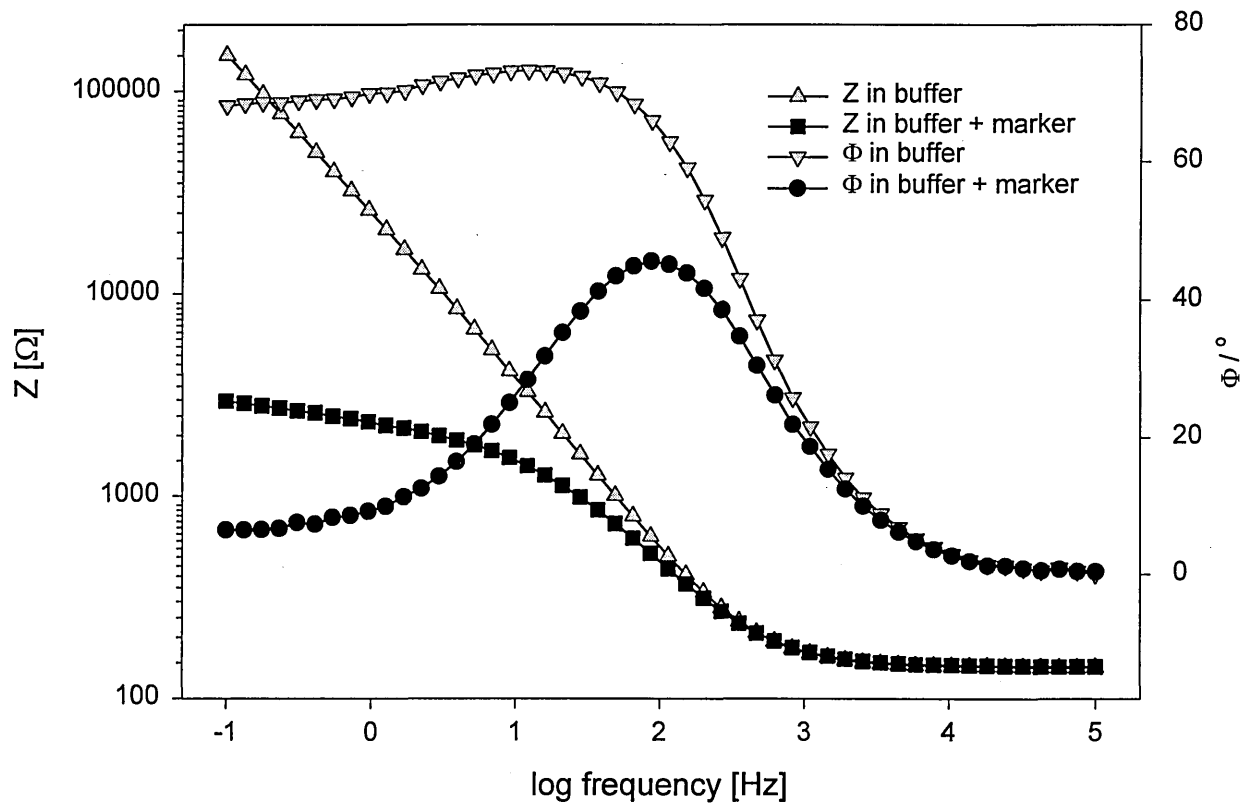


Fig. 19 C[4]RA coated electrode in different electrolytes

The modulation of the charge transfer resistance, is a measure of the permeability modulation. To quantify this, the spectra had to be fitted to an equivalent circuit. Corrosion studies dealing with failed coatings have established the following model, Figure 20. The capacitance of the intact coating is represented by C_c , R_{po} is the pore resistance of the ion conducting path that develops in the coating, R_{ct} is the charge transfer resistance, C_{dl} is the double layer capacitance and R_s is the solution resistance. This type of model has been successfully applied in many studies for the calculation of the coating degradation^[42, 43]. Since the degradation of a protective coating is in essence a change in the permeability of the coating, it was assumed that this model could be applied to the C[4]RA electrode. Alternative to this model there exists a simpler model, Figure 21, with a charge transfer resistance parallel to a constant phase element.

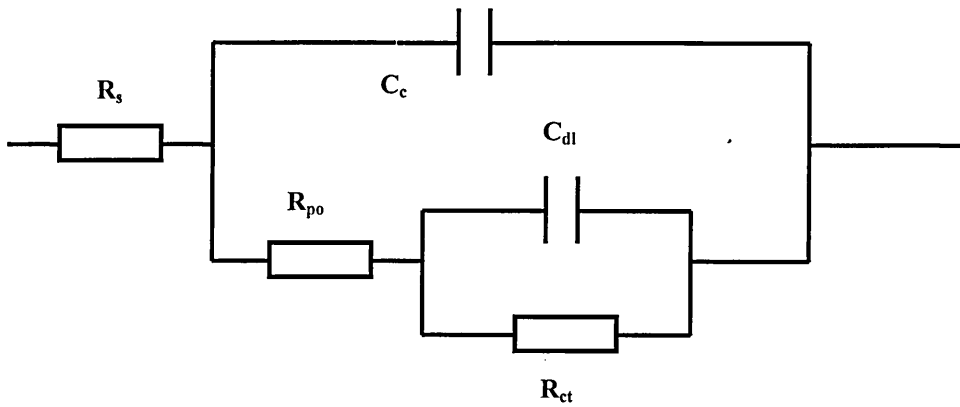


Fig. 20 Equivalent circuit for a failed coating as use in corrosion studies

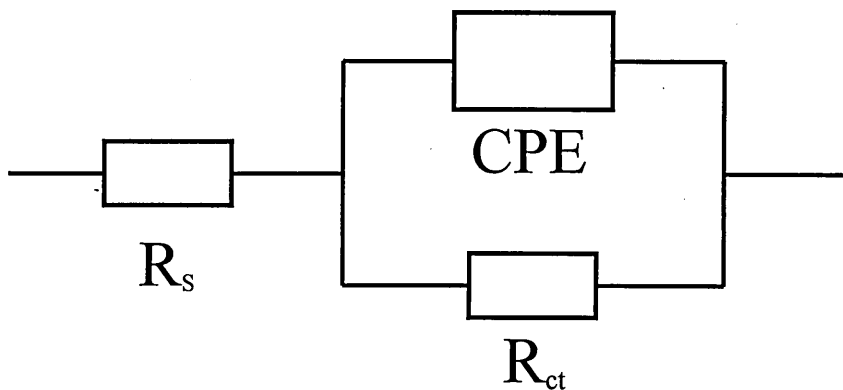


Fig. 21 Equivalent circuit for permeated electrode

Both models were used for the fitting, but the more complex model did not result in an order of magnitude superior fitting result, as judged from the error function. It was observed that results strongly depended on the initial input parameters. Therefore it was decided to apply Occam's razor, and use the simpler model. Figure 22 shows the chloroform induced impedance changes of a membrane. The fitted impedance, as derived from the model is also shown in the Bodeplot. Changes in the spectra occur for both the phase shift and the impedance, fitting the spectra to the equivalent circuit in Figure 21 yields values for the components as given in Table 1.

Concentration of analyte [mM]	R _{solution} [Ω]	Q [F]	n	R _{charge transfer} [kΩ]
0	145	0.3829 · 10 ⁻⁶	0.7936	14.49
3.75	145	0.3103 · 10 ⁻⁶	0.7945	11.57
7.5	145	0.2852 · 10 ⁻⁶	0.7954	6.86

Table 1 Fitted component values for the circuit elements according to Figure 21

The solution resistance is constant, and the charge transfer resistance describing the faradaic current caused by the oxidation of the marker decreases by a factor 1.25 for 3.75 mM and a factor of 2.1 for 7.5 mM of chloroform. This confirms the increased permeability of the membrane due to the calixresorcinarene analyte interaction. However, the observed change in the charge transfer resistance was not as large as was expected from the results of the cyclic voltammetry measurements. This may be attributed to the increased irreversibility of the hydroquinone oxidation/reduction reaction as discussed. The value of Q for the constant phase element decreased from 0.383×10^{-6} F to 0.285×10^{-6} F, whereas n is nearly identical in all cases. This also confirms a change in the structure of the calixarene membrane due to interaction with the analyte. The value of 0.79 for n can be regarded as reasonable for the given system with a substantial three-dimensional surface and a high degree of inhomogeneities.

The impedance measurements show that the membrane changes are largest for the lower frequencies, but they also show that the model used to represent the system, shows its largest discrepancy with the data in this range.

In Figure 23 the same spectra are shown, plus the fitted data for the 7.5 mM chloroform concentration, but this time resolved into real and imaginary parts. It can be seen that both parts are affected by the analyte.

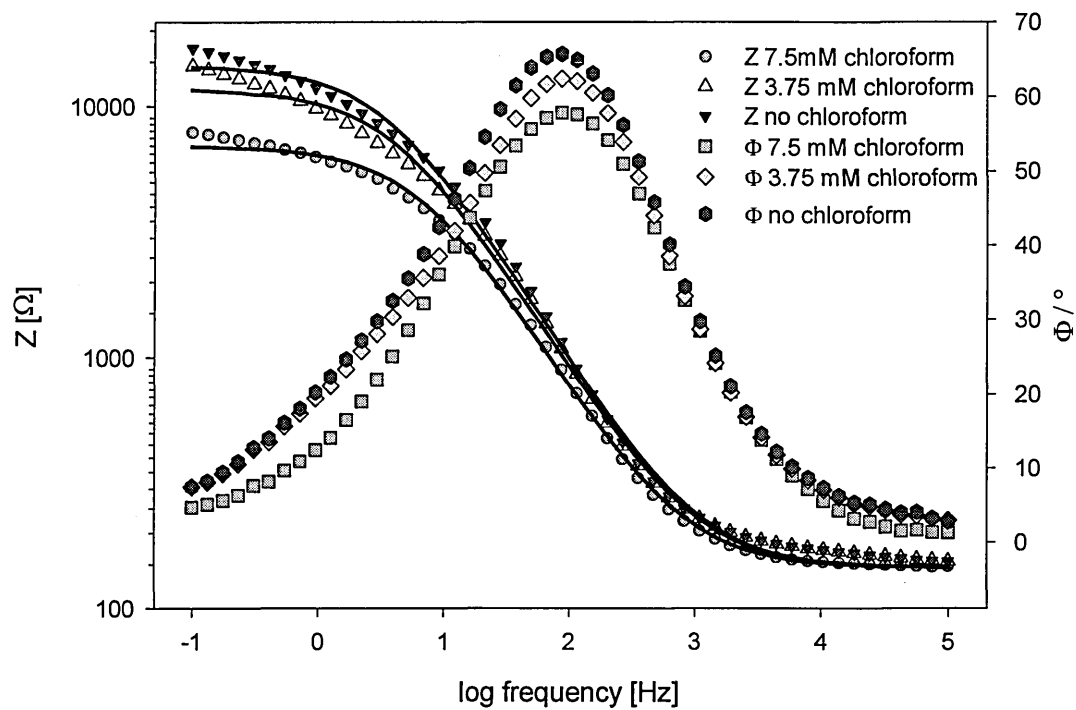


Fig. 22 Changes in the membrane impedance under addition of CHCl_3

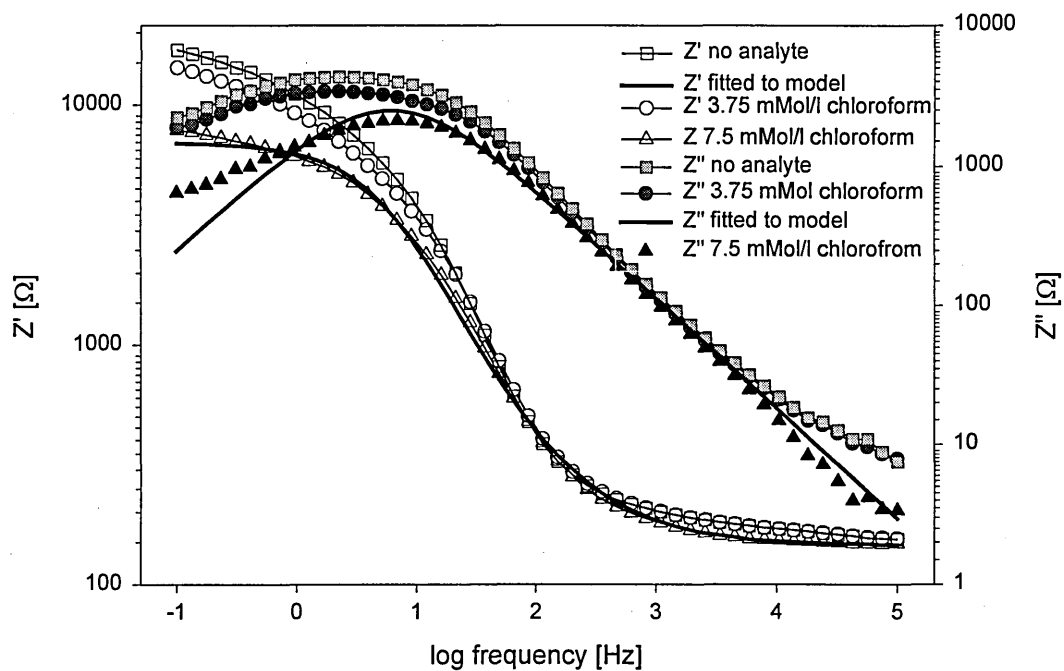


Fig. 23 Changes in the real and imaginary part of the impedance under addition of CHCl_3

The type of electroactive marker used for the permeability studies has a very strong effect on the impedance spectra of the electrodes. Ferrocyanide $\text{Fe}(\text{CN})_6^{3-}$ undergoing, oxidation when the working electrode is biased to +0.17 V, gives an impedance spectrum like that in Figure 24. This differs greatly from those obtained for HQ, the

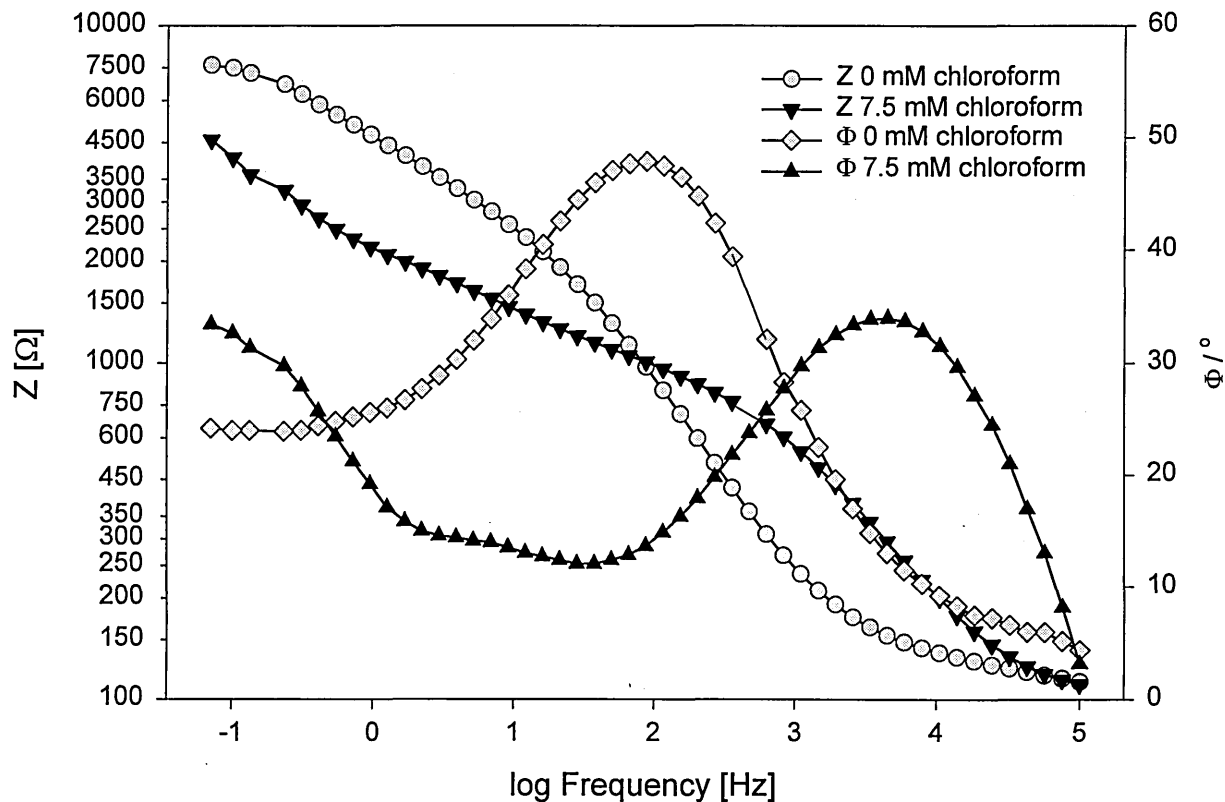


Fig. 24 Bodeplot of impedance changes upon CHCl_3 addition, with ferrocyanide permeability marker

impedance disperses over nearly the entire frequency spectrum, though nonlinear, and the phase shift for the lower frequency range is much higher. The addition of 7.5 mM of CHCl_3 produces a large phaseshift and reduces the impedance below 100Hz. The phaseshift though lower in amplitude, sets in at higher frequencies, it falls and begins to rise again at 50 Hz. These strong nonlinearities make it impossible to fit the spectra to an equivalent circuit. The general behaviour, that the charge transfer resistance is reduced, due to a higher permeability is confirmed, with the observed changes being

larger than those obtained with HQ. The strongly nonlinear behaviour can have its origin in:

- i) the strong electrostatic forces between the multiply negatively charged marker, impeding diffusion or migratory processes
- ii) accumulation of the marker in the membrane
- iii) solvation effects of the analyte with the marker

It is believed that especially the latter is responsible for an increase in the impedance at higher frequencies.

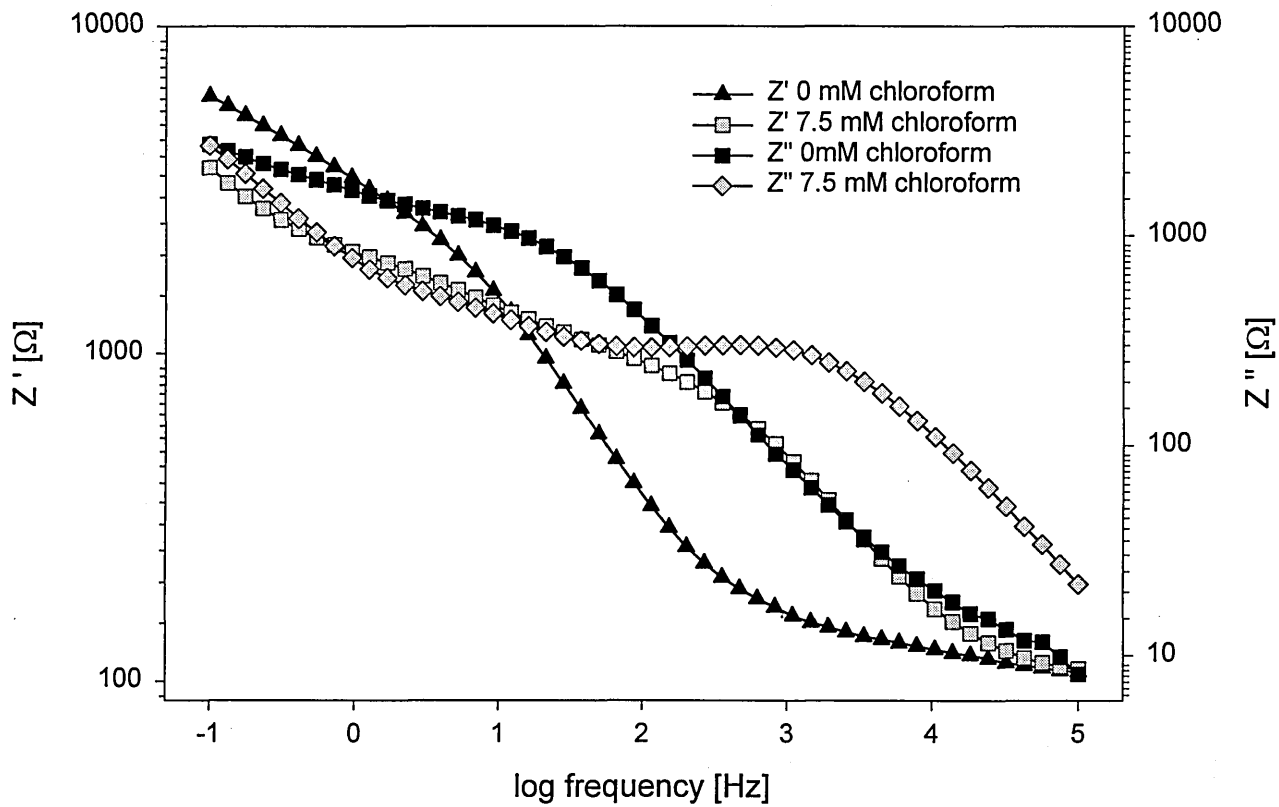


Fig. 25 Z' , Z'' over f representation of the membrane impedance with ferrocyanide as marker

It is interesting to note, that when the IS is split into its real and imaginary parts Figure 25, that the highest sensitivity is no longer found at the lower end of the spectrum but is located at 2000 Hz for the real part and at 30kHz for the imaginary part. The resistance is modulated by a factor of 5 and the reactance is modulated by a factor of 6.

9.3 SPR analysis of the membrane permeability

SPR was used, first in a static scan over time and then with a dynamic scan to investigate the membrane permeability.

For the static test, the photo-detector voltage is recorded over time, at a fixed angle of incidence, 70° . Any change in the thickness of the membrane, that could result from disintegration, peeling off or infiltration of the pure electrolyte would change the photo-detector response. Figure 26 shows that the film is stable, adheres well to the substrate and does not undergo changes when exposed to the buffered electrolyte. The drop in the detector voltage on injection of the electrolyte, corresponds to the change in the refractive index from 1 for air to 1.33 for water. After the injection is complete, the detector voltage is within the experimental accuracy a flat line.

A series of dynamic scans compared the response of the uncoated electrode and the C[4]RA coated one, upon the addition of 7.5 mM of chloroform, Figure 27. The scans for the uncoated electrode reveal no changes, whereas the coated one produces a pronounced curve shift. Analysis of the gold slide, determined the following substrate parameters Table 2.

refractive index	0.37208
extinction coefficient	3.39908
thickness	44.6350
error function	0.74

Table 2 Parameters as determined for the uncoated gold slide

These values were fixed for any subsequent analysis, then the electrode with the membrane was analysed, in pure electrolyte immersion, resulting in the parameters for the non permeated film, Table 3.

Since the absorption of the analyte, in combination with a permeation of the water, changes the refractive index and the thickness of the film, only a solution window, Figure 28, in which the exact solution for the Fresnel equations lie can be found.

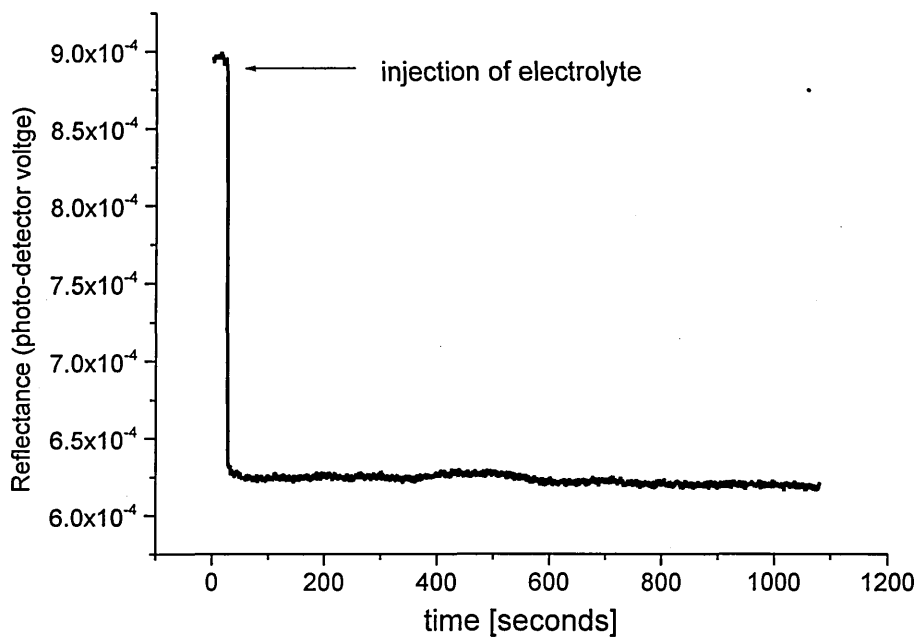


Fig. 26 Static SPR response of the C[4]RA covered electrode on flushing with electrolyte

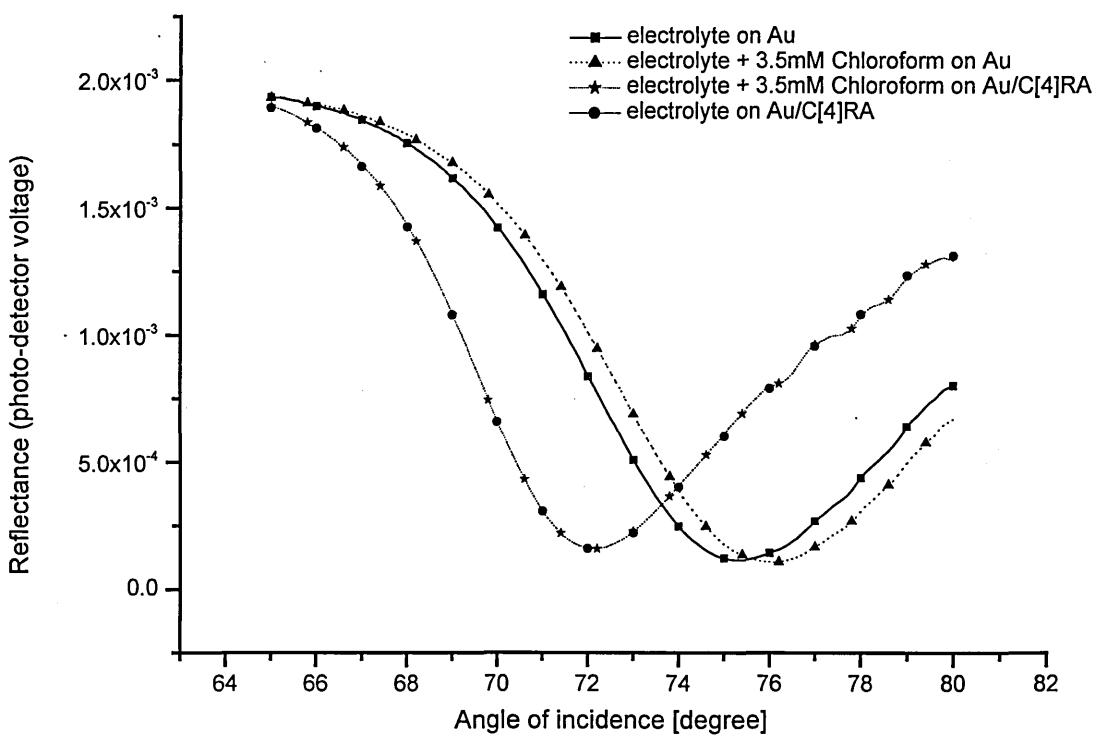


Fig. 27 Dynamic SPR response of the Au and Au + 16 ML C[4]RA electrode to chloroform

refractive index	1.47
extinction coefficient	0
thickness	16.34
error function	1.03

Table 3 Parameters for the C[4]RA membrane in exposure

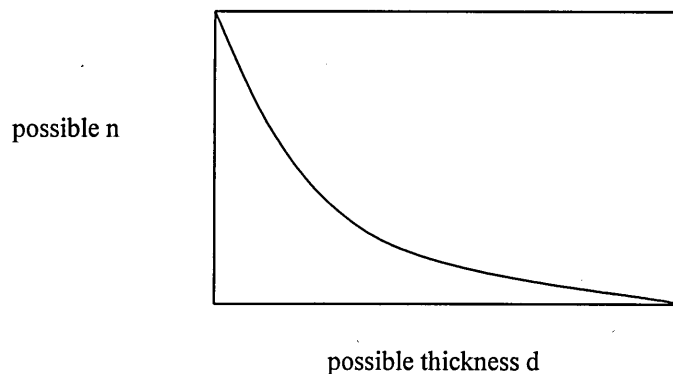


Fig. 28 Window of possible solutions all giving the same quality of fit

Since the refractive index represents the propagation speed of light in the medium, and therefore describes the interaction of light and matter, the interaction must increase with the absorption of guest molecules inside the membrane. Applying the permeability data gathered from the CV studies, the refractive index was estimated to be a superposition of n of the C[4]RA and n of water, with a value of 1.483. The calculation implemented, added the difference between the refractive index of water and vacuum multiplied by the permeability increase, to the refractive index of the C[4]RA according to (9).

$$n_{\text{C[4]RA}} + \text{permeability} \cdot (n_{\text{H}_2\text{O}} - n_{\text{vacuum}}) = n_{\text{of the permeated membrane}} \quad (9)$$

By then fitting the exposure results, and fixing n to 1.483, a thickness value for the permeated membrane of 17.85 nm was found, indicating a swelling by 1.5 nm, or 9.25 % of its original value.

Summary

In this chapter, it was shown that the permeability of the LB C[4]RA membrane is modulated by the presence of organic analytes in solution. Electrical measurements with a permeability marker, CV and IS, as well as optical studies (SPR) without marker confirmed this. These studies also pointed out that the variations in the membrane properties from membrane to membrane are subject to fluctuations. This constitutes a serious obstacle for the comparison of data derived from different membranes. Since imperfections in the LB coating method and limited purity of the compound used, are responsible for this, these issues can to be addressed. Selectivity of the membrane is a further point that can be improved upon. Most promising for this is the modification of the calix[4]resorcinarene used, by grafting on different substituting side groups providing specific interaction sites and allowing specific structural changes. Chemical sensing based on membrane permeability changes is still in its infancy, though it is a promising emulation of the remarkable signal amplification function of ion channel proteins.

9.4 References

- [1] M. Sugawara, K. Kojima, H. Sazawa, Y. Umezawa, *Thin Solid Films*, 59, 2842, 1987
- [2] M. Sugawara, M. Kataoka, K. Odashima, H. Sazawa, Y. Umezawa 180, 129, 1989
- [3] S.Nagase, M. Kataoka, R. Naganawa, R. Komatsu, K. Odashima, *Anal. Chem.*, 62, 1252, 1990
- [4] M. Sugawara, H. Sazawa, Y. Umezawa, *Langmuir*, 8, 609, 1992
- [5] K. Odashima, M. Kotato, M. Sugawara, Y. Umezawa, *Anal. Chem*, 65, 927, 1993
- [6] 305 A. Naik, Y. N. Kalia R.H. Guy, *Pharmaceutical Science & Technology Today*, 3, 9, 318-326, 2000
- [7] 306 M. Uto, E.K. Michaelis, I.F. Hu, Y. Umezawa, T. Kuwana, *Anal. Sci.*, 6, 221, 2000
- [8] H. Minami, M. Sugawara, K. Odashima, Y. Umezawa, M. Uto, E.K. Michaelis, T. Kuwana., *Anal. Chem.* 63, 2787, 1991
- [9] H. Minami, M. Uto, M. Sugawara, K. Odashima, Y. Umezawa, et al. *Anal. Sci.*, 7 Supplement, 1675, 1991

- [10] M. Maeda, Y. Tsuzaki, K. Nakano, M. Takagi, *J. Chem. Soc. Chem. Commun.*, 1529, 1991
- [11] M. Maeda, Y. Fujita, K. Nakano, M. Takagi, *J. Chem. Soc. Chem. Commun.*, 1724, 1991
- [12] M. Maeda, Y. Mitsuhashi, K. Nakano, M. Takagi, *Anal. Sci.*, 8, 83, 1992
- [13] M. Maeda, K. Nakano, S. Uchida, M. Takagi, *Chem. Lett.*, 1805, 1994
- [14] Y. Kenichi, S.B. Khoo, M. Sugawara, T. Sakaki et al. *J. Electroanalytical Chem.* 401, 65-79, 1996
- [15] P.D. Beer, P.A. Gale, G. Z. Chen, *Coordination Chemistry Reviews*, 185-186, 3-36, 1999
- [16] <http://www.bath.ac.uk/~chsacf/solartron/electro/html/cv.htm>;
- [17] *Laboratory Techniques in Electroanalytical Chemistry* by P.T.Kislinger, Dekker, 1996, ISBN: 0-8247-9445
- [18] *Electroanalytical Chemistry*, B.H. Vassos, G. W. Ewing, Wiley, 1983, ISBN: 0-471-09028-X P. 125
- [19] K. Winkler, *J. Electro. Chem.*, 358, 151, 1995
- [20] A.R. Bernardo, T. Lu. E. Cordova, L. Zhang, et al. *J. Chem. Soc. Chem. Commun.*, 529, 1994
- [21] L.G. Arnault, S.J. Formosinho, *J. Photochem & Photobiol A: Chemistry* 100, 15, 1996
- [22] *Instrumental Methods in Electrochemistry*, by R. Greef, R. Peat, L.M. Peter, D. Pletcher, J. Robinson, Chichester:Ellis Horwood,1985, P. 185
- [23] *CRC Handbook of Chemistry and Physics*, by D.R. Lide, CRC Press, 1995, ISBN: 0849304784
- [24] R. Hoeber, *Arch. Gesl. Physiol.*, 133, 237-259, 1910
- [25] H. Fricke, S. Morse *J. Gen. Physiol.*, 9, 153-167, 1925
- [26] H.G.L. Coster, J.R. Smith *Biochim. Biophys.Acta.* 373, 151-164, 1994
- [27] R.G. Ashcroft, H.G.L. Coster, D.R. Laver, J.R. Smith, *Biochim. Biophys.Acta*, 730, 231-238, 1983
- [28] T.C. Chilcott, S. Frost-Shartzner, M.W. Iverson et al., *C.R. Acad. Sci.*, 318, 761-771, 1996
- [29] G. Grundmeir, W. Schmidt, M. Stratmann, *Electrochimica Acta* 45, 2515-2533, 2000
- [30] J. Titz, G.H. Wagner, H. Spaehn, M. Ebert, W.J. Lorenz, *Corrosion* 46, 221, 1990
- [31] E.P.M. van Westing, G.M. Ferrari, J.H.W. de Wit, *Coros. Sci.* 34, 1511, 1993

- [32] F. Mansfeld, H. Shih, H. Greene, C.H. Tsai, in J.R. Scully, D.C.Silverman, M.W. Kendig, *Electrochemical Impedance – Analysis and Interpretation*, ASTM, Philadelphia, P. 37, 1993
- [33] M.W. Kendig, S. Jeanjaquet, J, Lumdsden in J.R. Scully, D.C.Silverman, M.W. Kendig, *Electrochemical Impedance – Analysis and Interpretation*, ASTM, Philadelphia, P. 407, 1993
- [34] *Electrochemical Methods – Fundamentals and Application*, by A.J. Bard, L.R. Faulkner, Wiley, 1980, ISBN: 0471055425
- [35] *Impedance Spectroscopy –Emphasizing Solid Materials and Systems*, by J.R. Macdonald, Wiley,1987, ISBN: 0471831220
- [36] H.G.L. Coster, T.C.Chilcott, A.C.F. Coster, *Bioelectrochemistry and Bioenergetics* 40, 79-98, 1996
- [37] B.A. Boukamp, *Solid State Ionics* 20, 31-44, 1986
- [38] B.A. Boukamp, *Solid State Ionics* 18&19, 136-140, 1986
- [39] A.C.F. Coster, H.G.L. Coster, T.C. Chilcott, J.R. Smith in preparation
- [40] W. H. Mulder, J. H. Sluyters, T. Pajossy, L. Nyikos, *J. Electroanal. Chem.* 285, 103, 1990
- [41] www.consultrsr.com/resources/cpe1.htm
- [42] R. M. Souto, H. Alanyali, *Corrosion Science*, 42, 12, 2201-2211, 2000
- [43] A. Palit, S. O. Pehkonen, *Corrosion Science*, 42, 10, 1801-1822, 2000

10 Summary, conclusions and suggestions for further work

A comprehensive literature review on calixarene/calixresorcinarene aspects was carried out. This included synthesis, conformations and applications, with the focal point being the employment of arenes in the field of chemical sensors and chemical analysis.

Central point for all utilisation of arenes for sensing applications is the formation of a sensing membrane. Therefore a detailed study regarding the different thin film formation techniques was undertaken. The C[4]RA was deposited in the form of Langmuir Blodgett films onto a variety of different substrates, including glass slides, silicon substrates and gold coated slides/electrodes. The properties of these membranes were analysed with respect to the film thickness and homogeneity. The thickness of one monolayer of C[4]RA was found to be 0.95 nm.

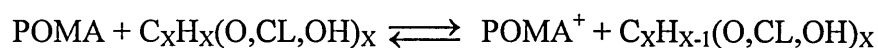
Alternative deposition methods evaluated were spin coating and casting. For the spin coated films a dependence of the film thickness on the spin speed and the concentration was found. In an first approximation the formation process can be described by a $d = c \cdot \omega^x$ law with coefficients for x of - 0.44 and - 0.48 and c of 1.16 and 1.57 for solution concentrations of 1 mg/ml and 2 mg/ml in chloroform, respectively. It is highlighted that the model is only an approximation, since it is believed that the model has limited validity for films that are only several times thicker than the individual molecular diameter. Membranes with a thickness of 250 nm were prepared by casting. A detailed study on the employment of C[4]RA as a deposition matrix for a non surface active polymer in the form of LB films was conducted. Influences of the mixing concentrations and training effects on the deposition were analysed. It was shown that a repeated compression cycle is required and changes the molecular arrangement of the composite membrane. The homogeneity of the membrane was investigated with, spectroscopic and SEM studies. It was found that the homogeneity is good, with structural changes occurring after long term exposures to saturated vapours of chloroform and ammonia. Thickness analysis, by SPR and ellipsometry, gave a value of 2.1-2.2 nm for the individual ML. Based on this a structural model of the membrane is proposed with two strands of the polymer over/under each C[4]RA layer.

UV spectroscopy was employed for a determination of the number of toluene molecules complexing inside a LB membrane. Good agreement for a 1:1 ratio between the number

of molecules complexing in the membrane and the number of baskets in the membrane was found. Interrogation of the absorbance peak at 200 nm, can form the principle of a very selective sensor since only aromatic compounds modulate it.

Conductivity measurements of the composite membrane carried out on interdigitated electrodes showed that the conductivity of the as deposited film is in the order of $1 \cdot 10^{-3}$ S/cm for a 1:1 by weight mixing ratio. Continuous purging with nitrogen showed that the conductivity decreases over time. A highly reversible interaction between HCl vapours and the polymer lead to a protonation of the latter resulting in a conductivity increase. Different time constants were observed for most analyte interaction between sorption and desorption, variations by a factors of up to 5.9 in the case for HCl were found. A similar conductivity increase was observed for the oxidising NO_2 and the reducing NH_3 . The NH_3 exposure showed that there is “memory effect” with a diminishing response on repeated exposures. The remarkable conductivity increase on exposure to ammonia is a feature of the composite membrane only. Cast films of POMA show the expected conductivity decrease. This difference is explained in terms of modifications in the available protonation sites, structural changes and a shift in the equilibrium reaction between NH_3 and $\text{NH}_2^- + \text{H}^+$.

Analyte interaction between solvent vapours, results again in a conductivity increase, with the response height being in decreasing order of acetone, toluene, methanol, iso-propanol, chloroform and hexane. A mechanism is proposed for the conductance increase, based on a protonation reaction according to the reaction equilibrium,



and additional structural changes. The application of the composite membrane to a charge flow capacitor, demonstrated a more practical utilisation of the membrane with this transducer. The capacitance changes are more easily measurable compared to the picoampere currents for the coated IDEs.

SPR studies were further used to further elucidate and quantify structural membrane changes and correlate these changes to the observed conductance changes. It was shown that there is a substantial difference in the film swelling for different analytes. The observed thickness changes were in decreasing order from chloroform over acetone, methanol, iso-propanol and toluene to hexane.

Analytes are grouped together based on the interaction taking place and interaction mechanisms are proposed.

The first utilisation of pure arenes for conduction type sensors was demonstrated with the aid of a charge flow transistor. The CFT was fabricated, with a gate opening of 50nm. A ca. 250 nm thick C[4]RA membrane was deposited by casting onto the gate and the modulation of the turn-on response upon exposure to organic solvent vapours was analysed. The turn-on modulation was normalised to the base value of the unexposed membrane and expressed in a modulation factor. The modulation of this factor on exposure to saturated solvent vapours was found to be 45.6 for chloroform, 15 for acetone, 13 for methanol and 0.3 for hexane. The devices showed no cross sensitivity to water vapours. A model for the mechanisms responsible for the modulation of the membrane conductance was developed. Ionic conductivity and a modulation of the electronic conductivity contribute to it. For cast films microcondensation of solvent vapours inside the membrane can lead to a “liquid” phase in which molecules dissociate at the high gate potential and contribute to an ionic conduction. The electrical conduction, which can be described by the hopping of delocalised electrons is modulated by changes in the activation energy and structural changes upon analyte complexation. It was further demonstrated that the CFT can be utilised as a explosion guard, for acetone, with a modulation of the turn-on response by a factor of 1.36 for the concentration of the lower explosion limit.

The detection of organic analytes in water within a system of working electrode, electrolyte, counter electrode was demonstrated. The working electrode consisted of microscope slides, coated with gold on top of which 12 ML of C[4]RA were deposited by the LB method. A detailed and simplified model for the electrode system was proposed. The system allowed the discrimination between polar and non polar organic species in water on the basis of the observed conductivity changes. Polar compounds, like ethanol, chloroform and acetone lead to an increased conductivity whereas non polar compounds like hexane and trichloroethylene lead to conductivity decrease. The response to a variety of analytes and concentration was studied, with the observed conductivity changes being non linearly dependent on the concentrations. Mechanisms for the analyte induced membrane changes are proposed and related to changes in the developed model. Contributing factors to those changes are permeability changes, changes in the dielectric constant, modification of the double layer build up and the modification of sodium ion absorbance into the membrane.

The system provides a very practical method for carrying out a broad spectrum analysis of the organic solvent content in water, with a possible application in the detection of fuel and solvents in water after spillage.

The mechanism of the changing permeability of the LB C[4]RA membranes was in detail studied with the aid of a permeability marker, in a potentiostat controlled system using cyclic voltammetry and impedance spectroscopy. Membrane stability without any redox action was observed in the range of -0.15 to $+0.8$ V. Analysis of the peak heights for the oxidising and reducing currents in the cyclic voltammograms showed that the permeability of the membrane increases under the addition of polar analytes like acetone and chloroform. In the case of 6.75 mM of chloroform the permeability increases by about 1500 %, for 13 mM of acetone by up to 260 %. A model for the working electrode was proposed with the permeability marker in the electrolyte. A modulation of the charge transfer resistance in this model by a factor of up to 2.1 for 6.76 mM of CHCl_3 was observed. Concurrent with the changes in the charge transfer resistance, the parameters for the constant phase representing the working electrode changed from $Q = 0.3829 \cdot 10^{-6}$ F for the unexposed membrane to $Q = 0.2852 \cdot 10^{-6}$ F for the exposed membrane, with a constant n . The value for n was described in terms of the fractal nature of the electrode surface. Permeability increase was independently shown, on the basis of surface plasmon resonance experiments, which further show the membrane stability. Analyte detection on the basis of permeability changes could find implementation as a novel sensing mechanism in electronic tongues.

Suggestions for further work

The thin film deposition deserves further attention with respect to the reproducibility, the developments of alternatives and the effects of the different depositions methods on the analyte interaction.

Efforts to improve the reproducibility of the LB deposition, could be directed toward an additional purification process of the C[4]RA. Chromatographic methods could be employed, to remove any traces of byproducts and residue of the starting material. Alternative deposition methods for ultra thin films could be self assembly, but this requires a chemical modification of the calixresorcinarene. For thicker membranes, as required for the charge flow transistor, sublimation in vacuum at elevated temperatures could provide an alternative. This technique may be able to provide smaller tolerance

margins. But verification of the non-destructive nature of the evaporation process, especially with respect to damage or loss of the aliphatic side chains is required.

Of all the transduction mechanisms investigated, the most interesting one with respect to the influence of the film structure, are the modified electrodes for the detection of organic solvents in water. Here in particular can the presence or absence of pin holes and a modified stacking structure make a substantial difference. With the aid of a self assembled monolayer of calixarene, a simultaneously extremely thin but surface covering film could be utilised, with the possibility for an increased sensitivity.

Modifying the used calixresorcinarene with respect to the number of repeating aromatic structures and/or the substituting side chains can tailor the sensitivity toward a desired target analyte. One important, relatively easy to implement step, would be the doubling or tripling of the aliphatic sidechains length.

A further material related substitution could be made on the site of the polymer. Comparison between literature values for similar or differently synthesised materials showed that there are polymers with a higher inherent conductivity and stability.

A modification of the dimensions of the CFT with respect to the opening in the gate, could make it possible to extend the range of detectable analytes, by increasing the turn-on time and henceforth the sensitivity. Also with the proof of principle accomplished, the prototype design could be changed to a more complex structure, including an interdigitated gate structure.

One additional novel sensing application for calixarene films deserves to be pointed out here: The sensing of the surface potential on calixarene membranes with the aid of a Kelvin probe vibrating capacitor. Surface potential changes upon sorption of some ketones have shown that the target molecules complex in an ordered way. This is registered by an increase in the surface potential. Experiments carried out with spun films of calix[4]resorcinarene $C_{15}H_{33}$ have shown discriminating responses between polar and non polar target analytes in the concentration range of 10000 ppm. This novel mode of recognition deserves further investigation.

Appendix 1

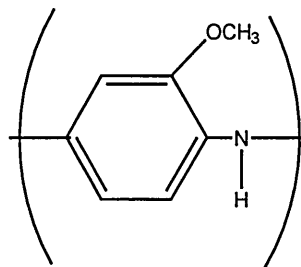
Synthesis and doping procedure of poly-ortho-methoxy aniline

Synthesis:

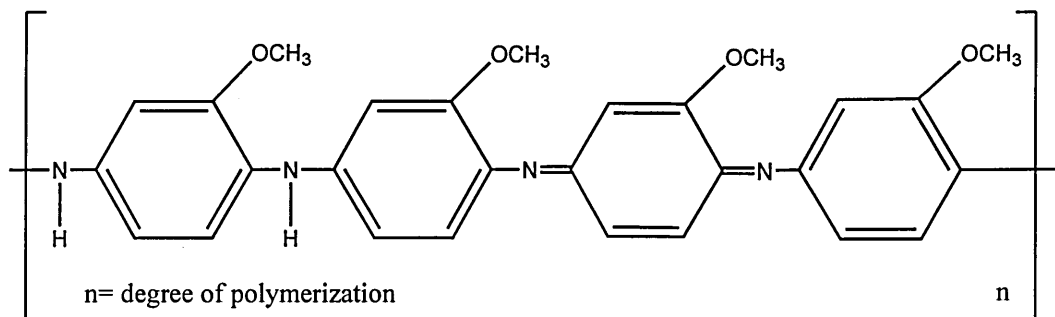
A 0.1 molar orthomethoxyaniline solution in aqueous hydrochloric acid, 1 mol, was cooled down to around 0°C in an ice bath. To this a solution of 0.15 mol ammonium peoxodisulphate ($\text{NH}_4\text{S}_2\text{O}_8$) in aqueous hydrochloric acid, 1 mol, was dropwise added over a period of 1.5 hours. During this process the solution was continuously stirred with a magnetic stirrer, after an additional reaction time of three hours the solution was brought back to room temperature and allowed to react for a further 24 hours. The resulting polymer salt was isolated from the reaction mixture by filtration. The powder was then washed with 1 molar strong hydrochloric acid. The resulting hydrochloric salt was subsequently neutralised with ammonium hydroxide (NH_4OH), 1 mol, to produce the polymer base. The base was washed first with NH_4OH , then water and finally with diethyl ether. After the final rinse the powder was dried out for 12 hours to remove any remaining solvent in an air oven at around 60 °C.

Doping:

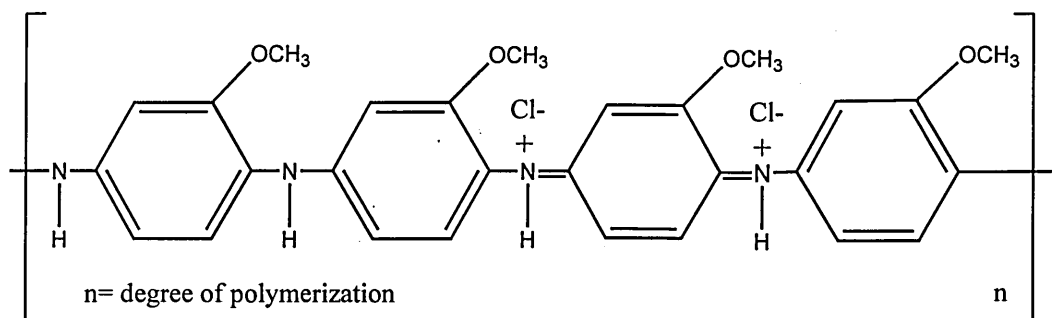
The polymer was doped by leaving the polymer base for 12 hours in aqueous hydrochloric acid, 1 mol, under continuous stirring. After that it was filtered and dried in an air oven at 60 °C for 12 hours. This resulted in poly-ortho-methoxy-aniline hydrochloric salt.



Monomer unit



Poly-ortho-methoxy aniline base



Poly-ortho-methoxy aniline HCl salt

Appendix 2

Description of the Surface Plasmon Resonance principle and measuring set-up

Surface Plasmon Theory

The following is a basic description of the SPR theory and the workings of the SPR set-up as used throughout this thesis. No attempt is being made to give a complete and exhaustive account of the research conducted with SPR or upon it. The description is intended as an aid, to understand the presented results, based on the fact, that this rather novel analytical tool is generally not yet as well known as other analytical methods.

Historically the first observation of SPR can be dated back to 1902, when Wood ^[1] described anomalous diffraction upon diffraction gratings. With a growing understanding of quantum mechanics the ground was laid for the first purposeful studies on SPR at the end of the 1960 by Otto ^[2] and Kretschmann ^[3]. The first practicable application of measurements based on SPR, was the determination of optical parameters of thin metal films ^[3].

A surface plasmon (SP) is a charge density oscillation that can exist at the interface of two media, with dielectric constants of opposite signs. For metal conductors the real part of the dielectric constant is $\epsilon_m < 0$ and for dielectrics $\epsilon_d > 0$, therefore SPs are normally found at metal-air interfaces or metal-dielectric interfaces as shown in Figure 1.

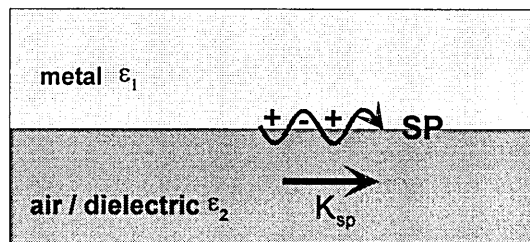


Fig. 1 SPR at a metal-dielectric/air interface

Most suitable for the excitation of SPR, are metals with a high negative value of the real part of the dielectric constant, like silver, gold and aluminium. Though silver gives a better a response, gold is chemically more stable and therefore it is the preferred material for chemical sensing applications.

The charge density wave is accompanied by an electromagnetic wave. Its field strength is at the maximum at the interface and decays evanescently into both media. This surface plasmon wave is a TM polarised wave, with its magnetic vector perpendicular to its direction of propagation. As with all electromagnetic waves the surface plasmon wave has a momentum, given by the wave vector K_{sp} (1).

$$K_{sp} \cong \frac{\omega}{c} \sqrt{\frac{\epsilon_m \epsilon_d}{\epsilon_m + \epsilon_d}} \quad (1)$$

$\epsilon_m = \epsilon_m \text{ real} + i\epsilon_m \text{ imaginary}$, ϵ_d =dielectric constant of dielectric, c = light speed, ω = surface plasmon frequency

SPs can be excited by monochromatic light and by electrons ^[4]. The following discussion of the excitation conditions is restricted to those for light, since this method was used.

For the excitation by light the momentum of the exciting light must match that of SPs wave momentum. For a beam of light falling in at the angle θ , the component of the wave vector parallel to the interface, K_p must be equal to K_{sp} , (2).

$$K_p = K \sin\theta = K_{sp} \quad (2)$$

For light travelling in a dielectric the wave vector is given by (3).

$$K = \frac{\omega}{c} \sqrt{\epsilon} \quad (3)$$

The necessity for matching wave momenta for the resonance conditions means that SPs cannot be achieved by direct illumination of metal surfaces, since the momentum for light coming out of the same medium, at which interface it is to excite SPR can never be enough. In order to increase the wavevector component of the exciting light it should be made incident onto the metal-dielectric interface through a higher index medium, such

as glass. At a given angle of incidence a matching condition between the SP momentum and the horizontal component of the incident beam can be achieved. The geometry of the wave vectors where no excitation takes place is given in Figure 2.

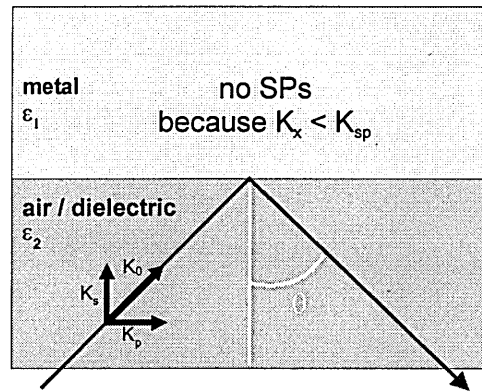


Fig. 2 Wave momenta are not matching therefore no SP excitation occurs

There are two different set-ups that allow a matching of the two wave momenta. These are the Otto configuration [2], involving an air gap between a prism and a metal layer, and the Kretschmann configuration. Only the latter was used in this study since it is a practically more convenient one. Figure 3 shows the Kretschmann arrangement for coupling light into SPs.

For this arrangement a metal film is deposited onto the face of a glass prism and the SPR is excited at the boundary between the metal and the air/dielectric, whereas the light beam is reflected at the glass metal interface. It is the wave, which originates at the glass metal interface that fulfils the coupling conditions at the metal dielectric interface. The prism is needed to raise the momentum of the light wave vector high enough and to set up the right angle on incidence for the light beam as shown in Figure 4.

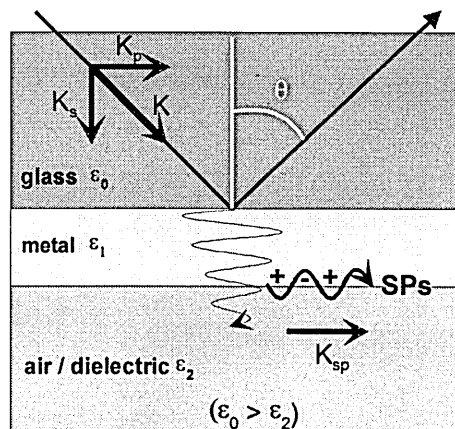


Fig. 3 SPR coupling with Kretschmann arrangement

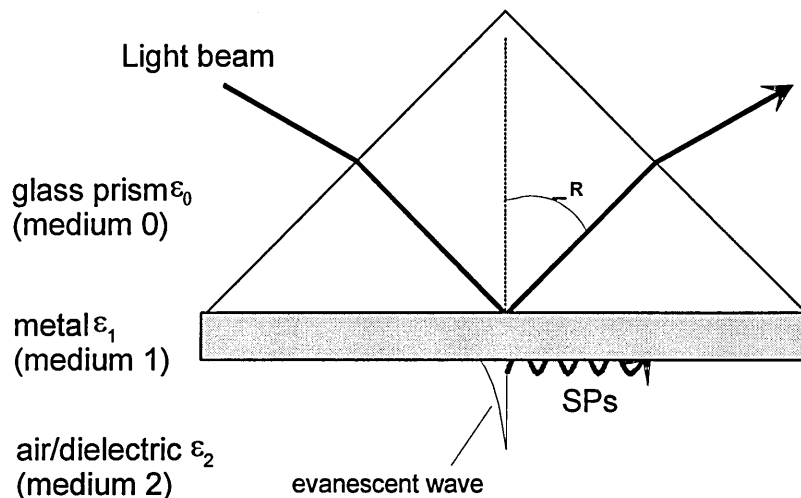


Fig. 4 Prism set-up for the Kretschmann configuration

This evanescent field has a decay length of a few tens of nanometer and therefore coupling SPs is only possible for thin metal films. In most cases the required metal film thickness for optimal coupling is about 40 nm for silver and 48 nm for gold.

If the angle of incidence is changed over a 90 degree range the wave momentum K_p takes on values from 0 to K_0 . Under one particular angle, K_p will match that of K_{sp} and coupling is achieved.

This coupling of light energy from incident beam into the SPR leads to a loss in the light energy that is reflected from the glass metal interface. Therefore the arrangement is called the Attenuated Total Reflection (ATR) configuration. Figure 5 shows the difference in the reflectivity of a uncoated prism (b), for which beyond 42 degrees total internal reflection occurs and the same prism with a metal layer on top (a), where at 44 degrees 95 % of the incident light energy is coupled into the SPs and therefore a dip in the reflected light intensity occurs.

Under the coupling of energies, from the light into the SPs, the electromagnetic field accompanying the SPs extends into the air/dielectric with an exponential decay from the interface with the typical penetration depth given for different metals and wavelength in Table 1 ^[5].

This shallow penetration depth makes the SPR extremely sensitive to changes in the dielectric properties of the material in this area. The whole energy (up to 95 %) that is analysed with this analytical tool is modulated within the penetration depth of the field, it is this fact that makes SPR so well suited for the analysis of thin films.

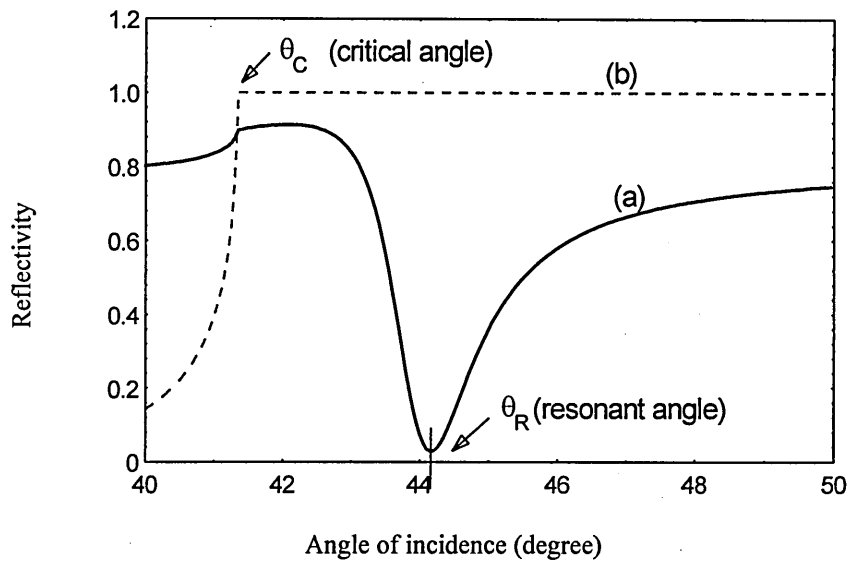


Fig. 5 Reflectivity curve of an uncoated glass prism (b) and coated prism (a)

	Silver	Silver	Gold	Gold
Light wavelength (nm)	630	850	630	850
Penetration depth into dielectric (nm)	219	443	162	400
Concentration of field energy in dielectric (%)	90	95	85	94

Table 1 Description of the electromagnetic field extension of SPs

Changes in the bulk dielectric, beyond the penetration depth, do not affect the coupling at all.

Influences of the various parameters on the SP reflectivity curve

The Fresnel equations given later, allow a quantitative description of the reflectivity curves for a scan over the angle of incidence. This section is provided to aid the visualisation of the rather complex mathematical correlation. Step by step the influence of the various parameters on the reflectivity curve, like the wavelength, changes in the media's refractive index, its thickness, its extinction coefficient and the thickness of the

metal film are presented in a graphical way. Only one parameter changes at one time, however two simultaneous parameter changes, like that of refractive index and thickness changes, as encountered when films swell under the sorption of analyte, can be viewed as a superposition of the two changes.

Kretschmann^[3] carried out studies on the influence of the changes in the wavelength of the light and the variations of the thickness of a silver layer. The SPR measured curves for different metal films are shown in Figure 6.

It can be seen that for a silver film thickness of 49 nm the reflectivity becomes less than 0.03%, which for this configuration is the optimum. This is contrasted by a minimum of 0.75 for films of 89 nm thickness, with minimum coupling. The broadening of the curve for very thin films of 20 and 37 nm thickness must be attributed to adsorption within the metal film. Together with the measurements for different wavelength of light, as shown in Figure 7, Kretschmann was able to determine the complex dielectric constants ϵ_{rAg} and ϵ_{iAg} of silver^[3].

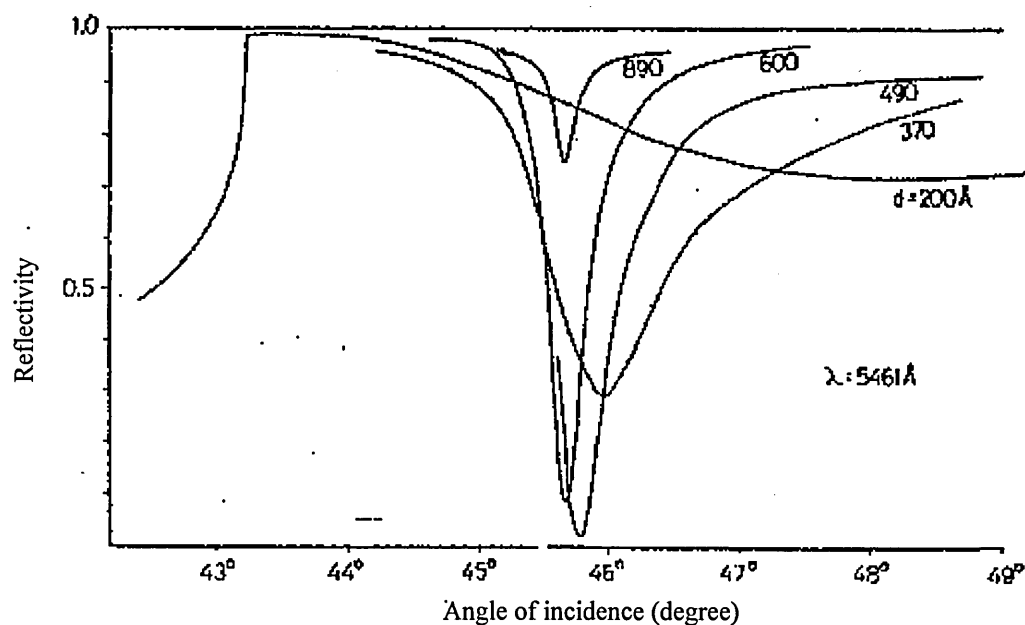


Fig.6 Influence of thickness changes in the metal layer on the reflectivity

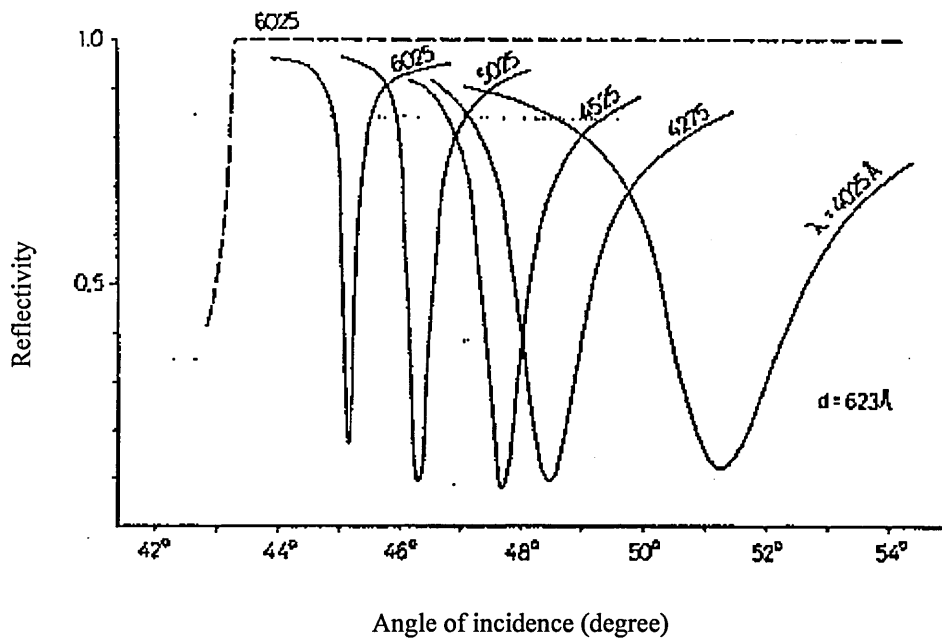


Fig. 7 Changes in the reflectivity curve depending on wavelength changes of the light

In Figure 7, it can be observed that with increasing wavelength the dip in the reflectivity becomes sharper and changes its position to smaller angles, whereas the absolute value of the minimum in reflectance stays, within the experimental error, the same.

The influence of different thin films deposited on top of the metal film are shown in Figure 8, for non-absorbing material. Figure 9 shows the same effect but for an absorbing material.

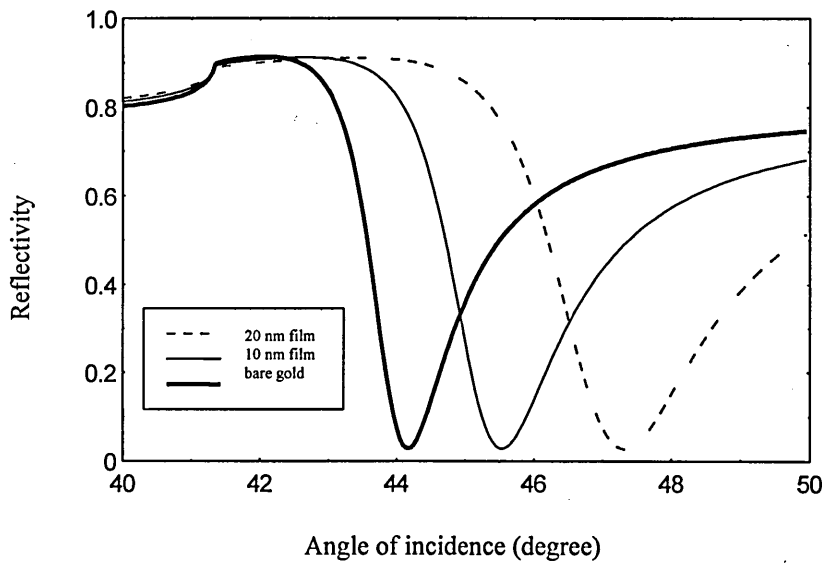


Fig. 8 Calculated results showing the different resonance conditions for a system of a 48

nm gold layer, with organic layers ($n = 1.45$) of 100 nm and 200 nm on top of the gold layer.

The above curves are calculated from the Fresnel equations, but similar results have been published by Pockrand [6] for a layered system of silver and nonabsorbing LiF layers of different thickness values.

In the same study the influence of carbon layers, which are strongly absorbing in the whole of the visible spectrum, was analysed. The results are shown in Figure 9.

Both systems experience the shift of the resonance minima to higher angles for increasing thickness, whereas the depth of the resonance is only affected for absorbing material, that is material having an extinction coefficient > 0 at the exciting wave length.

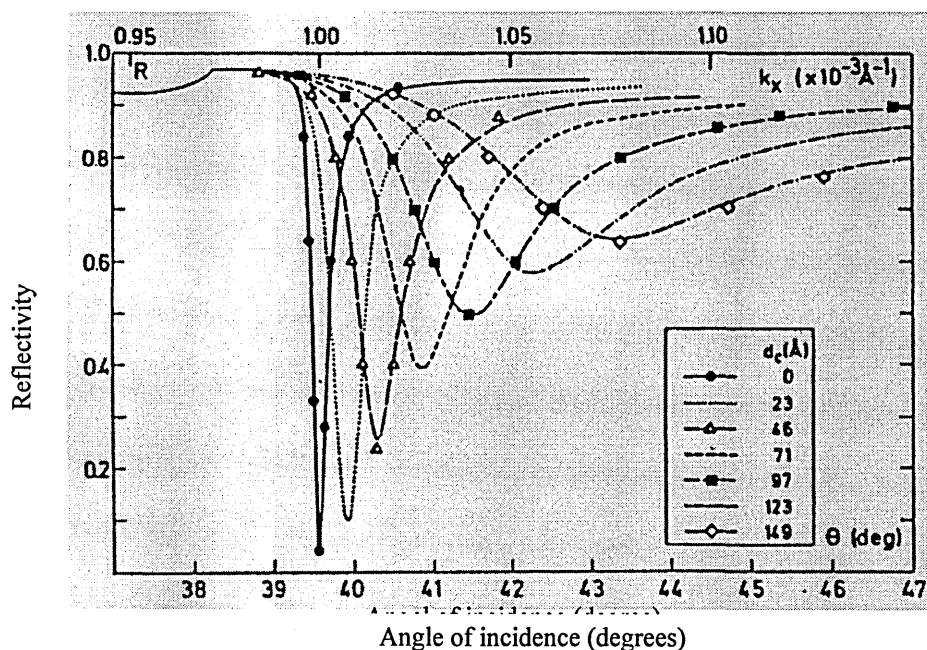


Fig. 9 Measured reflectivity curves for a 49 nm Ag film for light of 647nm wavelength and different carbon film thickness

The SPR experimental set-up

A schematic diagram of the experimental SPR set-up is shown in Figure 10. As a light source, a He-Ne laser with a wavelength of 632 nm is used. Since each laser beam has a near Gaussian distribution of its intensity the fringe part of the beam, is cut out by a

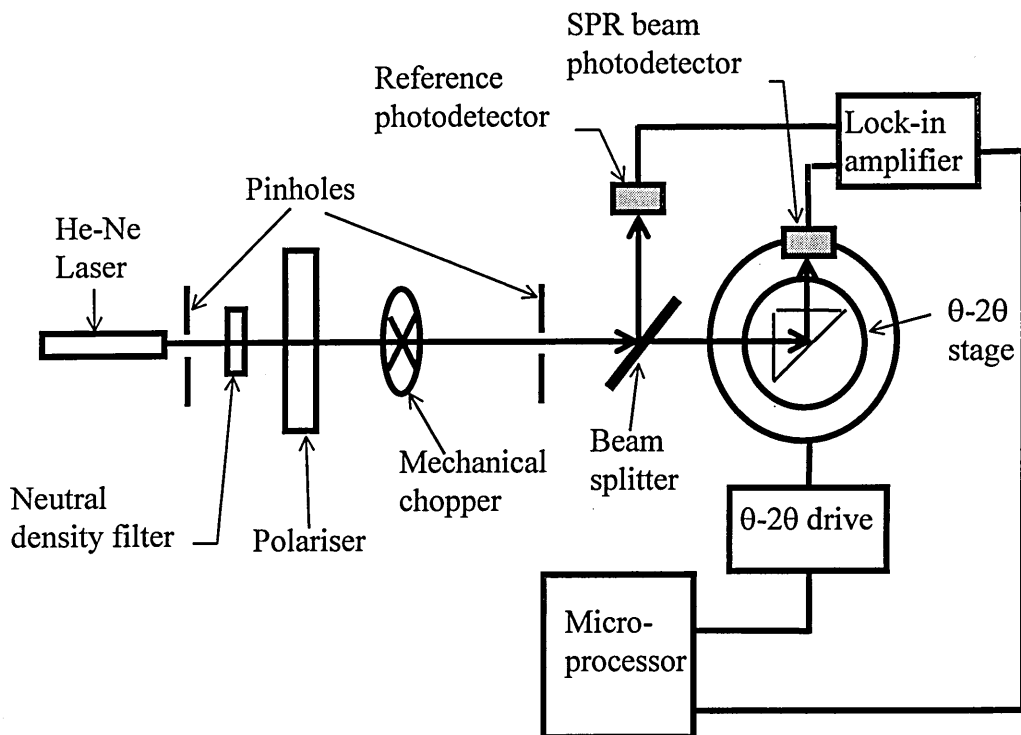


Fig. 10 Schematic of the SPR measurement set-up

narrow aperture. To reduce its intensity, the laser light is first passed through a neutral density filter and then through a p-polariser, which reduces the intensity and allows only the p- polarised portion of the light through. It then passes through a rotating chopper, controlled and co-ordinated with the rest of the set-up via a Scitec Instruments control unit and the PC. A lens focuses the beam through a second narrow aperture onto the face of the prism. Between the lens and the prism a glass plane works as a beam splitter, splitting the beam into a reference path and a measuring path. The reference signal is picked up by a photodetector and forms one part of the signal for the differential input of the lock-in amplifier, Stanford Research Systems Model SR830DSP. After being reflected from the prism the signal is picked up by a second photodetector and forms the other input for the lock-in amplifier. The computer controls the θ - 2θ turntable via a Mc Lean Stepping Motor Controller 3090 to allow for a scan of the angle of incident over 30 to 82 degrees, with an angular resolution of 0.05 degree. A θ - 2θ turntable is needed to keep the measuring photodetector aligned with the reflected beam from the prism, when the angle of incidence changes. During a measurement the differential output of the optical lock-in amplifier is recorded for every step. The function of the optical lock-in amplifier is twofold. It eliminates the noise caused by ambient light falling onto the photodetectors. This is achieved by subtracting the signal of the light falling onto the detector when the chopper blocks the path of the laser from the intensity when the light

is passing between the teeth of the chopper. This makes the experiments merely more convenient since if the measurements were conducted in complete darkness the chopper and the lock-in amplifier would not be necessary. The second function of providing a chopped signal to the photodetector is more vital. An AC signal can be generated from this and this enables a lower noise amplification.

Vibrational influences are minimised by mounting the whole set-up on an optical bench. Prior to any measurements the set-up requires calibration. This makes sure that the alignment of the light beam is correct and eliminates any offset in the angle measurements. Furthermore it defines the intensity for the total internal reflection of the prism, used to normalise the measurements.

For any gas or liquid exposure measurements a chamber needs to be attached to the prism. This is done by pressing a PTFE chamber, sealing with an O-ring onto the face of the prism via a simple screwing mechanism. This is shown schematically in Figure 11.

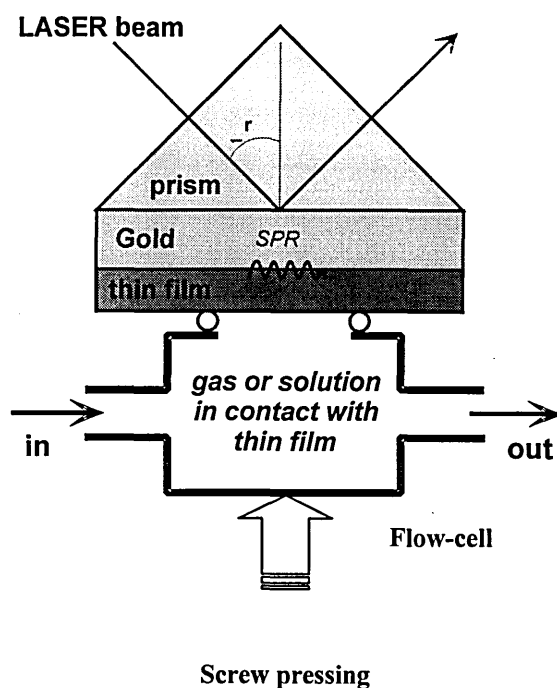


Fig. 11 Flow cell attached to measuring prism

Major application areas of SPR studies

Measurement of physical quantities

Measurements of displacement ^[7] and angular position ^[8] have been reported making use of the extreme sensitivity to changes in the angle of incidence. Others include a temperature sensor based upon the thermo-optic effect in hydrogenated amorphous silicon ^[9] or the determination of thin film properties for dielectric layers ^[10] and metals ^[3].

Chemical Sensing

In its simplest form measurements of the refractive index using SPR can be used to determine the concentration of analytes, as for example during the monitoring of distillation processes ^[11]. But the majority of applications rely on variations in a thin film on top of the metal, due to, adsorption, absorption and chemical reaction with the analyte. A variety of polymer based studies have been conducted, using polyethylene glycol film ^[12], polyfluoroalkylsiloxane ^[13], polydimethylsiloxane ^[14] and Teflon for the detection of different hydrocarbons, aromatic hydrocarbons and chlorinated hydrocarbons. Another major branch of studies dealt with phthalocyanine derivatives, toluene has been detected with copper–nickel phthalocyanine ^[15] and NO₂ with copper phthalocyanine ^[16] and cobalt phthalocyanine ^[17].

A few reports have appeared where the sensing action does not rely on a sensing membrane on top of the metal, but where the reaction under investigation affects the metal layer directly. One deals with the detection of molecular hydrogen by sorption of the hydrogen into a palladium film ^[18]. NO₂ was detected similarly by chemisorption onto an uncoated gold layer ^[19].

An interesting combination of anodic stripping voltammetry and SPR has led to the detection of Cu and Pb ions ^[20] in aqueous solution.

Biosensing

A great field in modern biology is the study of complex formations between biomolecules. These can be of the antigen/antibody, drug/protein, hormone/receptor or even bacteria/virus type. The high molecular weight of most of the involved molecules makes measurements of the film thickness and the refractive index changes very successful. One of the major challenges in those studies is the immobilisation of the sensing layer onto the metal of the substrate without changing the complexation properties. The reactions are highly specific and a slight distortion in the shape of the molecules upon immobilisation in a matrix can substantially change the complexing properties, by making complexing sites unavailable. The last 8 years have seen an explosion in literature dealing with SPR in bioanalytical applications, nearly 800 papers have appeared in this time. The first application of SPR to biosensing was demonstrated in 1983 ^[21]. Early works were mainly focussing on antigen-antibody reactions like the streptavidin-biotin reaction. In 1994 the first survey on a real-time interaction analysis appeared ^[22], this opened up the possibilities of determining the kinetic and thermodynamic constants of biomolecular interactions.

An emerging field is the examination of protein-protein and protein-DNA interactions ^[23], these allow even the detection of conformational changes in an immobilised protein. A novel principle, for a biosensor was presented by Sabot ^[24] where not the complexation of a biological species is registered but the removal of a polymer by degradation due to an enzyme reaction.

For a more complete overview of biosensors using SPR the reader is referred to the excellent database maintained by BIAcore ^[25].

Moving from an analytical tool to a sensor

So far only very few commercial products using SPR have entered the market. The first was developed by the Swedish company BIAcore, in 1990, which offers today a variety of instruments for biological systems ^[25]. A further step towards the realisation of a portable sensor is the development of the T1-SPR-1 experimenters kit from Texas Instruments ^[26]. This device is already portable and uses one shot samples but the analysis of the experimental data still relies on a PC operated program. The number of commercially available laboratory systems is steadily increasing ^[27, 28] and it can be

expected that developments of these, will eventually move towards integrated systems bordering on sensor like devices.

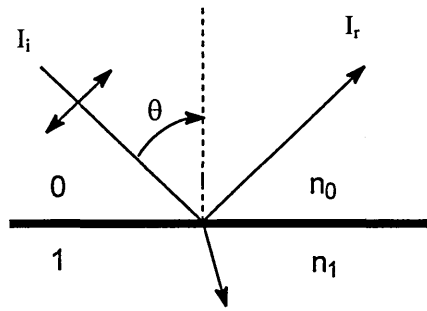
Future trends

It can be expected that the lower detection limit will be improved beyond the current mark of ca. 1pg/mm^2 surface coverage, allowing the detection of low concentrations of low molecular weight analytes. A further area, which is just emerging, is that of the multi-channel SPR detection. This will be of great aid for high throughput screening systems, as used for the testing of pharmaceuticals and in advanced recognition systems to filter out non specific background effects, in complex samples.

Fresnel equations

Fresnel developed the theory governing the reflection and refraction of light in a stratified system at the beginning of the 18th century. The stratified systems are not restricted to transparent media but also include strongly absorbing materials, like metals. The equations derived by Fresnel are widely applied in the calculation of optical properties of bi- or multilayer systems.

The reflectivity of a system depends on several optical parameters like: refractive index, number of strata, dimensions of strata, wavelength of the light, angle of incidence of the light and the polarisation of the light with respect to the normal of the angle of incidence. The polarisation of the light can be expressed from a combination of two equations, one for light polarised parallel to the plane of incidence (p-polarised) and one for light polarised perpendicular to the plane of incidence (s-polarised). The simplest system that is described by the Fresnel equations for the reflectivity is a two layer system, where the incident light traverses one layer and is partially reflected at the border between layer one and two, back into layer one. This is shown schematically for a p-polarised light beam (p- polarised light is necessary for SPR and the equations only apply for this) in Figure 13.



n_0 = refractive index of medium one, n_1 = refractive index of medium two, θ = angle of incidence, I_r = Intensity of reflected beam, I_i = Intensity of incident beam

Fig 13. Partial reflection of light in a two layer system

The reflectivity of the light when the plane of polarisation is parallel to the plane of incidence in terms of I_r and I_i is described by (4).

$$R_{01} = \frac{I_r}{I_i} = \frac{\epsilon_0 k_{1z} - \epsilon_1 k_{0z}}{\epsilon_0 k_{1z} + \epsilon_1 k_{0z}} \quad (4)$$

$\epsilon_i = n_i^2$, λ = wavelength of the light, ϵ_i = dielectric constant of medium i (this value is wavelength dependent and for absorbing media it is complex), n_i = refractive index of media i

with K defined by (5).

$$k_{iz} = \left(\frac{2\pi}{\lambda} \right) \sqrt{\epsilon_i - \epsilon_0 \sin^2(\theta)} \quad (5)$$

k_i = extinction coefficient, all subscripts 0 or 1 are referring to the respective media

The actual SPR experiments are based on a four layer system as schematically shown in Figure 14.

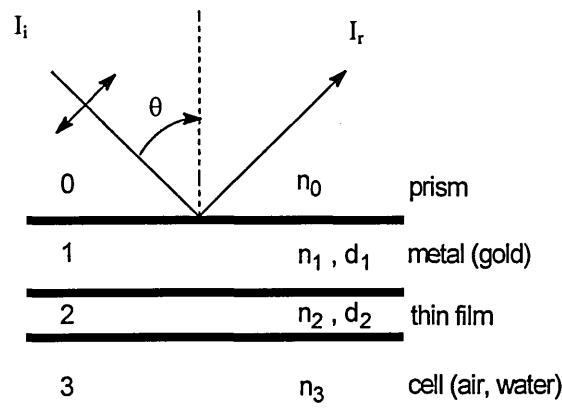


Fig. 14 Reflection condition in the SPR experiment

The gold is not in direct contact with the prism, but is on top of a glass side brought into contact with the prism by an index matching fluid, this can be reduced to a single layer, assuming no scattering and reflection at the border. For the above given system the reflectivity is a function of θ , n_0 , n_1 , d_1 , n_2 , d_2 , n_3 and λ .

Since n_1 and n_2 are normally complex the overall reflectivity is defined as follows, based on the results of the two layer system.

$$R_{0123} = R_{01} * \frac{Z_{0123}}{D_{0123}}$$

with

$$D_{0123} = \left(\frac{k_{3z}}{\varepsilon_3} + \frac{k_{1z}}{\varepsilon_1} \right) - j \cdot \operatorname{tg}(k_{2z}d_2) \left(\frac{k_{3z}k_{1z}}{k_{2z}} \frac{\varepsilon_2}{\varepsilon_1\varepsilon_3} + \frac{k_{2z}}{\varepsilon_2} \right) + r_{01} \exp(2jk_{1z}d_1) \left[\left(\frac{k_{1z}}{\varepsilon_1} - \frac{k_{3z}}{\varepsilon_3} \right) - j \cdot \operatorname{tg}(k_{2z}d_2) \left(\frac{k_{3z}k_{1z}}{k_{2z}} \frac{\varepsilon_2}{\varepsilon_1\varepsilon_3} - \frac{k_{2z}}{\varepsilon_2} \right) \right]$$

and

$$Z_{0123} = \left(\frac{k_{3z}}{\varepsilon_3} + \frac{k_{1z}}{\varepsilon_1} \right) - j \cdot \operatorname{tg}(k_{2z}d_2) \left(\frac{k_{3z}k_{1z}}{k_{2z}} \frac{\varepsilon_2}{\varepsilon_1\varepsilon_3} + \frac{k_{2z}}{\varepsilon_2} \right) + \frac{1}{r_{01}} \exp(2jk_{1z}d_1) \left[\left(\frac{k_{1z}}{\varepsilon_1} - \frac{k_{3z}}{\varepsilon_3} \right) - j \cdot \operatorname{tg}(k_{2z}d_2) \left(\frac{k_{3z}k_{1z}}{k_{2z}} \frac{\varepsilon_2}{\varepsilon_1\varepsilon_3} - \frac{k_{2z}}{\varepsilon_2} \right) \right]$$

The definitions of the indexes are identical to that given for the two layer system.

The experimental data recorded with the set-up was fitted to the above equations to extract the unknown parameters. For this a minimum least square fit procedure was employed. The program, that has been described in previous works ^[29], allows the determination of 5 variables, but it was practice to determine only 1 or at maximum two parameters in one fitting procedure. The following parameters, Table 2, were used as the starting values for the fitting procedure.

Material	Refractive index	Extinction coefficient
Glass	1.515	0
Gold	0.2	3.25
Air	1	0

Table 2 Starting values used during the fitting procedure

References

- ¹ R. W. Wood, *Phil. Mag.*, 4, 396, 1902
- ² A. Otto, *Z. Phys.*, 216, 398, 1968
- ³ E. Kretschmann, *Z. Phys.*, 241, 313, 1971
- ⁴ C. J. Powell and J. B. Swan, *Phys. Rev.*, 118, 640, 1960
- ⁵ J. Holmola et al, *Sens. & Actuat. B*, 54, 3-15, 1999
- ⁶ I. Pockrand, *Surf. Sci.*, 72, 577, 1978
- ⁷ G. Margehari, *Proc. SPIE* 2783, 211-220, 1996
- ⁸ J.K. Schaller, *Proc. SPIE* 3098, 476-486, 1997
- ⁹ B. Chadwick, *J. Appl. Phys* 32, 2716-2717, 1993
- ¹⁰ E. Helene et al, *Optics Communications*, 82, 425-431, 1991
- ¹¹ E.G. Ruitz, *Sens & Actuat A* 37-38, 221-225, 1993
- ¹² S. Miwa, *Thin Solid Films* 281-282, 215-225, 1993
- ¹³ A. Abdelghani, *Sens. & Actuat. B* 38-39, 407-410, 1997
- ¹⁴ M. Niggermann, *Sens. & Actuat. B* 34, 328-333, 1996
- ¹⁵ C. Granito, *Thin Solid Films* 284-285, 98-101, 1996
- ¹⁶ D.G. Zhu, *Sens. & Actuat. B*, 265-269, 1990
- ¹⁷ P.S. Vukusic, *Thin Solid Films* 221, 311-317, 1992

- ¹⁸ B. Chadwick, Appl. Surface Sci. 68, 134-138, 1993
- ¹⁹ G.J. Aswell, Electron. Letter. 32, 2089-2091, 1996
- ²⁰ C.C. Jung, Sens. & Actuat. B35, 143-147, 1996
- ²¹ B. Liedberg, Biosensors Bioelectron. 10, 299-304, 1983
- ²² I. Lundstrom, Biosensors Bioelectron. 9, 185-189, 1994
- ²³ D.R. Mernagh, Biol. Chem. 379, 497-503, 1998
- ²⁴ A. Sabot, Proc. Transducer 99, 333-335, 1999
- ²⁵ <http://www.biacore.com>
- ²⁶ <http://www.ti.com/spr>
- ²⁷ <http://www.biosensors.com>
- ²⁸ <http://www.biotul.com>
- ²⁹ Y.M. Shirshov 6th EUR. Con. Organised Films (ECOF 6) Sheffield, 517, 1996

Appendix 3

Production parameters and material details for the Charge Flow Transistor and Charge Flow Capacitor

Substrate: 3 inch (100) n-type silicon wafer, with a substrate resistivity of 1-10 Ω cm

Growth of the doping masking oxide: The wafers are loaded in a preheated oxidation furnace at 1000 °C for their wet oxidation. A saturated water vapour/nitrogen stream flows through the furnace chamber for 4 hours, this grows a 1 μ m silicon dioxide. The wafers are then unloaded from the 1 m long oxidation tube by withdrawing them at a rate of 10 cm every 20 seconds. Subsequently they are cooled down to room temperature.

Spin coating of negative photoresist: The wafer is mounted on a vacuum chuck and the photoresist (HNR 120) is pipetted onto the stationary wafer. It is then accelerated to 1000 rpm to allow an even spreading out and then to 5000 rpm at which speed it is kept for 25 seconds. The softbake is carried out on a hotplate at 85 degrees for 45 seconds. This process yields a resist thickness of 1 μ m.

Patterning of the negative resist: The exposure for the photolithography of the resist is done in a Carl Suss MJB3 mask aligner through mask 1. The exposure time is set to three seconds. The resist is then developed by bathing it in 100 % developer HNRD 120 for 45 seconds, immersion in 50 % developer/ 50 % n-butyl acetate for 10 seconds and finally rinsing with n-butyl acetate for 10 seconds and drying in a stream of nitrogen. The image is fixed on the wafer by hardbaking it for 60 seconds on a hotplate at 135 °C.

Silicon dioxide etch: The exposed silicon dioxide is etched in a commercial etch consisting of hydrofluoric acid with an ammonium fluoride buffer and water in a ratio of 7:1. The etch rate at this concentration is 100 nm/min, requiring an etchtime of 10 minutes. During the etch process the wafers are continuously agitated. After etch completion the wafers are spray rinsed with deionised water.

Removal of developed negative resist: The resist is removed in a barrel asher at an etch rate of about 25 nm/min, resulting in an ashing time of 45 minutes.

Contact etch: The thin silicon dioxide that grows under the energetic oxygen bombardment in the barrel asher, is removed in a contact edge with a solution of hydrofluoric acid in water in a concentration of 1:10. This etch only skims the surface of the oxide and at an etch rate of 10 nm/min the contact etch is completed in 2 minutes.

P-type diffusion doping: The silicon wafers are loaded, with boron-trioxide wafers between them, in a boat and introduced into the diffusion furnace. The oven is heated to 1050 degrees and under a stream of nitrogen the boron-trioxide migrates out of the boron wafer and is deposited onto the silicon wafer. From there it diffuses into the silicon according to the gas diffusion equations. The time for a p-type doping resulting in a surface concentration of $4 \cdot 10^{20}$ atoms is 50 minutes.

Removal of the doping masking oxide and the boron glaze: The SiO_2 and the boron glaze covering the whole wafer are removed by a 10-min etch in HF.

Growing the field oxide: The field oxide is again grown in a wet oxidation process. The growth rate is 200 nm/hour in a saturated water vapour/nitrogen atmosphere. The temperature is 1000 °C and the growth time is 5 hours. Simultaneously the heat treatment has an annealing effect on the introduced dopants subsequently the wafers are removed from the oven as described earlier.

Spin coating of negative photoresist: As described above.

Opening up the window for the gate oxide: The patterning of the wafer with mask 2 is identical to the patterning with mask 1. The same is true for the development and the silicon dioxide etch but this time with an increased etch time of 12 minutes. The remaining resist is again removed in the barrel asher and the accompanying thin oxide is removed by a further contact etch.

Growth of the gate oxide: The high quality gate oxide is grown with a process of dry oxidation, in a stream of pure oxygen at a temperature of 1000 degrees Celsius. The growth rate is 60 nm/hour and the resulting oxide thickness is 120 nm.

Verifying the gate oxide thickness via ellipsometric measurements: The oxide thickness is checked on a reference wafer on which the same oxide was grown.

Spin coating of negative resist: As described above.

Patterning for the contact holes leading to the p-type silicon wells: Mask 3 is used to transfer the pattern for the contact holes onto the wafer following the procedures described above.

Etching contact holes into the field oxide: The pattern on the resist is developed, fixed and after completion of the HF etch the remaining resist is again removed in the barrel asher.

Metallisation: The native oxide on the back of the wafer is removed by wiping it with cotton buds soaked in 40% HF, until the hydrophilic-hydrophobic surface transition occurs. The wafers are then loaded directly into an Edwards vacuum evaporator which is then pumped down to a pressure of 10^{-3} mbar. 100 nm of aluminium are then evaporated onto the back of the wafer at a rate of 3nm/second.

The evaporator is then opened and the wafer turned over and again pumped down. A seed layer of 3 nm of chromium is evaporated at a rate of 0.2 nm/second and without breaking the vacuum 100 nm of gold are evaporated onto the chromium at a rate of 3 nm/second.

Patterning the metallisation: The source, drain and gate need to be patterned, this is done with mask 4, using a positive photoresist. The positive resist (HIPR 6512) is pipetted onto the stationary wafer, accelerated to 1000 rpm to spread out and then further accelerated to 6000 rpm for 25 seconds. It is then softbaked at 90 degrees for 60 seconds. After exposure to the UV light through mask 4, it is developed with a two-stage puddle method. The wafer is completely covered with developer (HPRD402), by pouring it on, developed for 45 seconds and then washed with water. The following hardback at 120 degrees for 60 seconds fixes the pattern.

Metal etch: For the gold etch the wafer is mounted on a pedestal and the etch, consisting of 3% potassium iodide in 5% aqueous iodine, is poured over the wafer to form a puddle completely covering the wafer surface. After 60 seconds the etch is removed by pouring water over it. After drying the wafer in a stream of nitrogen the quality of the etch is inspected under an optical microscope. Then the chromium layer is etched with a commercial chromium etch, (Microposit Chrome Etch 18) by agitating the

wafer in a bath of it for 25 seconds. Completeness of the etch is again verified under the microscope. Finally the photoresist is removed by agitating the wafer in an acetone tank for 60 seconds and then rinsed with clean water and dried in nitrogen.

Heat treatment: To provide good ohmic contacts the wafer undergoes a heat treatment in an oven at 450 degrees for 30 minutes in a nitrogen atmosphere, this allows the metal to fuse and migrate into the substrate.

Passivation of the source, drain and gate: For the passivation, negative resist is spun on, patterned with mask 5, developed and hardbaked. The hardbaked resist now forms the passivation layer. This step completes the CFT production.

Several inspections during the process have been omitted in this description since they are depending on the experience of the user with the fabrication steps, and are therefore very individual parameters.

For the CFC, the production parameters for the individual steps are identical with that of the CFT, but only the following steps are needed.

Growing of the gate oxide: Dry oxidation of the silicon wafer to grow 120 nm of SiO₂.

Metallisation: Gold and chromium deposition on the front, and aluminium deposition for the back contact.

Patterning of the front metallisation: Spinning on positive resist, using mask 6, with subsequent developing and fixing.

Metal etch: Gold and chromium is selectively etched.

Removal of remaining photoresist: Rinsing with acetone.

Heat treatment: Enhancing adhesion.